Multiscale Modelling of Adsorption by MOFs - CO_2-Separation from Flue Gas and Olefin/Paraffin-Separation as Examples

Vom Promotionsausschuss der
Technischen Universität Hamburg
zur Erlangung des akademischen Grades
Doktor-Ingenieur (Dr.-Ing.)
genehmigte Dissertation

von

Stephan Theodor Herbert Bendt

aus
Hamburg

2020

1. Gutachter: Prof. Dr. Prof. e. h. Dr. h. c. Frerich J. Keil
2. Gutachter: Prof. Dr. Irina Smirnova
3. Gutachter: Prof. Dr. Georg Fieg
Tag der mündlichen Prüfung: 21. Juli 2020

Acknowledgments

I was very fortunate to work at the institute of chemical reaction engineering at the TUHH for almost six years. In this time, I have grown as a researcher and as a person because of all the wonderful people working and living beside me. Therefore, I would like to take the opportunity to express my appreciation to all of you.

First and foremost, I would like to express my deepest gratitude to Professor Frerich J. Keil, who gave me the opportunity to work as a scientist in his institute. The door to your office was always open, both literally and figuratively. You provided me with guidance, support, and trust during all those years. You allowed me to freely pursue my research interests and cooperate with other universities and groups to achieve my goals. I have learned a lot as a scientist under your supervision. For all of that I am and always will be very grateful to you. Thank you very much.

I would also like to thank Professor Raimund Horn for letting me continue my studies and integrating me as a member of your staff. Your encouragements and advice were always welcomed and helped me during my time at the institute tremendously. The same goes without saying for Oliver Korup as well. Your positive attitude created a great atmosphere every day.

Without the continuous technical support of Klaus Mandel the simulations, and thus, this thesis would not have been possible. Not only the maintenance of the cluster was very valuable but also my constant wishes for more cores and other things were never a problem. Thank you very much for your help. Mrs. Oppelaar was always there for me whenever administrative duties came up or when a little chat was needed. Thank you. Special thanks go out to Christina Laarmann. I cannot remember, how often we were chatting in the hallway, office or lab. You were always there if I needed help. Thanks a lot! Furthermore, I want to thank Achim Bartsch for the discussions and your counsel. You, too, always had an open ear and door for me. Thank you.

I got my first taste of molecular simulation while being under the supervision of Nils Zimmermann, who not only became a coworker but a friend. Your passion and teaching send me on the path towards this research topic, which is the main reason I started this journey in the first place. Furthermore, the encouragement and the advice you provided will always be something for which I am very grateful to you. Thank you very much. Another colleague and friend is Sven Jakobtorweihen, who helped me succeed in this research field. The time and energy you had to put into discussions helped me overcome roadblocks and propelled me towards success. Thank you very

much. The first student I supervised was Ying Dong, who later became a valued colleague and friend as well. The time talking about work, culture, and everything else in the kitchen is something I will always very fondly remember.

I was very fortunate to work alongside wonderful and capable people, who have become more than colleagues to me: Viktor, Bahne, Jan, Andres, Birte, and Sebastian. The friendship with all of you and the good times we had are very much appreciated. Thank you!

Many thanks go out to my other co-workers for the good time at work: Diana, Alexander, Timur, Ludwig and Michael. I had the opportunity and pleasure to supervise several very capable students during my time as a PhD student: Ying (project work, student assistant, and master thesis), Akira (bachelor thesis and student assistant), Merle (bachelor thesis and student assistant), Felix (project work), Nils (bachelor thesis and student assistant), Jonas (bachelor thesis), and Priyanga (student assistant). To me, the people I came to see and work with in the institute on a everyday basis were one of the main reasons those six years did not feel like work. This is something I will always cherish.

I have been blessed with some amazing friends who I have known for most of my life: Philipp, Mirko, Claudia, and Sarah. Thank you very much for your continuous support. The same goes for Georg and Denise, Wolfgang and Paula, Gerrit and Luzi as well as Arne and Tanja. Thank you! You are the best.

Last but not least, I want to say thank you to my family: Karin, Jürgen, Oliver, Ana, Meike, Thomas, Lia, Nina, and Lennard. Unfortunately, my grandparents and Katharina passed away before my graduation. Rest in peace. Of course, my parents, Heidrun and Uwe, played a huge part in my life. Without your support, understanding and counsel, I would not have been able to accomplish this. Your unconditional love and help even in the darkest of times made this achievement possible in the first place. Thank you both so very much.

Preface

All of the research presented in this work was carried out under the priority program SPP 1570 titled *"Poröse Medien mit definierter Porenstruktur in der Verfahrenstechnik – Modellierung, Anwendungen, Synthese"* supported by the Deutsche Forschungsgesellschaft (DFG). The part about CO_2 adsorption from flue gas was a joint project with Prof. B. Smit and his group from the Chemical Engineering and Chemistry Department at University of California Berkeley (USA) and the laboratory for molecular simulations at the École Polytechnique Fédérale de Lausanne (Switzerland). The results with respect to the olefin/paraffin-separation were done in cooperation with Prof. M. Hartmann's group of the Erlangen Catalysis Resource Center (Germany) and with Prof. H.-J. Holdt's group of the Institute of Inorganic Chemistry of Potsdam University (Germany).

Despite this being a single-author thesis, the first person plural will be used throughout the entire text. This is done to acknowledge and appreciate all the people who have contributed. In addition to the official supervisor, ideas, results, and problems were discussed with colleagues, project partners, and students. Consequently, 'we' is used as a subject.

Contents

Part I

Exposition

1 Introduction

Generally speaking, obtaining new knowledge, observing new phenomena or finding solutions to given problems are the driving forces behind all areas of scientific research. With the introduction of the computer, scientists have been empowered even more, since it allowed them to make "experiments", which are very hard to do or even impossible given their time or length scale or thermodynamic conditions, and thus, supporting experimental studies tremendously. It has been shown historically that scientists can tackle difficult challenges quickly and successfully at the same time once their efforts are focused on the same goal.

To date, the present climate change is one of the most important challenges for mankind and is, therefore, one of the top priorities for scientists. According to their 2001 report, the Intergovernmental Panel on Climate Change (IPCC) made human activities because of the greenhouse gas emissions responsible for the increase of greenhouse gas concentrations in the earth's atmosphere, and thus, the initiator of the global warming.[1] There had been claims that only parts of the scientific community agreed on the premise of the IPCC report or that the research regarding this topic inherits high uncertainty.[2,3] However, the opposite is the case as argued by Oreskes,[2] since multiple well-respected institutions, like the National Academy of Sciences, the American Meteorological Society, and the American Geophysical Union for example, published similar findings. Out of all greenhouse gases, carbon dioxide (CO_2) has been identified as one of the main culprits for the present climate change.[4] In 2017, Germany emitted 907 million tons of greenhouse gases into the atmosphere whereas CO_2 accounted for 88%.[5] Consequently, reducing the amount of its emissions into the atmosphere is an urging task.[4,6,7] Contributing with more than 85%, the main source of CO_2 emissions is the usage of fossil fuels, like coal, oil, and gas,[5] for which mainly the energy generation sector is responsible, especially coal-based power plants.[8–10] Hence, removing the greenhouse gas CO_2 from the flue gas of power plants

is an important step to prevent irreversible damages to the earth and its climate. The current state-of-the-art technology found in power plants, amine scrubbing, consists of an absorber and a stripper part.[11] In the former, the CO_2 is removed by absorption into the amine solution, which flows countercurrently to the gas. The regeneration of the saturated liquid is done in the stripper in which the saturated solution is heated, effectively removing the CO_2 from the amine solution. Because of the boiling of the solution, high amounts of energy are required during this step.[12,13] Adsorption processes, a potential alternative, do not include this energy expensive regeneration step and also work at ambient conditions. It was found that nanoporous materials, whether they are based on amine-functionalized silica,[14–19] carbon-based materials,[20–24] zeolites[20,25–31] or metal-organic frameworks (MOFs),[32–43] potentially make adsorption processes more than a valid option to replace the amine scrubbing technology.

Another important and difficult separation problem from an industrial point of view is the separation of olefin/paraffin-mixtures.[44,45] Olefins like propene and ethene are the two most important organic feedstocks in the chemical industry,[46] whereas ethene exceeded all other chemicals with a worldwide production of 141 million tons in 2011.[47] Those materials are widely used as precursors, especially for the production of plastics,[48] making them 2-4 times more valuable compared to their paraffin counterparts ethane and propane.[46] The separation of these two components is considered to be very difficult, because of similar properties and structures, leading to close boiling points: ethane (184.6 K) and ethene (169.5 K) as well as propane (225.6 K) and propene (230.9 K), respectively.[49,50] The state-of-the-art separation technique is the cryogenic distillation, which is a distillation at very low temperatures. This distillation column consists of over 200 trays and runs at a high reflux ratio, high pressures and very low temperatures in order to separate the compounds successfully.[44] In this distillation unit up to a third of the whole refrigeration energy of the ethene producing plant is consumed.[51] This results in a huge energy consumption of about 127 x 10^{15} J per year worldwide,[44] summing up to about 85% of the entire operational costs.[52] Thus, there is potential of saving a lot of energy and capital substituting this process with a less energy-demanding one.[44] Similar to the CO_2 sequestration from flue gas, (physical) adsorption processes, like pressure swing adsorption (PSA) or membrane processes, are referred to as promising alternatives to the cryogenic distillation. They could reduce the environmental impact and cost significantly due to a lower energy consumption and the wide range of potential adsorbents.[53,54] Research has been and still is dedicated to search for suitable materials, which have to be chemi-

cal, thermal, and pressure-stable enough to persist in a harsh environment present in the petroleum industry, while having the properties to separate the paraffin/olefin mixtures effectively.[55] Appearing as promising adsorption materials, metal-organic frameworks (MOFs) are widely considered to fulfill requirements of such materials, because of their large surface areas, high porosity, flexible and robust frameworks, and controllable properties.[56–59]

1.1 Goal

The goal of this thesis is to develop a methodology for a multi-scale design of adsorption processes based on computer simulations, which could support and complement the common experimental design process in engineering, exemplarily for the two aforementioned separation problems of CO_2 sequestration from flue gas and olefin/paraffin-separation using metal-organic frameworks (MOFs) as adsorption materials. Here, density functional theory (DFT), Monte Carlo (MC), Molecular Dynamics (MD), and fixed-bed adsorption process simulation are used as means to

- obtain adsorption and diffusion properties of guest species in a given adsorption material on an atomistic scale,
- simulate the fixed-bed adsorber behavior of the given system (adsorption material and guest molecules) at a large scale.

1.2 Outline

This work is divided into five parts: In the first part, *Exposition*, the reader is introduced to the motivation and the theoretical background (Chapter 2) of the thesis. It is explained what mechanisms and phenomenona are present in (nano-)porous materials, i.e. adsorption and diffusion. Furthermore, metal-organic frameworks (MOFs) are described as well as the fundamental basics regarding Density Functional Theory (DFT), Monte Carlo (MC), and Molecular Simulations (MD). The second part, *CO_2 sequestration from flue gas*, is dedicated to the CO_2 sequestration from flue gas of coal-fired power plants. It focuses on the adsorption (Chapter 3) and diffusion (Chapter 4) of CO_2 and water in Mg-MOF-74 as well as their interactions towards each other. In part III, *Olefin/paraffin-separation*, the separation of olefin/paraffin-mixtures is discussed. The results regarding adsorption properties of ZIFs and IFPs with respect to small hydrocarbons are presented in Chapter 5 and 6, respectively. The influence of framework flexibility for the diffusion of hydrocarbons

in ZIF-8, ZIF-9, and ZIF-71 is shown in Chapter 7. Part IV, *Adsorber simulation*, consists of Chapter 8, in which an adsorber code developed is tested and then used to simulate the separation of CO_2 from a N_2/CO_2-mixture using Mg-MOF-74 as well as an ethane/ethene-mixture using ZIF-8, showing that the separations are working in principle. Lastly, in the *Summary* part, the thesis is concluded (Chapter 9) and an outlook for future objectives is given (Chapter 10).

Theoretical Background 2

In this chapter the theoretical foundations of this work are discussed. The thermodynamic fundamentals of adsorption are given as well as ways to present data in form for adsorption isotherm functions. In addition to single component adsorption, systems with multiple types of guest molecules are described. Transport phenomena such as diffusion at the molecular and dispersion at the continuum scale and their respective definitions are also discussed. Since this thesis deals with the adsorptive properties of metal-organic frameworks, they are introduced with a short history revision and synthesis methods. A closer look is given to the materials investigated in this work: Mg-MOF-74, ZIF-8, ZIF-9, ZIF-71, IFP-1, IFP-3, IFP-5, and IFP-7. All investigations are based on three computer simulation techniques: density functional theory (DFT), Monte Carlo (MC), and molecular dynamics (MD). An introduction to DFT starts at Schroedinger's equation in the realm of quantum chemistry followed by the Born-Oppenheimer approximation ending at the description of DFT. The molecular simulations are introduced by an excursion to statistical mechanics before both methods are explained in detail. Monte Carlo (MC) simulations are a statistical way to probe a given system. Molecular dynamics (MD) simulations on the other hand rely on solving Newton's equation of motion to describe the system. Furthermore, general details regarding molecular simulations are discussed. Lastly, how adsorption processes are modelled on the continuum scale is presented. The governing partial differential equations are derived and ways to solve them are given.

2.1 Adsorption

Adsorption describes the process of enrichment of atoms, ions or molecules from a fluid phase or a dissolved solid at an interfacial layer.[60,61] The solid accumulating particles on its surface is named the adsorbent. The atoms, ions or molecules from the fluid phase are called adsorptive, and the adsorbed particles are named adsorbate, see Figure 2.1. Depending on the adsorption mechanism, the process is classified as either physisorption or chemisorption (Table 2.1). In case of physisorption, it is a reversible, exothermic process with desorption being its counterpart in which van der Waals forces induce the accumulation on the surface. Physisorption is non-selective, and thus, occurs (spontaneously) between any adsorbate-adsorbent system. In addition to that, multilayer binding is possible. If sharing or exchanging of electrons between adsorbent and adsorbate is involved, the adsorption process is called chemisorption. Here, adsorption interactions are the same as in (irreversible) chemical reactions, since covalent bindings are developed. The number of adsorbed layers formed is limited to one in this case. Both mechanisms differ for most setups in the magnitude of their respective heat of adsorption. Regarding chemisorption, the adsorption enthalpy is usually higher, however, this process requires activation energy and the rate of adsorption is lower. In general, the mechanism of adsorption depends on the reactivity of the surface, the nature of the adsorbate, and adsorbent as well as the present temperature.

Thermodynamically, the binding of adsorptive molecules to the solid surface reduces the degree of freedom of molecules, which corresponds to a loss of entropy ΔS. As already mentioned, since the enthalpy ΔH is negative, one can conclude that the process itself occurs spontaneously and is therefore

Table 2.1: Comparison of physisorption and chemisorption.[60]

Property	Physisorption	Chemisorption
Adsorption enthalpy	Low	High
Desorption	Reversible	Irreversible
Kinetics	Fast	Slow
Structure of sorbates	Multilayers possible	Just monolayers
Temperature	Low	Wide range
Interaction	Van der Waals forces	Chemical bonding
Selectivity	Low to moderate	High

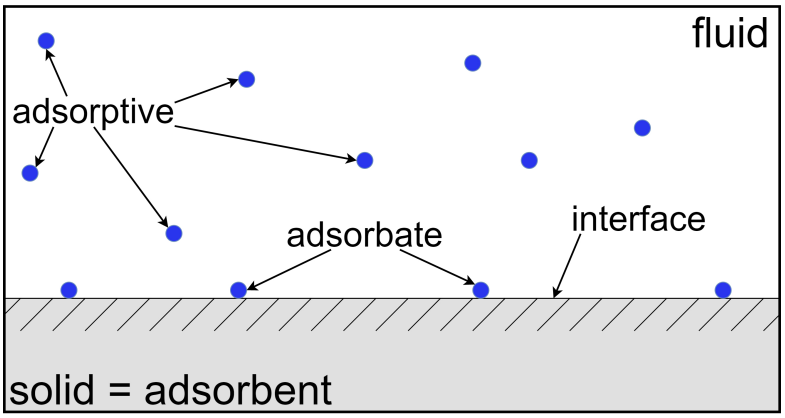

Figure 2.1: Nomenclature for the adsorption process.[60,61]

accompanied by a decrease in the Gibb's free energy of the system ΔG:

$$\Delta G = \Delta H - T\Delta S. \tag{2.1}$$

Let us look at a simple gas-solid system in which the solid has the mass m_s with zero molecules adsorbed, surface area A_s, and an amount n of a single (adsorbable) gas in a given volume V at temperature T. In this system three phases are present, see Figure 2.1: a solid phase s, a fluid phase g and an interphase σ. During the adsorption, molecules leave the (bulk) gas phase and become adsorbed at the surface/interphase, i.e. $dn_\sigma > 0$. Keeping T, V, A, and n of the system constant, the Helmholtz energy $F_{T,V,A,n}$, which is the thermodynamic potential of the adsorption system, has its minimum value at equilibrium:

$$\left(\frac{\partial F_{system}}{\partial n_\sigma}\right)_{T,V,A,n} = 0. \tag{2.2}$$

Gibb's dividing surface representation was used by Everett[62] to define F_σ for the interphase:

$$F_\sigma = F_{system} - F_g - F_s \tag{2.3}$$

With this knowledge one can expand Eq. 2.2:

$$\left(\frac{\partial F_{system}}{\partial n_\sigma}\right)_{T,V,A,n} = \left(\frac{\partial F_\sigma}{\partial n_\sigma}\right)_{T,A} + \left(\frac{\partial F_g}{\partial n_\sigma}\right)_{T,V} + \left(\frac{\partial F_s}{\partial n_\sigma}\right)_{T,A} = 0. \tag{2.4}$$

Eq. 2.4 is the general condition of equilibrium, which holds for a system whose the gas molecules are distributed between the adsorbed phase (at the surface excess concentration $\Gamma=\frac{n_\sigma}{A}$) and the gas phase (at the concentration $c_g=\frac{n_g}{V_g}$). A valid assumption is that during physisorption the bulk solid phase is not affected in any way, thus:

$$\left(\frac{\partial F_s}{\partial n_\sigma}\right)_{T,A} = 0. \tag{2.5}$$

Considering the solid to be inert, physisorption is the change of a molecule in the gaseous state to the adsorbed state. In a closed system at equilibrium we know that $dn=0=dn_\sigma+dn_g$. The equilibrium condition then becomes

$$\left(\frac{\partial F_\sigma}{\partial n_\sigma}\right)_{T,A} = -\left(\frac{\partial F_g}{\partial n_\sigma}\right)_{T,V} = \left(\frac{\partial F_g}{\partial n_g}\right)_{T,V}. \tag{2.6}$$

The last term in Eq. 2.6 is the definition of the gas' chemical potential in the gas phase μ_g. In a similar way, we can define a surface excess chemical potential for the gas "in" or on the interphaseμ_σ, respectively:

$$\mu_\sigma = \left(\frac{\partial F_\sigma}{\partial n_\sigma}\right)_{T,A} \tag{2.7}$$

Combining Eq. 2.6 and Eq. 2.7 one gets

$$\mu_\sigma = \mu_g \tag{2.8}$$

This means that at equilibrium the chemical potential of the adsorbate in the interphase is the same as the adsorptive in the (bulk) gas phase. Although adsorption properties are considered static properties, the process itself is clearly not. In equilibrium, the number of adsorbed molecules does not change, yet a molecule is only remaining in an adsorbed state for a limited amount of time. In fact, it is adsorbed for only a small fraction of a second. The system or the molecules are in a dynamic equilibrium (some molecules adsorb and some desorb) for which the following holds:

$$r_{ads} = r_{des}, \tag{2.9}$$

with r_{ads} being the adsorption and r_{des} the desorption rate, respectively.

One important property for the characterization of the affinity of guest molecules toward the solid surface is the (differential) adsorption enthalpy or heat of adsorption, respectively. It describes the generated or required

heat of a solid surface to adsorb a given amount of guest molecules. It can be obtained using a calorimeter, calculated from adsorption isotherms (Eq. 2.10) or Henry coefficients at different temperatures (Eq. 2.11) using the following equations:

$$\left(\frac{\partial(\ln p)}{\partial T}\right)_n = -\frac{\Delta H}{RT}, \tag{2.10}$$

or

$$\Delta H = -R\left(\frac{\partial K_H}{\partial T^{-1}}\right), \tag{2.11}$$

where R is the ideal gas constant, K_H the Henry coefficient, p the pressure of the isoster, and T the temperature.

With respect to adsorption materials, the most valuable information one is usually interested in, is the amount adsorbed per mass adsorbent q or θ, respectively. In general, the amount adsorbed is a function of temperature T, pressure p, and bulk gas phase composition x, i.e. q=q(T,p,x).

2.1.1 Adsorption isotherms

When only single component adsorption is considered, clearly the composition is no longer a factor. Adsorption with two or more species is the subject of Chapter 2.1.2. Because of that restriction, the uptake becomes q=q(T,p,x=1)=q(T,p). One can display the uptake as a function of temperature at constant pressure (adsorption isobars) or as a function of pressure at constant temperature (adsorption isotherms). It has been established historically to use adsorption isotherms (meaning T is constant) to characterize the uptake behavior of adsorbent materials, $q=q(p)_T$.

One famous description of adsorption isotherm is Gibbs adsorption isotherm, which is based on a thermodynamic description of the problem.[63] For this to work, Gibbs introduced the concept of a dividing surface between the gas and the solid phase without specifying the exact location. Referring back to Figure 2.1, temperature T_g, volume V_g, and the total number of molecules for all components i, n_g^i is specified for the gas phase, hence the total differential Helmholtz free energy can be defined as:

$$dF = -S_g dT_g - p_g dV_g + \sum_i^N \mu_g^i dn_g^i, \tag{2.12}$$

where S_g is the entropy of the gas phase, p_g the pressure, and μ_g^i the chemical potential of species i in the gas phase. The same relationship is true for the solid phase and the interface:

$$dF = -S_s dT_g - p_s dV_s + \sum_i^N \mu_s^i dn_s^i, \tag{2.13}$$

and

$$dF = -S_\sigma dT_\sigma - p_\sigma dV_\sigma + \sum_i^N \mu_\sigma^i dn_\sigma^i. \tag{2.14}$$

However, since the interphase has been defined to be a planar surface the product of ($p_\sigma \cdot dV_\sigma$) in Eq. 2.14 cannot be used. Instead an analogous two dimensional approach is taken, replacing the aforementioned term with πdA:

$$dF_\sigma = -S_\sigma dT_\sigma - \pi dA + \sum_i^N \mu_\sigma^i dn_\sigma^i. \tag{2.15}$$

π is the so-called spreading pressure. The integration at constant temperature, spreading pressure and chemical potential leads to

$$F_\sigma = -\pi A + \sum_i^N \mu_\sigma^i n_\sigma^i. \tag{2.16}$$

The total derivative of this equation becomes

$$dF_\sigma = -d\pi A - \pi dA + \sum_i^N \mu_\sigma^i dn_\sigma^i + \sum_i^N d\mu_\sigma^i n_\sigma^i. \tag{2.17}$$

One gets Gibbs' equation for planar surfaces by subtracting Eq. 2.17 from Eq. 2.15:

$$-d\pi A + \sum_i^N d\mu_\sigma^i n_\sigma^i - S_\sigma dT_\sigma = 0. \tag{2.18}$$

As a reminder, the temperature is considered to be constant, thus dT=0. And since only ne component is considered, this effectively reduces $\sum_i^N d\mu_\sigma^i n_\sigma^i$ to $d\mu_\sigma^i n_\sigma^i$:

$$-d\pi A + n_\sigma^i d\mu_\sigma^i = 0 \Leftrightarrow n_\sigma^i d\mu_\sigma^i = d\pi A. \tag{2.19}$$

Since the chemical potential for this one species must the same in each phase when in equilibrium, using the ideal gas assumption for the gas phase allows us to calculate the chemical potential of that one species on the interphase μ_σ^i:

$$\mu_\sigma^i = \mu_\sigma = \mu_g = \mu_{g,0} + R_g T \ln(p_g). \tag{2.20}$$

By inserting Eq. 2.20 into Eq. 2.19, one obtains the Gibbs adsorption isotherm equation:

$$\left(\frac{d\pi}{d\ln(p_g)}\right)_T = \frac{n}{A} R_g T. \tag{2.21}$$

Eq. 2.21 is a fundamental equation linking the gas pressure p_g with the spreading pressure π and the amount adsorbed n. The equation of state for an ideal surface at infinite dilution is thus

$$\pi A = n R_g T. \tag{2.22}$$

Solving Eq. 2.21 using the analogue of the ideal gas law leads to:

$$\left(\frac{d\pi}{d\ln(p_g)}\right)_T = \pi \Leftrightarrow \pi = C(T) p_g, \tag{2.23}$$

with C(T) being a function of temperature. This result is now used in the equation of state (Eq. 2.22):

$$n R_g T = A \cdot C(T) p_g \Leftrightarrow n = \frac{C(T) \cdot A}{R_g T} \cdot p_g = K_H(T) p_g. \tag{2.24}$$

with K_H(T) being the Henry constant. This equation means that at infinite dilution there is a linear relationship between the amount adsorbed and the bulk gas pressure. Strictly speaking, Eq. 2.24 is only valid at these conditions, however, it is also commonly used at higher pressures and uptake.

While Gibbs used a thermodynamic approach to describe adsorption isotherms, Langmuir took a kinetic one.[64] He starts at the dynamic equilibrium condition, see Eq. 2.9. This means that the rate of molecules striking the surface and sticking to it, i.e. adsorption, is equal to the rate of desorption, the reverse process. Derived from the kinetic gas theory, the rate of striking the surface and sticking to it in mole adsorbed per unit of bare surface area per unit time is:

$$r_{ads} = \frac{\alpha p}{\sqrt{2\pi M R_g T}}, \tag{2.25}$$

with α being the sticking coefficient. Furthermore, Langmuir assumes that adsorbed particles are attached to surface at definite localized sites, that each site is only capable of adsorbing one particle, that the energy state of each adsorbed particle is the same at all sites on the surface independent of the surface coverage, no lateral interactions take place, and the solid surface is homogeneous. Let θ be the fraction of unavailable adsorption sites. Since molecules can only adsorb at available spaces, the rate of adsorption then becomes

$$r_{ads} = \frac{\alpha p}{\sqrt{2\pi M R_g T}}(1-\theta). \tag{2.26}$$

The rate of desorption is equal to that rate, which corresponds to fully covered surface k_{des} multiplied by the fractional coverage:

$$r_{des} = k_{des}\theta = k_{des,\infty}\ exp\left(\frac{-E_{des}}{R_g T}\right)\theta, \text{ with } E_{des} = E_{ads}. \tag{2.27}$$

$k_{des,\infty}$ is the rate constant for desorption at T=∞ and E_{ads} is the adsorption energy. The average residence time of adsorption τ_{ads} can be calculated with the following expression:

$$\tau_{ads} = k_{des,\infty}^{-1} \cdot exp\left(\frac{-E_{des}}{R_g T}\right). \tag{2.28}$$

For physisorption τ_{ads}^{phys} typically is in the range of 10^{-13} to 10^{-9} s, while for chemisorption τ_{ads}^{chem} can range from 10^{-6} to 10^{9} s depending on the system.[60] Putting the expressions for the rate of adsorption (Eq. 2.26) and for the rate of desorption (Eq. 2.27) into Eq. 2.9, one obtains the well known Langmuir adsorption isotherm:[64]

$$\theta = \frac{b \cdot p}{1 + b \cdot p} \Leftrightarrow C_\mu = C_\mu^{max}\frac{b \cdot p}{1 + b \cdot p}, \text{ with} \tag{2.29}$$

$$b = b_\infty exp\left(\frac{-E_{ads}}{R_g T}\right) \text{ and} \tag{2.30}$$

$$b_\infty = \frac{\alpha}{k_{des,\infty}\sqrt{2\pi M R_g T}}. \tag{2.31}$$

C_μ is the uptake in mole per unit mass of adsorbent and C_μ^{max} is the saturation or maximum uptake in mole per unit mass of adsorbent.

A third approach to describe adsorption isotherms is simply using empirical correlations. The most famous one and one of the earliest formulations of adsorption isotherms in general is credited to Freundlich and therefore called Freundlich isotherm.[65] This isotherm has the following form:

$$C_\mu = K_F \cdot p^{\frac{1}{n}}, \tag{2.32}$$

where K_F and n are temperature dependent parameters. Despite the fact that the Freundlich isotherm was designed empirically, it has been shown that it has theoretical foundations.[60] A combination of the Langmuir and Freundlich isotherms was proposed by Sips:[66]

$$C_\mu = C_\mu^{max} \frac{(b \cdot p)^{\frac{1}{n}}}{1 + (b \cdot p)^{\frac{1}{n}}} \tag{2.33}$$

If the parameter n is equal to one, Eq.2.33 is basically the Langmuir isotherm for ideal surfaces. Therefore, n is often regarded as a measure of the heterogeneity of the surface, whereas the larger n is the larger the heterogeneity is. The functional form of the isotherm has been very useful when it comes to fitting experimental data.[60] The Freundlich as well as the Sips isotherms both have one distinct disadvantage: At the low pressure end of a given isotherm both types do not reproduce the "correct" Henry law behavior. One type of the empirical equations which satisfies this requirement is the Toth isotherm:

$$C_\mu = C_\mu^{max} \frac{b \cdot p}{(1 + (b \cdot p)^t)^{\frac{1}{t}}}. \tag{2.34}$$

Similar to the Sips isotherm, this isotherm is well equipped to fit experimental adsorption data due to its three parameters C_μ^{max}, b, and t.[60] Obviously, there are many other isotherm types to be found in literature, see Ref. 60 and Ref. 61.

As mentioned above, each individual isotherm type has some sort of theoretical foundation for its applicability. Take the Langmuir equation (Eq. 2.29) for example. The main assumption is that each available site has the same (energetic) characteristics, thus only one type of adsorption site exists even if one takes the heterogeneity factor of the Sips-isotherm (Eq. 2.33) into account. However, it is possible that in an adsorbent two or more types of adsorption sites are present. Such an example is Mg-MOF-74, see Chapter 3.

In order to take this behavior into account, it is common to use dual or multi site versions of the aforementioned isotherms. Note that the assumptions made for such isotherms are usually bend but not broken. In case of a dual site Langmuir adsorption isotherm each type of adsorption site interacts or influences one of the other sites in any way in addition to the general assumptions made for the Langmuir isotherm. The dual site Langmuir isotherm has the following form:

$$C_\mu = \sum_i^{N=2} \left(C_{\mu,i}^{max} \frac{b_i \cdot p}{1 + b_i \cdot p} \right) = C_{\mu,1}^{max} \frac{b_1 \cdot p}{1 + b_1 \cdot p} + C_{\mu,2}^{max} \frac{b_2 \cdot p}{1 + b_2 \cdot p}. \tag{2.35}$$

2.1.2 Mixture adsorption isotherms

When a second gas is introduced, the composition of the bulk phase becomes an important variable again . For the sake of simplicity, we consider a bulk gas phase with N components, whose composition does not change during the adsorption process. Markham and Benton[67] introduced an extended Langmuir isotherm for a binary mixture. In the following, their approach will be used to derive the competitive Langmuir isotherm for the system with N species. By definition, θ_T is the sum of the fractional loadings θ_i for each of the N components:

$$\theta_T = \sum_i^N \theta_i. \tag{2.36}$$

Also, Eq. 2.26 is still valid for each individual component. In this mixture case it becomes:

$$r_{ads,i} = \frac{\alpha_i p_i}{\sqrt{2\pi M_i R_g T}} \left(1 - \sum_j^N \theta_j \right) = k_{ads,i} p_i \left(1 - \sum_j^N \theta_j \right). \tag{2.37}$$

The rate of desorption of component i is proportional to its fractional loading, see Eq. 2.27:

$$r_{des,i} = k_{des,i} \theta_i. \tag{2.38}$$

At equilibrium, the rate of adsorption is equal to the rate of desorption:

$$\theta_i = \frac{k_{ads,i}}{k_{des,i}} \cdot p_i \cdot (1 - \theta_T) = b_i \cdot p_i \cdot (1 - \theta_T). \tag{2.39}$$

Then, one sums Eq. 2.39 with respect to i over all species N and solves for θ_T as a function of the partial pressure. This results in:

$$\theta_T = \frac{\sum_j^N b_j p_j}{1 + \sum_j^N b_j p_j}. \tag{2.40}$$

Consequently, the fraction of vacant sites is:

$$(1 - \theta_T) = \frac{1}{1 + \sum_j^N b_j p_j}. \tag{2.41}$$

The fractional coverage for species i, θ_i, (and the loading $C_{\mu,i}$) becomes:

$$(1 - \theta_T) = \frac{b_i p_i}{1 + \sum_j^N b_j p_j} \Leftrightarrow \frac{C_{\mu,i}}{C_{\mu,i}^{max}} = \frac{b_i p_i}{1 + \sum_j^N b_j p_j}. \tag{2.42}$$

The right hand side of Eq. 2.42 is the Langmuir isotherm for gas mixtures.

Ideal adsorption solution theory

Single-component isotherms can be easily measured via various adsorption techniques. However, obtaining mixture isotherms from experiments is still in its infancy.[68] That is why the prediction of multi-component data from single-component isotherms is of great importance. To provide a fast method of calculating mixture adsorption equilibria, very simple isotherm equations have been used, but they lack the accuracy of describing both gas-solid interactions and their dispersion at various points on the surface and interactions between adsorbate molecules. To solve these issues, several approaches have been developed, for example by Jaroniec and Rudzinski[69] or Danner and Choi.[70] Prausnitz et al.[71] developed the so-called ideal adsorbed solution theory (IAST) and it has been used successfully for a variety of systems.[53,72,73] The main advantage of IAST is the fact that no additional parameters besides the single component adsorption data are needed. Experimental investigations beyond this data are therefore not necessary, which minimizes the effort to calculate multi-component adsorption by a lot. In many cases it is not possible to obtain (or determine) explicit equations with IAST, and thus, numerical solvers have to be applied.[74]

One of the main ideas used in IAST is the application of activity coefficients γ_i in the mixture. The starting point is Gibbs free mixing energy g^m for the adsorbate:[71]

$$g^m(T, \pi, x_i, ...) = RT \sum x_i \ln(\gamma_i \cdot x_i). \tag{2.43}$$

The total Gibbs free energy of the mixture g(π,T) is:

$$g(\pi, T) = \sum_i^N x_i g_i^0 + g^m, \tag{2.44}$$

with g_i^0 being the Gibbs free energy of pure component i at given π and T. Moreover, derived via the Euler theorem, the Gibbs free energy (at constant T and π) is also:

$$G = \sum_i^N n_i \cdot \mu_i. \tag{2.45}$$

Eq. 2.43, 2.44, and 2.45 lead to the following relationship to obtain the chemical potential of each component i μ_i:

$$\mu_i = g_i^0(T, \pi) + RT \ln(\gamma_i \cdot x_i). \tag{2.46}$$

The term g_i^0(T,π) consists of two parts:

$$g_i^0(T, \pi) = g_i^0(T) + RT \ln[p_i^0(\pi)], \tag{2.47}$$

where g_i^0 (T) is the standard Gibbs free energy at ideal conditions and p_i^0 is a theoretical pressure of the pure component adsorbed if only component i was present whilst having the same π as in the mixture.[71] Inserting Eq. 2.47 into Eq. 2.46, one gets the chemical potential of component i in the adsorbed phase of the mixture:

$$\mu_i(T, \pi, x_i, \gamma_i) = g_i^0(T) + RT \ln[p_i^0(\pi)] + RT \ln(\gamma_i \cdot x_i). \tag{2.48}$$

As a reminder the chemical potential for component i in the (ideal) gas phase is

$$\mu_i(T, \pi, y_i) = g_i^0(T) + RT \ln(p_{bulk} \cdot y_i). \tag{2.49}$$

Since at equilibrium the chemical potential of each phase is the same, Eq. 2.48 and 2.49 are equal:

$$\begin{aligned} \mu_i(T,\pi,x_i,\gamma_i) &= \mu_i(T,\pi,y_i) \\ \Leftrightarrow \ln[p_i^0(\pi)] + \ln(\gamma_i \cdot x_i) &= \ln(p_{bulk} \cdot y_i) \\ \Leftrightarrow \ln[p_i^0(\pi) \cdot \gamma_i \cdot x_i] &= \ln(p_{bulk} \cdot y_i) \\ \Leftrightarrow p_i^0(\pi) \cdot \gamma_i \cdot x_i &= p_{bulk} \cdot y_i = p_i. \end{aligned} \tag{2.50}$$

For IAST to work it is necessary to assume that the mixture is ideal ($\gamma = 1$), the adsorption material is inert, and there is only one interphase for all adsorbed molecules. That also means that π is the same for all species present in the system. To calculate the spreading pressure π one circles back to the Gibbs isotherm in Eq. 2.18 and Eq. 2.19, respectively. It is assumed that the spreading pressure in the mixture at given pressure is the same as for the pure component at the theoretical pressure p_i^0. That means that x_i=1 in Eq. 2.48, which leads to the following formulation for the Gibbs isotherm:

$$A \cdot d\pi = n_i^0(p_i^0) \cdot RT d\{\ln[p_i^0(\pi)\}, \tag{2.51}$$

with n_i^0 is the adsorbed amount of the pure component i as a function of the theoretical pressure p_i^0. Rearranging Eq. 2.51 leads to the possibility of calculating the spreading pressure π via integration:

$$\pi = \pi(p_i^0) = \frac{RT}{A} \int_0^{p_i^0} \frac{n_i^0(p_i)}{p_i} dp_i \Leftrightarrow \Phi = RT \int_0^{p_i^0} \frac{n_i^0(p_i)}{p_i} dp_i. \tag{2.52}$$

Since A is constant for all components in the whole system it means that the product of π and A is constant too. Φ can be considered as a surface potential. Thus, Φ is dependent on the theoretical pressure p_i^0 and n_i^0 whereas the latter is basically the pure component adsorption isotherm information. Because of the assumptions made for IAST, Eq. 2.50 can be further simplified:

$$py_i = x_i p_i^0(\pi) \tag{2.53}$$

In general, the sum of all molar fractions for each phase, i.e. gas or adsorbed phase, have to be equal to one:

$$\sum_i^N x_i = \sum_j^N y_j = 1. \tag{2.54}$$

Table 2.2: The number of equations in Myers and Prausnitz IAS theory.[71]

Eq. number	Number of equations in the set
2.55a	1
2.55b	N-1
2.55c	N
2.55d	1
sum	2N+1

Table 2.3: The number of unknown variables in Myers and Prausnitz IAS theory.[71]

Variable	Number of unknown variables
Pure component pressure $\mathbf{p}_j^0$	N
Adsorbed mole fraction $\mathbf{x}_j$	N
Total adsorbed phase concentration n	1
sum	2N+1

To summarize, the set of equations needed for IAST are:

$$\frac{1}{n} = \sum_{i}^{N} \frac{x_i}{n_i^0} \tag{2.55a}$$

$$\Phi = \Phi_i^0 = RT \int_0^{p_i^0} \frac{n_i^0(p_i)}{p_i} dp_i \text{ for all i} \tag{2.55b}$$

$$py_i = x_i p_i^0(\pi) \text{ for all i} \tag{2.55c}$$

$$\sum_{i}^{N} x_i = 1 \tag{2.55d}$$

As a result, one obtains a set of equations with 2N+1 equations (Table 2.2) and 2N+1 unknown variables (Table 2.3). The IAS theory is consistent at the limit of zero pressure. The accuracy of the predictions depends on how well the single component adsorption isotherms are fitted, especially at low and high pressures.

Naturally, many evolutions of the ideal adsorbed solution theory can be found in literature, for example the real adsorbed solution theory (RAST) and the segregated ideal adsorbed solution theory (SIAST) just to name a

few. In the former approach, the activity coefficients γ are $\neq 1$ and thus have to be calculated by means of models like the g^E or the Uniquac model.[60,61] The latter model developed by Swisher et al.[75] is useful when the adsorption isotherm can be described using dual or multi site isotherm types. Let us assume that components A and B adsorption isotherms can be described by dual site Langmuir isotherms, see Eq. 2.35. In contrast to IAST, in which the adsorbed phase is one phase, SIAST treats each term in the dual site isotherms individually, meaning that in a dual site case two interphases are present whereas in phase one the first term of the dual site Langmuir isotherm is used for both A and B and in the second phase the second part. What it basically means is to loop over IAST a number of times equal to the number of sites used for the isotherm fit, e.g. if one has dual isotherms the number of phases present would be two. This method has the benefit that some numerical issues that could occur in pure IAST calculations are circumvent by this approach.

2.2 Transport phenomena

2.2.1 Diffusion

Diffusion is known as the tendency of matter to eliminate spatial variations in composition while reaching a state of equilibrium. Alternatively, it describes random movement based on Brownian motion in an equilibrium. For all temperatures above zero Kelvin it is an universal property of matter. It corresponds to the tendency towards maximum entropy or in other words maximum randomness.[76] The understanding of the movement of molecules in nanoporous environments is essential, since there are characteristic differences in the diffusion behavior in comparison to a bulk phase. For example, each component moves differently due to its physical and chemical properties.[77,78]
One distinguishes between two diffusion phenomena: transport diffusion and Brownian molecular motion.[76] If there is a gradient inducing a flux of matter, transport diffusion takes place whereas Brownian molecular motion describes the movement of single particles in the absence of a gradient.

Transport Diffusion

Diffusion under a gradient of, e.g. concentration, pressure and so on, is known as transport diffusion. Fick formulated his First Law of Diffusion with the

corresponding coefficient D^T describing the measure of a flux J of particles A due to a concentration gradient in the observed system:

$$J_A = -D^T \nabla c_A, \tag{2.56}$$

where c_A is the concentration of A.

The negative sign indicates a mass flow towards lower concentration.[76] Fick assumed that the concentration gradient is the driving force for particle motion. Thermodynamics, however, state that a gradient of the chemical potential μ is the true driving force. Based on that, the Onsager formulation defines the flux J as

$$J = -\frac{L}{k_b T} \nabla \mu, \tag{2.57}$$

where L is the single-component Onsager coefficient and k_B is the Boltzmann factor.[78] A relation betweenthe concentration gradient and the chemical potential gradient is given by the Darken-equation:[78,79]

$$\begin{aligned} D^T &= \Gamma D^C \text{ or alternatively} \\ \frac{c_i}{RT} \nabla \mu_i &= \Gamma_i \nabla c_i \text{ , with} \end{aligned} \tag{2.58}$$

$$\Gamma = \frac{d \ln p}{d \ln c}, \tag{2.59}$$

where Γ is the thermodynamic factor which can be obtained from the adsorption isotherm, p is the pressure, and c is the concentration.
The corrected diffusivity, D^C, describes the movement of all particles (similarly to the transport diffusion D^T) and can be interpreted as as intrinsic diffusivity of the molecules whereas the thermodynamic factor serves as a non-linear relationship between activity and concentration. If the system is thermodynamically ideal, which it is at infinite dilution of matter, and only in that case, then Γ becomes one and D^T is equivalent to D^C. To obtain the diffusion coefficient D^T experimentally one can use macroscopic methods like gravimetric, volumetric or frequency-response techniques under non-equilibrium conditions.[80]

Self-diffusion

Diffusion in the absence of a gradient is called self-diffusion or Brownian molecular motion which is referred to as a random walk of an individual

particle caused by the interactions with other particles with the corresponding diffusion coefficient being D^S.[78,79] It describes the movement of a single particle such that the self-diffusion does not vary with the fraction of molecules but may vary with the total concentration.[79] Einstein linked D^S to the mean-squared displacement in one dimension of one species in equilibrium due to Brownian motion:

$$\frac{\partial\langle r^2(t)\rangle}{\partial t} = 2 \cdot D^S. \tag{2.60}$$

In experiments self-diffusion can be measured by using microscopic techniques like pulsed field gradient (PFG) NMR.[81,82]

In conclusion, there are three important diffusion coefficients, D^T, D^C, and D^S, which become equal in the case of zero loading as described above. Self-diffusion is known as loading-dependent whereas the corrected diffusion is regarded as loading-independent (although this assumption does not always hold).[77] With the introduced thermodynamic correction factor Γ, equation 2.61 is obtained:

$$D^T \neq D^C > D^S. \tag{2.61}$$

2.2.2 Diffusion mechanisms in nanoporous media

After introducing diffusion coefficients, how does it actually come to such a diffusion event? Clearly, the mechanisms of gas diffusion in nanoporous media are dependent on the nature of the diffusing molecules and their interactions with their surroundings such as other molecules and the confinement.[76] Figure 2.2 shows the different diffusion mechanisms, namely Knudsen diffusion, molecular diffusion, configurational diffusion, and surface diffusion. They will be explained briefly in this section. For further information the reader is referred to Reference 79.

Diffusion Regimes

There are different diffusion regimes depending on the ratio of the kinetic diameter of the diffusing molecules to the pore diameter (see Figure 2.3). Knudsen diffusion is present when the Knudesen number Kn=$\frac{\lambda}{d}$ is far larger than 1, whereas λ is the mean free path a an molecule and d is the pore diameter. Reducing the pore readius such that Kn is smaller than 1 the molecular diffusion region is reached. In a region where the molecular diameter is comparable to the one of the pore, steric hindrances restrict the flux so that the molecules are restricted to move one after another.[79] This effect

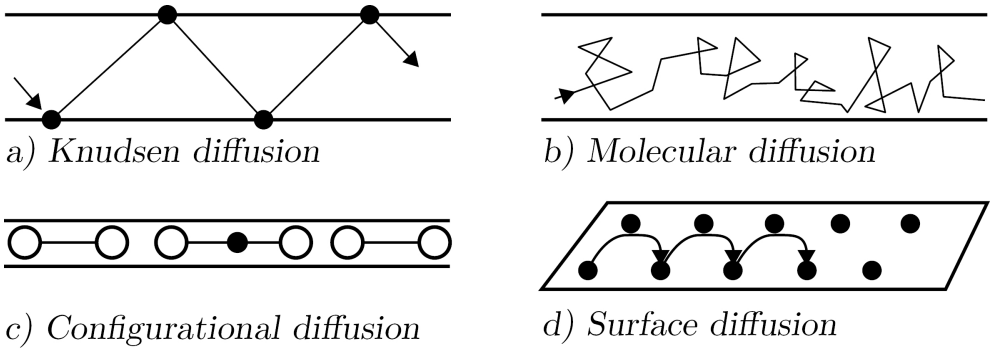

Figure 2.2: Illustration of the different diffusion mechanisms. Modified from Reference 83.

of the so-called intracrystalline or configurational diffusion regime allows a very efficient size-selective separation and is intensively investigated.[84,85]

As already mentioned, Knudsen diffusion appears when the mean free path λ of the molecules is larger than the pore diameter (see Figure 2.2 (a)). This happens either in small pores and/or at low pressure. As a result, molecules collide more often with the pore wall than with other molecules. The theory states that after reflecting from the wall the velocity of the molecule is independent of the incident velocity and its new direction is purely random.[79] The flux in the Knudsen regime can be described by a Fickian expression, in which the diffusivity D_K is only dependent on the pore size and on the mean molecular velocity derived from the kinetic gas theory:

$$D_{i,K} = \frac{d_p}{3}\sqrt{\frac{8RT}{\pi M_i}} \tag{2.62}$$

where d_p is the pore diameter, and M_i is the molecular weight of component i.

In macro- and mesopores where the pore diameter is larger than the mean free path λ the effect of molecule-wall collisions can be neglected (see Figure 2.2 (b)). The molecular motions are now dominated by the intermolecular collisions.[79]

Between the molecular and Knudsen diffusion there is a regime called transition region where the mean free path is comparable with the pore diameter. Both intermolecular and molecule-wall interactions are significant and diffusion is a combined effect. The *dusty gas* model is describing this phenomena successfully.[79]

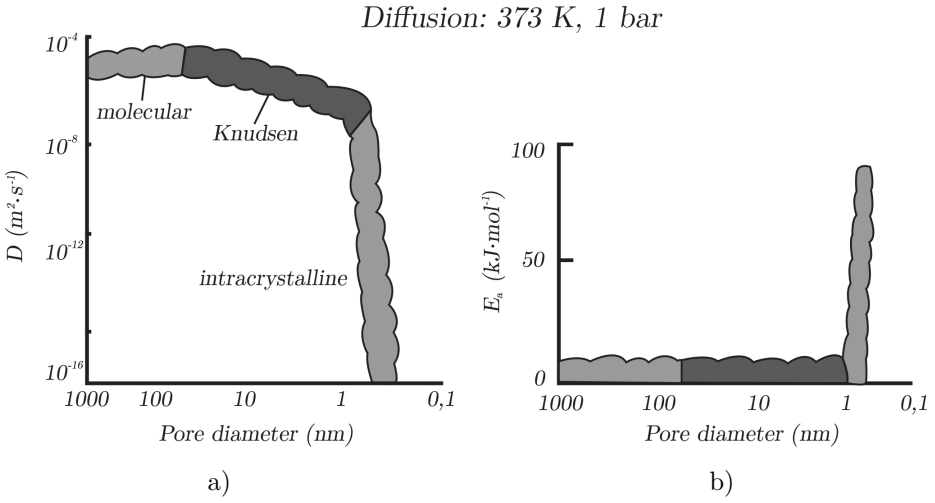

Figure 2.3: Illustration of the diffusion coefficients in the different regimes a) and the adsorption energy dependent b) on the pore diameter. Modified from Reference 83.

If one considers a pore network in which pores are connected by orifices or channels, whose diameters are slightly larger than the kinetic diameter of the present guest-molecules, it is called configurational diffusion. The molecules are restricted to migrate one after another, as seen in Figure 2.2 (c). In this thesis the focus is on this type of diffusion due to the scale of the pores and channels.

Activated Diffusion

Generally, molecules can adsorb on any given surface, for example on a pore wall inside a nanoporous material. These physically adsorbed molecules are relatively mobile but less than in the gaseous phase. In order to leave its site, an adsorbed molecule needs sufficient energy to jump over an energy barrier to a neighboring site. This diffusion of the adsorbed phase is called surface diffusion. This type of diffusion is an activated one, depending on the temperature following the Arrhenius form

$$D = D_\infty \exp \frac{-E_A}{RT}, \tag{2.63}$$

where D_∞ is a pre-exponential factor and E_A is the activation energy, which includes the sum of all energy barriers throughout the transition process to

the next site plus the energy required to form the vacancies. Thereby, both parameters can vary by the given lattice type and hopping mechanism.

The aforementioned size-selective separation can appear in the region of configurational diffusion as soon as the kinetic diameter of a species is too big relative to the pore size so that it cannot overcome the natural barrier, similar to a common sieve (see Figure 2.4 (a)). Another possibility is an activated process in which larger molecules, under the assumption that they are not sterically excluded, are strongly adsorbed, tending to occupy the pore space. Therefore, they hinder the smaller molecules to pass by competitive adsorption. The so-called *selective surface flow* has been verified experimentally but the main issue is that smaller molecules can never be completely excluded from the pores.[79]

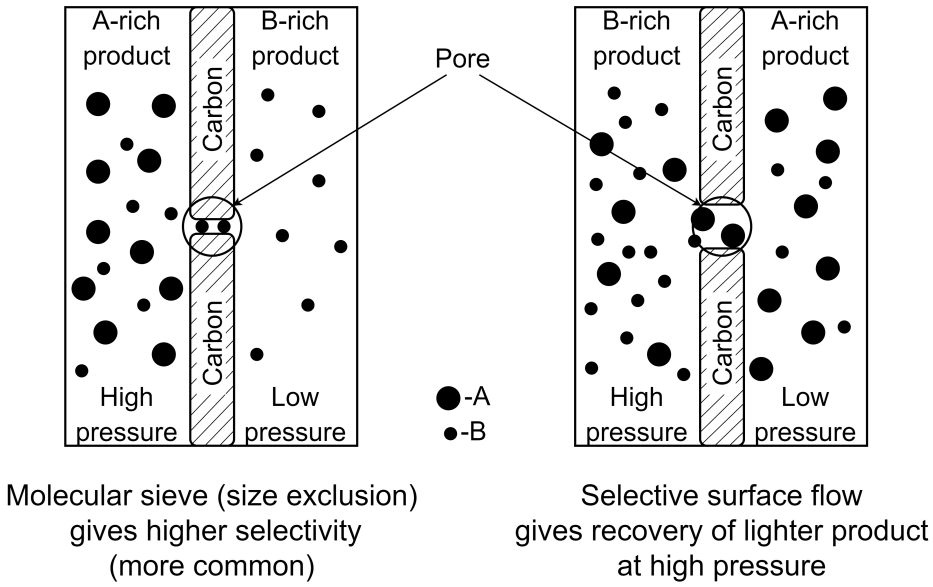

Figure 2.4: The two different mechanisms of molecular sieving taken from Reference 79.

In most of the investigated MOFs the diameter of the window between adjacent cages is close to the size of the guest molecules or even smaller. It is clear that the passage between two cavities is the bottleneck of any molecular propagation. When a molecule moves from one cage to another regardless of the window size, it is called a cage-to-cage jump. The rate of these jumps can be assumed to represent all types of mass transfer, including self-diffusion.[79,86,87] A theory to describe that process is known as Transition State Theory (TST). It was originally developed for chemical reactions but

has been adopted to activated processes in general since then. For molecular simulations, however, the Bennet-Chandler approach is well suited in which the transition frequency is the product of the free energy and reactive-flux contribution.[79,87] As the theory says it describes the transition from one state to another. Consider an one-dimensional system with cages, windows, and a molecule which is only represented by its center-of-mass. The topology of the system creates stable states (cages) and unstable states (windows). The stable states are local energy minima, whereas the surrounding unstable states are local energy maxima. A free-energy profile is obtained along the process coordinate q which is basically the transport coordinate of a molecule. The molecule always tends to go to the energy minima but is rather staying in the region between two dividing energy maxima than strictly being in the local minimum. The frequency of transition from cage A to cage B of a molecule is defined by the hopping rate $k_{A\to B}^{TST}$:

$$k_{A\to B}^{TST} = \sqrt{\frac{k_B T}{2\pi m}} P(q*) \tag{2.64}$$

where k_B is the Boltzmann constant, T is the temperature of the system, m is the mass of the hopping particle, and $P(q*)$ is the probability of finding the tagged molecule, which was initially in cage A, at the transition state $q*$ (local energy maximum).[87] So far, it was assumed that the molecule, once it moved from the transition state to either site A or B, eventually equilibrates there. This is contradicted by several observations, particulary at finite loadings.[87] One explanation is that hopping molecules may recross the transition state until finally reaching its target state (see Figure 2.5). A so-called *transmission coefficient* κ is introduced. It takes this phenomenon into account. κ is defined as follows:[87]

$$\kappa \equiv \frac{k_{A\to B}^{dcTST}}{k_{A\to B}^{TST}}. \tag{2.65}$$

The TST hopping frequency $k_{A\to B}^{TST}$ represents the maximum hopping rate possible whereas the dynamically corrected TST hopping rate $k_{A\to B}^{dcTST}$ gives the correction of those unsuccessful hopping attempts. Thus, κ can take any value between 0 and 1.[87]

As said above, the TST and dcTST can be used to determine the self-diffusivity D^S

$$D^S = \frac{1}{2n} k_{A\to ALL}^{EXIT} \lambda^2, \tag{2.66}$$

where the hopping rate $k_{A\to ALL}^{EXIT}$ describes the sum of all hopping rates over all windows exiting a cage, λ is the distance between low energy sites, and n defines the dimensionality of diffusion (1, 2, or 3).[88]

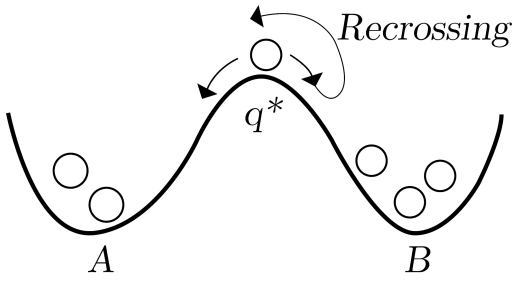

Figure 2.5: Illustration of the dynamically corrected TST. Modified from Reference 83.

2.2.3 Dispersion

The term dispersion describes all flow mechanic effects causing deviation from general plug flow behavior, like (back) diffusion for example.[89] The superposition of velocity fluctuations as well as molecular diffusion induce axial mixing, which depends linearly on the concentration gradient. This behavior can be described by Fick's law.[90] The axial dispersion coefficient D_{ax} can be calculated using the dimensionless Bodenstein number. This number is defined as the ratio of the transport velocity of the convective flow to the velocity of the dispersion flow:[90]

$$Bo = \frac{u \cdot L}{D_{ax}}, \tag{2.67}$$

with u being the velocity of the flow and L a characteristic length. If the Bodenstein number is large, the observed system behaves like a plug flow since the dispersion coefficient is very small. On the other hand, if the Bodenstein number approaches zero, dispersion is very prominent and intense mixing is observed, hence, the behavior becomes similar to a continuously stirred system. Another important dimensionless number is the (axial) Peclet number Pe_{ax}, which has the following relation to the Bodenstein number:

$$Pe_{ax} = Bo \cdot \frac{d_R}{L} = \frac{u \cdot d_R}{D_{ax}}, \tag{2.68}$$

where d_R is the diameter of the reactor. The axial dispersion coefficient of gaseous flow in a fixed-bed reactor can be calculated according to a emperical equation formulated by Wen and Fan:[91]

$$\frac{1}{Pe_{ax,P}} = \frac{0.3}{Re_P \cdot Sc} + \frac{0.5}{1 + \frac{3.9}{Re_P \cdot Sc}}, \tag{2.69}$$

where $\mathrm{Pe}_{ax,P}$ is the axial Peclet number of a particle in the system, Re_P the Reynolds number of that particle, and Sc the Schmidt number. These dimensionless numbers are defined as follows:

$$Pe_{ax_P} = \frac{\bar{u} \cdot d_P}{D_{ax}}, \tag{2.70a}$$

$$Re_P = \frac{\rho \cdot d_P \cdot \bar{u}}{\eta}, \tag{2.70b}$$

$$Sc = \frac{\nu}{D_{eff}}. \tag{2.70c}$$

Here, $\bar{u}$ is the superficial velocity, d_P the pellet diameter, ρ the gas density, η the dynamic viscosity, ν the kinematic viscosity, and D_{eff} the (effective) diffusion coefficient inside the pellet. Eq. 2.69 is valid for the following conditions:

$$0.008 < Re_P < 400 \text{ and } 0.28 < Sc < 2.2. \tag{2.71}$$

2.3 Metal-organic frameworks

Metal-organic frameworks (MOFs) are (nano-)porous materials consisting of organic and inorganic materials. These hybrid frameworks are called *organic coordination networks.*[92] They are synthesised via self-assembly of a connection part and a link whereas the former is a metal ion and the latter an organic ligand. Just based on that simple concept it is obvious, that the number of combinations of metals with organic linkers are seemingly limitless. In theory, one could design crystal structures to have certain pore sizes, topologies and general properties, such that this particular framework suits a given separation problem best or a catalytic reaction or gas storage or so on.[92] Naturally, the opportunity to engineer materials has attracted not only industry but also researches to maximize the potential of the MOFs.

Despite metal-organic frameworks being considered a relatively new family of nanoporous crystalline materials the first organic-inorganic hybrid coordination network was discovered by Hofmann et al. and named Hofmann complex in 1897.[93] The chemical formula of this structure was $Ni(CN)_2(NH_3) \cdot C_6H_6$. The actual structure, a square network bridged by cyanide-groups encapsulating the benzene in a channel, was found eventually by Powell et

al. using X-ray diffraction analysis in the 50s.[94] Subsequently in the 60s and 70s, more and more of those Hofmann complexes have been identified and synthesized. They consisted of various metals (Ni, Zn, Cu, and so on) and very different encapsulated organic molecules (benzene, aniline, pyrrole, and so on) while the cyanide-group was the connecting bridge for the complexes.[95–97]

Inspired by the idea of substituting the cyanide-groups with larger organic linkers to increase the pore sizes of the resulting complexes, scientists made progress in creating and defining a whole new class of materials. Most notably, Robson was able to create an organic coordination network by complexation of anions with tetrahedral bridging ligands in 1989.[98] While the cavities had a pore volume of only $700\mathring{A}^3$, it was the pioneer work and the starting strategy for the creation of larger organic coordination networks.[92]

5 years later, one more step towards the usage of organic coordination network was taken: A two dimensional square network solid [Cd(4,4′-bpy)$_2$(NO$_3$)$_2$] (bpy=bipyridine) with large cavities was created in an aqueous solution.[99,100] Moreover, Zaworotko and coworkers designed a coordination network [Zn(4,4′-bpy)$_2$]SiF$_6$, which had large non-interpenetrated channels and pore sizes comparable to those of zeolites. The same group replaced the Zn-ion with trigonal planar Cu^I centers, which resulted in a three dimensional porous network with reasonable chemical and thermal stability.[101,102] Consequently, the porous network was deemed suited for gas adsorption by researches. Among them, Kitagawa and his group were the first to create porous frameworks based on bipyridine linkers and metal ions such as Co, Ni, and Zn.[103] These solids had two channels running parallel to the b and c crystallographic axes. Before the crystals could adsorb gas molecules, they had to be activated by removing water molecules present in the channels via vacuum. While the adsorption properties were not impressive by themselves, the work highlighted the high potential for this class of materials with respect to adsorption. Another variation was the usage of two organic linkers which led to biporous coordination networks creating frameworks with two different type of channels.[104]

Officially, the first reported MOF was the MOF-5 (or IRMOF-1) developed by the group of Yaghi in 1999.[105] Consisting of Zn$_4$O building blocks combined with 1,4-benzodicarboxylate linkers, it is one of the most studied MOFs to date. Because of its large cavities ($\geq 8\ \mathring{A}$ in diameter) and channels ($\geq 6\ \mathring{A}$ in diameter), it has a rather high surface area and pore volume at approx. 2300 $\frac{m^2}{g}$ and 74%, respectively.[105,106] Another important structure was HKUST-1 (Cu$_3$(btc)$_2$, btc = 1,3,5-benzenetricarboxylate).[107] The dimeric cupric tetra-carboxylate units form square paddlewheel clusters

which became some sort of trademark for that structure.

Metal-organic frameworks are commonly synthesized via one-pot self-assembly reactions with metal salts and organic linkers in solution at moderate temperatures. At synthesis near room temperature, there are two ways to control the rate of reaction: either due to the slow evaporation of the solvent or the slow diffusion of the solvent molecules. At higher temperatures (up to 250 °C) and pressures, which is referred to as the solvothermal approach, the reaction rate is significantly higher and the control of the reaction is more difficult to obtain high-quality crystals compared to lower temperatures.[108] Additionally, microwave induced synthesis,[109] using ionic liquids[110] as well as solvent-free synthesis pathways[111] have been adopted recently. Moreover, multi step approaches have gained popularity due to their high level of controlability and construction complexity, by using metal-organic polyhedra as supermolecular building blocks.[112–114]

With the developments in material synthesis accompanied by computational simulations, thousands of MOFs were synthesized over the past twenty years.[92] The class of MOFs is basically a giant tool box for scientists. They are technological advanced materials which are capable of being used in various fields.[92] In the following, the crystals investigated in this work are introduced. Mg-MOF-74 was investigated because of its excellent separation properties regarding CO_2 adsorption. The ZIF family as well as the IFP family separate olefins from paraffins quite well, see Chapters 5 and 6. Their main advantage is that those structures are paraffin-selective, meaning that the desired product, the olefin, is more weakly adsorbed than the paraffin. That leads to the possibility for adsorption technologies, in which the olefin can be gained at high pressures during the adsorption step.

2.3.1 Mg-MOF-74

For certain MOFs, the removal of the solvent molecules (thermal activation) attached to the metal centers during synthesis can make these metal cations coordinately unsaturated and open to a direct approach by other molecules. These metal cations are called open metal sites (OMSs), also known as unsaturated metal centers (UMCs).[115] These OMSs can offer extra binding sites to the guest molecules especially at low loadings, and thus, enhance the capacity and selectivity towards certain guest molecules.[116] Also, these open metal cations serve as Lewis acids which are amenable for further functionalizations.[108] The thermal stability and the chemical stability is decent except when water (vapor) is introduced. Water dissociates into H_3O^+ and OH^- in proximity of the OMSs due to their strong electric field. The hydroxide ion

then "binds" with the metal ion which in turn elongates the metal-oxygen bond and damages the structure.[117]

The series of M_2(dobdc) (M = Mg, Co, Ni,...; dobdc^{4-} = 2,5- dioxido-1,4-benzenedicarboxylate) or M-MOF-74[118–121] or M-CPO-27 (CPO: Polymer of Oslo) are MOFs with honeycomb analogous structures with 1-dimensional channels, containing large micropores (11-12 $\AA$) and high concentrations of OMSs. Hence, it is isostructural regardless of the metal ion used. This was verified by X-ray defraction.[120,121] The carboxylate group coordinates two metal atoms in pinching mode while a third oxygen coordinates a third Mg-ion together with the oxygen atom of the deprotonated hydroxy-group in α-position to the carboxylate-group, hence forming a six-ring chelate complex. The oxido-group also coordinates one more magnesium atom. Thus, each α-oxido-carboxylate functionality of the ligand coordinates a total of four metal atoms. The crystallographic structure is depicted in Figure 2.7(a). Studies have shown that these OMSs are the primary coordination sites for guest molecules like water, CO_2, NO, and so on. Considerable effort was made to understand the effect different ions have on adsorption properties for various separation problems. It is important to note that this particular variant, the Mg-MOF-74 crystal, has emerged as one of the best frameworks to separate CO_2 from flue or natural gas.[35,122–130]

2.3.2 Zeolitic imidazolate frameworks (ZIF)

A unique subclass of MOFs are zeolitic imidazolate frameworks (ZIFs). Their crystalline structure is similar to zeolites. The organic linker is made of an imidazolate derivative (Im) and the most common metal centers (M) are Zn^{II} and Co^{II}. The application of other transition metals (e.g. Fe^{II}) has yet to show positive results regarding the desired porosity and high-symmetry structure.[131] Tetrahedral metal centers are coordinated by nitrogen atoms in 1,3 positions of the five-membered imidazole ring, creating an angle of 145° at the M-Im-M bond known from zeolites Si-O-Si bonding angle,[132] see Figure 2.6. By changing the metal, the linker, or both, a huge variety of ZIFs were constructed in recent years resulting in different topologies and functionality designs.[133] For 36 different tetrahedral structures 90 distinct ZIFs have been found until 2010.[133] However, all of them offer a regular and intracrystalline pore system which can be either 1-, 2-, or 3-dimensional. Solvothermal methods, which are introduced in the article of Park et al.,[131] are commonly used to synthesize ZIFs. According to the zeolite net structure, ZIFs can be classified the same way as their inorganic counterparts.[134] ZIF structures have been reported to possess larger pores than their equivalent

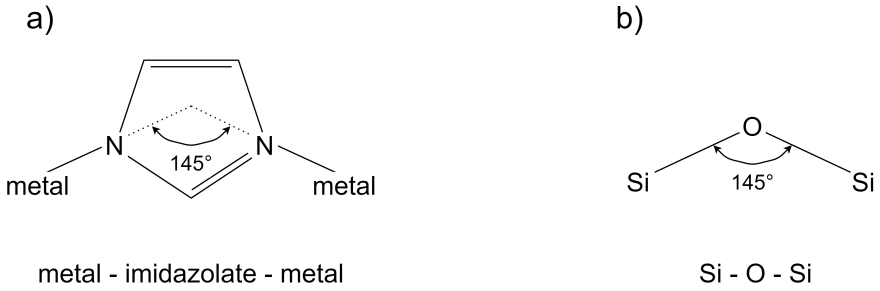

Figure 2.6: Main topology angle in ZIFs (a) and zeolites (b). Modified from Phan et al.[133]

inorganic counterparts. Moreover, their thermal stability and resistance to hydrolysis as well as other organic solvents outperform most MOFs (reported for ZIF-8 and ZIF-11).[131] ZIF structures of higher crystal symmetry (ZIF-8) excel in low physical densities and therefore high porosities and large surface areas.[132]

ZIFs are considered to be flexible, ever since experiments determined diffusion through pore apertures which are smaller than the critical molecule diameters.[85,135–138] The ZIFs investigated in this work are ZIF-8, ZIF-9, and ZIF-71, which were first reported by Park et al.[131] and Banerjee et al.,[33] respectively. The unit cell properties of the crystalls are shown in Table 2.4. ZIF-8 and ZIF-71 share a similar construction: for the metal center zinc is used. The hydrogen atoms connected to the C1 atoms in the ZIF-8 are replaced by chlorine in ZIF-71. At the same time the methyl group at the C2 is removed and only a hydrogen is left, see Figures 5.14 and 5.16, respectively. These relative small changes lead to an enormous difference in the topology. While ZIF-8 is known to have a *SOD* type topology, ZIF-71 is of *RHO* type. On top of that, the cage size and pore diameter increase from 11.6 $\AA$ to 16.5 $\AA$ and 3.4 $\AA$ to 4.2 $\AA$, respectively.[133] Despite ZIF-8 and ZIF-9 having the same net topology their building blocks are very different (Figures 5.14 and 5.15): ZIF-9 consists of cobalt ions and the linker includes a phenyl group instead of a methyl group. This leads to a change in the unit cell properties. ZIF-8 forms a cubic crystal instead of a hexagonal one like ZIF-9. By using the larger phenyl linker, the helium void fraction of the systems is greatly reduced, see Table 2.4 Representations of the unit cells can be seen in Figure 2.7(b), (c), and (d).

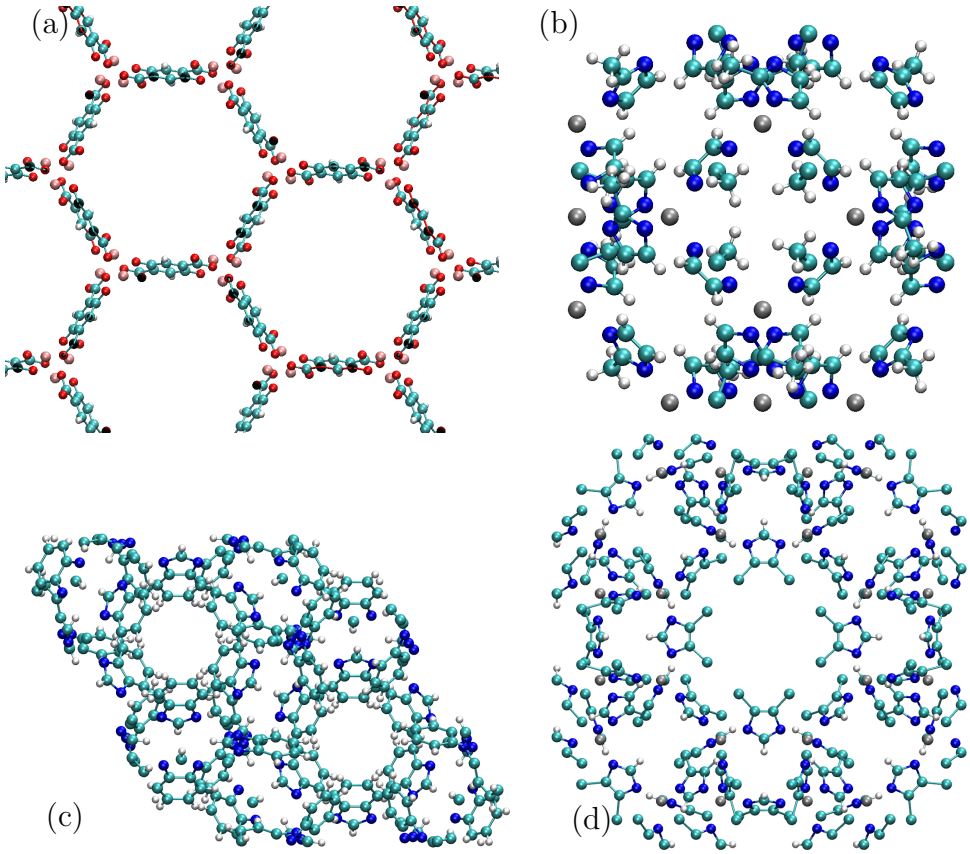

Figure 2.7: Representation for the crystal frameworks of Mg-MOF-74 (a), ZIF-8 (b), ZIF-9 (c), and ZIF-71 (d).[33,120,131]

2.3.3 Imidazolate frameworks Potsdam (IFP)

Another subclass are the imidazolate frameworks Potsdam (IFPs) which are closely related to the zeolitic imidazolate frameworks (ZIFs). The main difference can be found within the conncetivity of the metal centers to the organic linkers: The metal ions are pentacoordinated by donor atoms of three ligands to form a distorted environment with a trigonal-bipyramidal geometry;[140] they are not tetracoordinated like in ZIF structures. Moreover, the IFP structures are built from 2- substituted imidazolate-4-amide-5-imidates that were generated in situ by partial hydrolysis of 4,5 dicyano-2-substituted imidazole under solvothermal conditions in DMF and in the presence of a metal nitrate hydrate salt with R = methyl (IFP-1, IFP-5), R = bromo (IFP-3), and R = methoxy (IFP-7) and the connecting metal centers Zn^{2+} (IFP-1, IFP-3, IFP-7) and Co^{2+} (IFP-5).[139–143] The different pore sizes of the obtained one-dimensional channel structures are achieved by the different

Table 2.4: Overview of the geometric properties of the metal-organic frameworks investigated in this work.

MOFs	Cell length (nm)			Cell angle (deg)			Number of atoms	Helium void fraction
	a	b	c	α	β	γ	(-)	(-)
Mg-MOF-74[120,126]	2.611	2.611	0.692	90	90	120	162	0.700
ZIF-8[131]	1.699	1.699	1.699	90	90	90	276	0.492
ZIF-9[131]	2.294	2.294	1.575	90	90	120	522	0.264
ZIF-71[33]	2.855	2.855	2.855	90	90	90	816	0.475
IFP-1[139]	1.792	1.792	1.845	90	90	120	342	0.457
IFP-3[140]	1.790	1.790	1.863	90	90	120	288	0.411
IFP-5[141]	1.778	1.778	1.865	90	90	120	342	0.437
IFP-7[142]	1.753	1.753	1.863	90	90	120	360	0.344

substituents of the linker molecules that extend in the open pore structure. The crystalgraphic structures are shown in Figure 2.8.

The IFP-n family is rare in the sense that pentacoordinated Zn^{2+} ion is very uncommon in MOFs. IFP-1 became the first MOF in which fivefold coordination to the Zn^{2+} ion by only one ligand type was created.[139] The 3D coordination forms 1D hexagonal channels running along the z-axis, see Figure 2.8. The channel walls are created by the rigid and planar pentadentate imidazolate–amide–imidate linkers whereas the Zn^{2+} ions are located almost on the edges of the hexagonal symmetry. The thermal and chemical stability as well as the rigidity are at least on par with ZIFs.[133]

2.4 Quantum chemistry calculations

Quantum chemistry calculations are used to understand the behavior and properties of atoms and molecules on a molecular level. In general, it is distinguished between an *ab initio* and a (semi-)emperical ansatz. While the former does not use any "help" in the form of approximations, it is computationally more demanding. The latter makes use of such auxiliaries speeding up the simulations at the cost of accuracy or in the worst case may not even be applicable to the system at all. Strictly speaking, density functional theory is part of the empirical methods, however only some fitting parameters are needed. Thus, it is sometimes referred to as an *ab initio* method.

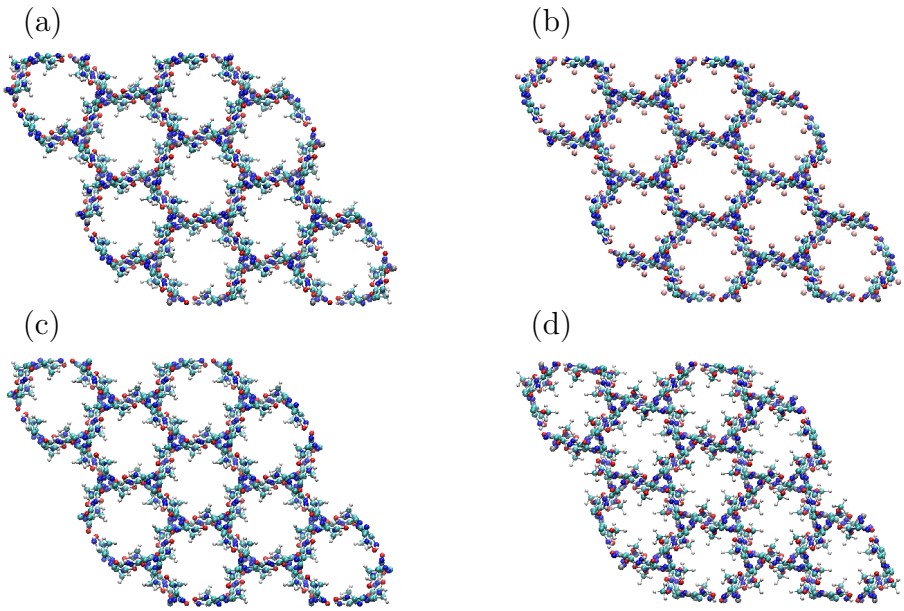

Figure 2.8: Representation for the crystal frameworks of IFP-1 (ion: Zn^{2+}, R=methyl)(a), IFP-3 (ion: Zn^{2+}, R=bromo) (b), IFP-5 (ion: Co^{2+}, R=methyl) (c), and IFP-7 (ion: Zn^{2+}, R=methoxy) (d).[139–143]

2.4.1 Schrödinger equation

The fundamental equation with respect to quantum chemistry is Schrödinger's equation in its time-independent form, see Eq. 2.72:

$$\left\{-\frac{\hbar}{2m}\nabla^2 + \mathscr{V}\right\}\Psi(\boldsymbol{r}) = E \cdot \Psi(\boldsymbol{r}), \tag{2.72}$$

Here, a single electron with mass m is moving through an external field $\mathscr{V}$ and can be found at vector $\boldsymbol{r}$. $\hbar$ is the reduced Planck's constant, Ψ is the wave function of the system, and E is the energy of the electron. Introducing the Hamiltonian operator $\mathscr{H}$ as

$$\mathscr{H} = -\frac{\hbar}{2m}\nabla^2 + \mathscr{V} \tag{2.73}$$

to the system, Eq. 2.72 is given in the following compressed form:

$$\mathscr{H}\Psi(\boldsymbol{r}) = E \cdot \Psi(\boldsymbol{r}). \tag{2.74}$$

Eq. 2.74 basically tells us to find wave functions Ψ, which when operated on by $\mathscr{H}$ are equal to energies E. Famously, this system has an exact solution

in the case of hydrogen. For elements with higher atomic numbers this system cannot be solved analytically anymore. However, it is still possible to write the problem in a general way similar to Eq. 2.74 where X nuclei with their respective coordinates $\boldsymbol{R}$ and Y electrons with their respective coordinates $\boldsymbol{r}$ are present. Since the same fundamentals must apply, this leads to:

$$\mathscr{H}\Psi(\boldsymbol{R},\boldsymbol{r}) = E\Psi(\boldsymbol{R},\boldsymbol{r}). \tag{2.75}$$

When one assumes that no relativistic effects, (external) electrostatic or magnetic fields are present as well as only Coulomb interactions between the particles are allowed, the Hamiltonian takes the following form:

$$\mathscr{H}(\boldsymbol{R},\boldsymbol{r}) = T_n + T_{el} + V_{n,el} + V_{el,el} + V_{n,n}, \tag{2.76}$$

where T_n is the operator of the kinetic energy of the nuclei in Hartree atomic units defined as

$$T_n = -\frac{1}{2}\sum_{i}^{X}\frac{\nabla_i^2}{M_i}, \tag{2.77}$$

T_{el} is the operator of the kinetic energy of the electrons defined as

$$T_{el} = -\frac{1}{2}\sum_{j}^{Y}\nabla_i^2, \tag{2.78}$$

$V_{n,el}$ is the attraction energy between the electrons and the nuclei with the charges Z_i defined as

$$V_{n,el} = -\frac{1}{2}\sum_{i}^{X}\sum_{\nu}^{Y}\frac{Z_\nu}{r_{i,\nu}}, \tag{2.79}$$

$V_{el,el}$ is the repulsion energy between the electrons defined as

$$V_{el,el} = \frac{1}{2}\sum_{i}^{Y}\sum_{j}^{Y}\frac{1}{r_{i,j}}, \tag{2.80}$$

$V_{n,n}$ is the repulsion energy between the nuclei defined as

$$V_{n,n} = -\frac{1}{2}\sum_{i}^{X}\sum_{j\neq i}^{X}\frac{Z_i Z_j}{r_{i,j}}. \tag{2.81}$$

2.4.2 Born-Oppenheimer approximation

Since it is not possible to find analytical solutions for more complicated versions (many-body versions) of Schrödinger's Equation (Eq. 2.75), it is mandatory to find approximations, which are as accurate as possible in order to gain approximate wave functions. The Born-Oppenheimer approximation was published in 1927, which effectively "separates" the very fast moving electrons from the very slow nuclei. That idea transforms the system into a state, in which only the electrons are moving while the nuclei are frozen at their respective positions.[144] Consequently, the kinetic energy of the nuclei, T_n, equals zero and the repulsion interaction between the nuclei , $V_{n,n}$, is a constant value. The remaining terms of the Hamiltonian operator in Eq. 2.76 are called the electronic Hamiltonian. The wave function solving this system is therefore called electronic wave function $\Psi_{electronic}$. It describes the motion of the electrons and only depends parametically from the coordinates of the nuclei. The same applies for the electronic energy $E_{electronic}$. As a result, the equation is valid for a given system geometry:

$$\mathscr{H}_{electronic}\Psi_{electronic}(\boldsymbol{R},\boldsymbol{r}) = E_{electronic}\Psi_{electronic}(\boldsymbol{R},\boldsymbol{r}). \tag{2.82}$$

Unless one is considering highly energetic systems including nuclei, the Born-Oppenheimer approximation can be considered as valid for the majority of cases.

2.4.3 Density functional theory

There are many different ways and methods to deal with the solution of the many-body Schrödinger equation, such as the Hartree-Fock method or post-Hartree-Fock methods. The latter ones are very accurate, yet the computational costs are very high. An alternative approach is the density functional theory (DFT) in which the total (electronic) energy is considered a function of the electron density distribution of a given system. Instead of the multi electron wave functions, for which each individual coordinates of each individual electron is computed, the electron density is based on only 3 coordinates, resulting in less demanding computations.

The basis for this theory was given by Thomas[145] and Fermi[146] in 1927. It was expanded upon by Hohenberg and Kohn in 1964,[147] who introduced two theorems with respect to the functional theory. The first one is called the "Existence Theorem", which states that once the electron density calculated for a given position at the ground state, any ground state property is exclusively defined. Thus, every ground state property is a functional of

the electron density distribution. That means the electron density can be computed from multi electron wave functions Ψ_0, which are related to the ground state energy E_0 as follows:

$$\mathscr{H}\Psi_0 = E_0\Psi_0. \tag{2.83}$$

Now, the ground state is not only defined by wave functions but by the ground state electron density ρ_0 as well, thus:

$$E_0 = E_0(\rho_0). \tag{2.84}$$

Similar to the wave functions the variational principle holds for the electron densities as well, which states that any Ψ' different from Ψ_0 corresponds to a different electron density ρ' and a different (larger) E':

$$E_0(\rho') \geq E_0(\rho_0). \tag{2.85}$$

Consequently, the second theorem (Eq. 2.85) says that once the functional for the electron density ρ' and its corresponding energy E' is found, it can be approximated by using approximate densities. As a result, the density can be further optimized by minimizing $E(\rho')$ due to the variational method. Furthermore, the ground state of a system can now be calculated without the knowledge of wave functions themselves but only by knowing electron densities:

$$E_0 = E_0(\rho_0) = \int V_{ext}(\boldsymbol{r})\rho_0(\boldsymbol{r})d\boldsymbol{r} + F(\rho_0(\boldsymbol{r})), \tag{2.86}$$

where $V_{ext}(\boldsymbol{r})$ is defined as the nuclear attraction potential energy for an electron at position vector $\boldsymbol{r}$. There is an additional constraint that must be met, namely the integral of the electron density ρ over all space must be equal to the number of electrons present in the system, e.g.:[148]

$$N = \int \rho(\boldsymbol{r})d\boldsymbol{r}. \tag{2.87}$$

The main problem, however, is the unknown functional $F(\rho(\boldsymbol{r}))$. In 1965, Kohn and Sham[149] were able to address this problem with their theorem which in turn was named after them. They divided the unknown functional $F(\rho(\boldsymbol{r}))$ into three parts:

$$F(\rho_0(\boldsymbol{r})) = E_{KE}(\rho_0(\boldsymbol{r})) + E_H(\rho_0(\boldsymbol{r})) + E_{XC}(\rho_0(\boldsymbol{r})), \tag{2.88}$$

where E_{KE} describes the kinetic energy of the non-interacting Y electrons with the corresponding orbitals ψ_i, $E_H(\rho_0(\boldsymbol{r}))$ is the classical electron-electron repulsion, and $E_{XC}(\rho_0(\boldsymbol{r}))$ is the exchange-correlation energy functional. The former two are defined as follows:

$$E_{KE}(\rho(\boldsymbol{r})) = \sum_i^Y \int \psi_i^*(\boldsymbol{r}) \left(-\frac{\nabla^2}{2}\right) \psi_i(\boldsymbol{r}) d(\boldsymbol{r}), \tag{2.89}$$

$$E_H(\rho(\boldsymbol{r})) = \frac{1}{2} \int \int \frac{\rho(\boldsymbol{r}_1)\rho(\boldsymbol{r}_2)}{|\boldsymbol{r}_1 - \boldsymbol{r}_2|} d\boldsymbol{r}_1 d\boldsymbol{r}_2. \tag{2.90}$$

Note that in Eq. 2.89 the electron density $\rho(\boldsymbol{r})$ of the real system is used although non-interacting electrons are considered. The term $E_{XC}(\rho_0(\boldsymbol{r}))$ consists of the exchange and correlation energy between the electrons and the difference between the correct kinetic energy of the system and $E_{KE}(\rho(\boldsymbol{r}))$. Now inserting Eq. 2.89 and Eq. 2.90 as well as the electron nuclear interaction energy into Eq. 2.86 leads to the complete set of Kohn-Sham equations:

$$\begin{aligned} E(\rho(\boldsymbol{r})) = &\sum_i^Y \int \psi_*^i(\boldsymbol{r}) \left(-\frac{\nabla^2}{2})\psi_i(\boldsymbol{r}\right) d(\boldsymbol{r}) + \frac{1}{2} \int \int \frac{\rho(\boldsymbol{r}_1)\rho(\boldsymbol{r}_2)}{|\boldsymbol{r}_1 - \boldsymbol{r}_2|} d\boldsymbol{r}_1 d\boldsymbol{r}_2 \\ &+ E_{XC}(\rho_0(\boldsymbol{r})) - \sum_j^X \frac{Z_i}{|\boldsymbol{r} - R_i|} \rho(\boldsymbol{r}) d(\boldsymbol{r}). \end{aligned} \tag{2.91}$$

The electronic density of the system $\rho(\boldsymbol{r})$ can be calculated as the sum of the square moduli of a set of one-electron orthonormal orbitals according to Kohn and Sham:[149]

$$\rho(\boldsymbol{r}) = \sum_i^Y |\psi_i(\boldsymbol{r})|^2. \tag{2.92}$$

By introducing Eq. 2.92 into Eq. 2.91 while applying the variational principle at the same time, the result is the so-called one-electron Kohn-Sham equation:

$$\left[-\frac{\nabla^2}{2} - \left(\sum_j^X \frac{Z_j}{|\boldsymbol{r}_{1,j} - \boldsymbol{R}_j|}\right) + \int \frac{\rho(\boldsymbol{r}_2)}{|\boldsymbol{r}_1 - \boldsymbol{r}_2|} d\boldsymbol{r}_2 + V_{XC}(\boldsymbol{r}_1)\right] \psi_i(\boldsymbol{r}_1) = \epsilon_i \psi_i(\boldsymbol{r}_1), \tag{2.93}$$

where ϵ_i are the orbital energies and V_{XC} is the functional derivative of the exchange-correlation energy E_{XC} which is defined as follows:

$$V_{XC}(\boldsymbol{r}) = \frac{\delta E_{XC}(\rho(\boldsymbol{r}))}{\delta \rho(\boldsymbol{r})}. \tag{2.94}$$

Ultimately, in order to determine the total energy of the system, Eq. 2.91 needs to be solved. This needs to be done in an iterative, self-consistent way: Initially, an initial electron density is guessed and put into Eq. 2.93. In return one obtains a system of molecular orbitals which produce an improved, more accurate electron density. This process is carried out until a converged solution is found. The idea of DFT is in simple words to group all unknown terms into one, here E_{XC}. Then, calculate all known interaction terms correctly and approximate the unknown as accurately as possible. Consequently, all terms present in Eq. 2.91 and Eq. 2.93 with the exception of the exchange-correlation energy E_{XC} is computed. This makes the decision which exchange-correlation functional to use very important and has significant implication on the outcome of the calculations. In general, E_{XC} can be defined as follows:

$$E_{XC}(\rho(\boldsymbol{r})) = \int \rho(\boldsymbol{r}) \cdot \epsilon_{XC}(\rho(\boldsymbol{r})) \cdot d(\boldsymbol{r}), \tag{2.95}$$

where ϵ_{XC} is the energy density acting on the system as a function of the electron density. One of the first approximations for the functional is called the *local density approximation* (LDA). It has its origins from an uniformly distributed electron gas, for which the exchange potential is easily calculated using the following equation:

$$V_X^{LDA} = -\frac{3}{4}\left(\frac{3}{\pi}\right)^{\frac{1}{3}} \rho^{\frac{1}{3}} \Rightarrow E_X^{LDA}(\rho) = -\frac{3}{4}\left(\frac{3}{\pi}\right)^{\frac{1}{3}} \int \rho^{\frac{4}{3}}(\boldsymbol{r}) d(\boldsymbol{r}) \tag{2.96}$$

The other half of the functional is obtained numerically by means of quantum Monte Carlo simulations and "translated" into a function, in which V_C^{LDA} is dependent on ρ.[150] A more complex approach makes not only use of the local value of the density but also includes the gradient, meaning that the exchange-correlation energy is a function the two:

$$E_{XC}^{GGA}(\rho) = \int f[\rho(\boldsymbol{r}), \nabla\rho(\boldsymbol{r})] d(\boldsymbol{r}) \tag{2.97}$$

This ansatz is called *generalized gradient approximation* (GGA). Widely used functionals of this forms were created by Perdew, Burke, and Ernzerhof

(PBE),[151,152] which do not include empirical parameters, and Becke.[153,154] Using the Hartree-Fock method, an exact calculation of the exchange energy, in combination to DFT methods, so-called hybrid functionals were engineered. The most famous one is the B3LYP functional, which essentially is a combination of the 3-parameter dependent functional (B3) by Becke[155–157] for the exchange part and the correlation functional by Lee,Yang, and Parr (LYP):[158]

$$E_{XC}^{B3LYP} = (1-\alpha)E_X^{LDA} + \alpha E_X^{HF} + \beta\delta E_X^B + (1-\gamma)E_C^{LDA} + \gamma E_C^{LYP}, \quad (2.98)$$

with $\alpha = 0.20$, $\beta = 0.72$, and $\gamma = 0.81$.

2.5 Molecular simulations

It is a common misinterpretation to assume that (molecular) simulations are not equivalent to scientific experiments, yet the similarities are quite clear: In both cases an external field is induced on the system to be observed and based on the conclusion of the experiments. While the real life experiments in the laboratory makes use of the real life physics around us, a similar environment needs to be created within the simulation box. Focusing on molecular simulations from here on out, classical physics and statistics are used to simulate reality by a computer. From here on forward, the fundamentals behind molecular simulations is given by introducing the concepts of statistical mechanics/thermodynamics, Monte Carlo, and molecular dynamics simulations, whereas the book by Frenkel and Smit *"Understanding Molecular Simulation: From Algorithms to Applications"*[159] served as a guideline for this introduction.

2.5.1 Statistical thermodynamics

Statistical thermodynamics, sometimes referred to as equilibrium statistical mechanics, links the status of micro states of any given system to macroscopic properties of it. In general, the condition a given system is in is not based on the trajectories or the momentum of the individual particles but the probability to find it in a specific micro state and its corresponding energy related to the system. Real life systems consist of atoms and molecules, which means that the number of particles (usually) exceeds 10^{23}, making the number of energy states almost infinite. Each particle or object, respectively,

has an individual position and momentum. That means that a system with N particles has N positional and N momentum vectors:

$$\left(\boldsymbol{r}^N, \boldsymbol{p}^N\right) \equiv (\overbrace{\overbrace{\boldsymbol{r}^1, \boldsymbol{r}^2, ..., \boldsymbol{r}^{N-1}, \boldsymbol{r}^N}^{configurational}; \overbrace{\boldsymbol{p}^1, \boldsymbol{p}^2, ..., \boldsymbol{p}^{N-1}, \boldsymbol{p}^N}^{momenta}}^{phase}). \tag{2.99}$$

The part containing the positional vectors is 3N large and is called *configuration space*, whereas the rest consists of the momenta vectors is also 3N large and is called *momenta space*. The 6N system containing all information is defined as *phase space*. In a given system Ω(E,N,V) represents the total number of eigenstates with the total energy E and a total number of particles N in the volume V. Considering each state to be distinguishable, that means the probability to find a given microstate with a predefined of energy E_i is:

$$P_j = \frac{1}{\sum_j \Omega_j(E_i)}. \tag{2.100}$$

Let us consider a system consisting of two (weakly interacting, energy exchanging) subsystems 1 and 2 which have the corresponding energies E_1 and E_2, whereas E= E_1 + E_2. By defining E_1, E_2 is predetermined and the total number of degenerate states of the system is not the sum but the product of microstates in each subsystem:

$$\Omega_{System}(E) = \Omega_{System}(E_1, E_2) = \Omega_1(E_1) \cdot \Omega_2(E_2). \tag{2.101}$$

Since the energy of the system is constant, one can rewrite Eq. 2.101 to:

$$\begin{aligned} &\Omega(E_1, E - E_1) = \Omega_1(E_1) \cdot \Omega_2(E - E_1) \\ \Leftrightarrow\ &\ln[\Omega(E_1, E - E_1)] = \ln[\Omega_1(E_1)] + \ln[\Omega_2(E - E_1)] \end{aligned} \tag{2.102}$$

Although every energy state of the system is equally likely, the number of eigenstates corresponding to a given energy distribution depends on E_1. In order to find the most likely value of E_1 we need to maximize $\ln[\Omega(E_1, E - E_1)]$:

$$\begin{aligned} &\left(\frac{\partial \ln[\Omega(E_1, E - E_1)]}{\partial E_1}\right)_{N,V,E} = 0 \\ \Leftrightarrow\ &\left(\frac{\partial \ln[\Omega_1(E_1)]}{\partial E_1}\right)_{N_1,V_1} = \left(\frac{\partial \ln[\Omega_2(E_2)]}{\partial E_2}\right)_{N_2,V_2}. \end{aligned} \tag{2.103}$$

With β defined as follows

$$\left(\frac{\partial \ln[\Omega(E,N,V)]}{\partial E}\right)_{N,V} \equiv \beta(E,N,V), \tag{2.104}$$

we can rewrite Eq. 2.103 as

$$\beta_1(E_1,N_1,V_1) = \beta_2(E_2,N_2,V_2). \tag{2.105}$$

Since energy can be exchanged, that means that the (thermodynamic) equilibrium is reached when Eq. 2.103 or Eq. 2.105 is satisfied and $\ln(\Omega)$ has reached its maximum. The second law of thermodynamics states that the entropy S of a system has reached its maximum when at thermal equilibrium. Hence, Boltzmann defined the following relationship:

$$S = k_B \ln(\Omega), \tag{2.106}$$

with k_B being Boltzmann's constant (=1.38066·$10^{-23}\frac{J}{K}$). Thus, there is a proportional relationship between entropy and the total number of microstates of the system. Furthermore, if systems in contact do not exchange energy anymore, one considers them to be equal in temperature T, which is thermodynamically defined as:

$$\frac{1}{T} = \left(\frac{\partial S}{\partial E}\right)_{N,V}. \tag{2.107}$$

Consequently, β is:

$$\beta = \frac{1}{k_B \cdot T}. \tag{2.108}$$

In the next step, one assumes system 1 is in the energy state E_i and in thermal equilibrium with system 2, a infinitely large heat bath. The bath has the Energy E_2=E-E_1 and its degeneracy is given by Ω_2(E-E_1). Hence, the probability P_1 to find system 1 in state E_i is as follows:

$$P_i = \frac{\Omega_2(E-E_i)}{\sum_j \Omega_2(E-E_j)}. \tag{2.109}$$

The problem now becomes to compute $\ln[\Omega_2(\text{E-E}_i)]$. Therefore, we use the Taylor expression around E_i =0. That leads to:

$$\begin{aligned} \ln[\Omega_2(E - E_i) &= \ln[\Omega(E)] - E_i \cdot \frac{\partial \ln[\Omega_2(E)]}{\partial E} + \mathscr{O}(\frac{1}{E}) \\ \Leftrightarrow \ln[\Omega_2(E - E_i) &= \ln[\Omega(E)] - \frac{E_i}{k_B T} + \mathscr{O}(\frac{1}{E}). \end{aligned} \tag{2.110}$$

This relationship can now be used to rewrite Eq. 2.109:

$$P_i = \frac{exp\left(-\frac{E_i}{k_B T}\right)}{\sum_j exp\left(-\frac{E_j}{k_B T}\right)}. \tag{2.111}$$

Eq. 2.111 is the famous Boltzmann distribution for a given system with temperature T. It also allows us to define the canonical partition function Q as:

$$Q = \sum_i exp\left(-\frac{E_i}{k_B T}\right). \tag{2.112}$$

These two equations can be used to calculate the average energy of the system $\langle E \rangle$ as the sum of the product of every energy state E_i times its probability to exist P_i:

$$\langle E \rangle = \sum_i E_i \cdot P_i = \frac{\sum_i E_i \cdot exp\left(-\frac{E_i}{k_B T}\right)}{\sum_j exp\left(-\frac{E_j}{k_B T}\right)} = \frac{\partial \ln Q}{\partial \frac{1}{k_B T}}. \tag{2.113}$$

Since one is essentially looking at a quantum based state in the sense that discrete energy (eigen-)states are present, it is necessary to convert the idea of partition function from a quantum mechanical standpoint to a classical one. This is done by integrating over the (complete) phase space (Eq. 2.99). Without going into detail on the exact math, the canonical partition function can be written as (see Eq. 2.112 for comparison):

$$Q \equiv \frac{1}{h^{dN} N!} \int d\boldsymbol{p}^N d\boldsymbol{r}^N exp\left\{-\beta\left[\sum_i \frac{p_i^2}{2m_i} + \mathscr{U}(d\boldsymbol{r}^N)\right]\right\}, \tag{2.114}$$

with d being the dimensionality of the system and $\mathscr{U}$ the potential energy. Alternatively:

$$Q \equiv \frac{1}{\Lambda^{3N} N!} \int d\boldsymbol{r}^N exp\left\{-\beta \mathscr{U}(d\boldsymbol{r}^N)\right\}, \tag{2.115}$$

with

$$\Lambda = \sqrt{\frac{h^2}{2\pi m k_B T}}\ . \tag{2.116}$$

In order to take the indistinguishability of the particles into account, the factor $\frac{1}{N!}$ has been included. The bridge between the quantum and the classical state can be found in the volume h^{dN}, which states that each quantum state corresponds to the given volume in the classical one.

Accordingly, one can derive a similar expression for an average of an observable property A:

$$\langle A \rangle = \frac{\int d\boldsymbol{p}^N d\boldsymbol{r}^N exp\left\{-\beta\left[\sum_i \frac{p_i^2}{2m_i} + \mathscr{U}(d\boldsymbol{r}^N)\right]\right\} \cdot A(\boldsymbol{p}^N, \boldsymbol{q}^N)}{\int d\boldsymbol{p}^N d\boldsymbol{r}^N exp\left\{-\beta\left[\sum_i \frac{p_i^2}{2m_i} + \mathscr{U}(d\boldsymbol{r}^N)\right]\right\}}, \tag{2.117}$$

Averages over all possible quantum states are referred to as an *ensemble* average. Yet, experiments are carried out as a function of time meaning that instantaneous properties are measured and then averaged. This correlates to molecular dynamics simulations, in which Newton's equations of motion are solved. Generally speaking, one does not sample eigenstates (the Monte Carlo approach). The *ergodicity* hypothesis basically links those two methods together. For a more detailed derivation the reader is referred to Ref. 159:

$$\overline{A_i(r)} = \langle A_i(r) \rangle_{NVE}. \tag{2.118}$$

Eq. 2.118 means that in order to measure an observable property of a system, one can determine that quantity by averaging over time ("molecular dynamics") or by averaging over the ensemble ("Monte Carlo"). Please note that many systems are in fact not ergodic, hence the hypothesis.

2.5.2 Monte Carlo

Since Eq. 2.114 and Eq. 2.117 are considered to be the basis for all classical simulations with respect to many-body systems, there needs to be a method to compute the averages of observables, thus the introduction of Monte Carlo.

One can make the case that the sheer amount of meshing points needed to solve the aforementioned equations is exceedingly large and not realistically applicable. In the following the fundamentals of the main adjustments to make the Monte Carlo method effective for solving this type of equations are presented.

First, Monte Carlo in its purest form is explained. Consider the following integral, which one wants to solve numerically:

$$I = \int_a^b f(x)dx. \tag{2.119}$$

While methods like Simpson's rule or the basic quadrature are valid options here, one could try to find the average of $\langle f(x)\rangle|_a^b$:

$$I = (b-a)\cdot\langle f(x)\rangle. \tag{2.120}$$

Sampling $\mathrm{f(x)}|_a^b$ randomly L times with $\mathrm{L}\rightarrow\infty$, the correct result for $\langle f(x)\rangle$ is obtained. When transferring this idea to Eq. 2.117, one can see that one problem arises. Since this is brute force approach, L must be very large, In addition, energy states are often sampled, whose the Boltzmann factors are basically zero, and thus, do not contribute to the average. Hence, importance sampling, which is a method of variance reduction at its core, has been introduced by Metropolis et al.[160] in 1953. Unfortunately, it is generally not possible to compute integrals of the type represented in Eq. 2.117, e.g. $\int d\boldsymbol{r}^N exp\left[-\beta\mathscr{U}(\boldsymbol{r}^N)\right]$. In what is later called the Metropolis method,[160] they found out that there is a method to compute the ratio of the two integrals present in the following equation:

$$\begin{aligned}\langle A\rangle =& \frac{\int d\boldsymbol{r}^N exp\left[-\beta\mathscr{U}(\boldsymbol{r}^N)\right]\cdot A(\boldsymbol{r}^N)}{\int d\boldsymbol{r}^N exp\left[-\beta\mathscr{U}(\boldsymbol{r}^N)\right]}\\ \Leftrightarrow \langle A\rangle =& \frac{\int d\boldsymbol{r}^N exp\left[-\beta\mathscr{U}(\boldsymbol{r}^N)\right]\cdot A(\boldsymbol{r}^N)}{Z}.\end{aligned} \tag{2.121}$$

Furthermore, the probability density $\mathscr{N}$ to find the system in a given configuration $\boldsymbol{r}^N$ is defined as:

$$\mathscr{N}(\boldsymbol{r}^N) \equiv \frac{exp\left[-\beta\mathscr{U}(\boldsymbol{r}^N)\right]}{Z} = \frac{exp\left[-\beta\mathscr{U}(\boldsymbol{r}^N)\right]}{\int d\boldsymbol{r}^N exp\left[-\beta\mathscr{U}(\boldsymbol{r}^N)\right]} \geq 0. \tag{2.122}$$

A well known example to explain the difference between the conventional quadrature and the Metropolis method is the measurement of the Nile depth,

see Ref. 159. The quadruple method is dependent on its (static) step size and it is possible that the depth of the Nile is measured without the Nile being there, i.e. on land. In the Metropolis scheme, one measures the depth while standing in the water and then moving forward randomly. If one is to go out of the water and on land, said measurement is rejected and one is backtracked into the river again. In other words, the Nile depth will only be measured where the Nile actually is. Clearly, the latter method is superior to the former in terms of effectiveness.

So, how is that principle translated to molecular simulations of the Monte Carlo type. First, we construct a system with N particles, whose configuration $\boldsymbol{r}^N$ has a non-vanishing Boltzmann factor. This state is now denoted as "o" (for old). Thus, the Boltzmann factor is $exp\left[-\beta\mathscr{U}(o)\right]$. By disturbing the system o with a small random displacement δ, a "new" trial configuration is obtained: state "n" with the Boltzmann factor $exp\left[-\beta\mathscr{U}(n)\right]$. Similar to the example with the Nile, it must be decided whether that new configuration is accepted or not. There are many possible rules to do so, however, only the Metropolis scheme will be discussed here.[160]

Let us assume that in equilibrium it is equally likely starting from o with the probability density to exist of $\mathscr{N}(o)$ to get to configuration n with the probability density to exist of $\mathscr{N}(n)$. This must be the same as to go from n to o. In other words, the average number of accepted trial moves resulting in the transition from o to a different configuration n must be equal to the number of accepted trial moves from all n states to o. This basically leads to the required fulfillment of the so-called detailed balance:

$$\mathscr{N}(o)\pi(o \to n) = \mathscr{N}(n)\pi(n \to o) \tag{2.123}$$

with $\pi(o \to n)$ being the transition probability to go from o to n. This probability π can be further broken down into two factors, similar to how Monte Carlo works. The transition matrix $\alpha(o \to n)$ is the probability to perform a certain trial move from o to n and is usually referred to as the underlying matrix of the Markov chain.[161] The next step is whether the move is accepted or not with the probability $acc(o \to n)$, thus:

$$\pi(o \to n) = \alpha(o \to n) \cdot acc(o \to n). \tag{2.124}$$

Please note that in the simplest from α is symmetric, e.g. $\alpha(o \to n) = \alpha(n \to o)$, but that is not necessarily the case. In case of symmetry however, the detailed balance is reduced to:

$$\mathscr{N}(o) \cdot acc(o \to n) = \mathscr{N}(n) \cdot acc(n \to o) \tag{2.125}$$

Introducing the definition for the probability density from Eq. 2.122 to Eq. 2.125, one gets:

$$\frac{acc(o \to n)}{acc(n \to o)} = \frac{\mathscr{N}(n)}{\mathscr{N}(n)} = exp\left\{-\beta[\mathscr{U}(n) - \mathscr{U}(o)]\right\}. \tag{2.126}$$

Now, Metropolis et al. defined their rules on how to accept the moves as follows:

$$\begin{aligned} acc(o \to n) &= \frac{\mathscr{N}(n)}{\mathscr{N}(o)} && \text{if } \mathscr{N}(n) < \mathscr{N}(o) \\ acc(o \to n) &= 1 && \text{if } \mathscr{N}(n) \geq \mathscr{N}(o). \end{aligned} \tag{2.127}$$

This acceptance rule works in the following way: Based on state o one creates a new state n. After that, the energy of state n is compared to the one of state o with two possible outcomes. The first one is $\mathscr{U}(n) \leq \mathscr{U}(o)$. In that case the move is accepted. In the opposite case, e.g. $\mathscr{U}(n) > \mathscr{U}(o)$, the ratio of the Boltzmann factor is compared to a random number. If the former is smaller than said number, the move is accepted. If the latter is smaller, it is rejected:

$$acc(o \to n) = \min\left(1, exp\left\{-\beta[\mathscr{U}(\boldsymbol{r}_n^N) - \mathscr{U}(\boldsymbol{r}_o^N)]\right\}\right). \tag{2.128}$$

Eq. 2.128 is the acceptance rule for the canonical (NVT) ensemble, in which the number of particles N, the volume of the simulation box V, and the temperature T are kept constant, defining the canonical ensemble as the "natural" ensemble for Monte Carlo simulations, since no additional considerations are involved. Consequently, the moves that can be carried out are (pre-)defined, i.e. the random walks allowed in the phase space of the system. The most frequently used trivial move is the translational shift of any given particle in space (without rotation). As for any move it needs to be completely random, random number generators are used to obtain new positions. After the total energy of the system in the old state $\mathscr{U}(o)$ has been calculated, a random displacement is added to the randomly chosen molecule i:

$$\boldsymbol{r}^i(o) \to \boldsymbol{r}^i(n) = \boldsymbol{r}^i(o) + \Delta, \text{with } \Delta = \left[\begin{pmatrix} -0.5 \cdot \Xi \\ -0.5 \cdot \Xi \\ -0.5 \cdot \Xi \end{pmatrix} \cdots \begin{pmatrix} +0.5 \cdot \Xi \\ +0.5 \cdot \Xi \\ +0.5 \cdot \Xi \end{pmatrix}\right] \tag{2.129}$$

where Ξ is the maximum displacement allowed. Note that Ξ can vary depending on the code but it is generally advised to achieve 50% successful move attempts. Due to the periodic boundary conditions, which will be explained in Chapter 2.5.4, the absolute maximum displacement can only be the box size itself. The total energy of the new configuration $\mathscr{U}(n)$ is calculated and the acceptance rule in Eq. 2.128 is applied. If accepted, the new configuration becomes the old one in the subsequent step or the old configuration is restored and is still the old configuration. Also trivial is the rotation of molecule i, which is done by multiplying the positional vector with a rotation matrix using randomly generated angles. The third move applicable in the NVT ensemble is the regrow move. Here, molecule i is deleted and build completely new at a randomly generated position. While it sounds very similar to the other two, it is more complicated when larger molecules are involved. Hence configurational-bias Monte Carlo was introduced.[162–165] To illustrate the problem at hand, let us consider monomer m. The probability to insert monomer m successfully is α. If we now assume a polymer k consisting of n monomers, the probability to insert the polymer becomes approximately α^n. In dense systems or systems with framework atoms present, $\alpha \ll 1$ and consequently, only short chains can be inserted at high success rates. In the configurational-bias scheme, positions are tested up to k times before inserting a monomer and the insertion fails if all k trails fail for each monomer. Thus, the probability changes to approximately $\alpha[1-(1-\alpha)^k]^{m-1} = \alpha\phi^{m-1}$. A more detailed description is given in Ref. 159.

Clearly aside from the canonical (NVT) ensemble, there are other ones relevant for molecular simulations, which keep certain properties of the system constant. One is the microcanonical (NVE) ensemble, in which the number of particles N, the volume V, and the energy E of the system is kept constant. It will be shown in Chapter 2.5.3 that this is the "natural" ensemble for molecular dynamics simulations. In reality, one is usually not able to control the volume and/or energy of the system. Instead most experiments are carried out under conditions of constant pressure p and temperature T, i.e. the isobaric-isothermal ensemble (NPT). Here, the volume of the simulation box is not constant due to the pressure enforced onto the system. This ensemble works well for homogeneous fluids but in case of inhomogeneous systems, e.g. crystalline solids, changing the size of the simulation box might not be sufficient enough to probe the phase space. In the isotension-isothermal ensemble, the configuration of the simulation box (cell box length, cell box angles and so on) are allowed to change as well in order to avoid creating grain boundaries or other highly stressed configurations.

Lastly, there are ensembles which allow for a fluctuation of the number of particles present in one simulation box: the Gibbs ensemble and the grand canonical ensemble. The former is mainly used to calculate vapor–liquid equilibria and the latter is mainly used in adsorption simulations. Note that each ensemble is able to probe those two mentioned experiments, whereas one is better suited than the other with respect to the application, i.e. the Gibbs ensemble is better suited for vapor–liquid equilibrium simulations and vice versa. Generally, they both work in a similar way. Let us assume a homogeneous fluid in a simulation box. Assuming a specific density and temperature, there will be a transition/decomposition to an inhomogeneous fluid with a gas and a liquid phase present. In this system it is very likely that the interphase of those two phases takes the majority of space inside the simulation box. Since one is generally interested in the bulk properties of each phase, it becomes clear that this setup does not provide a satisfactory representation. One way to circumvent this is to make the simulation box (very) large. This theoretically solves the issue at the cost of long equilibration and thus computation time. In the second approach, the Gibbs ensemble approach, one makes use of the thermodynamic equilibrium definition:

$$\mu^{\text{gas}} = \mu^{\text{liquid}}, \tag{2.130}$$

with μ being the chemical potential. The idea of the Gibbs ensemble is now to set up to boxes, which are coupled with one another in such a way that molecules can be exchanged between them. As a result, no interphase is generated and only bulk phase properties are sampled with one box representing the gaseous and one the liquid phase. The move allowing for such behavior is called a swap move. One molecule is taken out of box number one and inserted into box number two. Strictly speaking, the Gibbs ensemble is not a real ensemble despite the constant chemical potential μ, pressure p, and temperature T. The reason this ensemble does not exist is as follows. If only intensive parameters are specified, e.g. pressure, temperature, and chemical potential, extensive variables like volume become unbound, since the intensive parameters are considered to be linear dependent on each other. Hence, at least one extensive variable is needed. This definition is satisfied in the grand canonical ensemble which keeps μ, V, and T constant. In a real life adsorption experiment, the mass of the adsorbent (which in turn can be related to its volume) is defined as well as the surrounding temperature and pressure, which is linked to the chemical potential via an equation of state. Since adsorption is an exothermal, spontaneous process gas molecules will diffuse into the crystal and the chemical potential of the guest molecules is in equilibrium with the ones in the (infinitely) large reservoir outside the

crystal, e.g. the bulk phase. These are exactly the conditions present in the grand canonical ensemble. Since it plays a similar important role as the NVT ensemble, the statistical mechanical foundations will be discussed in detail. Starting from 2.115 one assumes a cubic system with $L = V^{\frac{1}{3}}$ and N identical particles. Consequently, we can rewrite the positional vector $\boldsymbol{r}^i$ for molecule i:

$$\boldsymbol{r}^i = \boldsymbol{s}^i \cdot L. \tag{2.131}$$

This leads to:

$$Q(N,V,T) = \frac{V^N}{\Lambda^{3N} N!} \int_0^1 \cdots \int_0^1 d\boldsymbol{s}^N exp\left\{-\beta \mathscr{U}(\boldsymbol{s}^N, L)\right\} \tag{2.132}$$

Next, we assume that the system is separated by a piston from an ideal gas reservoir with a fixed total volume of V-V_0 and M-N particles, meaning that the volume of our system plus the reservoir equals V_0 and has M particles in it. The partition function of the system is a product of the two present subsystems:

$$Q(N,M,V,V_0,T) = \frac{V^N (V_0 - V)^{M-N}}{\Lambda^{3M} N!(M-N)!} \int d\boldsymbol{s}^{M-N} \int d\boldsymbol{s}^N exp\left\{-\beta \mathscr{U}(\boldsymbol{s}^N, L)\right\} \tag{2.133}$$

Eq. 2.133 is the partition function for the isobaric isothermal ensemble and serves as starting point for the grand canonical one since we exchange particles instead of volume. The (potential) energy of the system changes upon insertion from $\mathscr{U}(\boldsymbol{s}^N)$ to $\mathscr{U}(\boldsymbol{s}^{N+1})$. Hence, the partition function of the system including the subsystems becomes:

$$Q(M,V,V_0,T) = \sum_{N=0}^{M} \frac{V^N (V_0 - V)^{M-N}}{\Lambda^{3M} N!(M-N)!} \int d\boldsymbol{s}^{M-N} \int d\boldsymbol{s}^N exp\left\{-\beta \mathscr{U}(\boldsymbol{s}^N, L)\right\} \tag{2.134}$$

Since we now know how the partition function of the system looks like, imagine a move in which a particle is taken from the reservoir and inserted into our system with the constraint that the relative position inside each box is the same, e.g. $\boldsymbol{s}^i_{outside} = \boldsymbol{s}^i_{inside}$. The resulting probability density for this system becomes:

$$\mathscr{N}(\boldsymbol{s}^M, N) = \frac{V^N (V_0 - V)^{M-N}}{Q(M, V, (V_0 - V, T)) \cdot \Lambda^{3M} N!(M-N)!} exp[-\beta \mathscr{U}(\boldsymbol{s}^N)]. \tag{2.135}$$

One now assumes that a particle is taken out of the reservoir and put into the observable system with volume V. Choosing the transition matrix in a symmetric way and using the detailed balance in Eq. 2.123 one gets the following acceptance rules:

$$acc(N \to N+1) = \frac{V(M-N)}{(V_0 - V)(N+1)} exp\left\{-\beta\left[\mathscr{U}(\boldsymbol{s}^{N+1}) - \mathscr{U}(\boldsymbol{s}^N)\right]\right\}, \tag{2.136}$$

$$acc(N+1 \to N) = \frac{(V_0 - V)(N+1)}{V(M-N)} exp\left\{-\beta\left[\mathscr{U}(\boldsymbol{s}^{N}) - \mathscr{U}(\boldsymbol{s}^{N+1})\right]\right\}. \tag{2.137}$$

Up to this point the outside reservoir is finite. From M$\to \infty$ and (V_0-V)$\to \infty$ follows that the outside volume becomes infinite with the density of $\rho = \frac{M}{(V_0 - V)}$. For an ideal gas the chemical potential μ can be calculated as follows:

$$\mu = k_B T \ln \Lambda^3 \rho. \tag{2.138}$$

Thus, in the limit of $\frac{M}{N} \to \infty$ Eq.2.134 becomes

$$Q(\mu, V, T) \equiv \sum_{N=0}^{\infty} \frac{exp(\beta \mu N) V^N}{\Lambda^{3N} N!} \int d\boldsymbol{s} \cdot exp[-\beta \mathscr{U}(\boldsymbol{s}^N)], \tag{2.139}$$

and the corresponding probability density

$$\mathscr{N}_{\mu VT}(\boldsymbol{s}^N, N) \propto \frac{exp(\beta \mu N) V^N}{\Lambda^{3N} N!} exp[-\beta \mathscr{U}(\boldsymbol{s}^N)], \tag{2.140}$$

whereas Eq. 2.139 and 2.140 serve as the basic framework for Monte Carlo simulations in the grand canonical ensemble.

One very important technique is called Widom insertion.[166] This is a particle insertion method, which allows the user to sample the chemical potential and the free energy of a given system. While there is not really a restriction

to which ensemble it can be applied in, it is most commonly used in the canonical ensemble. It is known that the chemical potential μ is defined as follows:

$$\mu = \left(\frac{\partial G}{\partial N}\right)_{PTN} \tag{2.141}$$

$$\mu = \left(\frac{\partial F}{\partial N}\right)_{VTN} \tag{2.142}$$

$$\mu = \left(-T\frac{\partial S}{\partial N}\right)_{VEN}, \tag{2.143}$$

with G being the Gibbs free energy, F the Helmholtz free energy, and S the entropy. The Helmholtz free energy of any given system in an canonical ensemble is

$$F(N,V,T) = F_{id}(N,V,T) + F_{ex}(N,V,T) = -k_B T \ln(Q) \tag{2.144}$$

Hence, the Helmholtz free energy consists of an ideal gas part and an excess part. With Eq. 2.132 one gets

$$F(N,V,T) = -k_B T \ln\left(\frac{V^N}{\Lambda^{dN} N!}\right) \ln\left\{\int d\boldsymbol{s}^N exp\left[-\beta \mathscr{U}(\boldsymbol{s}^N, L)\right]\right\}. \tag{2.145}$$

For N$\rightarrow \infty$, one can conclude from Eq. 2.143 that the following holds:

$$\mu = -k_B T \ln\left(\frac{Q_{N+1}}{Q_N}\right) \equiv \mu_{id}(\rho) + \mu_{ex} \tag{2.146}$$

Including the explicit form similar to Eq. 2.145, one gets

$$\mu = -k_B T \ln\left(\frac{\frac{V}{\Lambda^d}}{N+1}\right) - k_B T \ln\left\{\frac{\int d\boldsymbol{s}^{N+1} exp[-\beta \mathscr{U}(\boldsymbol{s}^{N+1})]}{\int d\boldsymbol{s}^N exp[-\beta \mathscr{U}(\boldsymbol{s}^N)]}\right\} \tag{2.147}$$

Since μ_{id} can be obtained analytically, the focus is on the excess part of μ. Separating the potential energy of the (N+1) system into the N system and the interaction energy of the (N+1)th particle with the rest ($\Delta\mathscr{U} = \mathscr{U}(\boldsymbol{s}^{N+1}) - \mathscr{U}(\boldsymbol{s}^N)$), one obtains an expression for the excess chemical potential μ_{ex}:

$$\mu_{ex} = -k_B T \ln \left(\int d\boldsymbol{s}_{N+1} \langle exp(-\beta \Delta \mathscr{U}) \rangle_N \right). \tag{2.148}$$

Here, $\langle \cdots \rangle_N$ is the canonical ensemble average over the configurational space of the given system, and thus, can be sampled using the Metropolis scheme. While the equations look complex, it is easy to understand what this mechanism does: One can imagine to insert "ghost" particles into the system and calculate the energy of the system without actually accepting the insertion move. As a result, these energies are averaged and introduced into the equation.

2.5.3 Molecular dynamics

The Monte Carlo technique samples the (complete) phase space of a given system, it does not, however, behave like a normal real life experiment, since time and to a certain degree physics does not play a role. Random walks move the particles randomly inside the simulation box. Molecular dynamics on the other hand is very similar to reality, because the evolution of a system with time is portrayed, following Newton's laws of motion. Hence, it is the closest (molecular) simulations can come to describe real life events. Clearly, in this classical many-body approach quantum effects are also neglected.

The foundations of this molecular simulation are Newton's laws of motion. The first one states that if all forces acting on an object are equal to zero, the movement of said object is not altered whether it is moving already nor at a stand still. The second one relates force and momentum in the following way:

$$\boldsymbol{F}(t) = \frac{d\boldsymbol{p}}{dt} = m\frac{d\boldsymbol{\nu}}{dt} + \nu\frac{dm}{dt} \tag{2.149}$$

Unless relativistic effects have to be taken into account, which is not the case in the systems investigated in this study, the latter term $\nu\frac{dm}{dt}$ is equal to zero. The third law states that the force acting on object A is the exact same but opposite force acting on object B, i.e.:

$$\boldsymbol{F}_{AB} = -\boldsymbol{F}_{BA} \tag{2.150}$$

It will be explained thoroughly in Chapter 2.5.4, how energies and forces are computed in molecular simulations. For now, it will be discussed how the evolution of the system is managed. This means in context of molecular dynamics in what way Newton's equation of motion are solved or integrated,

respectively. There are different algorithms to do this numerically. One of the simplest yet (usually) one of the best is the (Velocity-)Verlet algorithm, a simplistic integrator. Starting from a random position $\boldsymbol{r}$(t) for a given particle, one is now interested in the position in the next time step Δt. In order to obtain this position, a Taylor expansion around time t is carried out. For the sake of simplicity, it is done for just one dimension, hence $\boldsymbol{r}$=r:

$$r(t+\Delta t) = r(t) + r'(t)\Delta t + r''(t)\Delta t^2 + \frac{\Delta T^3}{3!}r''' + \mathscr{O}(\Delta t^4) \tag{2.151}$$

Another way to write Eq. 2.151 is

$$r(t+\Delta t) = r(t) + v(t)\Delta t + \frac{F(t)}{2m}\Delta t^2 + \frac{\Delta T^3}{3!}r''' + \mathscr{O}(\Delta t^4). \tag{2.152}$$

In case the position at time (t-Δt) is needed, one derives that in a similar way:

$$r(t-\Delta t) = r(t) - v(t)\Delta t + \frac{F(t)}{2m}\Delta t^2 - \frac{\Delta T^3}{3!}r''' + \mathscr{O}(\Delta t^4). \tag{2.153}$$

Now Eq: 2.152 and 2.153 are summed up, which leads to

$$r(t+\Delta t) + r(t-\Delta t) = 2r(t) + \frac{F(t)}{m}\Delta t^2 + \mathscr{O}(\Delta t^4) \tag{2.154}$$

or approximately

$$r(t+\Delta t) \approx 2r(t) - r(t-\Delta t) + \frac{F(t)}{m}\Delta t^2. \tag{2.155}$$

Obviously, an error is introduced from Eq. 2.154 to 2.155 in the order of Δt^4 with Δt being the time step in our simulation. Interestingly, the Verlet algorithm does not need the velocity to compute new positions. However, it is possible to compute it anyway using the trajectory of the particle. In that case the following relationship holds:

$$\begin{aligned} r(t+\Delta t) - r(t-\Delta t) &= 2\nu(t) + \mathscr{O}(\Delta t^3) \\ \Leftrightarrow \nu(t) &= \frac{r(t+\Delta t) - r(t-\Delta t)}{2\Delta t} + \mathscr{O}(\Delta t^3). \end{aligned} \tag{2.156}$$

This method allows calculating the (instantaneous) temperature and kinetic energy with an error of $\mathcal{O}(\Delta t^3)$. Unfortunately, the velocity is not calculated at the same time as the positions. This drawback can be circumvented. Combining Eq. 2.155 and 2.156 results in:

$$\nu(t) = \frac{r(t)}{\Delta t} - \frac{r(t-\Delta t)}{\Delta t} + \frac{F(t)}{2m}\Delta t. \tag{2.157}$$

The same ansatz can be derived for ν(t +Δ t) and then added to Eq.2.157 resulting in:

$$\nu(t) + \nu(t+\Delta t) = \frac{r(t+\Delta t)}{\Delta t} - \frac{r(t-\Delta t)}{\Delta t} + \frac{F(t)+F(t+\Delta t)}{2m}\Delta t. \tag{2.158}$$

Rearranging the equation above gives a relationship between ν(t) and ν(t +Δt):

$$\nu(t+\Delta t) = \nu(t) + \frac{F(t)+F(t+\Delta t)}{2m}\Delta t. \tag{2.159}$$

Repeating the same approach for r(t-Δt), one obtains an expression to determine the new position at (t+Δt) including the velocity:

$$r(t+\Delta t) = r(t) + \nu(t)\Delta t + F(t)\frac{\Delta t^2}{2m}. \tag{2.160}$$

Eq. 2.159 and 2.160 are the integration scheme called velocity-Verlet. This algorithm calculates the velocities at the same (time) step as the positions. Because of its advantages, like simplicity, quickness, little memory usage, and time reversibility, it is the most commonly used integrator for molecular dynamics simulations. This algorithm has basically three steps of operation to generate the properties of a particle at time (t+Δt) starting from time t:

1. From r(t), ν(t), and F(t) one obtains r(t+Δt), see Eq. 2.160.
2. Based on the new positions r(t+Δt), F(t+Δt) can be obtained.
3. Knowing ν(t), F(t), and F(t+Δt), one can determine ν(t+Δt).

It is important to understand what a good integrator is and what properties it should possess. The most obvious criteria are computing time, time step size, and accuracy. The faster the algorithm and the less memory it requires is of importance for the computational time needed to simulate the system. Consequently, one wants to make the time step as large as possible

to increase the efficiency but at the same time as small as possible to avoid the generation of large force gradients between time steps. In addition, in Newton's system the energy of a system is conserved. This is related to the accuracy of the integrator, because the energy drift due to numerical issues needs to be minimized. Note that it is usually more crucial, that the long time drift is minimal while the short term drift is the less important of the two. The velocity-Verlet algorithm for example has moderate short term but little long term drift.[159] Furthermore, time reversibility is also important. These constraints are fulfilled by the (velocity-)Verlet algorithm. Consequently, since in a molecular dynamics simulation the particle number N, the volume V, and the energy of the system E are constant, the natural ensemble MD simulations sample is the microcanonical (NVE) ensemble. As the (total) energy of the system is constant, it is obvious that the sum of the kinetic energy E_{kin} and the potential energy E_{pot} has to be constant. Furthermore, temperature and pressure fluctuate dut to their relation to the respective energy parts. Because of the way molecular dynamics simulations work, it is more convenient to use ensembles, in which the temperature, pressure or both are constant, e.g. the canonical and the isothermal-isobaric ensemble, respectively. This idea however seems a bit counterintuitive, considering the fact that the integrator was chosen specifically to conserve energy and to be time reversible. Before it can be explained how to keep the temperature constant, it is necessary to define what "constant temperature" in this context actually means. Let us assume that we couple our NVE ensemble to a heat bath to impose a constant temperature, transforming the ensemble to a NVT one. Accordingly, the probability to find a specific velocity is given by the Maxwell-Boltzmann distribution:

$$P(\nu) = 4\pi \left(\frac{m}{2\pi k_B T}\right)^{\frac{3}{2}} \nu^2 exp\left(-\frac{m\nu^2}{2k_b T}\right) \tag{2.161}$$

From the kinetic gas theory one gets a relationship between the kinetic energy per particle (hence the $\langle \cdots \rangle$) and the (imposed) temperature of the system:

$$\langle \frac{1}{2} m\nu^2 \rangle = \frac{1}{2} k_B T \tag{2.162}$$

This leads to something called the instantaneous temperature T(t). Since the kinetic energy of the system fluctuates, so does the temperature:

$$T(t) = \sum_{i=0}^{N} \frac{m_i \nu_i^2(t)}{k_b N_f}, \tag{2.163}$$

with N_f being the degrees of freedom of the system:

$$N_f = 3N - 3. \tag{2.164}$$

Thus, to get an correct value for the temperature one has to average over many fluctuations and that average is what is measured in experiments as well.

One of the first and commonly used method of temperature control was developed by Andersen.[167] In his approach, a heat bath is coupled to our system to obtain a constant temperature, as mentioned above. This interaction is represented by stochastic impulse forces, which act on randomly chosen particles regularly. In general, this method makes use of Monte Carlo moves to transition the system into the desired NVT ensemble. In between the temperature regulation by MC steps, Newton's laws of motion are integrated as if the system was simulated in a NVE ensemble. Prior to the simulation in the NVT ensemble with constant temperature, one needs to define the frequency of the stochastic collisions ϕ, which in turn define the strength of the heat bath coupling. Assuming that successive collisions are uncorrelated, the distribution of time intervals between those collisions, P(t,ϕ) becomes a Poisson form.[168] More specifically, P(t,ϕ) is the probability that the next collision will occur within the interval of [t,t+dt]:

$$P(t, \phi) = \phi \cdot exp(-\phi t) \tag{2.165}$$

The work sxcheme of this method is as follows: Firstly, initial position $\boldsymbol{r}$(t=0) and velocities $\boldsymbol{\nu}$(t=0) or momenta $\boldsymbol{p}$(t=0), respectively, are generated. To obtain the next time step (t+Δt), Newton's laws of motion are integrated using a simplistic integrator, such as the velocity-Verlet algorithm for example. Next, a certain number of particles will interact with the coupled heat bath with the probability of being selected equal to $\phi\Delta$t. For those particle(s) selected, a new velocity will be taken from a Maxwell-Boltzmann distribution (Eq. 2.161) for the imposed temperature T. Other particles' velocity are not altered in any way. While this method yields accurate results for time-independent properties independent from ϕ,[159] the system is disturbed in an unphysical way, which manifests itself in the fact that time-dependent properties are altered and do not represent reality. Furthermore, the momentum is not conserved. Koopman and Lowe[169] developed the method further by manipulating the relative velocity of a pair of particles. A successful collision with the bath results in assigning a new Maxwell-Boltzmann distribution based velocity. With this approach the linear and angular momentum is conserved which is an advantage over Anderson's version.

In contrast to the Andersen and Lowe-Andersen thermostat, Nose[170,171] proposed a method for deterministic molecular dynamics. Furthermore, the former belong to the category of local thermostats, the latter is deterministic and global. Nose makes use of an extended-Lagrangian which extends the "normal" Lagrangian with additional and artificial coordinates as well as velocities. An extended-Lagrangian was developed by Andersen to make constant pressure MD simulations possible.[167] However, the original proposition by Nose required extensive optimization for each step along the way. A much more commonly used scheme is the Nose-Hoover thermostat. Here, Hoover[172,173] expanded on the ground work layed down by Nose. In simple words what this thermostat does is it scales the forces and velocities of the system by introducing artifical particles, thus, creating a new Hamiltonian for the system. Usually, the total energy defined by the Nose-Hoover Hamiltonian is conserved. However, if a system is simulated with the additional constraint that no external field is present ($\sum_i \boldsymbol{F}_i$=0) and more than one conservation law needs to be obayed, the Nose-Hoover thermostat transforms itself to a chain of Nose-Hoover heat baths, the Nose-Hoover chains, which each have their own Nose-Hoover frequency. This solves all the problems mentioned above. For a more detailed view on how to derive this thermostat or the other two mentioned as well as how barostats function, the reader is referred to ref. 159.

2.5.4 How to model in molecular simulations

In the following, a more detailed view on the inner workings of molecular simulations is given. It will be explained how simulations are run, how energies and forces are calculated and more.

Structure of molecular simulations

The structure Monte Carlo and molecular dynamics simulations are in principle very similar compared to one another despite the methods with which the results are generated, as discussed in Chapter 2.5.2 and 2.5.3, respectively. For the purpose of explaining the structure, only simulations will be described in which equilibrium properties are sampled. The system is a nanoporous rigid crystal, in which a fixed number of methane molecules are (going to be) present. It all starts with a initialization phase followed by a production phase. The former is basically used to 'guide' the simulation towards an equilibrated state while in the production phase the system is sampled and results are obtained, see Figure 2.9.

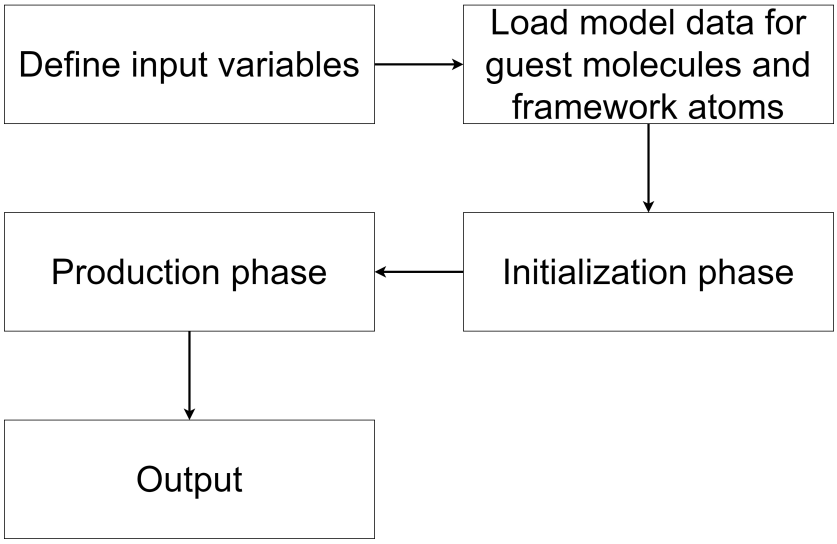

Figure 2.9: Sketch of the inner workings of molecular simulations.

Starting with the Monte Carlo simulation, the first thing in the initialization phase is to put the crystal framework atoms at the positions specified in the given frameworks file provided by the user. Subsequently, methane molecules need to be put into the simulation box. This is done by introducing them randomly into open space. To ensure this, moves similar to those in a normal GC ensemble are carried out: Molecules from an infinitely large reservoir are inserted into the simulation box if the resulting energy is lower than before the insertion. This is done until the desired number of molecules is reached. Now, all types of moves that are specified according to the user and the ensemble selected can be carried out randomly on random methane molecules. This phase is done until the specified number of initialization steps are reached. This limit can vary and depends on the system and implementation of the program. The user has to ensure that the system is in equilibrium. This is usually done by checking the (total) energy of the system, which should be at a minimum and should not fluctuate too much, see Figure 2.10, whereas small fluctuation are common and by design due to the Metropolis' algorithm properties.[160]

Once it has been established that the system is an equilibrated state, the production phase can commence. This is basically the main part of the simulation since only here the results are obtained. Commonly, all moves allowed in the initialization phase are allowed in this phase as well. Regularly at a defined step size, the properties one is interested in are sampled and the values stored. After the predefined number of steps the production phase

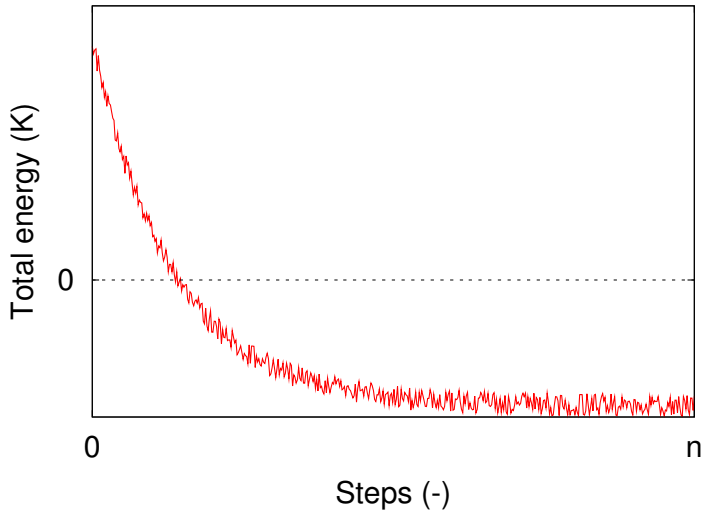

Figure 2.10: Total energy of a given system as a function of number of steps in Monte Carlo simulations.

finishes and the averages of said properties are calculated and written in the output. The user has to make sure that the production phase is long enough. One simple check is to determine whether the relative standard deviation of the observed is small enough.

In case of molecular dynamics simulations, the initialization phase starts with the assignment of velocities to each individual methane molecule according to a Maxwell-Boltzmann distribution at the predefined temperature T. This process is repeated until the defined temperature T is reached. Note that the instantaneous temperature may fluctuate greatly while at the same time the average temperature of the system does not fluctuate much. Subsequently, the production phase starts, in which Newton's equations of motion are solved as described in Chapter 2.5.3. It is not uncommon that molecular dynamics simulation packages, such as GROMACS[174] for example, do not have MC moves integrated (yet). Therefore by means of Monte Carlo simulations, an equilibrated state at the desired conditions has to be generated and then imported into the molecular dynamics suite. Since an integration step is equivalent to a time step, it is mandatory to run the MD simulations sufficiently long enough. In contrast to the MC simulation, part of the production phase must not be used for sampling, since the methane molecules are not in a truly equilibrated state. The simulation starts with the molecules having velocities and positions, which have no foundation at a time prior to t_0, in turn leading to a ballistic behavior at the beginning. An indicator is

the mean-squared displacement (MSD), which will be explained in Chapter 2.7.2. One generally samples in time intervals for which the slope of the MSD is equal to 1.

Periodic boundary conditions

Simulations are usually used to compute some sort of bulk phase properties, be it for fluids, solids or inside porous material. Let us image a simple cubic crystal of N atoms. It has been shown that the number of atoms on the surface is proportional to $N^{-\frac{1}{3}}$ and depending on N the percentage can be 50% for N=10^3 or 6% for N=10^6 and so on.[159] To compensate for that one makes use of so-called periodic boundary conditions. That means that the/an image of the simulation box is repeated ad infinitum in each direction. Consequently, all particles within the original simulation box interact with all of its surrounding atoms including the ones from the periodic images. One is basically trading away finite size effects for periodicity effects, yet the latter are not as problematic.

Energy calculation

Up to this point, it was discussed a lot about energy or force calculations without mentioning how it is actually done during the simulations, be it Monte Carlo or molecular dynamics simulations. The total energy consists of the intramolecular energy and intermolecular energy:

$$E_{total} = E_{inter} + E_{intra}. \tag{2.166}$$

The intermolecular energy can be further subdivided into two contributions: an electric one based on Coulomb interactions between two charges and van-der-Waals interactions. The Coulomb interaction energy is computed as follows:

$$E_{inter}^{Coulomb}(r_{ij}) = \sum_{elec} \frac{q_i q_j}{r_{ij}}, \tag{2.167}$$

with q_i and q_j being the charge on interaction center i and j and r being the distance between interaction center i and j. Van-der-Waals interactions are described by pairwise interaction between two different interaction centers as well. Note that molecules can have more than one center, for example propane is modelled to have three.[175] One distinguishes between attractive and repulsive parts of a force field. While the former part is usually modelled as a function of r_{ij}^6 the modelling of the repulsive part, which is due

to the overlap of electron clouds, is different between different potentials. Popular choices to compute van-der-Waals interaction energies include the Buckingham potential (Eq. 2.168), in which the repulsion part is modelled as an exponential function,[176] or a Lennard-Jones (LJ) potential in its original form, which is computationally a bit more efficient (Eq. 2.169). Other variants of the LJ potential include the 9-6[177] and the 14-7 LJ potential.[178] While the Buckingham potential is considered to represent the repulsive part more accurately, it has the drawback that the exponential function becomes attractive again for small r_{ij}:

$$E_{inter}^{vdW}(r_{ij}) = A \cdot exp(-B \cdot r) - \frac{C}{r_{ij}}, \tag{2.168}$$

with A, B, and C represent suitable constant parameters depending on the interaction centers. The basic Lennard-Jones function looks as follows:

$$E_{inter}^{vdW}(r_{ij}) = 4\epsilon \left[\left(\frac{\sigma}{r_{ij}} \right)^{12} - \left(\frac{\sigma}{r_{ij}} \right)^{6} \right], \tag{2.169}$$

with ϵ being the potential well depth and σ the finite distance at which the potential becomes zero. As established above, one wants to calculate the (pairwise) interaction energies in an infinitely large bulk system. While it seems not demanding to do so in close range, it gets out of hand quickly with increasing distance from one given particle. Therefore, different methods have been proposed to compute the interaction energy for the infinite crystal. The here mentioned methods usually revolve around the introduction of a cut-off radius r_{cut}, which should be sufficiently large to account for the most important interactions, e.g. the ones with the highest contributions, and the "rest". The most simplistic approach is to calculate the interactions normally if $r_{ij} \leq r_{cut}$ and set them to zero at $r_{ij} > r_{cut}$.

$$E_{inter,trunc}^{vdW}(r_{ij}) = \begin{cases} E_{inter,LJ}^{vdW}(r_{ij}), & r \leq r_{cut} \\ 0, & \text{otherwise} \end{cases} \tag{2.170}$$

This clearly introduces a huge systematic error since long interactions are neglected. To compensate for that, it is actually possible to calculate the tail correction. For that, let us start by looking at the average potential energy of a particle:

$$E_i^{average} = \frac{1}{2} \int_0^{\infty} 4\pi r^2 \rho(r) E(r) dr, \tag{2.171}$$

where ρ(r) is the average number density at distance r from the particle. The factor $\frac{1}{2}$ is introduced in order to avoid double counting of interactions (Newton's third law of motion). Next, only the part of the integral with r≥r_{cut} remains and it is equal to the tail contribution we are missing due to setting the potential to 0 at r_{cut}. Furthermore, we postulate that at this length r the density ρ(r) is equal to an average density ρ. Thus in case of the LJ potential (Eq. 2.169):

$$\begin{aligned} E_i^{average} =& \frac{1}{2} \cdot 4\pi\rho \int_0^\infty r^2 E(r) dr \\ =& \frac{1}{2} \cdot 4\pi\rho \cdot 4\epsilon \int_0^\infty r^2 \left[\left(\frac{\sigma}{r_{ij}} \right)^{12} - \left(\frac{\sigma}{r_{ij}} \right)^{6} \right] dr \\ =& \frac{1}{2} \pi\rho\epsilon\sigma^3 \left[\frac{1}{3} \left(\frac{\sigma}{r_{cut}} \right)^{9} - \left(\frac{\sigma}{r_{cut}} \right)^{3} \right] \end{aligned} \tag{2.172}$$

A second approach is to still truncate the potential but also to shift it such that the potential equals zero at r_{cut}:

$$E_{inter,trunc-shift}^{vdW}(r_{ij}) = \begin{cases} E_{inter,LJ}^{vdW}(r_{ij}) - E_{inter,LJ}^{vdW}(r_{cut}), & r \leq r_{cut} \\ 0, & \text{otherwise} \end{cases} \tag{2.173}$$

The advantage here is that there are no discontinuities in the potential and the derivative, which is especially important for molecular dynamics simulations. Clearly, results based on this approach differ from the unaltered potential but it can be accounted for by the tail correction in Eq. 2.172. A third variant is called the minimum image convention in which r_{cut} is not spherical. As the name suggests, only the interaction with the nearest image of a given particle is calculated. This approach however must not be used in molecular dynamics.

Based on the given energies, the forces present between interaction centers i and j are obtained as the derivative of the interaction energy with respect to the distance r_{ij}:

$$F_{ij}(r_{ij}) = -\frac{dU_{ij}(r_{ij})}{dr_{ij}}. \tag{2.174}$$

The resulting force acting on one particular interaction center is given as the sum of all forces in every direction:

$$F_i = \frac{1}{2} \sum F_{ij}(r_{ij}). \tag{2.175}$$

Now that it is established how to calculate intermolecular van der Waals energies and forces, the following part will be focused on the intramolecular ones, which are calculated as follows:

$$E_{intra}^{vdW} = E_{bond}^{vdW} + E_{angle}^{vdW} + E_{torsion}^{vdW}, \tag{2.176}$$

whereas E_{bond}^{vdW} represents the bonding energy, E_{angle}^{vdW} the bending energy, and $E_{torsion}^{vdW}$ the torsion energy. Please note that in most situations interactions between two atoms present in a singular molecule more than three bonds away, e.g. atom 1 to atom 4, are treated as if they are intermolecular, and neglected otherwise, since the interactions are already described by the intramolecular interactions. Moreover for simplicity sake, since there exist many different functions describing the interaction for each interaction type, only the commonly used or most simplistic form is shown here. The bonding energy E_{bond}^{vdW} takes the elongation and contraction between i and j into account:

$$E_{bond}^{vdW}(r_{ij}) = \frac{1}{2} k_B (r_{ij} - r_{ij}^0)^2, \tag{2.177}$$

with r_{ij}^0 being the equilibrium distance and k_B the spring constant of the harmonic spring. In similar fashion the bending potential E_{bend}^{vdW} is modelled by a harmonic potential:

$$E_{bend}^{vdW}(\theta_{ij}) = \frac{1}{2} k_A (\theta_{ij} - \theta_{ij}^0)^2, \tag{2.178}$$

with θ_{ij}^0 being the equilibrium angle and k_A the spring constant of the harmonic spring. Clearly, this potential becomes relevant for molecules including three or more atoms. Adding a forth one unlocks the possibility of torsion angle interaction energy $E_{torsion}^{vdW}$ to the molecule. In the following, the expression used by the OPLS potential for the proper torsion is shown:[179]

$$E_{torsion,proper}^{vdW}(\phi) = k_0 + \frac{k_1}{2}(1+\cos\phi) + \frac{k_2}{2}(1+\cos 2\phi) + \frac{k_3}{2}(1+\cos 3\phi), \tag{2.179}$$

with k_0, k_1, k_2, and k_3 being suitable parameters. Furthermore, the influence of improper torsion to ensure planar geometries needs to be quantified as well:

$$E^{vdW}_{torsion,improper}(\omega) = \frac{k_{imp}}{2}[1 + \cos(2\omega - \pi)], \tag{2.180}$$

where ω is the improper angle corresponding to the deviation from the planar plane. Everything combined ultimately leads to the complete description of the total energy of the system or the uniquely total acting force on each interaction center, respectively.

At this point, everything van der Waals related has been covered and one can move on to the Coulomb interactions. At first glance, one assumes that they can be handeled similarily: At r_{cut} the potential is truncated and the tail correction part is determined with the following equation, see Eq. 2.171 for comparison:

$$E^{Coulomb}_{tail} = \frac{n\rho}{2} \int_{r_{cut}}^{\infty} dr E(r) 4\pi r^2. \tag{2.181}$$

There is a problem though: The result for $E^{Coulomb}_{tail}$ diverges unless the energy function $E(r) \propto r^{3;4;...;\infty}$. In case of the Coulomb potential, $E^{Coulomb} \propto \frac{1}{r}$. Thus, it is not possible to use this approach, once electrostatics and dipole interactions need to be taken into account. Simply neglecting long range interactions at $r \geq r_{cut}$ leads to large inaccuracies and is therefore not possible. In the following it is briefly described how one can deal with these types of interactions using the example of the Ewald summation,[180] which is frequently used. Other techniques are particle-mesh based or fast dipol methods. For those methods as well as the full derivation of the Ewald summation, the reader is referred to ref. 159. Here, only the working principle is described. Let us start by creating a electrostatic neutral cube with the length L, in which N charged particles are present. Periodic boundary conditions apply here too. The goal is to calculate the electrostatic energy of the system which is:

$$E^{Coulomb} = \frac{1}{2} \sum_{i=1}^{N} q_i \Phi(r_i) \text{ with } \Phi(r_i) = \sum_{j,\boldsymbol{n}}{}' \frac{q_j}{|\boldsymbol{r}_{ij} + \boldsymbol{n}L|}, \tag{2.182}$$

where the prime denotes that the sum is over $\boldsymbol{n}$ periodic images over all particles j except for if $\boldsymbol{n}$=0 and i=j. As mentioned before this expression does not converge. To circumvent this problem Ewald proposed the following: Each individual point charge q_i is shielded by a diffuse charge distribution in a form of a rapidly decaying Gaussian distribution with the opposite sign, e.g. $-q_i$, thus exactly canceling out the point charge. Since now an artifical

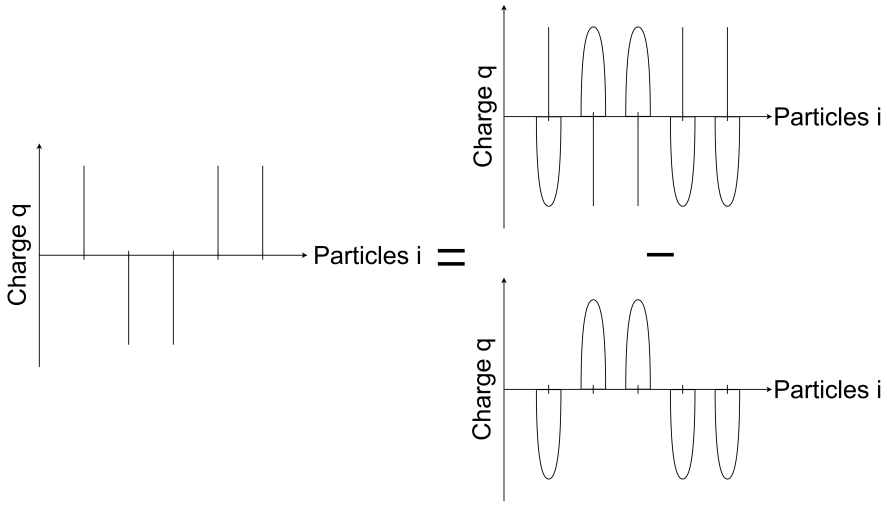

Figure 2.11: The point charges of a system can be constructed as a set of screened charges minus the negative screened charges.

charge density is introduced, it needs to be canceled out. Hence, a second diffuse charge distribution is created (not introduced to the system) with cancels out the first one. Its charge is then accordingly q_i. A schematic representation of that idea is presented in Figure 2.11. This leads basically to the following equation:

$$q_i^{\text{point charge}} = q_i^{\text{point charge + shield distribution}} - q_i^{\text{shield distribution}}. \tag{2.183}$$

Eventually, this methodology allows to represent the diffuse charge distribution by Fourier series since it is a smoothly varying and periodic function with a width of $\sqrt{\frac{2}{\alpha}}$:

$$\rho_{Gauss}(r) = -q_i \cdot \left(\frac{\alpha}{\pi}\right)^{\frac{3}{2}} exp(-\alpha r^2), \tag{2.184}$$

where α is a parameter whose value will be chosen based on computational considerations. In essence, at the defined cut-off radius, r_{cut}, is divided into a part $r \geq r_{cut}$ and $r < r_{cut}$. The former will be evaluated in the real space while the second part, which does not converge in real space, is evaluated in reciprogal space because it converges there. It is important to note that by this technique, the Ewald summation, the contribution to the electrostatic energy of all periodic images as well as the simulation box itself is taken into account.

Partial atomic charges themselves are generated separately from DFT calculations. First, the electrostatic field of the framework is calculated under vacuum conditions. This is commonly stored on a grid mapping said framework. The next step is to employ a scheme or method to fit point charges to each atom, atomtype or element so that the electrostatic potential obtained at the DFT level is reproduced. To this end, we use the REPEAT algorithm as described in ref. 181, which has proven itself to be accessible, fast, and accurate.

Ultimately, the total energy of the system E_{total} is a sum of various terms, which all need to be taken into account:

$$E_{total} = E_{inter} + E_{intra} = \left(E_{inter}^{Coulomb} + E_{inter}^{vdW}\right) + \left(E_{bond}^{vdW} + E_{angle}^{vdW} + E_{torsion,proper}^{vdW} + E_{torsion,improper}^{vdW}\right) \tag{2.185}$$

2.6 Adsorption process simulation

it is important to simulate the adsorption process not only on the molecular scale but also on the industrial scale because, ultimately, that is the part the industry is most interested in. Clearly, understanding the phenomena present at the molecular level, e.g. the adsorption and diffusion properties, are vital in the development of suitable adsorption materials, it is also of major importance to design the process as efficient and optimal as possible. Since one is bound to a limited amount of experiments beyond the laboratory scale due to the time and resources needed, simulations have become a common tool to help with the design. The foundation for the simulation is a set of partial differential equations which are based on adsorption, desorption, mass transport, and flow mechanics as well as starting and boundary conditions.

2.6.1 Assumptions and the ansatz of the model

In order to simulate such complicated real life systems effectively, it is useful to reduce the degree of complexity while maintaining accuracy of the simulation results. In this work, the following assumptions have been made to satisfy the aforementioned constraints. Clearly, these influence the outcome of the simulations depending on the impact of each individual assumption which are:

- A pseudo-homogeneous, one dimensional model is used.

- The adsorber is considered to work isothermally, meaning no energy balance is considered and heating of the bed due to adsorption enthalpy is neglected.
- Radial gradients for concentrations, velocities, and loadings of the adsorber bed are neglected.
- The fixed-bed is considered to be a homogeneous (solid) phase.
- The radial pressure drop is zero and the pressure along the column can be described using the Ergun equation.
- The gas phase is considered to behave ideally.
- Pore diffusion and axial dispersion are assumed to be constant.
- The mass transport resistance can be described by either an equilibrium model (the equilibrium loading for the given conditions are reached instantaneously, no transport resistance)[89] or by a linear driving force approach formulated by Glueckauf.[182]

Next, we will briefly discuss the restrictions above to put them into perspective with respect to their impact on the simulation results with the exception of the dimension of the model itself. Obviously, one could model the fixed-bed in full detail with the real packing structure or a randomly generated one in full 3D with CFD approaches, it is, however, often very time consuming to do so while the general information received is not increased accordingly. Yet, in case of detail engineering or problems, which can be a function of their position in a 2D or 3D environment, CFD simulations with full details are very helpful in this regard. Assuming that the adsorber is modelled isothermally, some partial differential equations can be neglected. However, it comes at a great cost. Adsorption processes are very exothermal, see Chapter 2.1. Moreover, the increased temperature has a negative effect on the saturation capacity of the adsorbent. In real systems depending on the adsorption enthalpy temperatures differences of 30 K and higher have been observed experimentally.[183] Ignoring radial gradients for concentrations, velocities, and so on is usually valid in case the flow is distributed (more or less) equally throughout the apparatus, whose diameter needs to be sufficiently large compared to the particle diameter. As a rule of thumb the ratio should be at least 10 in favor of the reactor or column diameter.[89] In simulations this is easily controlled by the input parameters defined by the user. As for the ideal gas assumption, this one is usually valid as long as the working condition of the adsorber is not in the proximity of the critical points of the gases present.

As already mentioned, two phases are present in the adsorber: a solid and a fluid one. Each of these phases has their own mathematical framework

which will be presented in the following sections 2.6.2 for the solid phase and 2.6.3 for the fluid phase. An in-depth description of the derivation presented here can be found in the books by Ruthven et al.[184] and Bathen et al.,[89] respectively.

2.6.2 Mass balance of the solid phase

The mass balance for the solid phase can be derived from imagining a spherical particle surrounded by bulk gas. The mass flow into the particle $\mathrm{d}\dot{m}_{Ads}$ is equal to the instationary storage term:

$$\frac{\partial m_{store}}{\partial t} = \frac{\partial m_P}{\partial t} = d\dot{m}_{Ads} \tag{2.186}$$

The adsorption mass flow can be described using a linear driving force approach as formulated by Brenner in the following way:[185]

$$d\dot{m}_{Ads} = k_{Ads} \cdot (1-\epsilon) \cdot A \cdot A_P \cdot M \cdot (\theta_{equil} - \theta) \cdot dz, \tag{2.187}$$

whereas k_{Ads} is adsorption rate coefficient, ϵ $(= \frac{V_{void}}{V_{total}})$ is the porosity of the bed, A is the surface area, M the molar mass, A_P is the volumetric surface area of the particle, θ_{equil} is the saturation loading at the given conditions, and θ the actual loading of the particle. As for the left hand side of Eq. 2.186, since the mass of the particle itself does not change just its loading, one can derive this relationship:

$$\frac{\partial m_{store}}{\partial t} = m_{solid} \cdot M \cdot \frac{\partial \theta}{\partial t} = \rho_{solid} \cdot (1-\epsilon) \cdot A \cdot M \cdot \frac{\partial \theta}{\partial t} \cdot dz, \tag{2.188}$$

with ρ_{solid} being the density of the solid and $\frac{\partial \theta}{\partial t}$ the change of loading of the particle with time.

Combining Eq. 2.186, 2.187, and 2.188 leads to the complete partial differential equation for the solid phase:

$$\frac{\partial \theta}{\partial t} = \overbrace{\frac{k_{Ads} \cdot A_P}{\rho_{solid}}}^{k_G} (\theta_{equil} - \theta) = k_G(\theta_{equil} - \theta). \tag{2.189}$$

Here, k_G is the so-called Glueckauf coefficient. Glueckauf used an empirical correlation involving the particle diameter r_P and the effective diffusion coefficient D_{eff} to calculate k_G:

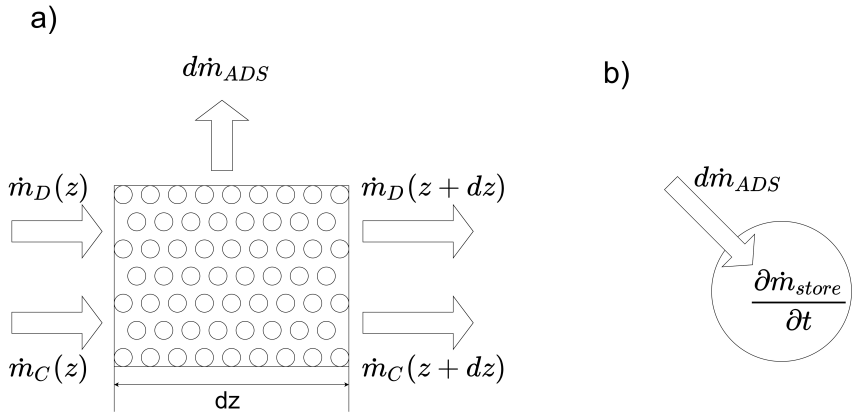

Figure 2.12: Derivation for the two mass balances in a fixed-bed adsorber: (a) the fluid phase and (b) the solid phase.

$$k_G = \frac{15 D_{eff}}{r_P^2}. \tag{2.190}$$

This linear driving force ansatz is widely used in simulations. However, it is used without actually validating the accuracy of the approach itself.[183] It has the benefit that the Glueckauf coefficient can be retroactively fitted to match the experimental results. Instead of the above mentioned Glueckauf method, one can simply use the idea that there is no transport resistance present in the system which means

$$\frac{\partial \theta}{\partial t} = \frac{\partial \theta_{equil}}{\partial t}. \tag{2.191}$$

These two methods have been implemented into the program developed during this thesis. Obviously, there exist many more ways to model the solid phase more accurately at the cost of more computational time and more complex equations, see ref. 183 for more information.

2.6.3 Mass balance of the fluid phase

In a similar way to the solid phase the derivation of the mass balance for the fluid phase is done for a small volume of the column dV(= A·dz). In the fluid phase one distinguishes between two mass flows: the convective mass flow $\dot{m}_C$ and a dispersive one $\dot{m}_D$. Flowing into the observed volume element therefore are $\dot{m}_C$(z) and $\dot{m}_D$(z) while leaving dV are $\dot{m}_C$(z+dz) and $\dot{m}_D$(z+dz). The additional mass flow present is the flow into the solid phase $d\dot{m}_{Ads}$. Thus, one has

$$\frac{\partial m_{store}}{\partial t} = \overbrace{\dot{m}_C(z) + \dot{m}_D(z)}^{Incoming} - \overbrace{\dot{m}_C(z+dz) - \dot{m}_D(z+dz)}^{Outgoing} - d\dot{m}_{Ads}. \quad (2.192)$$

Problematic are the outgoing flows and how to describe them mathematically. Using a Taylor series one can write those terms as follows:

$$\begin{aligned} \dot{m}_i(z+dz) &= \dot{m}_i(z) + \frac{\partial \dot{m}_i}{\partial z}dz + \frac{1}{2!}\frac{\partial^2 \dot{m}_i}{\partial z^2}dz + \frac{1}{3!}\frac{\partial^3 \dot{m}_i}{\partial z^3}dz + \mathscr{O}(z) \\ &\approx \dot{m}_i(z) + \frac{\partial \dot{m}_i}{\partial z}dz \end{aligned} \quad (2.193)$$

With this approximation Eq. 2.192 becomes

$$\begin{aligned} \frac{\partial m_{store}}{\partial t} &= \dot{m}_C(z) + \dot{m}_D(z) - \dot{m}_C(z) - \frac{\partial \dot{m}_C}{\partial z}dz - \dot{m}_D(z) - \frac{\partial \dot{m}_D}{\partial z}dz - d\dot{m}_{Ads} \\ &= -\frac{\partial \dot{m}_C}{\partial z}dz - \frac{\partial \dot{m}_D}{\partial z}dz - d\dot{m}_{Ads}. \end{aligned} \quad (2.194)$$

Now knowing the general mass balance one needs to derive relationships for $\dot{m}_C(z)$ and $\dot{m}_D(z)$. Starting with the convective mass flow, it depends on the the concentration c, the superficial velocity u, and superficial volume flow $\dot{V}$, all of which are dependent on z:

$$\frac{\partial \dot{m}_C}{\partial z} = M\frac{\partial}{\partial z}\left(c \cdot \dot{V}\right) = M\frac{\partial}{\partial z}\left(c \cdot A \cdot u\right) = M \cdot A\left(u\frac{\partial c}{\partial z} + c\frac{\partial u}{\partial z}\right) \quad (2.195)$$

The dispersive mass flow can be described by a relationship similar to Fick's law:

$$\frac{\partial \dot{m}_D}{\partial z} = -D_{ax} \cdot M \cdot A \cdot \epsilon \cdot \frac{\partial^2 c}{\partial z^2}, \quad (2.196)$$

with D_{ax} being the axial dispersion coefficient which can be calculated as explained in Chapter 2.2.3.

The instationary storage term m_{store} is:

$$\frac{\partial m_{store}}{\partial t} = \epsilon \cdot A \cdot M \cdot dz \cdot \frac{\partial c}{\partial t}. \quad (2.197)$$

The mass flow $\mathrm{d}\dot{m}_{Ads}$ has been already defined in Eq. 2.187. Merging Eq. 2.187, 2.194,2.195, 2.196, and 2.197 one gets the fluid phase mass balance:

$$\frac{\partial c}{\partial t} = D_{ax}\frac{\partial^2 c}{\partial z^2} - \frac{c}{\epsilon}\frac{\partial u}{\partial z} - \frac{u}{\epsilon}\frac{\partial c}{\partial z} - \frac{k_G \cdot (1-\epsilon)}{\epsilon}(\theta_{equil} - \theta). \tag{2.198}$$

In reality, usually a second (inert) gas is present, such as helium or others. Thus, the total present concentration becomes in the simplest case:

$$c_{total}(t,z) = \sum_i c_i(t,z) = c_A(t,z) + c_{helium}(t,z). \tag{2.199}$$

If the gas flows frictionless through the column, c_{total}(t,z) is not a function of z anymore: c_{total}(t,z)=c_{total}(t). To account for the pressure drop caused by friction the Ergun equation is used:[186]

$$-\frac{\partial p}{\partial z} = 150\left(\frac{(1-\epsilon)^2}{\epsilon^3}\right)\frac{\mu}{(2r_p)^2}\cdot u + 1.75\left(\frac{1-\epsilon}{\epsilon^3}\right)\frac{\rho_{fluid}}{2r_p}\cdot u^2, \tag{2.200}$$

where p is the total pressure, μ the viscosity of the bulk gas, ϵ the bed porosity, ρ_{fluid} is the fluid density, and r_p is the radius of the particle. It is common practice to assume that the gas phase properties are constant. Using an equation of state, such as the ideal gas law, one can link the pressure to the concentration in the following way:

$$p = cRT. \tag{2.201}$$

In order to solve the system of partial differential equations, the Danckwert's boundary conditions are applied. For the inlet at z=0:

$$\nu \cdot (c_i - c_i^{inlet}) = D_{ax,i}\frac{\partial c_i}{\partial z},\ i = 1,2,...,N \text{ and } \nu = \nu^{inlet}. \tag{2.202}$$

The corresponding outlet Danckwert's boundary conditions are:

$$\frac{\partial c_i}{\partial z} = 0, i = 1,2,...,N \text{ and } \frac{\partial u}{\partial z} = 0. \tag{2.203}$$

2.7 General simulation details

In this chapter, the general simulation details for Monte Carlo and molecular dynamics simulations are presented.

2.7.1 Monte Carlo

All MC simulations were performed using the COTA software package. In order to shorten the duration of further simulations, grid calculations were carried out, which divided the unit cell into cubes with a side length of 0.1$\mathring{A}$. The energies at the grid nodes were calculated based on the LJ parameters of the frameworks. The LJ potential was cut off and shifted to zero at 15$\mathring{A}$. The side lengths of the simulation box in all three dimensions should be at least twice as big as the cutoff radius. Thus, the number of unit cells used in the simulation box varies from structure to structure depending on the dimensions of the unit cells. Periodic boundary conditions in all dimensions were applied. In MC simulations using the NVT ensemble, the probabilities of the MC steps, translation, rotation, and regrow were 20 %, 10 %, and 70 %, respectively. Using the grand canonical ensemble, the probability distribution of the MC steps swap, translation, rotation, and regrow were 50 %, 12.5 %, 12.5 %, and 25 % for single component simulations, respectively. Helium void fractions and Henry coefficients at zero loading were calculated in a canonical ensemble. The simulation was based on the Widom particle insertion method,[166] which utilizes a trial particle to calculate thermodynamic properties. The MC simulations probes the simulation box containing the framework atoms with a helium atom.[175] Since the noble gas helium is adsorbed very weakly because of his nature being a noble gas, it only "adsorbs" in free pore volume or volume not occupied by any framework atom, respectively. Thus, the helium void fraction is a number between 0 and 1 and multiplied with the volume of the unit cell yields the freely accessible pore volume. Another important parameter the isosteric heat of adsorption, Q_{st}, can be calculated from these simulations at zero loading utilizing the average total energy of only one molecule in the simulation box and ideal gas phase simulations according to the following equation:[187]

$$h_{ads} = Q_{st} = \langle U_{hg} \rangle - \langle U_{ig} \rangle - RT, \tag{2.204}$$

where $\langle U_{hg} \rangle$ is the average total energy of the host-guest interactions, $\langle U_{ig} \rangle$ the average energy of the adsorptive in the ideal gas state and R and T are the ideal gas constant and the temperature, respectively. Moreover, isosteric heats of adsorption at different loadings (due to different operating pressures) can be calculated from single component GCMC simulations according to following equation:[78]

$$h_{ads} = Q_{st} = RT - \frac{\langle U \cdot n \rangle - \langle U \rangle \langle n \rangle}{\langle n^2 \rangle - \langle n \rangle^2}, \tag{2.205}$$

with $\langle U \rangle$ and $\langle n \rangle$ being the ensemble averages for the total energy and the number of molecules in the system, respectively.

To compare the isotherms from simulations to isotherms from experiments the absolute loading obtained in simulations has to be converted into the excess loading determined in experiments. The excess amount adsorbed is given by:[188]

$$n_{excess} = n_{abs} - \frac{pV_{pore}}{ZRT}, \tag{2.206}$$

where n_{excess} is the excess amount adsorbed, n_{abs} is the absolute amount adsorbed, p is the pressure, V_{pore} is the pore volume and Z is the compressibility factor. This conversion is necessary because in experiments only n_{excess} is measured. What that means is depending on the pressure or conditions of the bulk phase in general, a certain fraction of the molecules present in the simulation box are not adsorbed, and thus, "belong" to a gas phase inside the crystal. The pore volume V_{pore} is calculated by obtaining the helium void fraction as discussed above.

2.7.2 Molecular dynamics

For MD simulations to function, one requires some sort of starting configuration. Since we are interested in (self-)diffusion at equilibrium conditions, we need to start our MD simulation at this particular state. MC simulations allow to generate the system one is interested in in an equilibrated state. Thus, prior to the MD simulations, the system was equlibrated using MC simulations for over 10^5 steps depending on the system. Afterwards, the output was converted to a proper format and used as an input for the MD simulations. All MD simulations were carried out using the GROMACS package version 5.1.1.[174] Here, Newton's equations of motion were integrated via velocity Verlet algorithm with a time step of 1 fs (=10^{-15}s). Periodic boundary conditions were applied in all directions. Temperature control was realized by using Nose-Hoover chain (NHC) thermostat as implemented in GROMACS 5.1.1.[174] The long-range electrostatic interactions were calculated using the Particle-Mesh-Ewald method.[189,190] Unless interaction parameters between guest molecules and framework atoms were specified in the force field, they are determined using the Lorentz-Berthelot mixing rules. As a trade-off between the computational time and reliable statistics, the simulations ran at least 50 ns. Loading dependencies of the diffusivities were studied from one molecule per unit cell up to saturation at 300 K. In order to achieve good statistics, at least 60 molecules were put in the simulation box. According to

the total number of molecules and the desired loading, the size of the simulation box had to be varied. After equilibration, the production phase started during which the trajectories of the system were saved and the mean-squared displacement (MSD) were recorded using the Order-N algorithm.[159] In this work, the Einstein equation was followed, i.e. the diffusivities were obtained from the slope of the MSD with time.

One class of observable properties are dedicated to measure the local structure of a fluid, be it in the gas phase or inside a crystal. Most commonly used is the pair distribution function, g(r), see Figure 2.13, which is of interest because g(r) plays an important role in theories concerning liquid states. Furthermore, when Fourier transformed one obtains the structure factor, which can be measured by experiments. The pair distribution function itself is the ratio between the average number density ρ(r) at a distance r from a given atom and the number density ρ_{ig}(r) at a distance r for a given atom in an ideal gas environment with similar overall density. By definition, g(r)=1 resembles an ideal gas and any deviation from this can be attributed to intermolecular interactions.[159] In other words, it is a function which determines the probability of finding a particle at distance r away from the reference particle with is centered at r=0. The pair distribution function is measured periodically during molecular simulations. The distance between reference particle A and particle B is calculated and discretized. The results are then translated into a histogram and repeated for all particles and normalized using ρ_{ig}(r).

One of the important dynamic properties that can be obtained by MD simulations is the diffusion coefficient, which has been introduced in Chapter 2.2.1. For the sake of simplicity the given system consists of only one species, whereas half of the molecules will be considered "tagged" and the other half non-tagged. There are two possible ways to obtain the (self-)diffusion coefficient for this species. In a MD simulation the self-diffusivity of a component T ("tagged") can be obtained via the mean-squared displacement (MSD) at long times or the velocity autocorrelation function. The former is used more frequently in order to compute D_T^S . Therefore, the Einstein equation is used:

$$D_T^S = \frac{1}{2d} \lim_{t\to\infty} \frac{1}{N_T} \frac{d}{dt} \left\langle \sum_{i=1}^{N_T} \left(r_i^T(t) - r_i^T(t=0) \right)^2 \right\rangle , \tag{2.207}$$

where d is the dimension of the system (1, 2 or 3), t is the time, N_T is the total number of molecules of component T, $r_i^T(t)$ is the position of molecule i of component T at time t, and $r_i^T(t=0)$ is the position of molecule i of component T at time $t = 0$.

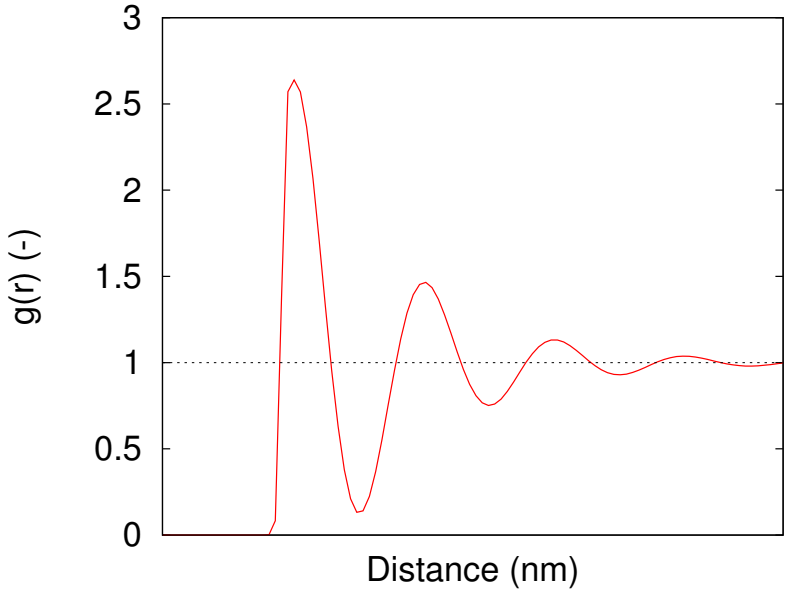

Figure 2.13: Pair distribution function g(r) for a Lennard-Jones fluid.

As for the velocity correlation function the Green-Kubo relation is applied:

$$D_T^S = \frac{1}{dN_T} \int_0^\infty \left\langle \sum_{i=1}^{N_T} v_i^T(t) v_i^T(t=0) \right\rangle dt, \tag{2.208}$$

where v_i^A is the velocity of particle i of component A. Both methods yield the same results[191] and since both are time averages it is important to stress that the longer the simulation is the better the statistics are. Moreover, especially in nanoporous media, the movement of the particles are restricted by the confinement. To cover the interactions of a particle with the confinement as well as with other particles in the system one needs to run a sufficient long simulation until both interactions take place as seen in the $\lim_{t\to\infty}$ and the integral $\int_0^\infty$.

The corrected diffusivity D_A^C describes the collective diffusion behavior of all particles of component A and can be interpreted as the the movement of the center of mass of one species. It can also be computed from Einstein equation:

$$D_A^C = \frac{1}{dN} \lim_{t\to\infty} \frac{1}{N_T} \frac{d}{dt} \left\langle \sum_{i=1}^{N_T} \left(r_i^T(t) - r_i^T(t=0) \right)^2 \right\rangle, \tag{2.209}$$

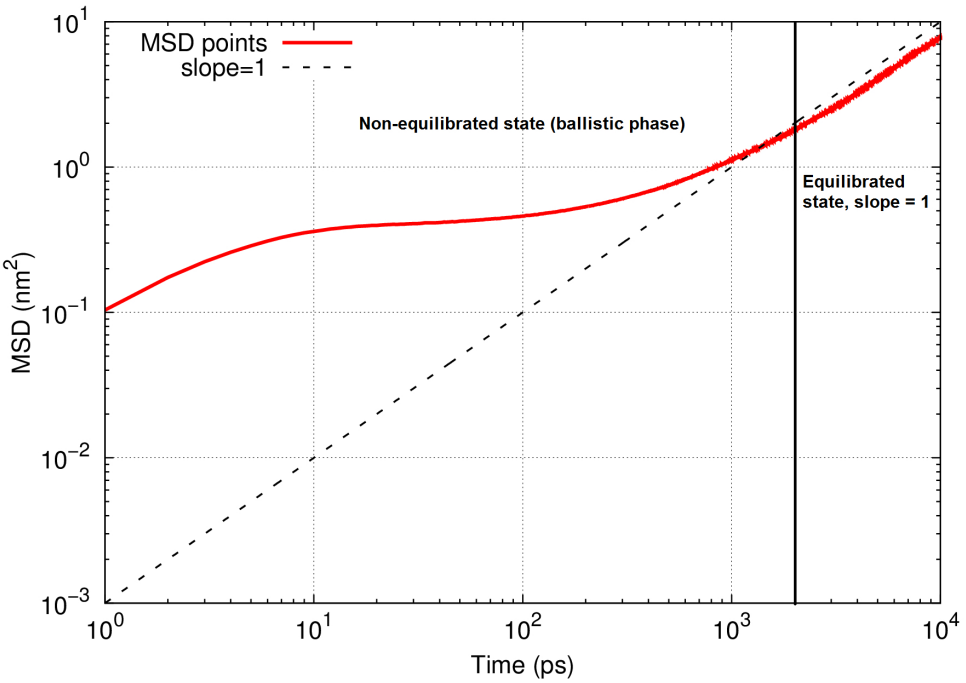

Figure 2.14: Mean-squared displacement as a function of (simulation) time.

The connection between an one-dimensional diffusion coefficient and a three-dimensional is as follows:

$$D_T^S = \frac{D_{T,x}^S + D_{T,y}^S + D_{T,z}^S}{3}. \tag{2.210}$$

An important issue when using MSD for calculating diffusivity (Eq. 2.207 and Eq. 2.209) is that the simulation time should be long enough so that the extrapolation to "infinite time", i.e. $\lim_{t\to\infty}$, is reliable. The diffusion regime is attained, when particles are free to go through the full periodic lattice and able to collide with other particles from other sites. In this regime, both self- and collective motions become linear with time from which the (long time) diffusivity for the components of interest can be obtained.[192]

2.7.3 Adsorber program

The pressure swing adsorption program was based on the work by Andreas Heyden et al.[193] in 2001. The code is written in FORTRAN 90, has been sorted and divided into several modules. The workflow of the code is given in Figure 2.15.

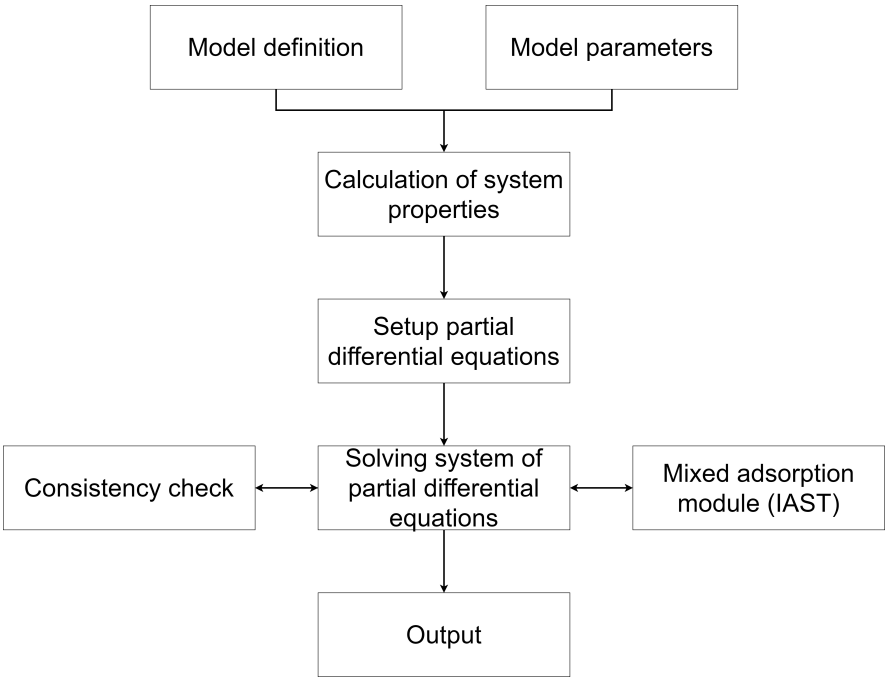

Figure 2.15: Workflow of the adsorber program.

In the first part of the program several global parameter are initialized and the model itself is set up. Options, such as with or without pressure drop (Ergun equation, Eq. 2.200), which mass transport model for the solid phase is applied (Eq. 2.189 or Eq. 2.191), whether dispersion is present or no,t are declared. Pressure, temperature, and other parameters defining the starting and boundary conditions are set. To solve the set of partial differential equations, one needs to calculate the axial dispersion coefficient, equilibrium or saturation loading at the given conditions and effective diffusion coefficients: The former property, D_{ax}, can be calculated using Eq.2.69 for which the Reynolds and Schmidt numbers are computed. For those the (dynamic) viscosity is estimated using the approximation by Lucas et al.,[194] and diffusion coefficients in gas mixtures from correlations developed by Fuller er al.[195] The pressure dependency of diffusion coefficients in gas phase mixtures is modelled according to Dawson et al.[196] The equations for calculating properties like viscosity and dispersion coefficients were updated from the diploma thesis using the "VDI-Wärmeatlas".[194]

The core of the program solves the set of partial differential equations (PDEs) described previously in Chapter 2.6. This is done using the finite element method (FEM). To describe the method in simple words, one discretizes the adsorber in N parts with the same length. As a result, the system

of PDEs morphs into a system of ordinary differential equations (ODEs), which are solved more easily, using 4^{th} order Runge-Kutta.[197] In this work however, we used the NAG library for the FORTRAN language. While in principle the time and length step size could be varied depending on the gradient of the system, we found out that this option destabilized the program significantly. During solving the set of ODEs it is necessary to calculate equilibrium and saturation uptakes for each component present in the system. Usually, competitive adsorption isotherms are used for that task as no further calculations are involved. In this work however, we integrated as IAST module to compute the required mixture adsorption isotherms on the fly. While it does increase the computation time, it also makes the code more flexible for other problems and only the pure component isotherms are needed as input.

Part II

CO_2 sequestration from flue gas

3

Multiscale modelling of carbon dioxide and water in Mg-MOF-74: from electronic structure calculations to adsorption isotherms

Classical force fields are not able to describe the adsorption in MOFs containing open metal sites correctly, because the interactions between the framework atoms, Mg in particular, and gas molecules are not sampled accurately. In this chapter, a force field is proposed to overcome these limitations. Its accuracy is assessed by performing a series of molecular simulations. Here, the adsorption of water and carbon dioxide in Mg-MOF-74 is modelled. The model is defined in terms of electrostatic, repulsive, and attractive contributions, the parameters of which are independently derived from first-principles calculations. The force field accurately reproduces the most relevant part of the ab initio potential energy surface as well as pair-correlation functions obtained from molecular dynamics simulations. The model is further applied for calculating adsorption properties and isotherms within MC and MD simulations. The obtained force field shows an improved description of the experimental adsorption isotherms compared to the standard water and carbon dioxide models, which allows us to expect its good performance for other large-scale simulations of water in Mg-MOF-74. Moreover, with the same concept the adsorption of CO_2 is modelled successfully.

3.1 Introduction

The modular nature of metal-organic frameworks (MOF) leads to extraordinary structural diversity accompanied by a large variety of physical and chemical properties.[198] To date, advanced synthesis techniques offer a high degree of tunability of MOF structures,[59] which makes these materials very promising for various technological applications.[58] In particular, much progress has been made in designing materials, which combine high surface areas and affinities toward the adsorption of specific molecules, leading to intriguing applications in gas separation and storage.[58,108,199–201]

Because of the sheer number of possible crystal structures, screening processes based on adsorption capacity and selectivity,[41,127,202–205] or parasitic energy[206] are necessary to identify the best ones. Among the variety of different hybrid structures, one of the best candidates for practical use is Mg-MOF-74, which has been shown to be extremely efficient in capturing carbon dioxide (CO_2),[35] one component of flue gases, because of its high capacity and selectivity towards CO_2, which is attributed to its so-called "open metal sites" (OMS) or coordinately unsaturated metal sites (CUS).[35,40,126–128,207–211] Subsequently, a number of theoretical studies has been devoted to this system focused on the detailed description of adsorption and transport properties of CO_2 in Mg-MOF-74.[122–130] In the beginning most of the studies regarding Mg-MOF-74 have been focused on the separation of CO_2 from binary mixtures with methane (natural gas) or nitrogen (flue gas). However, in reality flue gas consists of N_2 (70-75%), CO_2 (15-16%), H_2O (5-7%), and O_2 (3-4%), whereas impurities, such as SO_2, NO_x, and CO, are in the ppm-range.[7,212–214] As a result, the adsorption of each species in Mg-MOF-74 has been investigated.[215–217] It was found that CO_2 is more favorably adsorbed than the likes of NO_x,[215,216] SO_2,[215,216] CO,[40,122] and O_2,[215,216] because the former adsorbs quite strongly to the OMS.[40,122,126,127,218] This environment induces problems, when it comes to molecular modelling of interactions between any OMS containing frameworks and guest molecules, such as CO_2, SO_2, water, and propene, which have the potential to be influenced by that field. Despite the consistent understanding of CO_2 adsorption in Mg-MOF-74 at different scales, the role of the other flue gas components in this process is much less understood. In this regard, particular attention should be drawn to water, which is reported to bind considerably stronger to Mg-MOF-74 compared to CO_2. Thus, it presents more of a problem when one is considering Mg-MOF-74 for real life applications.[35,40,126–128,130,207–210] According to Park et al.,[219] the reason for the high interaction strength between the CO_2 guest molecules and the OMS is because of a strong local electrical field by the

electronic density of the Mg^{2+}-ion, which results in interaction of the CO_2 electrons with the empty orbitals of the magnesium as in a coordination bond. As a result, the performance of Mg-MOF-74 for CO_2 capture can be significantly hindered by ubiquitous water molecules.[220] However, reliable theoretical understanding of the influence of water at a large scale is still missing.

To get insight into the behavior of guest molecules in MOFs at realistic conditions (e.g., at operating pressures and temperatures), one requires information on thermodynamic characteristics, such as adsorption isotherms and transport coefficients. A possible way to obtain such quantities reduces to the parametrization of well-established macroscopic models (e.g., multisite Langmuir adsorption model) intended to describe the quantity of interest.[127,221] The applicability of such an approach is quite limited because of the essentially empirical nature of the underlying models, being valid under only specific conditions. An alternative and more natural way implies the use of large-scale classical simulations, which are based on simplified interatomic potentials (force fields). This approach allows one to calculate macroscopic averages in a wide range of external conditions, though at a higher computational cost. The quality of the results, however, is directly related to the reliability of the force fields employed.

Previous studies have shown that the existing "universal" force fields often fail to correctly describe the interaction between guest molecules and MOFs because of the nontypical coordination of metal ions.[125,126,222] Therefore, the development of specific force fields for molecule-framework interactions turns out to be a key requirement for an accurate description of adsorption and transport characteristics of gas molecules in MOFs. With respect to Mg-MOF-74, recent works on this subject are related to *ab initio* parametrization of force fields for CO_2 adsorbate,[125,126,129] which yield results in close agreement with experiments. Despite certain achievements in this field, parametrization of force fields remains a challenging and time consuming task, which cannot be performed on a routine basis. Kundu et al.[218] calculated *ab initio* Langmuir isotherm equilibrium constants from Gibbs free energies to successfully reproduce CO and N_2 adsorption isotherms. This method evolved into GCMC simulations on a lattice independent of a predetermined isotherm and applied to predict the adsorption isotherms for CH_4/CO_2-mixtures.[223] Another successful approach was to generate small clusters out of the environment around the OMS[126,224,225] or use plane-wave DFT to sample the entire unit cell.[226–228] Subsequently, the DFT-based potential energy surface is fit to common force field functions, e.g. Lennard-Jones and Buckingham potential, and then to use them in GCMC simula-

tions. If the adsorption sites obtained from classical force fields coincide with the ones obtained from DFT, Kim et al.[229] adjusted the adsorption energies during GCMC simulations based on the UFF single point energy values from DFT. As a result, the simulated adsorption isotherms agreed very well with the experimental data. Furthermore, changing the guest molecule model by adding interaction sites,[225] by multiplying force field interaction parameters with constants,[215,230] or developing polarizable force fields have proven to be a viable method to calculate adsorption isotherms in Mg-MOF-74 as well.[231] Lin et al.[226] report on the force field for water in Mg-MOF-74 derived from first-principles calculations and applied for the calculation of adsorption isotherms similarly to what is done in the following. The results they obtained in ref. 226 show noticeably higher loadings at high pressure compared to our results, which is not surprising considering the different interaction model as well as parametrization scheme employed in ref. 226. In view of the increasing interest in potential applications of Mg-MOF-74, there is a need for further activities in this direction. Furthermore, the development of force fields for other flue gas components represents an important step toward the understanding of realistic performance of MOFs with respect to the carbon capture.

While Yazadin et al.[211] showed an beneficial influence of water on CO_2 adsorption, the majority of publications on the adsorption of water showed that in fact the opposite is true: Canepa et al.[127] calculated higher adsorption energies for H_2O (73.3 $\frac{kJ}{mol}$) than for CO_2 (48.2 $\frac{kJ}{mol}$). When pure component isotherms for each species were compared, it was observed that the uptake for H_2O was higher, and saturation was reached at very low pressures.[210,227,232–234] Yu et al.[220] calculated adsorption isotherms for humid and dry N_2/CO_2 mixtures in order to see the negative influence of water on the adsorption capacity using grand-canonical Monte Carlo (GCMC) simulations. Lin et al.[226] also determined adsorption isotherms for CO_2/H_2O mixtures with GCMC, showing in the process that very small fractions of water in the gas phase can drastically decrease the CO_2 uptake in Mg-MOF-74. Recently, Daglar and Keskin[235] screened over 3800 MOFs for membrane applications regarding $CO_2/N_2/H_2O$ separation. Zuluaga et al.[117] were able to explain the reason for the loss in capacity using DFT. OH^-- ions, which come to existence in the proximity of the OMS because of the water dissociation reaction, occupying the adsorption spot. Furthermore, the complex elongates the metal-oxygen bond, and thus, weakens the structural integrity.

In this chapter, a force field model and parametrization scheme for the interaction of water and carbon dioxide with Mg-MOF-74 is proposed. The model parameters are obtained by fitting to results of first-principles density

functional calculations augmented by nonlocal van der Waals corrections. The derived force field is validated by a direct comparison between the radial distribution functions obtained from classical and *ab initio* molecular dynamic (MD) simulations as well as Monte Carlo simulations (MC) in case of water. As for CO_2, only comparisons with adsorption isotherms are considered, since enough trustworthy data are available. Furthermore, we also determined adsorption energies at zero loading (meaning the adsorption energy for the very first molecule adsorbed inside the framework) and residence probability plots. Finally, we computed the adsorption isotherms for water and CO_2 in Mg-MOF-74 by performing grand canonical Monte Carlo (GCMC) simulations by using the obtained force field for different temperatures. It is found that the conventional TIPnP models (n = number of interaction sites)[236,237] and CO_2 described by the TraPPE model,[238] respectively, combined with the universal force field (UFF)[239] plus the DREIDING[240] force field are not capable to describe the experimental isotherms with reasonable accuracy. In contrast, the DFT derived potential is able to reproduce the experimental data and available adsorption properties more accurately.

3.2 Framework structure and computational details

The structure of the Mg-MOF-74 (also referred to as CPO-27-Mg) consists of Mg^{2+} ions that are connected via dobdc^{4-} (dobdc = 2,5-dioxido-1,4-benzenedicarboxylate) linkers, forming the walls of one-dimensional pores. The conventional unit cell of Mg-MOF-74 has hexagonal symmetry ($R\bar{3}$ space group) and contains 18 Mg^{2+} ions and 9 dobdc^{4-} linkers resulting in 162 atoms per cell, as shown in Figure 3.1. One of the main features of the MOF-74 family of compounds is the specific coordination of the metal ions having no bonds in the pore volume. This results in largely unscreened electric fields inside the pores, which significantly affects the interaction with adsorbates. This accounts for the known difficulties in the description of the molecule-framework coupling within the "universal" force fields.

We used the following computational approaches. We started from DFT calculations to obtain reference data for the force field fitting. All DFT calculations were carried out by means of the projected augmented-wave method (PAW)[241] as implemented in the Vienna *ab initio* simulation package (VASP).[242,243] Exchange-correlation effects have been taken into account within the dispersion-corrected nonlocal vdW-DF functional, which consists of three parts: (i) exchange part of the revised Pedrew-Burke-Ernzerhof

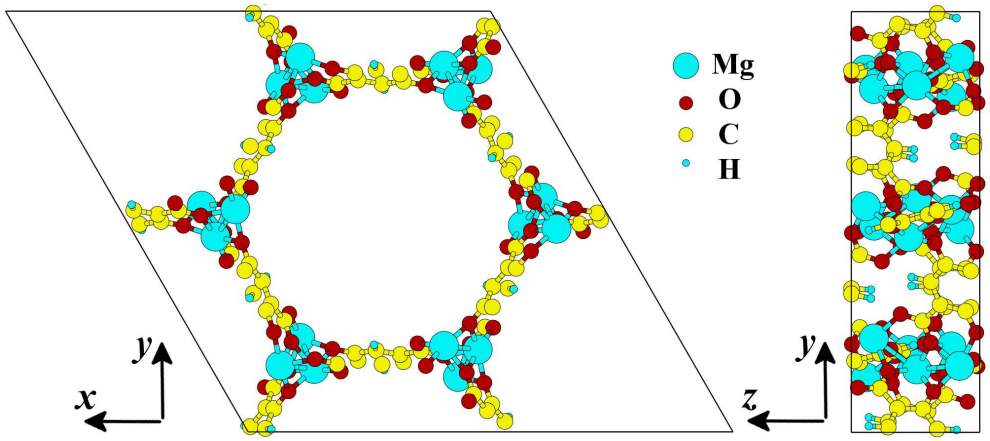

Figure 3.1: Schematic representation of the conventional unit cell of Mg-MOF-74.

(revPBE) functional, (ii) local correlation part of standard local density approximation (LDA) functional, (iii) non-local correlation part, incorporating effective many-body density response.[244–247] Apart from good transferability in general, this functional has previously been successfully applied to studies of small molecules in Mg-MOF-74.[123,124,127,128,130] We employed an energy cutoff of 400 eV for the plane-wave basis and the convergence threshold for the total energy of 10^{-5} eV, ensuring accurate calculations of the adsorption energies. To minimize undesirable interactions between the molecules in the limit of one molecule per cell, the conventional unit cell of Mg-MOF-74 was doubled in the direction of the pore channel and the following lattice parameters were used: a=b=26.114 Å and c=13.834 Å.[126] Because of the relatively large cell, the Brillouin zone was sampled at the Γ-point only.

The parameters of the force field model for the interaction between framework and guest molecules were fitted to first-principles data by means of a nonlinear least-squares method as described in the following section. To validate the parametrization of the proposed model, we performed a series of *ab initio* and classical molecular dynamics (MD) simulations and make a direct comparison between the resulting pair correlation functions. First-principles MD simulations were performed by using the (VASP) package,[248,249] whereas for classical MD simulations, the LAMMPS code was employed.[250] The same simulation cell was used for all MD simulations as for the single-point DFT calculations. In both MD cases, we used the Nosé-Hoover thermostat with the damping parameter of 20 fs, while the time integration step was set to 1 fs. To describe the water-water interactions in classical MD simulations, the TIP3P model was taken.[159,236]

Grand canonical Monte Carlo (GCMC) simulations were employed in order to compute adsorption isotherms for water in Mg-MOF-74 at 280 K, 300 K and 320 K. Residence probabilities, radial distribution functions, and adsorption energies were calculated by NVT-MC simulations at 300 K. In all simulations, the MOF structure was rigid,[126] because this assumption only induces a small error compared to simulations using a flexible structure as shown for zeolites by Vlugt and Schenk.[251] In each simulation, the simulation box contained in terms of the above mentioned parameters 2 x 2 x 4 unit cells in x, y, and z direction, respectively. A cutoff radius (r_{cut}) for the force field of 20 Å was used. Periodic boundary conditions were applied in every direction. Ewald summation technique was used for calculating long range electrostatic interactions with a relative precision of 10^{-6}.

For simulations carried out using TIPnP water models (n = number of interaction sites), the Lennard-Jones and Coulomb potentials were used to calculate interaction energies. For the framework atoms, Lennard-Jones parameters were taken from the universal force field (UFF)[239] and point charges from Dzubak et al.[126] The water is modelled as outlined by Jørgensen et al.[236] for TIP3P and TIP4P, and by Mahoney et al.[237] for TIP5P. However, for MC simulations, the corresponding Lennard-Jones parameters and point charges were taken from Price and Brooks for TIP3P,[252] from Horn et al. for TIP4P,[253] and from Rick for TIP5P,[254] because these groups refined each model for the use of the Ewald summation technique. Carbon dioxide was modelled according to the TraPPE model.[238] Lorentz-Berthelot mixing rules were applied to describe guest molecule-framework interactions.

For simulations employing the DFT derived force field, the framework-adsorbate interaction energy was calculated by Eq. 3.1. The coefficients for each individual interaction can be found in Table 3.1, and the point charges for the atom types in Figure 3.2. The water-water and CO_2-CO_2 interactions were calculated with the corresponding Lennard-Jones potential and the point-charges for the TIP3P model as mentioned before. Note that in this set of simulations, the atoms of the water molecule have different point charges depending on whether interacting with framework atoms or other adsorbate molecules.

The chemical potential in MC simulations was connected to the pressure by the Peng-Robinson equation of state. The allowed MC moves were translation, rotation, regrow and swap with the corresponding probabilities for each move of 12.5%, 12.5%, 25% and 50%, respectively. The swap moves were only used in GCMC. Before the adsorption properties and isotherms were computed, energy grids with a spacing of 0.15 Å were created in order to reduce the calculation time for the simulations.[159]

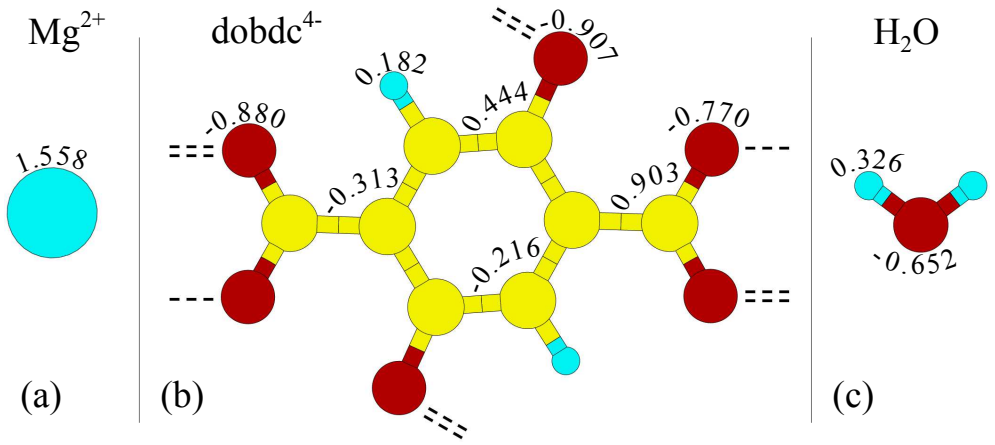

Figure 3.2: Partial atomic charges for the metal (a) and linker (b) constituents of the framework and for the water molecule (c) obtained by fitting to the *ab initio* electrostatic potential within the REPEAT scheme.[181]

For the DFT-derived force field and the TIP*n*P models, radial distribution functions were estimated for 100 K, 200 K and 300 K with a loading of 24 molecules per unit cell (UC) and adsorption enthalpies were calculated at 280 K, 300 K and 320 K using the Widom insertion method at zero loading as described by Frenkel and Smit[159] and Smit and Siepmann.[255] Residence probability plots were calculated at 300 K with 1, 12, 24, 48, and 72 molecules per UC. The adsorption isotherms were calculated for 280 K, 300 K and 320 K with a pressure range from 0 to 3000 Pa, which is slightly lower than the saturation pressure of water at 1 bar and 300 K ($p_{sat} \approx 3500$ Pa), thus avoiding (partial) condensation. For the TIP*n*P water and CO_2 models, only isotherms for 300 K were computed. NVT simulations for obtaining residence probabilities and radial distribution functions run $1{\cdot}10^5$ initialization steps to ensure equilibrium and $7.5{\cdot}10^5$ production steps, in which the ensemble was sampled. GCMC simulations started from an empty MOF structure and consisted of $1{\cdot}10^6$ initialization and $1.5{\cdot}10^6$ production steps. Note, because the pressure is very low, the fugacity coefficient is considered to be unity, thus; the excess amount of adsorption equals the absolute amount.

3.3 Force field model

There are two main adsorption sites in Mg-MOF-74: the metal ion and linker sites, which we will refer to as primary and secondary adsorption sites, respectively. At both sites, the electronic structure of the framework remains

essentially unperturbed upon the adsorption of H_2O,[130] which indicates the absence covalent bonding, and also allows us to exclude any significant role of the polarization and charge-transfer effects in the water-MOF binding. The same holds for CO_2. Therefore, the interaction between the water molecules and framework can be qualified as physisorption.

In contrast to strong chemical bonding, the force field description of physisorption is significantly simplified. Specifically, we propose that the guest molecule-framework interactions can be described in a pairwise additive way by the potential

$$\phi(r_{ij}) = \frac{q_i q_j}{r_{ij}} + A_{ij} e^{-B_{ij} r_{ij}} - \frac{C_{ij}}{(r_{ij} + D_{ij})^6}, \tag{3.1}$$

where the first term describes the electrostatic (Coulomb) interaction potential $\phi_{\text{Coul}}(r)$, while the second and third term correspond to the repulsion $\phi_{\text{rep}}(r)$ and attractive (van der Waals) $\phi_{\text{disp}}(r)$ potentials, respectively. The total interaction energy of a molecule with the framework is given by $E = \sum_{i>j} \phi(r_{ij})$, in which the sum runs over pairs of molecule and framework atoms. In Eq. 3.1, r_{ij} denotes the distance between i atom in the molecule and j atom of the framework, q_i and q_j are partial charges associated with single atoms; A_{ij} and B_{ij} characterize the steepness of the repulsion potential between the atoms i and j, whereas C_{ij} and D_{ij} determine the shape of the corresponding attraction potential. The two last terms in Eq. 3.1 resemble the well-known Buckingham potential model with the exception that an additional damping parameter D_{ij} is introduced to obtain a more accurate and physically reasonable description of the dispersion interactions.[256] We note that a similar strategy has been recently used to obtain coefficients for the interactions between CO_2 and Mg-MOF-74.[126]

To obtain the parameters of the above-mentioned model, we utilize the following strategy. We first parametrize the Coulomb term E_{Coul} by computing the partial atomic charges separately for the water molecule and MOF, which reproduce the electrostatic potential obtained at the DFT level. To this end, we use the REPEAT algorithm as described in ref. 181. As mentioned before, the point charges for CO_2 can be taken from literature.[126] Then, we perform a series of DFT calculations for different molecular configurations organized into three paths, each of which correspond to the propagation of the molecule in the direction of (i) Mg^{2+} ion; (ii) center of the carbon ring in the dobdc^{4-} linker; (iii) one of the oxygen atoms close to the magnesium. For each of the three paths, we consider four different orientations of the molecule, resulting in twelve potential energy curves as shown in Figure 3.3. Overall, almost 600 single-point energy calculations have been

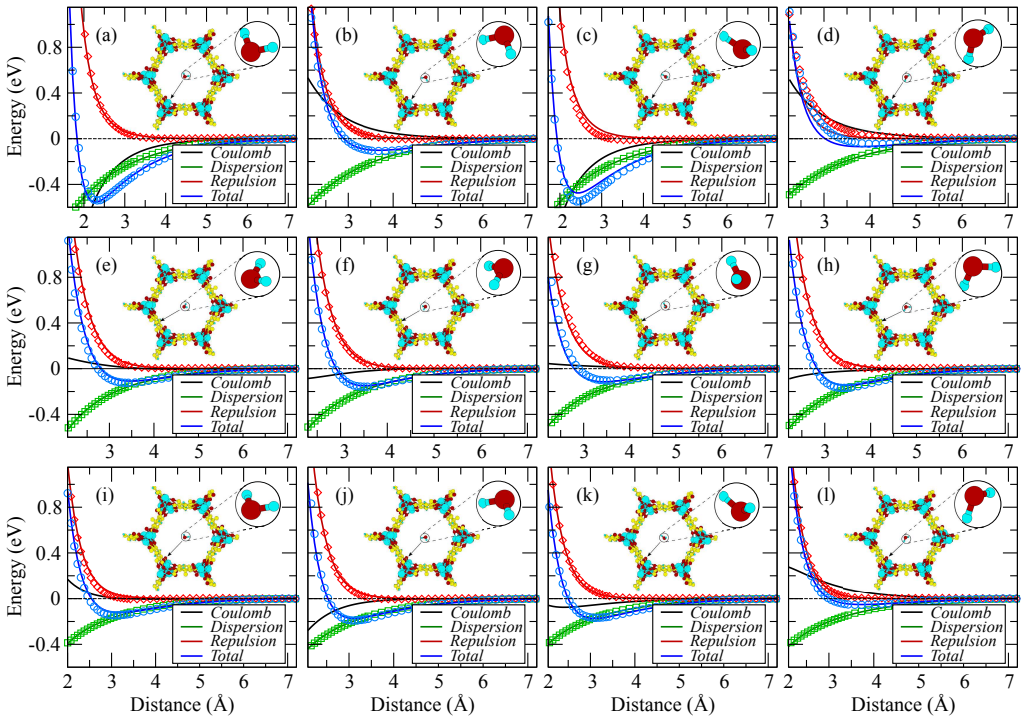

Figure 3.3: Comparison of different contributions to the potential energy curves of water calculated with the model force field (solid lines) and original *ab initio* data (points). The curves are given for three different paths and four orientations of the molecule as described in the text. Zero energy corresponds to the energy in the center of the cell. The arrows indicate the direction of the molecule propagation along the corresponding path.

carried out. As the next step, the total energy $E_{\mathrm{tot}}^{\mathrm{DFT}}$ of each configuration is decomposed into the attractive and repulsive terms $E_{\mathrm{disp}}^{\mathrm{DFT}}$ and $E_{\mathrm{rep}}^{\mathrm{DFT}}$, respectively. Within the employed computational method (the vdW-DF approach), the dispersive term can naturally be decomposed as the non-local contribution to the exchange-correlation functional,[257] while the repulsive term can formally be defined as $E_{\mathrm{rep}}^{\mathrm{DFT}} = E_{\mathrm{tot}}^{\mathrm{DFT}} - E_{\mathrm{Coul}} - E_{\mathrm{disp}}^{\mathrm{DFT}}$. In Figure 3.3, it is shown that $E_{\mathrm{rep}}^{\mathrm{DFT}}$ is positive for each considered configuration, which points to a negligible role of the polarization effects and justifies the choice of the proposed model. Finally, the contributions E_{disp} and E_{rep} are independently fitted to the corresponding energies $E_{\mathrm{disp}}^{\mathrm{DFT}}$ and $E_{\mathrm{rep}}^{\mathrm{DFT}}$. The fitting parameters A_{ij}, B_{ij}, C_{ij}, and D_{ij} were constrained to be positive, in accordance with their physical meaning. It should also be noted that in the fitting of the dispersive and repulsive contributions, all atoms of the same element were treated equivalent, while in the partial charge fitting, symmetrically

Table 3.1: Pairwise force field parameters for the interaction between a water molecule and Mg-MOF-74 atoms (according to Eq. 3.1). Notations $O_w(H_2O)$ and $H_w(H_2O)$ denote oxygen and hydrogen atoms in the water molecule and $C(CO_2)$ and $O(CO_2)$ denote carbon and oxygen atoms in the CO_2 molecule, whereas the other atomic types (Mg, O, C, H) belong to the framework.

Atom -Type	Force field parameter	Atom—Mg	Atom—O	Atom—C	Atom—H
O_w (H_2O)	A (10^6 K)	102.23	8.9403	6.3494	0.0000
	B (Å^{-1})	5.00	3.30	3.08	0.000
	C (10^6 K)	10.908	3.7868	2.6265	0.0000
	D (Å)	2.83	1.75	1.55	0.000
H_w (H_2O)	A (10^6 K)	8.1230	2.6451	0.8242	15.838
	B (Å^{-1})	4.54	4.079	3.48	3.61
	C (10^6 K)	4.9563	1.7433	2.1429	0.0000
	D (Å)	3.21	2.93	2.99	0.000
C (CO_2)	A (10^6 K)	11.0731	4.1735	10.5890	0.0000
	B (Å^{-1})	3.665	3.226	3.300	0.000
	C (10^6 K)	0.0002	4.2266	1.6513	0.0000
	D (Å)	0.003	1.725	1.443	0.000
O (CO_2)	A (10^6 K)	80.1863	12.4836	5.1702	0.5990
	B (Å^{-1})	4.962	3.455	3.050	2.722
	C (10^6 K)	1.7933	0.0740	6.1242	0.0000
	D (Å)	1.342	0.001	2.150	0.000

nonequivalent atoms of the same element were treated separately.

The partial charges for nonequivalent atoms of the framework and for the water molecule are shown in Figure 3.2. They are essentially the same as those obtained in ref. 129 within the same derivation scheme. In Table 3.1, the pairwise force field parameters obtained within the above described fitting procedure are listed. A comparison between the first-principles and model potential energy curves are given in Figure 3.3. One can see that for all paths and molecule orientations considered, the original potentials are very well-reproduced by the force field. Some discrepancies, which can be seen in Figures 3.3(c) and (d), are within the uncertainty of the *ab initio* data. This slight imperfection can primarily be attributed to the nonoptimal choice of the interaction centers within the given model. To obtain a more consistent agreement, additional interaction centers should be introduced, e.g., in accordance with the localization of the bonding orbitals and lone pairs in the system. Such complicated consideration, however, does not seem to be justified for the DFT reference data, having a limited accuracy because of the approximate nature of the exchange-correlation functional.

The obtained potential energy curves resolved into different contributions allow us to analyze the interaction nature of water and CO_2 with MOF in the vicinity of different adsorption sites. As can be seen from Figure 3.3, the behavior of both dispersion and repulsion contributions is essentially similar for water in all cases. Being virtually independent of the adsorption site, these two contributions are only slightly dependent on the molecular orientation, which is not surprising given that the charge density distribution around the molecule is not spherical. By contrast, the third contribution (Coulomb) is significantly different for different orientations and adsorption sites. Specifically, the sign of the electrostatic interactions varies with respect to the direction of the dipole associated with the water molecule, while the corresponding magnitude is appreciably higher near the Mg^{2+} ion. Close to the linker, the electrostatic term is significantly smaller and does not make any noticeable contribution to the total interaction energy. Therefore, the binding of water to the Mg site results from an interplay between the Coulomb and van der Waals interactions, whereas at the linker site it is almost exclusively determined by the van der Waals interactions. Therefore, we expect that the water molecules initially occupy all open metal sites before the linkers are covered.

3.4 Validation of the force field and radial distribution functions

Up to now, we have shown that the derived force field quite accurately reproduces a number of potential energy curves obtained from the DFT calculations (Figure 3.3). Those curves, however, do not cover the whole potential energy surface and the reliability of the force field is not fully justified. To further validate the force field, it is instructive to calculate some macroscopic properties and compare them with those obtained from reliable reference calculations. To this end, we perform a series of both classical and *ab initio* MD simulations for different temperatures by considering an intermediate loading of 24 water molecules per simulation cell distributed in such a way that only one pore channel is filled with molecules, whereas adjacent channels remain empty. This situation corresponds to a loading of one molecule per primary and secondary adsorption site in the filled channel. The simulations were started from the ground-state DFT geometry and were performed for 12000 steps including 2000 steps of equilibration. Finally, we calculate the radial distribution functions (RDF) between the magnesium–oxygen and linker–oxygen sites with oxygens belonging to water molecules. In a later step, the

same RDFs were computed also by NVT-MC simulations. This step is not needed for CO_2, because in literature exist multiple data regarding adsorption properties derived from DFT. It is reasonable to assume that the model is accurate if the values for adsorption energy and so on agree

In Figure 3.4, we show the corresponding RDFs for water at T=100 K, 200 K and 300 K. One can see there is a good agreement between the *ab initio* and classical RDFs, which is especially clear for T =200 K and 300 K. Although all the main peaks are also reproduced for T=100K, their heights are somewhat different, making the agreement slightly worse. Unequal heights of the RDF peaks points to different residence probabilities of water molecules at the corresponding distances. Apart from the force field imperfection itself, the discrepancies can be attributed to the natural limitations of the classical MD simulations, such as rigid molecule approximation and simplified nature of the water-water interactions (TIP3P model). The latter has an especially strong effect at low temperatures, which is the reason of the poor applicability of the TIP3P model for solid phases of water.[258] The results allow us to compare and evaluate the positions of the peaks, i.e. equilibrium distances, for different types of simulations with different mechanisms obtaining thermodynamic properties (MC and MD simulations). The results of the classical MD and MC simulations are presented in Figure 3.10. The comparison with the other water models TIP4P+UFF and TIP5P+UFF is shown in Figure 3.11.

For the DFT-derived force field, it can be observed form Figure 3.10 that for all three temperatures, the positions as well as the heights and widths of the peaks match very well for MD and MC simulations. The first peak is found at an equilibrium distance of $\approx$ 2.3 Å. This is very close to the Mg-ion, proving a strong interaction between the open-metal sites (OMS) and the water molecule. As expected, the force field reproduces the DFT predicted RDFs in MC simulations just as well as the classical MD and gives insight to the water density in the proximity of the OMS of the Mg-MOF-74. In contrast, the TIP3P+UFF and TIP4P+UFF models do not provide accurate prediction of the DFT benchmark, failing to describe the equilibrium distance and probability density. TIP5P+UFF provides an improvement over those two models but still are not capable of reproducing the equilibrium distance. Overall, both first-principles and classical simulations with the derived force field yield consistent results, which allows us to expect a good performance of our force field with respect to other ensemble-averaged characteristics, particularly, adsorption isotherms.

Once RDFs are obtained, it is insightful to analyze the occupation of the primary and secondary adsorption sites. In Figures 3.4 (a)–(c), one can see

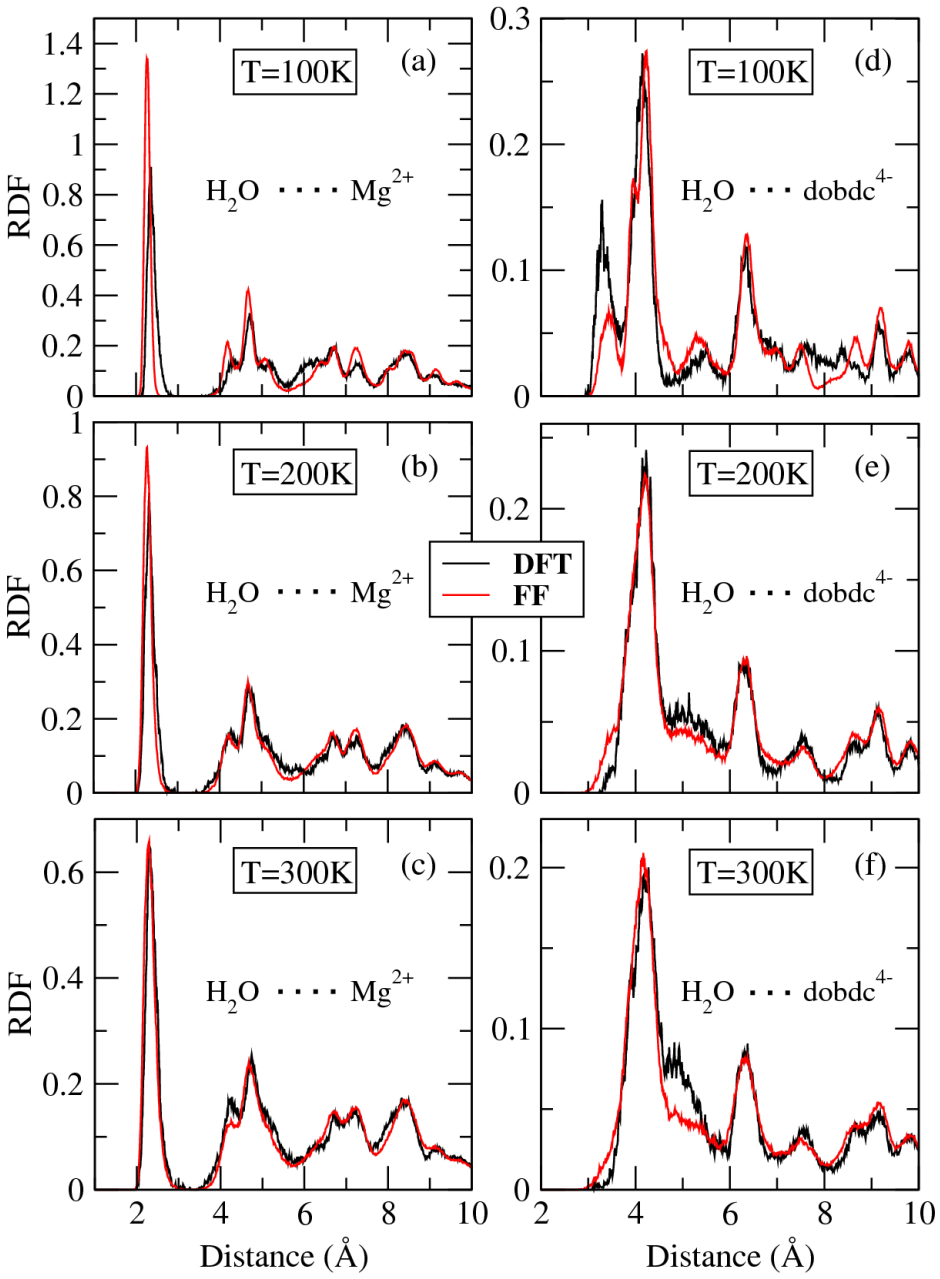

Figure 3.4: Radial distribution functions (RDF) obtained from first-principles (DFT) and classical (derived force field) molecular dynamic simulations for T=100, 200 and 300K. The RDFs are calculated for the magnesium–oxygen (a)–(c) and linker–oxygen (d)–(f) sites, where oxygen belongs to water and linker site corresponds to the center of the carbon ring in the dodbc^{4-} linker.

that all the peaks do not change their shape and remain essentially the same for all the given temperatures. This indicates that the molecules adsorbed near the Mg^{2+} ion remain strongly bound to this site up to T=300 K with the equilibrium distance $d \approx 2.4$ Å (the position of the highest peak in Figures 3.4(a)–(c)). In contrast to the Mg site, there are no indications of adsorption to the linker site at T=200 K and 300 K. Indeed, the peak corresponding to the water-linker equilibrium distance $d \approx 3.5$ Å and clearly visible at T=100 K (Figure 3.4(d)), does not appear at higher temperatures (Figures 3.4(e) and (f)). Instead, there is an additional probability density in the range 4.7–7.0 Å, which corresponds to the motion of desorbed molecules in the region between the ion and linker sites. Therefore, in contrast to OMS, linker adsorption sites make a significantly less important contribution to adsorption of water at temperatures significantly higher than 100 K.

3.5 Adsorption properties and isotherms for water

3.5.1 Residence probabilities and adsorption enthalpies

After demonstrating that the energy surface of the framework is well reproduced by the fitting functions, and that the radial distribution functions (RDFs) between DFT, MD and MC match accurately, MC-NVT simulations then are used to calculate residence probability plots of H_2O within the framework. The results for five different loadings (i.e. 0.05, 0.67, 1.33, 2.67 and 4 H_2O molecules per Mg) at 300 K are shown in Figures 3.5(a)–(e). The plots show a cut in the transverse plane of the channel in $x - y$ direction (front view), while the volume is oriented longitudinally into the z-direction. 'Yellow' indicates the highest while 'black' indicates the lowest probability to find an oxygen atom of a water molecule within the framework.
At low loadings, represented by 0.05 and 0.67 molecules per Mg, the water molecules can be found with the highest probability in close proximity of Mg (here represented as orange '+') and very rarely in the center of the channel (here indicated by a green '×', see Figure 3.5(a) and (b). The results confirm the obtained RDFs in which the positions of water are seen next to the main adsorption sites,i.e., next to the metal ions. In Figure 3.5(c) – (e), one can see the residence probabilities of oxygen of a water molecule, when we surpass the loading condition of saturation of the Mg and linker sites ($= 18^{molecules}/_{UC} \approx 8.2^{mol}/_{kg}$). In Figure 3.5(c), the adsorption sites near the Mg-ions are still the most occupied spots, however, one can identify weak 'hot-spots' close to the

organic linkers as predicted by DFT calculations, which indicate that H_2O is found around the linker site but not exactly on them. Additionally, another 'hot-spot' above the OMS is visible indicating favorable interactions between the Mg-ion, the adsorbed and a second water. Yazaydin et al.[211] reported an enhanced uptake of CO_2, when H_2O molecules were precoordinated next to the OMS. The water molecules provided a stronger and larger adsorption site because of favorable interactions between the CO_2 and H_2O-Mg cluster site. Thus, besides hydrogen bonding, the same effect might also apply to the water molecules and explain the appearance of the third site. At loadings beyond 1.33 water molecules per Mg, the probability to find water near the channel center increases, since all adsorption sites are already occupied. At saturation loading around 4 molecules per Mg ($\approx 32^{mol}/_{kg}$) complete pore filling can be observed (Figure 3.5(e)). Summing up, the MOF-74 pore is filled by occupying the Mg sites first, then the linkers, and ultimately, after adsorbing at the walls the channel is packed with the water molecules.

In addition to RDFs and residence probability plots, we estimated adsorption enthalpies at 300 K for the TIP3P model and the DFT-derived force field by using MC and compared them to DFT literature data by Canepa et al.[127] (Table 3.2). The errors are the standard deviations of the averages of the energies calculated during the production steps. As can be seen, our force field is quite accurate at reproducing the value of ref. 127, underestimating it by just 10%, whereas the TIP3P+UFF model is significant lower (> 30% less than the DFT result). In Table 3.7, the results for TIP4P+UFF and TIP5P+UFF are listed as well, which underestimate the DFT results by $\approx 25\%$.

Table 3.2: Adsorption energies for water in Mg-MOF-74 at zero loading calculated at 300 K for the DFT derived force field and TIP3P compared to DFT literature data.

Method	Model/Literature	Temperature (K)	Energy ($^{kJ}/_{mol}$)
MC	TIP3P	300	40.9 ± 0.1
	This work		-70.9 ± 0.1
DFT	Canepa et al.[127]	298	-76.2 ± n/a

Up to this point, we have sampled the potential energy surface of the framework and derived an appropriate potential function, see Eq. 3.1. Then, we validated our force field by comparing adsorption properties computed by MC and MD to the DFT benchmarks. The comparison shows that the obtained force field is accurate enough, whereas the TIPnP+UFF are incon-

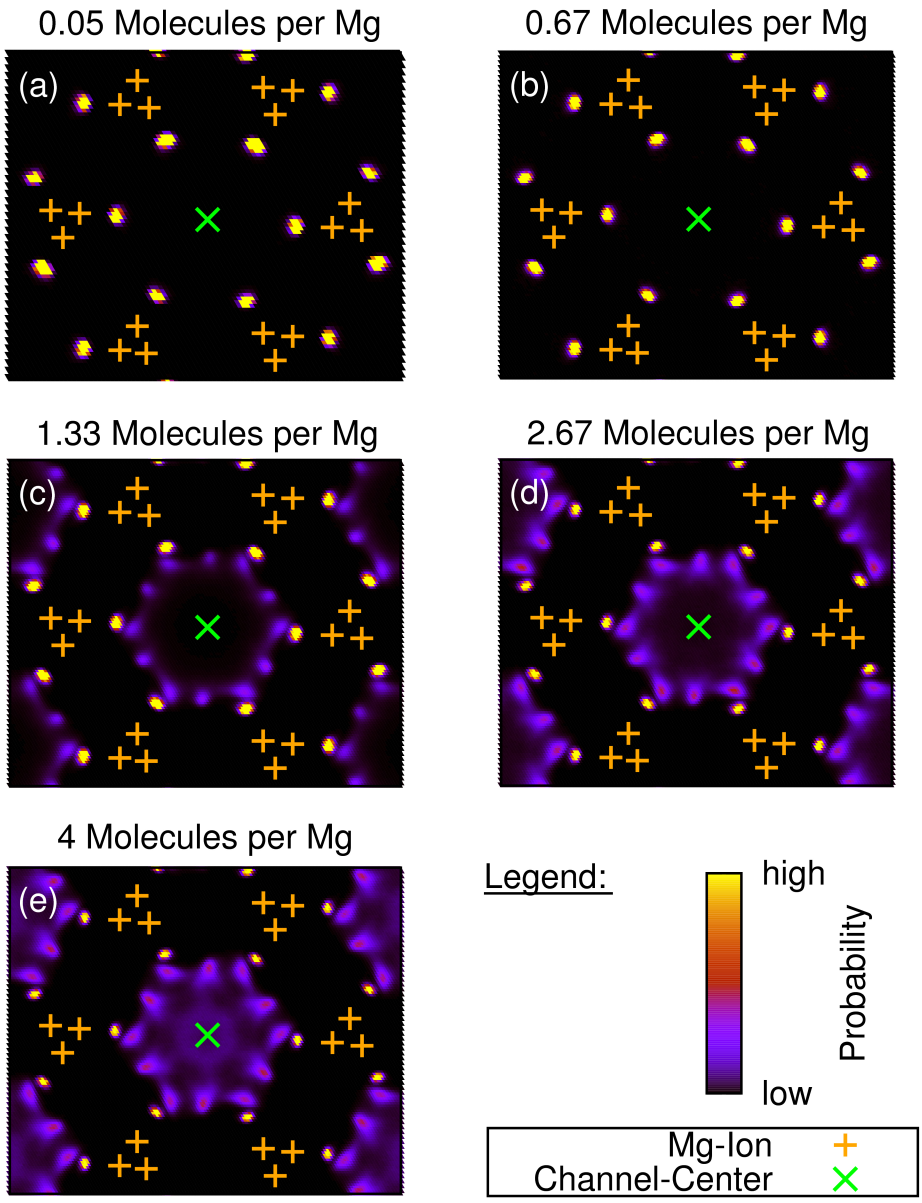

Figure 3.5: (a) – (e): residence probability of oxygen of a water molecule insight Mg-MOF-74 for 1 (a), 12 (b), 24 (c), 48 (d), and 72 (e) molecule(s) per UC at 300 K, respectively, whereby 'yellow' indicating the highest and 'black' the lowest probability, Mg-ions are represented by orange (+) and the center of a channel by green (×).

sistent with respect to the DFT results and previously published data.

3.5.2 Adsorption isotherms

At the final step, we compute adsorption isotherms and compare the results with the available experimental data as well as the standard TIPnP+UFF water models, which is provided as a benchmark. The experimental data were taken from Grant Glover et al.,[232] Schoenecker et al.,[233] DeCoste et al.,[234] and Yang et al.[259] All data are presented in Figure 3.6. It should be mentioned that there are indicators that Mg-MOF-74 is not stable in the presence of water over a longer period of time, although the peaks of the XRD spectra are kept at their original positions, and even the FTIR spectra change only slightly (see e.g. ref. 234). That means there might be some reorganization in the MOF framework but not a complete dissolution. Furthermore, the synthesis approach has considerable influence on the adsorption properties of Mg-MOF-74 as well.[259]

One can see that IUPAC-Type I isotherms are observed for all experimental data sets.[260] The experimental isotherms exhibit steep slopes in the low-pressure regime, which shows a strong affinity of water toward the framework, especially OMS. In the higher-pressure region ($>$ 1000 pa), the loading does not increase significantly with increasing pressure, indicating saturation. Despite the qualitative similar shapes of the isotherms, the saturation loadings of the experimental data sets are different. One possible origin may be due to different synthesis strategies as argued by Yang et al.[259] Their two data sets ("Yang et al.(1)" and "Yang et al.(2)") underline this argument. However, even though Grant Glover et al.[232] and Schoenecker et al.[233] both used the same solvothermal method, yet their maximum loadings vary. In particular, they reported saturation loadings around 25 $^{mol}/_{kg}$ and 35 $^{mol}/_{kg}$ as well as different BET surfaces (1200 $^{m^2}/_{g}$ and 1400 $^{m^2}/_{g}$), respectively. Summarizing the available experimental data, the saturation loading varies from 20 $^{mol}/_{kg}$[234] to 35 $^{mol}/_{kg}$[233,259] as well as the shapes of the isotherms, which vary from group to group with the one exception of Schoenecker et al.[233] and Yang et al.(1).[259] One can see that in spite of the several experimental works available, no one can be regarded as conclusive with respect to the adsorption isotherms for water in Mg-MOF-74.

We now turn to the analysis of the numerical results. Note that the error bars can be read as uncertainties of the obtained mean amount of molecules inside the framework during the production steps of the simulations. The TIPnP+UFF models fail to describe all the experimental data over the investigated pressure, in particular in the range 0-500 pa. The models are

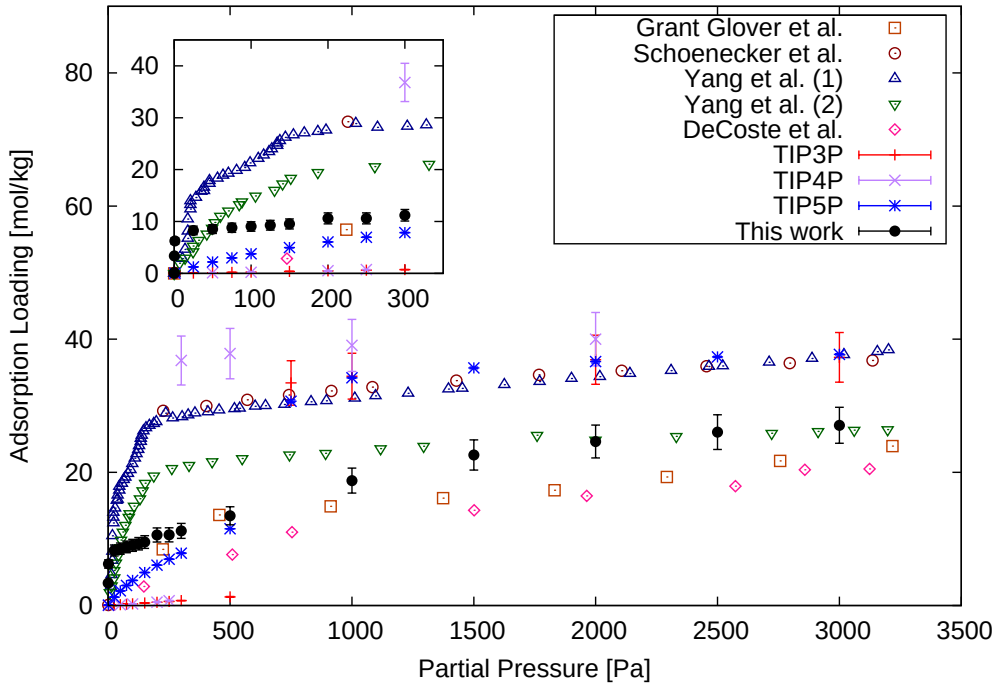

Figure 3.6: Adsorption isotherms of water for Mg-MOF-74 at 300K; open symbols represent experimental data: (□) Grant Glover et al.,[232] (○) Schoenecker et al.,[233] (◊) DeCoste et al.,[234](△) and (▽) Yang et al.[259] Closed symbols represent simulation data: TIP3P+UFF (+), TIP4P+UFF (×), TIP5P+UFF (∗) and DFT derived force field from this study (•).

Table 3.3: Differences in point charges between TIP3P model by Price et al.[252] and DFT-derived force field (Figure 3.2).

Atom	TIP3P model[252]	DFT-derived force field
$O(H_2O)$	-0.834	-0.6521
$H(H_2O)$	0.417	0.32605

not able to predict the steep slopes, which are observed for the experimental data. This result can be attributed to the poor description of the OMS-water interaction (here: Mg-H_2O).[125,126,222] The reason is that this environment the generic force fields are fitted to differ greatly from the chemical vicinity caused by OMS.[115] TIP3P+UFF predicts (almost) zero molecules inside the MOF in the region of 0-500 pa. At 750 pa, however, the loading exhibits a "jump" to almost the saturation loading, resembling a steeplike function. The same behavior is observed for the TIP4P+UFF model, for which the "jump" is found at 300 pa. The TIP5P+UFF satisfactory predicts an increase of loading with pressure, though it fails to reproduce the shape of any experimental curve. A "jump" in loading is also noticeable at 750 pa. At higher pressures, all TIPnP+UFF models qualitatively reproduce the experimental results quite well. This is most likely caused by the domination of adsorbate-adsorbate interactions due to the high loading. This reduces the effect of the OMS and creates a vicinity near the bulk water phase, to which the models are fitted.[236,237,258]

In contrast, the DFT derived force field qualitatively describes the experimental data noticeably better, in particular at low loadings. It reproduces the shape of the isotherm as a function of pressure over the complete investigated pressure range. The more accurate results compared to the TIPnP+UFF models are related to the improved description of the framework-adsorbate interactions, especially the OMS-adsorbate interaction as described earlier. Nevertheless, the first points at 0.1 and 1 pa show an overestimation of the loadings (6.0 $^{mol}/_{kg}$ for the simulation compared to $\approx$ 0.5 $^{mol}/_{kg}$ for the highest experimental data at 1 pa). The Henry coefficient calculated for zero loading is very high (161.3 $^{mol}/_{(kg \cdot pa)}$) as well, thus showing the overprediction in the lowest-pressure regime. The deviation can be attributed to the perfect crystal structure, which is assumed in the simulations and cannot be reproduced by experiments because of real life crystalls having defects. Furthermore, precise measurements at very low pressures are difficult. In the intermediate pressure regime ($>$ 100 pa and $<$ 2000 pa), the DFT-derived force field reproduces the slight increase of loading with pressure as observed in the experimental data sets. As for higher pressures ($>$ 2000 pa), the simulated isotherm lies well within the ranges of the experimental data, but below the TIPnP+UFF results. We note that as the TIP3P model is used to describe the adsorbate-adsorbate interaction, such results are expected. The divergence might be due to the adjustment of the framework interaction for which the point charge of the oxygen atom was reduced from -0.8340e (original TIP3P model)[252] to -0.6521e (DFT-derived force field), thus affecting water-framework interactions at large distances. Note that the point charges

on the hydrogen were adjusted accordingly, see Table 3.5. The charge difference makes the Coulomb interaction energy with the framework less negative, and thus, less hydrophilic compared to the TIP3P+UFF model. As a result, less loading is predicted. Therefore, the choice of the point charges is of great importance for the shape of the adsorption isotherm. To be more realistic, the point charges should be changed with loading and position of the water molecules, which has not been considered within the present work.

We also computed adsorption isotherms at 280 K and 320 K at the same conditions. The results are shown in Figure 3.12. The results are fitted to the SIPS isotherm (see Eq.3.2) with high accuracy.[66] The coefficients resulting from the fits can be found in Table 3.6. One can observe that over the entire pressure range, lower temperature leads to higher the loading, as expected. For all temperatures, the saturation loading for the Mg sites ($\approx 8.25\ ^{mol}/_{kg}$) is reached at very low pressures. At higher loadings, the isotherm behavior is more strongly temperature-dependent. Note that the saturation pressure is a function of temperature, thus at 280 K, the saturation pressure is exceeded at 1200 Pa.

Overall, the DFT-derived force field obtained predicts the experimental data for water generally well and more accurately then the TIPnP+UFF water models over the investigated pressure range. The variety of experimental data do not allow us to describe any of the measurements with quantitative accuracy. Nevertheless, it can be concluded that our theoretical results are close to the isotherms reported by Grant Glover et al.,[232] DeCoste et al.,[234] and Yang (2) from Yang et al.[259]

3.6 Adsorption properties and isotherms for carbon dioxide

In contrast to properties regarding water adsorption, the amount of work dedicated to design force fields from DFT calculations is considered to be extensive.[125,126,215,226] Furthermore, the experimentally obtained adsorption isotherms for carbon dioxide agree well with each other regardless of the group reporting in contrast to water adsorption. Consequently, we believe that if our force field is able to reproduce adsorption energies as well as adsorption isotherms obtained by simulation there is no real need to compare more sophisticated methods like radial distribution functions and so on. The adsorption energy is a metric for how well the interaction between the framework atoms and the guest molecules are described. The adsorption isotherm takes into account every influence at once, showing how precise the force field

captures the loading dependency. In Table 3.4, the results for the adsorption energies of CO_2 are given. The full DFT calculation by Canepa et al.[127] agrees reasonably well with the fully developed force field model, since the deviation is less than 10% (48.2 $\frac{kJ}{mol}$ to 45.3 $\frac{kJ}{mol}$). Furthermore, two sets of point charges for the CO_2 molecules were used: one for CO_2-CO_2 interactions and one for CO_2-framework interactions, similar to how water was modelled.

Table 3.4: Adsorption energies for carbon dioxide in Mg-MOF-74 at zero loading calculated at 300 K for the DFT derived force field and the TraPPE model[238] compared to DFT literature data.

Method	Model/Literature	Temperature (K)	Energy ($^{kJ}/_{mol}$)
MC	TraPPE[238]	300	31.1 ± 0.2
	This work		45.3 ± 0.1
DFT	Canepa et al.[127]	298	48.2 ± n/a

In general, the adsorption isotherms for water and carbon dioxide look quite similar despite being measured at different pressure ranges. It should be noted that the isotherms are only measured and calculated up to one bar since this is the pressure range in which the adsorber is supposed to function. Pressures beyond that are simply out of the scope of this work.

The adsorption isotherm for CO_2 by Mason et al.[209] can also be classified as IUPAC-Type I isotherm.[260] At low pressures a steep slope in the isotherm can be seen indicating a strong interaction between the CO_2 molecules and the open metal sites. Once the main adsorption sites, e.g. the OMS, are saturated (around 8 $\frac{mol}{kg}$) the second, less attractive sites at the organic linkers are occupied. The same behavior was proven for water, see Figure 3.5. However, CO_2 molecules are less stabilized than water is when the full ring is occupied. In other words, if the main adsorption sites (OMS) and the sites at the organic linkers are saturated, water is more stable and more strongly bound at those sites than CO_2 is. Consequently, the very steep slope obtained for water, which is bascially going from 0 $\frac{mol}{kg}$ to 30 $\frac{mol}{kg}$ or more, is

Table 3.5: Differences in point charges between TIP3P model by Price et al.[252] and DFT-derived force field.

Atom	TIP3P model[238]	DFT-derived force field
$C(CO_2)$	0.700	0.656
$O(CO_2)$	-0.350	-0.328

not found for CO_2, see Figure 3.7. The fact that the experimental isotherm by Mason et al.[209] does not capable to even reach 8 $\frac{mol}{kg}$ at one bar, indicates that the sample was not synthesized optimally.

It is clear that the isotherm data obtained from simulations predict up to 20% higher loading than the experimental ones (Figure 3.7). This comes to no surprise, since in simulations the perfect crystal structure is examined compared to the one synthesized. The latter version will never be perfect and have some sort of defects, effectively reducing the pore volume and OMS density. Yet, the behavior of the experimental data is well reproduced by Dzubak et al.,[126] Sun et al.,[215] and Lin et al.[226] Sun et al. did not use DFT calculations and fitting the results method to its fullest potential the results deviate slightly. The isotherms by Dzubak et al.[126] and Lin et al.,[226] which are based on fully DFT-derived force fields are in very good agreement with each other. Now comparing the adsorption isotherm from this work with the two aforementioned ones, it is obvious that the agreement is also good. Because of the fact that Dzubak et al.[126] and Lin et al.[226] examined closely adsorption properties together with the reproduction of their resulting adsorption isotherm, we believe that our force field captures the interactions present in the CO_2-Mg-MOF-74 system equally well.

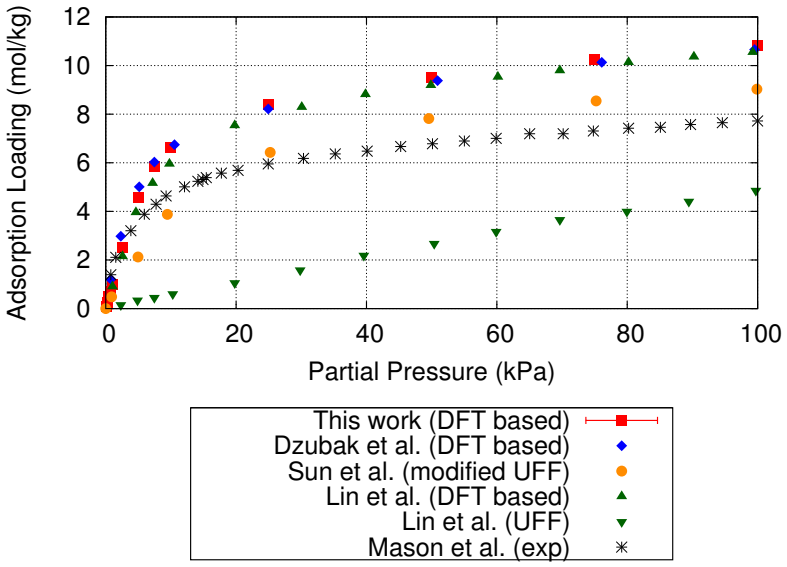

Figure 3.7: Adsorption isotherm for CO_2 in Mg-MOF-74 at 313 K. Simulation data are taken from Dzubak et al.,[126] Sun et al.,[215] and Lin et al.[226] Experiments have been carried out by Mason et al.;[209] errorbars are too small to be visible.

3.7 Refit to Lennard-Jones function

Since the energy and force calculations in GROMACS are the most efficient using Lennard-Jones functions, the parameters have been refitted from a function with four parameters to one with two and, furthermore, only one set of point charges for the guest molecules were used instead of two. Obviously, that leads to a loss in accuracy. It is important though to quantify this inaccuracy and whether or not the information-rich DFT-based force field with 4 parameters can be simplified like this. Therefore, we compare adsorption energies and adsorption isotherms, which are based on DFT calculations for the case 4 parameters or 2 are used, to experimental and simulation data.

The fastest property to compute is the adsorption energy at zero loading. As for H_2O, the adsorption energies are presented in Table 4.8. The results based on the Lennard-Jones version of the force field underestimates the DFT value by Canepa et al.[127] and the previously published force field[227] by less than 5 $\frac{kJ}{mol}$ or 7%, respectively. For CO_2, see Table 4.4, the Lennard-Jones based model underestimates the DFT value by more than 6 $\frac{kJ}{mol}$ indicating that the framework-guest interactions are stronger in reality than described by the Lennard-Jones version. The most likely reason for the deviation is the accuracy loss because of the reparametrization from 4 parameters to 2, in particular for the framework oxygen atoms with the oxygen of the CO_2 molecule. That means the framework-guest interactions are described sufficiently well.

Yet, comparing adsorption isotherms for CO_2 and H_2O in Mg-MOF-74 show that the experimental isotherms are still predicted well. For water the experimental adsorption isotherms reported by Yang et al.[210] and DeCoste et al.[234] as well as simulated ones by Lin et al.[226] and Rudenko et al.[227] are compared to the fit obtained in this chapter in Figure 3.8. There are a lot more experimental isotherms to be found in literature, however, the ones selected here are the maximum and minimum of those. The simulated isotherms by Lin et al.[226] and the ones from this work follow the trend of the experiments well whereas the former lies outside the range of experiments and the latter lies within. The isotherm based on the force field used in this chapter does not capture the trend of the experimental isotherms perfectly, as evident by the small step at around 150 pa and by the fact that a saturation loading is reached at around 33 $\frac{mol}{kg}$. Yet, the isotherm is well within the range stretched by the experimental data. Considering the fact that the degrees of freedom have been reduced, the force field is representing the reality accurately enough. The adsorption isotherms for CO_2 presented in Figure 3.9 were measured and calculated at 313 K and up to 1 bar. There

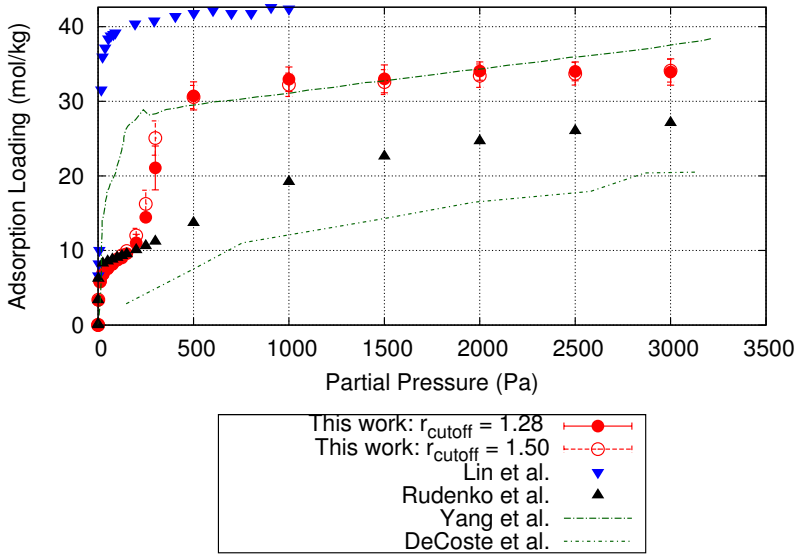

Figure 3.8: Adsorption isotherm for H_2O in Mg-MOF-74 at 300 K. The data from Yang et al.[210] and DeCoste et al.[234] represent the maximum and minimum experimental isotherms for reference, respectively. The data from Rudenko et al.[227] and Lin et al.[226] are used as reference for simulation based isotherms.

is one experimental data set by Mason et al.,[209] which serves as the model baseline for the simulated adsorption isotherms of Dzubak et al.,[126] Sun et al.,[215] Lin et al.,[226] and our own. The simulated adsorption isotherms follow the trend of the experimental one measured by Mason et al. yet predict higher uptakes. That was expected, since the crystal used in the simulation box is assumed to be perfect with no defects, whereas in experiments not all sites are available to the guest molecules.[126] Our force field is in good agreement with the other DFT-derived force fields because of the reasonable agreement with the adsorption energies and adsorption isotherms. Due to the refit of the original force field,[227] it was necessary to verify that the cutoff radius r_{cutoff} for the electrostatic and van der Waals interactions does not influence the outcome of the simulations significantly. Therefore, adsorption isotherms for CO_2 and H_2O in Mg-MOF-74 were calculated with two different r_{cutoff}: 1.28 nm and 1.50 nm. The results can be seen in Figure 3.9 for CO_2 and Figure 3.8 for H_2O, respectively. The agreement between the refit and the original force field is very good for both guest molecules. If one compares the adsorption energies for the two radii, see Tables 4.4 and 4.8, a similar result to the isotherms is found as the energies are within 3% of each other.

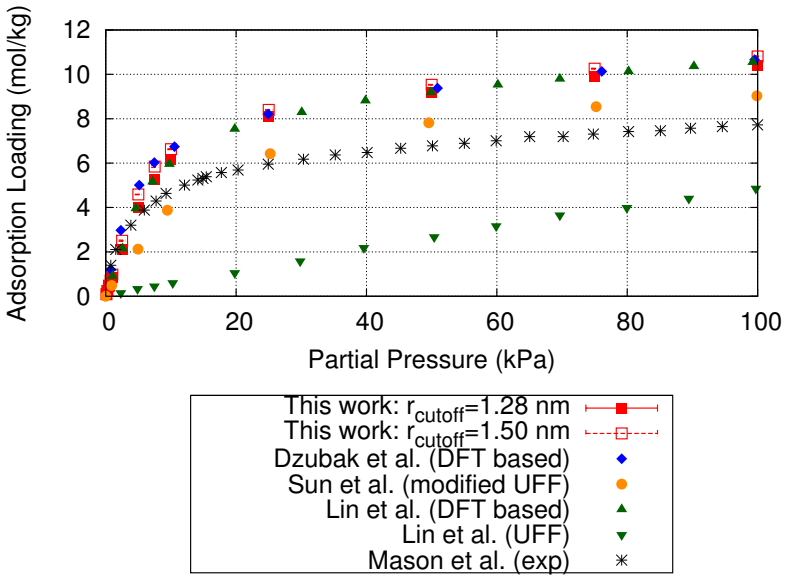

Figure 3.9: Adsorption isotherm for CO_2 in Mg-MOF-74 at 313 K. Simulation data are taken from Dzubak et al.,[126] Sun et al.,[215] and Lin et al.[226] Experiments have been carried out by Mason et al.[209] Errorbars are too small to be visible.

Ultimately, it can be seen that the greater r_{cutoff} calculates only marginally larger uptake than the smaller one, while the simulation time is increased by up to 50%. As a result, we chose to set r_{cutoff} to 1.28 nm to combine fast simulations with high accuracy.

In conclusion, the refitted force field used in this chapter is not as accurate as the DFT-derived force fields in their full function, but the agreement with literature data for adsorption energies and isotherms is still high. It describes the framework-guest interaction well and is deemed suitable for describing the interaction using Lennard-Jones functions.

3.8 Conclusions

To sample the potential energy surface for water and CO_2 in Mg-MOF-74, DFT calculations were used to fit and parameterize potential energy functions. The DFT-derived force fields reproduce the static DFT results very accurately. In case of water, we calculated radial distribution functions with the DFT, MD and MC approaches at different temperatures. The results agree well, providing insight on the density distribution of water inside the

framework, and further validate the obtained force field. Finally, we performed GCMC simulations to calculate adsorption isotherms with the DFT derived force field and compare the results with the available experimental data, as well as the standard TIPnP+UFF and TraPPE+UFF models. The standard TIPnP+UFF water models and TraPPE+UFF for CO_2, however, could not achieve the same accuracy. We have shown that our force field (both variants) provide a significantly improved description of the experimental data compared to the TIPnP+UFF and TraPPE+UFF models. It correctly describes the saturation loading and shape of the isotherms, and thus, demonstrates essentially better performance over the available literature models. However, the absence of conclusive experimental adsorption isotherms of water in Mg-MOF-74 does not allow us to fully assess the predictive power of the obtained force field, which is left for further investigations. Overall, the results provide a deeper understanding of the water and CO_2 adsorption in MOFs with open metal sites, while the proposed force field derivation scheme can be used for the simulation of other gases in MOFs as well.

3.9 Supporting information

3.9.1 Referred figures and tables

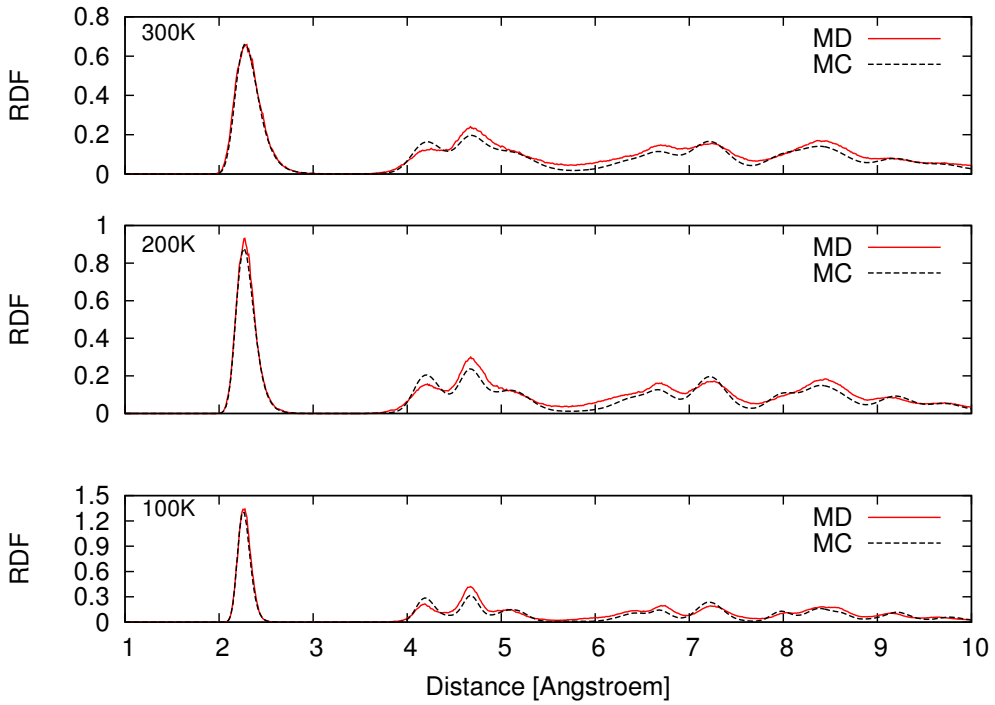

Figure 3.10: Radial distribution functions of water for the DFT-derived force field obtained from MD and MC simulations at different temperatures (100 K, 200 K and 300 K); MD results are presented in red and MC in black.

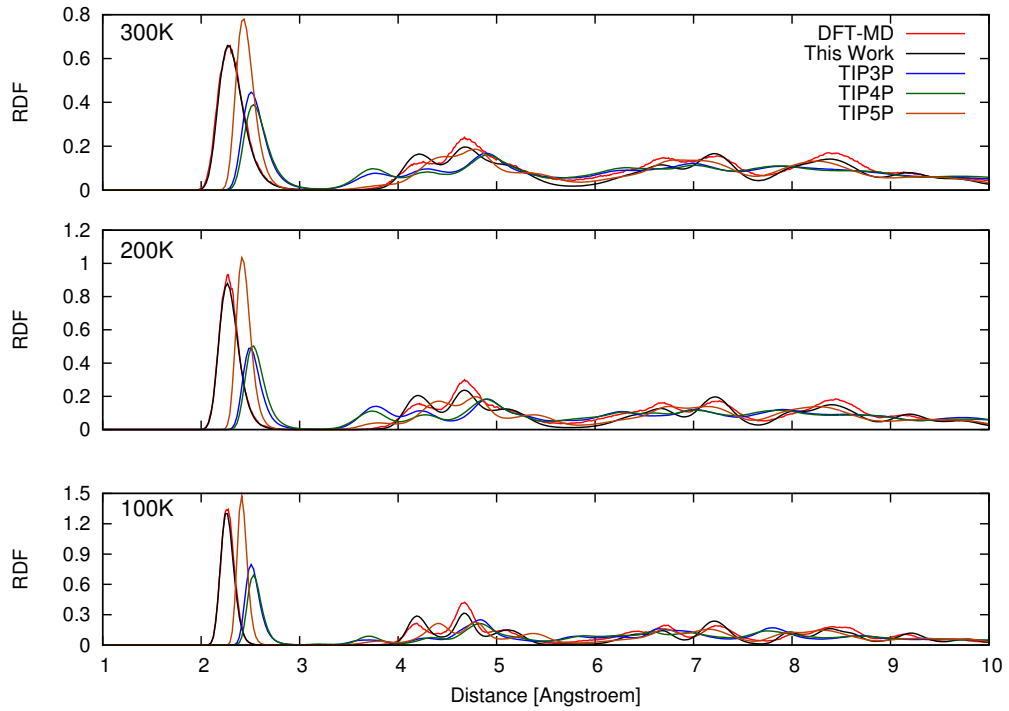

Figure 3.11: Radial distribution functions of water for the DFT-derived force field (MC in black, MD in red), TIP3P[252]+UFF[239] (blue), TIP4P[253]+UFF[239] (green) and TIP5P[254]+UFF[239] (brown) at three different temperatures (100 K, 200 K and 300 K).

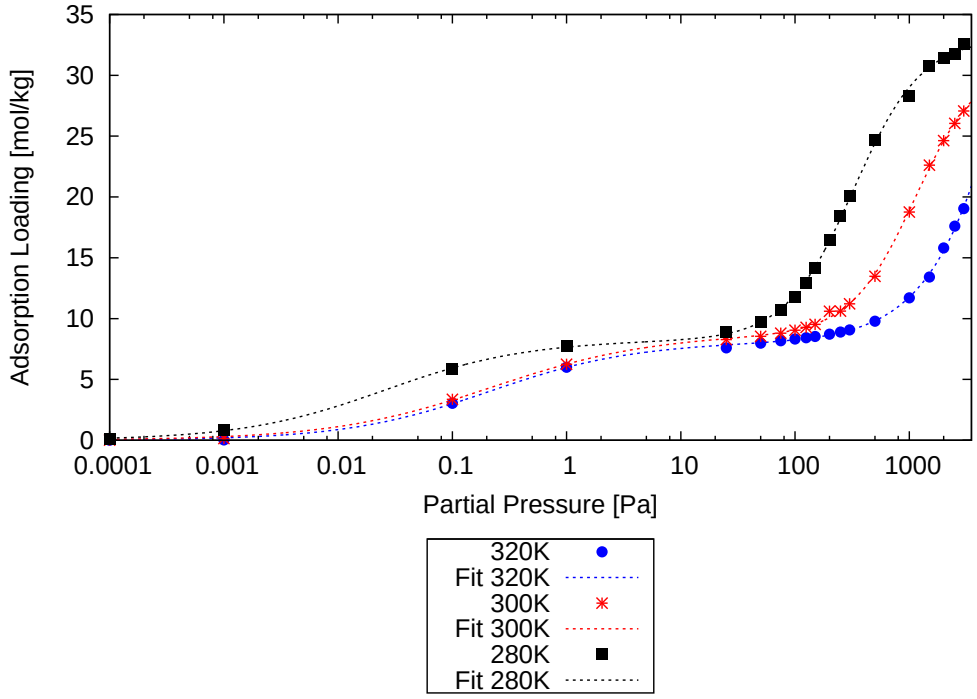

Figure 3.12: Adsorption isotherms for water in Mg-MOF-74 at 280 K (□), 300 K (∗) and 320 K (•) as a function of pressure.

In Figure 3.12, the simulated adsorption isotherm for water at 320 K, 300 K and 280 K based on the DFT-derived force field are presented. The loading θ as a function of pressure was fitted to dual site SIPS isotherms, which has the following form:[66] The coefficients resulting from the fits are summed up in Table 3.6.

$$\theta(p) = \frac{C^A_{Max} \cdot (K^A \cdot p)^a}{1 + (K^A \cdot p)^a} + \frac{C^B_{Max} \cdot (K^B \cdot p)^b}{1 + (K^B \cdot p)^b}. \tag{3.2}$$

Table 3.6: Coefficients obtained by fitting the simulation data of each temperature separately to the dual site SIPS isotherm for the adsorption of water in Mg-MOF-74 (Eq. 3.2).[66]

Coefficients	320 K	300 K	280 K
C^A_{Max}	8.6522	8.6638	8.1810
K^A	0.8181	4.6490	40.2576
a	0.656	0.633	0.699
C^B_{Max}	24.3126	21.9029	25.1700
K^B	$2.767{\cdot}10^{-4}$	$9.523{\cdot}10^{-4}$	$2.980{\cdot}10^{-3}$
b	1.462	1.580	1.416

Table 3.7: Adsorption energies for water in Mg-MOF-74 at zero loading.

Model/Method	Temperature in K	Energies ($^{kJ}/_{mol}$)
TIP3P+UFF	300	40.9 ± 0.1
TIP4P+UFF		39.6 ± 0.3
TIP5P+UFF		53.5 ± 3.2
This work	300	70.9 ± 0.1
Canepa et al.[128] (DFT)	298	76.2 ± n/a

3.9.2 Force field parameters

Table 3.8: Point charges for the Mg-MOF-74 framework atom types from the REPEAT[181] approach and the water models (M and L denote the pseudo atoms of the respective water model);[252–254] for atom types see Figure 3.2.

Atomtype framework	Charge (e)	Water models	Atomtype	Charge (e)
Mg	1.5578		H	0.4170
O_a	-0.7700	TIP3P[252]	O	-0.8340
O_b	-0.8799		—	—
O_c	-0.9067		H	0.5242
C_a	0.9026	TIP4P[253]	O	0.0000
C_b	-0.3131		M	-1.0484
C_c	0.4437		H	0.2410
C_d	-0.2164	TIP5P[254]	O	0.0000
H	0.1821		L	-0.2410

Table 3.9: Lennard-Jones (LJ) parameters for the Mg-MOF-74 framework atom types the water, and CO_2 models (M and L denote the pseudo atoms of the respective water model); for atom types see Figure 3.2.

Model	Atomtype	ϵ (LJ) in Kelvin	σ (LJ) in Ångstrøm
Framework	Mg^a	55.857	2.691
	$O_a{}^b$	30.193	3.118
	$O_b{}^b$	30.193	3.118
	$O_c{}^b$	30.193	3.118
	$C_a{}^b$	52.838	3.431
	$C_b{}^b$	52.838	3.431
	$C_c{}^b$	52.838	3.431
	$C_d{}^b$	52.838	3.431
	H^b	22.142	2.517
TIP3P [252]	H	0.000	0.000
	O	76.420	3.151
TIP4P [253]	H	0.000	0.000
	O	81.900	3.164
	M	0.000	0.000
TIP5P [254]	H	0.000	0.000
	O	89.573	3.097
	L	0.000	0.000
CO_2 [238]	C^c	27.000	2.800
	O^d	79.000	3.050

[a] UFF [239]
[b] Dreiding-FF [240]
[c] point charge e=0.700
[d] point charge e=-0.350

4 Diffusion of water and carbon dioxide and mixtures thereof in Mg-MOF-74

Self-diffusion coefficients for CO_2, H_2O and mixtures thereof in Mg-MOF-74 have been determined using molecular simulations. The crystal structure was modelled as rigid and flexible, respectively, with the intent to identify the impact of the flexibility of the framework on the diffusivity. The results show that especially at low loadings the mobility of the molecules is enhanced in flexible lattices due to a small difference in adsorption energy and the enlarged equilibrium distance to the main adsorption sites. In mixtures the flexibility has the same influence, however, due to the presence of the secondary species, water is predominantly located in the close proximity of the magnesium ion which effectively leads to a segregation effect from the more freely moving CO_2.

4.1 Introduction

We have shown in the previous chapter that classical force fields, like UFF[239] and DREIDING[240] for example, cannot describe the potential energy surface around the OMS, which leads to false predictions of the experimental adsorption isotherms compared the the ones obtained from GCMC.[126,215,225–227,230] Therefore, DFT and *ab initio* quantum chemical calculations have been employed as a mean to overcome this problem which has been shown to be successful for the prediction of adsorption properties, see Chapter 3. Consequently, the prediction of adsorption for water and carbon dioxide has improved significantly. Since the mechanism of adsorption itself is not a static property nor is the mass transport in the fixed bed or in the pellets: diffusivity plays an important role in all of this as well, usually working against the adsorption. This means that the mobility of guest molecules inside a framework is dependent on the interaction strength between the host network and the gas species, whereas the higher the isosteric heat of adsorption the lower the mobility.

Since the focus of research lies mainly with the adsorption of guest molecules in Mg-MOF-74, the number of studies regarding the diffusion of them is very small. Canepa et al.[127] investigated the diffusion of CO_2, H_2O and H_2 barriers along the z-axis of the framework. Marti et al.[261] studied the orientation of CO_2 molecules as a function of loading with NMR and DFT while Xu et al.[262] used ^2H SSNMR spectroscopy to look at orientations of D_2O and other molecules in Mg-MOF-74. Lin et al.[129] calculated free energy maps along the channel axis to identify orientations of the CO_2 molecules and diffusion barriers along the path using Monte Carlo simulations. To the best of our knowledge, only Krishna and van Baten[263] reported values for self-diffusivity of CO_2 in Mg-MOF-74 with the restriction, that the aforementioned special nature of the OMS were not taken into consideration in their paper.

Another important factor for modelling diffusion is the flexibility of the MOFs. Compared to zeolites, MOFs are considered highly flexible, which for instance, can lead to breathing effects or linker rotation among other things.[137] The influence of flexibility in MOFs on diffusion has received some attention recently. For example, ZIF-8 was investigated for its flexibility,[264,265] and to determine why it is capable to adsorb molecules with a considerably larger kinetic diameter than the (rigid) pore diameter.[136,266] Amirjalayer et al.[267] reported that because of the framework flexibility benzene molecules diffuse more slowly through MOF-5 than in the rigid case. Recently, Braun et al.[268] investigated multiple thermostats frequently used in

molecular dynamics simulations. They were able to show that velocity rescaling algorithms, e.g. thermostats, can cause artifacts violating the equipartition theorem. As an example for such artifacts, they showed that the influence of the framework flexibility in the study by Amirjalayer et al.[267] was mainly the result of the chosen Berendsen thermostat. Consequently, one needs to be aware, whether the deviation between a rigid and a flexible lattice is caused by the the flexibility and not by thermostat artifacts. Also, it was shown that for zeolites the introduction of flexibility can cause the free energy to be less negative, allowing molecules to diffuse faster.[269] To date, the understanding of the MOF-lattice flexibility modelling process is still in its infancy, and experiments are essential to verify simulation results.[269,270]

In this chapter, we calculate self diffusion coefficients for pure CO_2 and H_2O systems as well as mixtures thereof in Mg-MOF-74. We compare results based on the UFF and the QM-based force field derived in the previous chapter. Furthermore, the influence of flexibility of the framework on the self-diffusion coefficients is investigated.

4.1.1 Adjustments and differences of the force fields

In order to calculate intermolecular energies and forces, two force fields are used. The first one is based on the UFF[239] (from here on called "UFF-FF") and the second is based on the one derived in the previous chapter, using the refitted version(from here on called "DFT-FF").[227] In each case CO_2 is described by the TraPPE,[238] and for the UFF-FF the framework atoms are modelled based on the UFF.[239] The differences between the force fields are that in the UFF-FF Lorentz-Berthelot mixing rules are used to calculate cross-term parameters and H_2O is modelled according to the TIP5P-Ew water model.[237,254] In the DFT-FF the mixing rules involving framework atoms are replaced by specifically derived interaction parameters, which reproduce the potential energy surface obtained from DFT calculations using the TIP3P[236,252] model.[227] For all interaction parameters in each force field, description of framework atoms and guest molecules, and a more detailed discussion on the accuracy of the force fields, the reader is referred to Chapter 4.4.

4.1.2 Simulation details

All MD simulations were carried out using the GROMACS package version 5.1.1.[174] The setup was as follows: For each loading (one molecule per unit cell and so on) two constraints have to be met: First, the number of molecules

was chosen so that at least 64 molecules are put into each simulation box to obtain good statistics each run. Second, the size of the simulation box must be twice the cutoff radius in every direction. As a result, the numbers of unit cells per direction vary from 3x3x7 to 1x1x5 in x-, y-, and z-direction, respectively, whereas the smallest box possible is the 1x1x5 unit cell configuration. A schematic unit cell of Mg-MOF-74 is given in Figure 3.1.

To ensure that the system is sampled in an equilibrated state, a minimum of $5{\cdot}10^5$ Monte Carlo steps in the NVT ensemble were carried out, using only the regrow move with the pre-defined number of molecules, ranging from 1 molecule per unit cell to 36 molecules per unit cell or 66 molecules per unit cell for CO_2 or H_2O, respectively. As for mixtures, the swap identity move is added, whereas both moves have a probability of 50% to occur. The loading represents the maximum uptake of the structure for the respective guest molecule according to GCMC-generated adsorption isotherms.[126,226,227] In the next step, Maxwell-Boltzmann distributed velocities are assigned to each molecule individually. The production phase was run with a time step of 1 fs for at least 50 ns, see chapter4.4 for further information. The equations of motion were integrated using the velocity-Verlet algorithm. The desired temperature of 300 K was controlled by means of the Nose-Hoover-thermostat (τ_t = 1 ps) as implemented in GROMACS 5.1.1.[174] The framework was either kept rigid or flexible depending on the simulation. Flexibility was modelled as described in the UFF.[239] Please note that the DFT-FF is not specifically designed for the flexible lattice but for the rigid one. As a result, the force field might not reproduce vibrational frequencies or experimentally determined lattice parameters, which are essential for flexible force fields,[271] and thus, the interaction parameters between host atoms and guest molecules have not been refined for that case. However, we believe that the parameters determined for the rigid case are a reasonable approximation, since the average position of the framework atoms in the flexible lattice agrees well with the ones in the rigid case, as is evident by the calculated adsorption energies and isotherms (see chapter 4.4). Periodic boundary conditions were applied in all directions in all simulations. A cutoff radius of 12.8 $\AA$ for the van der Waals and Coulomb interactions was employed. The long-range electrostatic interactions were calculated using the Particle-Mesh-Ewald method.[189,190] Unless interaction parameters between guest molecules and/or framework atoms have been specified in the force field, they are determined using the Lorentz-Berthelot mixing rules. The (self-)diffusion coefficient for one simulation can be calculated using the velocity auto-correlation function or the mean-squared displacement (MSD). We opted for the latter. The Einstein equation relates the diffusion coefficients to the average MSD of molecule i

(for all i in the system):

$$D_{xyz}^{self} = \frac{1}{2 \cdot 3} \cdot \lim_{t \to \infty} \frac{\partial \langle \Delta \mathbf{r}_i^2(t) \rangle}{\partial t} = \frac{1}{6} \cdot \lim_{t \to \infty} \frac{\partial \langle \mid \mathbf{r}_i(t) - \mathbf{r}_i(0) \mid^2 \rangle}{\partial t} \tag{4.1}$$

D_{xyz}^{self} describes all three space directions. It is possible to calculate each direction individually, for example in z direction:

$$D_{z}^{self} = \frac{1}{2} \cdot \lim_{t \to \infty} \frac{\partial \langle \mid r_{z,i}(t) - r_{z,i}(0) \mid^2 \rangle}{\partial t} \tag{4.2}$$

Then, the dimensionally averaged D_{xyz}^{self} is obtained by:

$$D_{xyz}^{self} = \frac{D_{z}^{self} + D_{y}^{self} + D_{z}^{self}}{3} \tag{4.3}$$

Mg-MOF-74 and its derivatives consist of honeycomb-like channels in z-direction without intersections. Because of that, only diffusion coefficients in that direction are of interest, and hence, D_{xyz}^{self} equals D_{z}^{self}. Pair distribution functions were generated from the trajectories of the guest molecules. For the evaluation for both, the diffusion coefficients and the pair distribution functions, the trajectories of each molecule are taken within the simulation time of 5 to 45 ns to avoid artifacts at the beginning of the simulation and insufficient sampling at the end.

4.2 Results

4.2.1 Comparison of the force field in the rigid crystal

It has already been established that classical force fields fail to describe the interactions between the open metal sites (OMS) and certain guest molecules, which interact strongly with them. The improvement of DFT derived force fields with respect to adsorption isotherms has been well documented in the literature.[126,225–227] As for dynamic properties, to the best of our knowledge, this has not been the case yet. In Figure 4.1, the self-diffusion coefficients for CO_2 at 300 K obtained from simulations as a function of loading are compared to results published by Krishna et al.,[263] which are calculated using UFF[239] and DREIDING.[240] Our results, based only on the UFF, reproduce the trend of the reference data well. With increasing number of molecules inside the simulation box the diffusion becomes slower. This loading dependency is commonly observed in nanoporous materials.[272] With increasing

loading collisions between molecules occur more frequently, and thus, the diffusion resistance is increased for each molecule, effectively slowing all of them down.[273] The deviation between Krishna et al.[263] and our results can be explained by the fact, that slightly different point charges were assigned to the framework atoms. Self-diffusivities calculated using the DFT derived force field yield a reduced mobility, lowering the diffusion by a factor of almost ten at low loadings to twice at higher ones. This is expected since the estimated adsorption energy is lower for the UFF than for the DFT based force field, see Chapter 4.4. Furthermore, the behavior of the diffusivity as a function of loading became more complex: At low loadings the diffusivity decreases with an increase of loading, until a minimum is reached at 15 to 18 molecules per unit cell. Then, a second maximum is found at 30 molecules per unit cell. The reason for this behavior may be explained in the following way: It is unlikely that the decrease in diffusivity is caused by molecule-molecule collisions, since the channel is quite large and saturation is far from being reached. 18 molecules per unit cell is an important level of loading, since there are 18 OMS or 18 Mg-ions per unit cell. At this or close to this loading, statistically, the OMS (the main adsorption sites of this crystal)[126] are saturated. Thus, leading up to that limit and because of the strong interactions with the OMS, a higher fraction of molecules is adsorbed and found in (close) proximity of the adsorption site, e.g. the Mg-ion, where the molecules are trapped and their movement is slowed down. The fraction of non-adsorbed, fast moving molecules decreases. When the loading is increased above 18 molecules per unit cell, the diffusivity increases, because all the OMS are occupied and, because of more and more CO_2-CO_2 interactions, the attraction strength of the OMS is somewhat diminished; the weaker adsorption sites close to the linkers are occupied. In other words, because of the adsorbed CO_2 molecules the channel wall becomes less attractive and the channel itself smaller, resulting in faster movement of the guest molecules in the middle of the channel, until there is less and less free space. At loadings higher than 30 molecules per unit cell the molecule-molecule collisions are much more frequent, and there is less and less free pore volume available. As a result, the self-diffusivity decreases similar to the UFF-based results. It is interesting to note that, for the highest loadings, for which the interaction energies are dominated by molecule-molecule interactions, the diffusion coefficients predicted by either force field are very close to each other.

The loading dependency of the self-diffusion coefficient for H_2O is shown in Figure 4.2. To the best of our knowledge, there are no data available in the literature. The results based on the UFF increase monotonically with loading to a plateau value as the maximum. The diffusivity ranges from

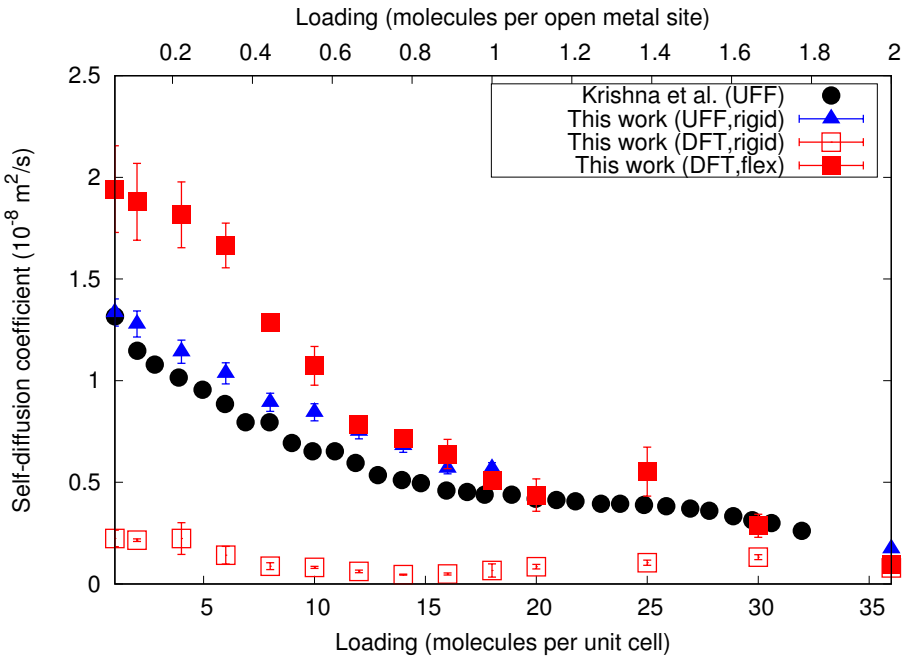

Figure 4.1: Self-diffusion coefficients based on different force fields for CO_2 in Mg-MOF-74 at 300 K as a function of loading. The simulation data by Krishna et al.[263] are based on DREIDING and UFF.

approximately $1{\cdot}10^{-11}$ $\frac{m^2}{s}$ at 1 molecules per unit cell up to $1.8{\cdot}10^{-9}$ $\frac{m^2}{s}$ at high loadings exceeding 40 molecules per unit cell. This loading dependency follows the type III self-diffusion process described by Kärger et al.[272] Because of the very strong interaction with the Mg-sites at low loadings, the movement of the water molecules is slow and limited. With increasing number of molecules in the framework, the relative number of strong interaction sites are reduced, which leads to an increase of the overall mobility. This mechanism was experimentally verified and reported by Kärger et al.[272] Another influence could be the strong attraction between water molecules, e.g. hydrogen bridges: One water molecule passes by, is able to free a trapped molecule, and drags the freed one along with it. That ultimately leads to cluster formation, which then have a lower occupancy within the channel.[274] When approaching the aforementioned plateau at around 40 molecules per unit cell, the increased number of molecules reduces the available pore volume and more and more water-water collisions take place. This results in a transport resistance, which balances out the cluster movement of the water molecules. The results obtained using the DFT-based force field are basically identical for loadings higher than 20 molecules per unit cell, which

corresponds to the saturation of the OMS of the framework. The influence of the different force fields is seen at low loadings at which interactions are still dominated by framework-water interactions. Two findings stand out at loadings below the threshold of 20 molecules per unit cell: First, the diffusivity is lower by roughly a magnitude. In fact, the deviation increases with loading up to a factor of 15 at 15 molecules per unit cell. This was to be expected, as the UFF cannot predict the adsorption capacity at low pressures accurately compared to the DFT-FF, because the former underestimates the interaction energy between the framework atoms, the Mg in particular, and water molecule(s).[226,227] Since the interaction is stronger between those in the DFT-FF, the guest molecules diffuse more slowly. Second, while the trend of the DFT-FF based results are the same as the UFF ones, one can see a "step" at around 18 molecules per unit cell. At levels where almost all of the OMS are occupied, the self-diffusion coefficients increases greatly, because the adsorbed water molecules form a layer around the pore wall and, thus, "shield" the passing water molecules from the Mg-ions, resulting in enhanced mobility. At loadings beyond that threshold, the reason for the course of diffusivities is the same as for the UFF.

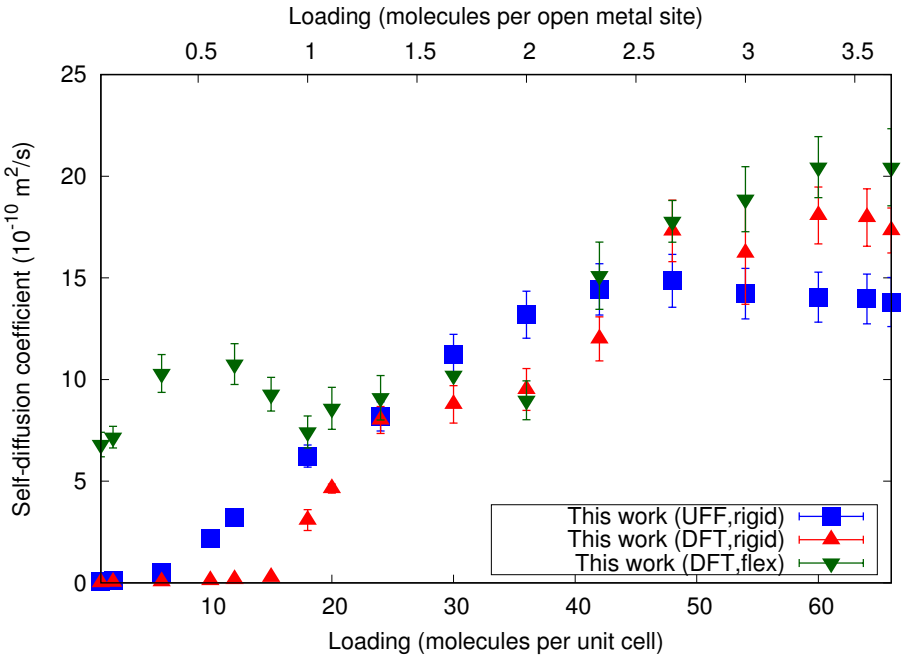

Figure 4.2: Self-diffusion coefficients based on different force fields for H_2O in Mg-MOF-74 at 300 K as a function of loading.

4.2.2 Influence of framework flexibility on CO_2 and H_2O diffusion

For an investigation of the influence of the flexibility of the framework, simulations were carried out in which the framework was modelled as being flexible using the UFF to describe intramolecular interactions (bond, angle, and torsion), while the intermolecular forces were described by the DFT-FF. The limitations of the force field (as described above) should be kept in mind. This allows us to have an indication on whether flexibility reduces or enhances the diffusivity of CO_2 and water in Mg-MOF-74. The self-diffusivity of CO_2 in the flexible framework, see Figure 4.1, decreases monotonically with increasing loading to a minimum at around 20 molecules per unit cell. A maximum is then reached at 25 molecules per unit cell after which the self-diffusion coefficients decrease again. This behavior of the flexible case resembles closely the one obtained for the rigid framework. Consequently, since the behavior is the same, such that there is a similar reasoning for it, as explained above. It is remarkable, however, that the flexibility causes the molecules to move much faster through the nanoporous structure: For 1 molecule per unit cell the self-diffusion coefficient for the flexible framework is almost 10-fold the value for the rigid one. The adsorption energy of the rigid and flexible system is less negative than calculated by DFT (difference of around 6 $\frac{kJ}{mol}$), see Table 4.4, meaning that the interaction is not as strong, and consequently, the transport resistance is lower and the mobility higher. At the highest loading (36 molecules per unit cell) all force fields predict similar diffusivity at around $1{\cdot}10^{-9}$ $\frac{m^2}{s}$. This shows that the movement at high loadings is dominated by interactions between the CO_2 molecules themselves, and flexibility of the crystal becomes less and less important. However, the fact that for the flexible case the framework could expand, and in this way reduce the impact of the high loading on the mobility, does seemingly not play a role, because the volume gained by the flexibility seems to be quite insignificant compared to the total volume. This hypothesis is supported by comparing the pair distribution functions for CO_2 in the rigid and flexible case, respectively, see Figure 4.5 and Figure 4.7(a). At low loadings, e.g. one molecule per unit cell, it is obvious that the CO_2 molecules are much closer to the Mg-ions in the rigid case compared to the flexible one (Figure 4.7(a)), which indicates a stronger interaction and lower diffusivity. These observations are consistent with the free energy profiles. As the loading increases, the difference does not vanish but becomes less efficacious. This coincides with the findings on framework flexibility reported by Zimmermann et al.[269] It is noticeable that the increase of diffusivities at loadings (slightly) above the OMS saturation occurs at a lower number of molecules and is higher

compared to the rigid case due to the influence of the framework.
As for water (Figure 4.2), the influence of flexibility on the diffusivity is quite obvious and can be broken down into two loading regimes: At loadings above 24 molecules per unit cell, the diffusion in the flexible framework is only slightly higher (less than 10%) than in the rigid one because of the assumed absolute higher free energy.[269] At loadings below this threshold, however, the impact of the framework flexibility is much more pronounced, ranging up to a factor of 100 for 1 molecule per unit cell. For an understanding of how this effect occurs, one compares the adsorption energy at infinite dilution for both cases, see Table 4.8. It can be observed, that the interaction energy for the guest molecules in the rigid crystal is 71.2 $\frac{kJ}{mol}$, which is around 3 $\frac{kJ}{mol}$ higher compared to the flexible case. Hence, this results in a reduced diffusivity. While it explains the differences at loadings higher than 24 molecules per unit cell, it cannot solely be the reason for the deviation in the low loading regime. When taking a look at the pair distribution functions, see Figure 4.6 and Figure 4.7(b), the impact of the flexibility is more obvious: For example, at 1 molecule per unit cell the first water molecules are found at a distance with respect to the Mg-atoms of about 2-3 nm in the rigid and at around 4 nm in the flexible case. Furthermore, the likelihood to find water molecules at those distances is much higher in the flexible lattice. In other words, not only is the interaction not as strong in the flexible case as in the rigid one, the moving framework atoms cause the water molecules to be further away from the adsorption sites, which ultimately leads to the much higher movement and diffusion coefficients. Additionally, the difference in the pair distribution functions at higher loadings for both cases becomes less and less prominent (Figure 4.7(b)). The function of the diffusivity in the flexible case itself has a rather complex behavior. It can be divided into three regimes due to the present minima and maxima: The first one is from 0 to 18 molecules per unit cell (low loading), the second from 18 to 36 molecules per unit cell (medium loading), and higher than 36 molecules per unit cell (high loading), respectively. The first boundary (18 molecules per unit cell) corresponds to the loading at which all open metal sites are occupied and the second one (36 molecules per unit cell) to where the water molecules occupy the organic linker as adsorption sites, effectively covering the channel wall completely.[227] In the low loading regime, a maximum is found at around 12 molecules per unit cell. While in the rigid case the self-diffusion coefficient monotonically increases with loading, the movement of the framework atoms cause a reduction in the mobility of the water molecules. Since the increase in diffusivity with loading in the rigid framework was attributed to the formation of (small) water clusters, it seems reasonable to assume that the introduction of flexibility inhibits the formation of them to a certain degree probably because of

the lattice vibration, which eventually leads to more isolated molecules adsorbing at the main adsorption sites (the Mg-ions). Because of the break-up caused by the lattice vibration even at higher loadings, more and more small water clusters are present in the system, which leads to the reduction of mobility caused by adsorption at loadings above 12 molecules per unit cell. In the medium range, a maximum is found at 30 molecules per unit cell. While the dispersion effects of the framework still hinder the cluster formation, the fact that the OMS are not available anymore together with the fact that the secondary adsorption sites are not as strong, leads to a general increase of the self-diffusion coefficient. Above 36 molecules per unit cell, all sites, e.g. the pore walls, are saturated and the cluster formation is not hindered. This results in an increase in mobility, until the structure is fully packed at which point the diffusivity goes down because of steric hindrance. Please note that we have not been able to prove this theory of the influence of coalescence and break-up in our simulations, but based on our results and experience there seems to be a valid argument for it.

4.2.3 Self-diffusivity in mixtures

As the next step, self-diffusion coefficients for CO_2 and H_2O mixtures in the rigid and the flexible framework were determined, respectively. We chose the following mixture ratios: rich on water (10/90), rich on CO_2 (90/10), and one equimolar (50/50). Please note that those ratios represent the ratios of molecules of either species present inside the simulation box, i.e. the crystal, and not the bulk gas phase. These ratios allow the investigation of the behavior of each species in different scenarios easily. In addition, the number of molecules for the "10%"-species is low. Consequently, the statistics lead to rather large error bars, in particular for water. The results for the self-diffusion coefficients for CO_2 and for H_2O for the rigid crystal case are given in Figure 4.3 and for the flexible one in Figure 4.4, respectively. Comparisons for each component individually can be found in Figure 4.8.

The introduction of framework flexibility does not have any different implications as in the pure components cases of CO_2 and H_2O, respectively, see Figure 4.8. In the case of CO_2, the influence of the flexibility decreases with increasing loading up to a level, where the results are basically indistinguishable. While the CO_2 molecules diffuse slower in the mixture, water moves slightly more quickly. Overall, the molecules still have a larger equilibrium distance to the open metal sites compared to the rigid framework, which overall enhances the mobility for both species as alluded to in the previous chapter.

In the rigid case, see Figure 4.3, it is obvious that the CO_2 molecules move more quickly than the also present H_2O ones. The diffusivity as a function of loading for CO_2 is relatively independent on the fraction of water present in the mixture, since all values are relatively similar to one another. However, when more water is in the system, the movement of the CO_2 molecules is faster, since the free and nonadsorbed water molecules seemingly do not slow them down. Additionally, minima and maxima can be found at around 15-20 molecules per UC and around 30 molecules per UC, respectively. The reasoning for this is a bit more complex. Despite of the occupation of the Mg-site by the water molecules the now created water cluster around the ion becomes an attractive site. As a result, CO_2 molecules adsorb on this complex which leads to a reduction of the mobility. Basically, up to the point where water is predominant in the system, CO_2 is barely influenced by it. Furthermore, compared to the pure CO_2 results shown in Figure 4.1, the diffusivity is only reduced by approximately 20% in general because of the slower movement of water. As for H_2O, water molecules barely move at all, resulting in self-diffusion coefficients lower than 10^{-13} $\frac{m^2}{s}$, which is too low to be calculated accurately with MD, and consequently, all values below that threshold are considered to be zero. The reason for water not moving is simple: Since water molecules interact much more strongly with the open metal sites as indicated by their respective adsorption energies (Tables 4.4 and 4.8), they are only found in close proximity to the Mg-ions surrounded by CO_2 molecules and nowhere else. In test runs at low molecule numbers, the starting conditions of the MD simulations were manipulated in such a way that more water molecules were put closer to the middle of the channel. However, those runs yielded the same results as the original ones because of the fact that the water almost immediately moves towards the OMS to adsorb. This proves that there is a strong segregation effect due to the OMS of Mg-MOF-74, rendering Maxwell-Stefan-Diffusion predictions likely to be inaccurate. Even with an increase of water molecules due to the increase of water fraction, most of the water is adsorbed at the Mg-ions or located nearby. Since space is limited, more and more of them can move freely among the CO_2 molecules, which in turn leads to an increase in diffusivity. At high loadings in the CO_2-rich mixture, the self-diffusion coefficients of water follow the trend of the CO_2 ones albeit at roughly 50% of their values. This indicates that the freely moving water molecules are dragged along by their CO_2 counterparts.

In Figure 4.4, the results for the self-diffusivities in the flexible case are presented. Similar to the results based on the rigid crystal, the diffusivities of CO_2 are higher than the ones for water, which is the expected result. With

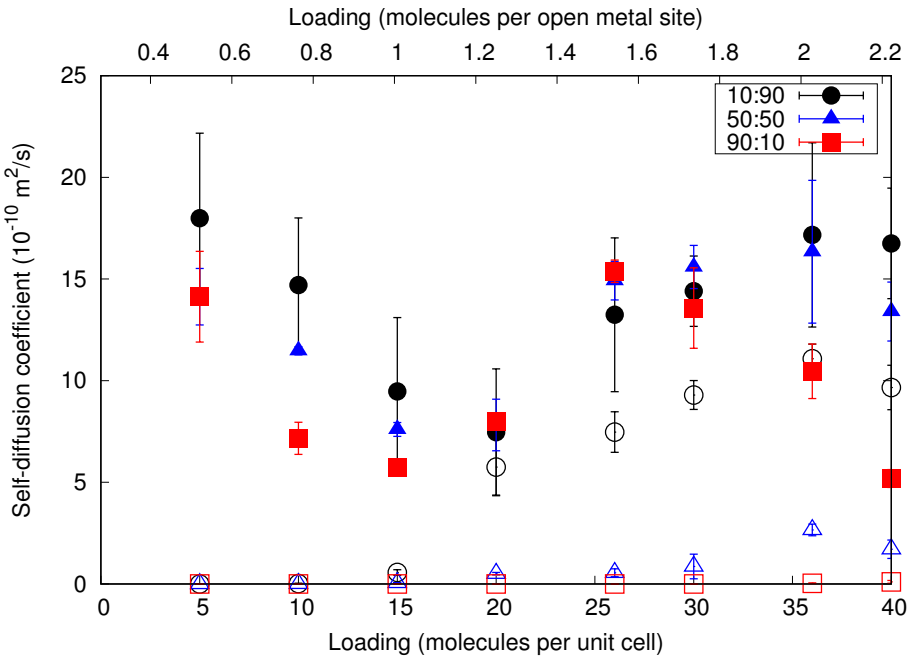

Figure 4.3: Self-diffusion coefficients in the rigid framework for CO_2 (closed symbol) and H_2O (open symbols) in three CO_2/H_2O-mixtures (90/10 (black dot), 50/50 (blue triangle), and 10/90 (red square)) at 300 K based on the DFT-FF.

the exception of CO_2 in the 90/10 mixture, the diffusivity is monotonically decreasing with loading. In the latter case the behavior follows the trend of the pure CO_2 results, showing that the effect water has in this situation is a decrease of mobility by circa 25%. The absence of a maximum at higher loadings in the other investigated mixtures is likely caused by the slowing effect the water molecules have on CO_2. This eventually leads to the fact that, at loadings above 35 molecules per UC, CO_2 and H_2O have the same diffusivity. The self-diffusion coefficients for H_2O as a function of loading are very similar to the pure component results, having a maximum at 10-15 molecules per UC and a maximum at 15-20 molecules per UC, for example. However, the CO_2 molecules in the system accelerate the water ones so that the overall mobility is increased compared to the pure water diffusion.

4.3 Conclusions

In this chapter, the diffusion behavior of CO_2 and H_2O in Mg-MOF-74 and the impact of framework flexibility on their diffusivity were investigated.

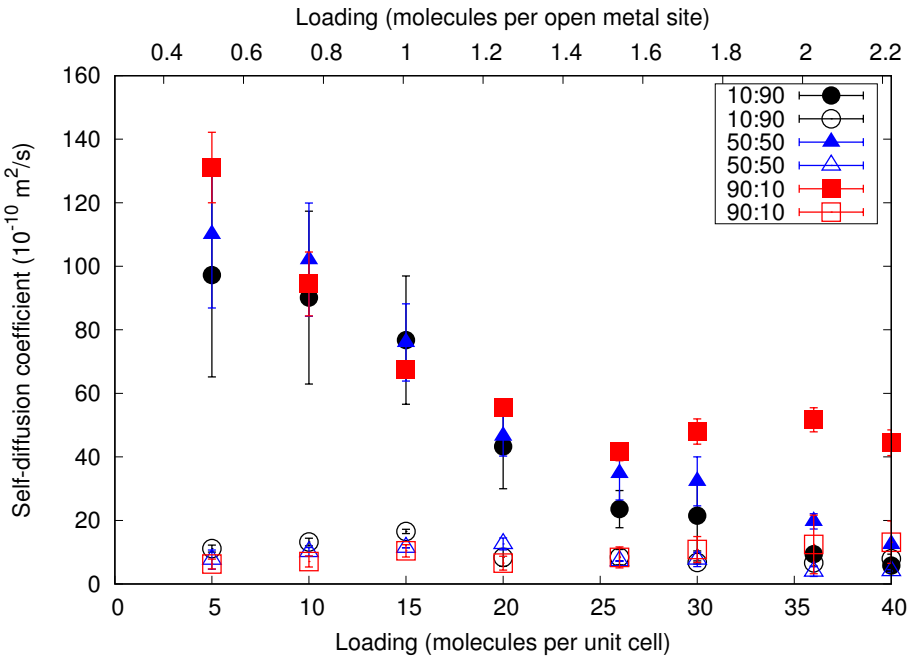

Figure 4.4: Self-diffusion coefficients in the flexible framework for CO_2 (closed symbol) and H_2O (open symbols) in three CO_2/H_2O-mixtures (90/10 (black dot), 50/50 (blue triangle), and 10/90 (red square)) at 300 K based on the DFT-FF.

Molecular simulations were carried out to calculate self-diffusion coefficients at different loadings, whereas the crystal was modelled as rigid and flexible, respectively, for the pure components individually and in mixtures of them. Initially, the force field derived from DFT was compared to experiments and simulations available from literature in order to verify diffusion results inside the rigid framework. Once the force field was established, self-diffusion coefficients for CO_2 and H_2O in the flexible crystal were determined. It was shown that the main consequence of the flexibility was an enlarged equilibrium distance of the guest molecues to the open metal site, i.e. the Mg-ion, compared to the rigid crystal, while the adsorption energy did not change dramatically. Consequently, the higher mobility resulted in higher self-diffusion coefficients. For both species the impact of the introduced flexibility was the highest at lower loadings, up to 20 molecules per unit cell for water and up to 30 molecules per unit cell for CO_2, respectively. Lastly, mixtures of both components were investigated. The results for the self-diffusion coefficients showed that there is a segregation between the stronger adsorbing water molecules and the CO_2 inside Mg-MOF-74. Thus, the former stayed closely to the open

metal sites, which in turn lead the latter to move more freely. In general, the presence of water had a slowing down effect on the CO_2 molecules and CO_2 an accelerating effect on water at the same time. The results indicate that, because of these consequences of the segregation, diffusion models, such as Stefan-Maxwell, are not able to predict diffusivities for this system of CO_2 and H_2O in Mg-MOF-74 successfully.

4.4 Supporting information

4.4.1 Referred figures and tables

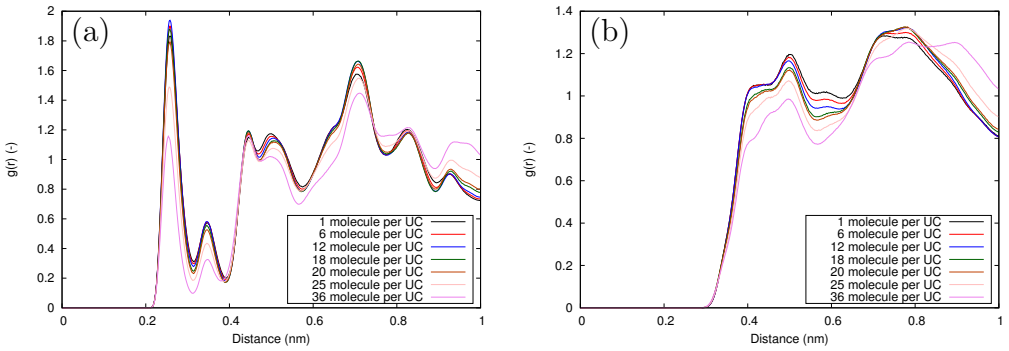

Figure 4.5: Pair distribution function for the carbon of the CO_2 molecule with respect to the Mg-atoms in the rigid (a) and in the flexible (b) framework. The results are based on the DFT-FF as described in the main article. The distance of 1 nm is approximately the mean distance form a Mg-ion to the channel center.

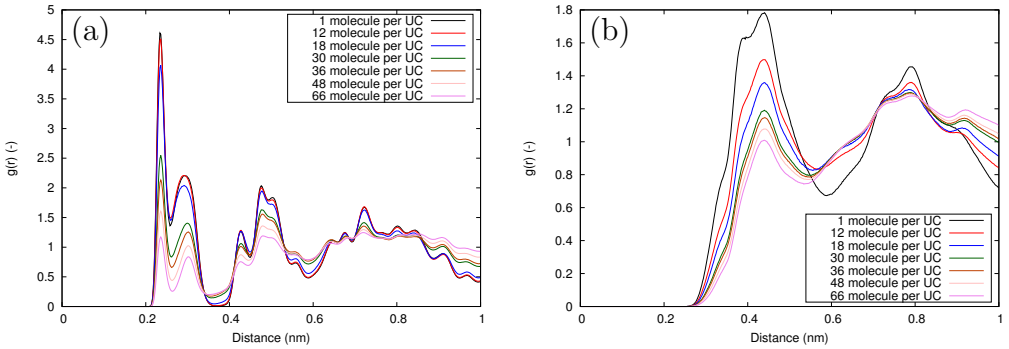

Figure 4.6: Pair distribution function for the oxygen of the water molecule with respect to the Mg-atoms in the rigid (a) and in the flexible (b) framework. The results are based on the DFT-FF as described in the main article. The distance of 1 nm is approximately the mean distance form a Mg-ion to the channel center.

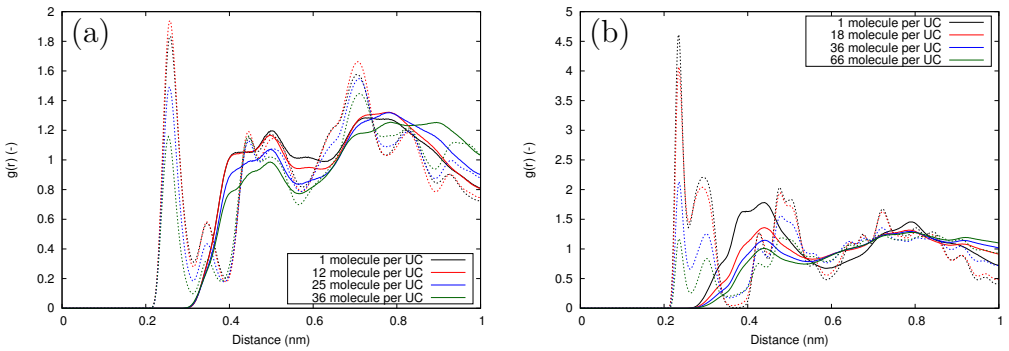

Figure 4.7: Comparison of the pair distribution function for the carbon of the CO_2 molecule (a) and the oxygen of the water molecule (b) with respect to the Mg-atoms in the framework. The dotted lines represent the results for the rigid case and the unbroken lines for the flexible one. The results are based on the DFT-FF as described. The distance of 1 nm is approximately the mean distance form a Mg-ion to the channel center.

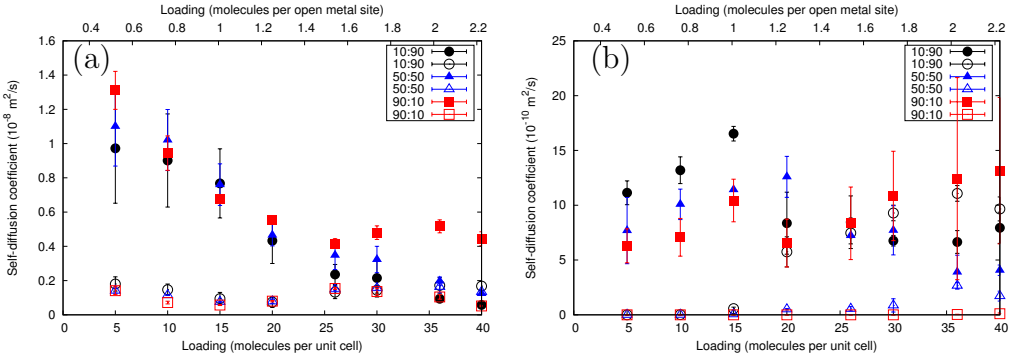

Figure 4.8: Self-diffusion coefficients for CO_2 (a) and H_2O (b) in three CO_2/H_2O-mixtures (90/10 (black dot), 50/50 (blue triangle), and 10/90 (red square)) as a function of total loading based on the DFT-FF in the rigid (open symbol) and in the flexible (closed symbols) framework. The lines represent the pure rigid (full line) and the flexible (dashed line) data, respectively.

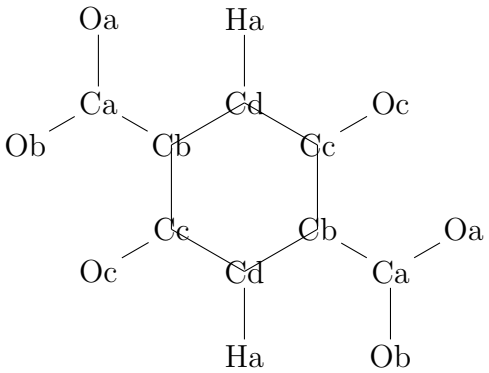

Figure 4.9: Description (schematically) of the atomtypes found in the organic linker of the framework.

4.4.2 Force field parameters

Table 4.1: Atomtypes used in the simulation with their corresponding point charges and Lennard-Jones parameters taken from the UFF,[239] TIP3P(-Ew),[236,252] TIP5P,[237,254] TraPPE,[238] and our previous chapter.[227]

Atomtype	charge (elemental charge)	ϵ ($\frac{kJ}{mol}$)	σ (nm)	ϵ (K)	σ (Å)
Mg	1.558	0.464	0.269	55.857	2.691
Oa	-0.770	0.251	0.312	30.193	3.118
Ob	-0.880				
Oc	-0.907				
Ca	0.903	0.439	0.343	52.838	3.431
Cb	-0.313				
Cc	0.444				
Cd	-0.216				
Ha	0.182	0.184	0.257	22.142	2.571
H_H_2O (TIP3P)	0.417	0.000	0.000	0.000	0.000
O_H_2O (TIP3P)	-0.834	0.637	0.315	76.420	3.151
H_H_2O (TIP5P)	0.241	0.000	0.000	0.000	0.000
O_H_2O (TIP5P)	0.000	0.745	0.310	89.378	3.097
L_H_2O (TIP5P)	-0.241	0.000	0.000	0.000	0.000
O_CO_2	-0.700	0.656	0.305	79.000	3.050
C_CO_2	0.350	0.224	0.280	27.000	2.800

4.4.3 Influence of the simulation length

Next, the influence of the simulation length was investigated. For that, MD simulations with 1, 2, 10, 20, and 36 CO_2 molecules per unit cell at 300 K for 10, 30, 50, and 100 ns were carried out using the rigid framework. The results for the (self-)diffusion coefficients are given in Table 4.7. It can be seen that the self-diffusivity varies with simulation length regardless of the loading of the simulation box. The highest diffusion coefficients are calculated for 10 ns. Based on the MSD data the diffusion regime has not been reached yet resulting in diffusion coefficients and usually high errors. Similarly, the results for 30 ns almost agree with the ones for 50 ns and 100 ns, however, the corresponding errors for the diffusivity is still quite

large, whereas the diffusion regime (slope of the fit = 1) is almost reached. Simulating the systems for 50 ns or longer led to small errors and similar diffusion coefficients. The MSD plots (Figure 4.11, 4.12, and 4.10) show exemplarily for all simulations that the diffusion regime is reached and in a steady state. Thus, we chose the simulation length to be (at least) 50 ns for all of our calculations.

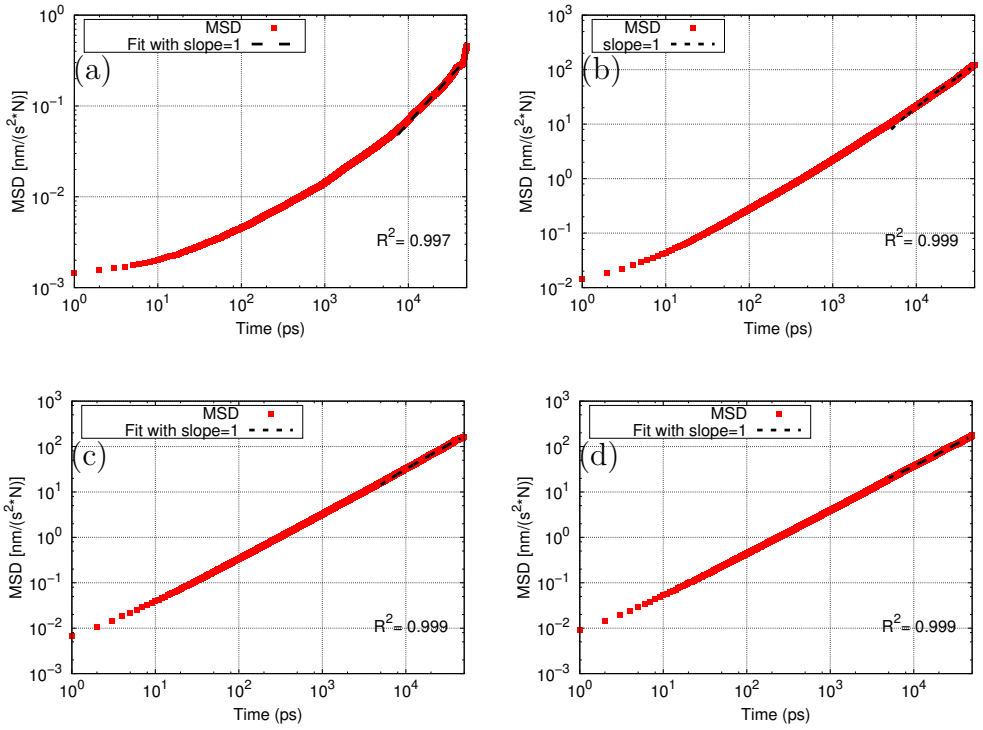

Figure 4.10: Mean-squared displacement (MSD) for H_2O in the rigid (a,c) and flexible (b,d) Mg-MOF-74 as a function of simulation time at 2 (a,b) and 36 (c,d) molecules per unit cell, respectively.

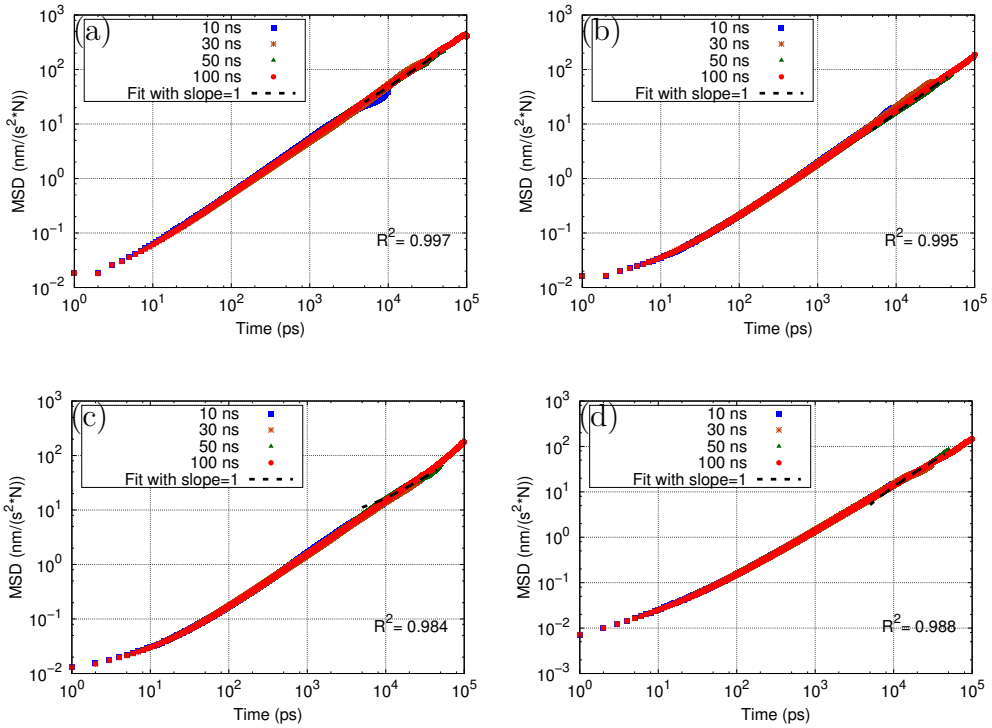

Figure 4.11: Mean-squared displacement (MSD) for CO_2 in the rigid Mg-MOF-74 as a function of simulation time for 10 ns (blue), 30 ns (brown), 50 ns (green), and 100 ns (red) at 1 (a), 10 (b), 20 (c), and 36 molecules per unit cell (d), respectively.

Table 4.2: Crossterm parameters for guest molecules based on the methodology refitted from previous chapter:[227] Mixing parameters are refitted to Lennard-Jones functions.

Guest molecule atomtype	Framework atomtype	ϵ ($\frac{kJ}{mol}$)	σ (nm)	ϵ (K)	σ (Å)
H_H_2O	Mg	0.6605	0.239	79.444	2.390
	Oa	0.2295	0.263	27.605	2.626
	Ob				
	Oc				
	Ca	0.2172	0.273	26.126	2.734
	Cb				
	Cc				
	Cd				
	Ha	0.0001	0.602	0.011	6.018
O_H_2O	Mg	2.1587	0.244	259.630	2.442
	Oa	0.8380	0.315	100.792	3.145
	Ob				
	Oc				
	Ca	0.5169	0.340	62.171	3.401
	Cb				
	Cc				
	Cd				
	Ha	0.0000	1.000	0.000	1.000
O_CO_2	Mg	2.4069	0.234	289.479	2.343
	Oa	0.0378	0.387	4.459	3.874
	Ob				
	Oc				
	Ca	0.7499	0.327	90.190	3.269
	Cb				
	Cc				
	Cd				
	Ha	0.0001	0.100	0.000	1.000
C_CO_2	Mg	0.0001	0.594	0.0013	5.938
	Oa	1.3583	0.281	163.366	2.807
	Ob				
	Oc				
	Ca	0.3655	0.345	43.963	3.451
	Cb				
	Cc				
	Cd				
	Ha	0.0000	1.000	0.000	1.000

Table 4.3: Interaction parameters for framework bonds based on the UFF.[239]

i	j	r_0 (nm)	k_0 ($\frac{kJ}{mol \cdot nm^2}$)	$k_0^{reduced}$ ($\frac{kJ}{mol \cdot nm^2}$)
Mg	Oa	0.2035	135662.5	45220.8
Mg	Ob	0.2035		
Mg	Oc	0.2035		
Oa	Ca	0.1272	594414.3	198138.1
Ob	Ca	0.1272		
Oc	Cc	0.1343	505222.2	168407.4
Ca	Cb	0.1461	325952.2	108650.7
Cb	Cc	0.1379	387408.8	129136.3
Cb	Cd	0.1379		
Cc	Cd	0.1379		
Cd	Ha	0.1081	299306.3	99768.8

Table 4.4: Adsorption energies for CO_2 in Mg-MOF-74 at 300 K.

Force field	Cutoff radius (nm)	Adsorption energy ($\frac{kJ}{mol}$)		
		Monte Carlo	Molecular Dynamics	DFT
Canepa et al.[127]	—	—	—	48.2
Based on Rudenko et al.[227]	2.00	45.3 ± 0.1	—	—
This work (rigid, DFT)	1.28	41.9 ± 0.9	42.0 ± 1.0	—
	1.50	42.8 ± 1.8	—	—
UFF	1.28	31.1 ± 0.2	31.9 ± 0.5	—
This work (flexible, DFT)	1.28	—	42.1 ± 1.3	—

Table 4.5: Interaction parameters for framework angles based on the UFF.[239]

i	j	k	k_θ ($\frac{kJ}{mol \cdot rad^2}$)	$k_\theta^{reduced}$ ($\frac{kJ}{mol \cdot rad^2}$)	θ_0 (deg)
Oa	Mg	Oa	8924.67	2974.89	109.47
Oa	Mg	Ob			
Oa	Mg	Oc			
Ob	Mg	Oc			
Oc	Mg	Oc			
Mg	Oa	Mg	1881.19	627.06	120
Mg	Oa	Ca	3501.58	1167.19	
Mg	Ob	Ca			
Mg	Oc	Mg	1881.19	627.06	
Mg	Oc	Cc	3334.18	1111.39	
Oa	Ca	Ob	12761.60	4253.87	
Oa	Ca	Cb	8501.23	2833.74	
Ob	Ca	Cb			
Ca	Cb	Cc	6327.47	2109.16	
Ca	Cb	Cd			
Cc	Cb	Cc	6914.26	2304.75	
Oc	Cc	Cb	8655.69	2885.23	
Oc	Cc	Cd			
Cb	Cc	Cd	6914.26	2304.75	
Cb	Cd	Cc			
Cb	Cd	Ha	3559.03	1186.34	
Cc	Cd	Ha			

Table 4.6: Interaction parameters for framework dihedrals based on the UFF.[239]

i	j	k	l	k_ϕ ($\frac{kJ}{mol}$)	$k_\phi^{reduced}$ ($\frac{kJ}{mol}$)	ϕ (deg)	m (-)
Oa	Mg	Oa	Mg	0.00	0.00	180	2
Oa	Mg	Oa	Ca				
Ob	Mg	Oa	Mg				
Ob	Mg	Oa	Ca				
Oc	Mg	Oa	Mg				
Oc	Mg	Oa	Ca				
Oa	Mg	Ob	Ca				
Oc	Mg	Ob	Ca				
Oa	Mg	Oc	Mg				
Oa	Mg	Oc	Cc				
Ob	Mg	Oc	Mg				
Ob	Mg	Oc	Cc				
Oc	Mg	Oc	Mg				
Oc	Mg	Oc	Cc				
Mg	Oa	Ca	Ob	94.05	31.35		
Mg	Oa	Ca	Cb				
Mg	Ob	Ca	Oa	10.45	3.48		
Mg	Ob	Ca	Cb				
Mg	Oc	Cc	Cb	94.05	31.35		
Mg	Oc	Cc	Cd				
Oa	Ca	Cb	Cc	10.45	3.48		
Oa	Ca	Cb	Cd				
Ob	Ca	Cb	Cc				
Ob	Ca	Cb	Cd				
Ca	Cb	Cc	Oc	52.25	17.42		
Ca	Cb	Cc	Cd				
Cd	Cb	Cc	Oc				
Cd	Cb	Cc	Cd				
Ca	Cb	Cd	Cc				
Ca	Cb	Cd	Ha				
Cc	Cb	Cd	Cc				
Cc	Cb	Cd	Ha				
Oc	Cc	Cd	Cb				
Oc	Cc	Cd	Ha				
Cb	Cc	Cd	Cb				
Cb	Cc	Cd	Ha				

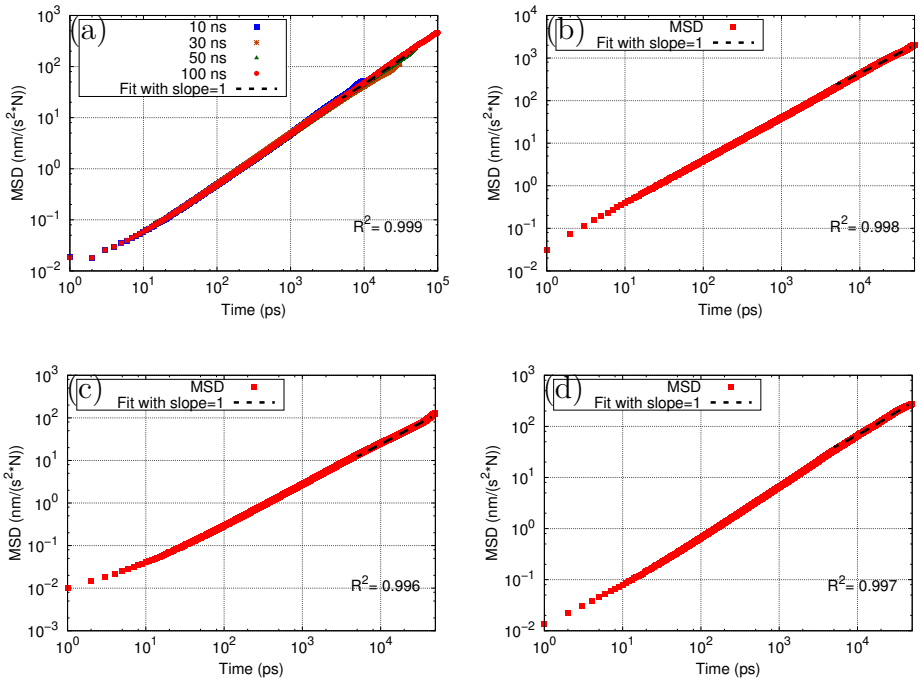

Figure 4.12: Mean-squared displacement (MSD) for CO_2 in the rigid (a,c) and flexible (b,d) Mg-MOF-74 as a function of simulation time at 2 (a,b) and 36 (c,d) molecules per unit cell, respectively.

Table 4.7: Diffusion coefficients for CO_2 based on simulation length based on the force field used in this work.

Molecules per unit cell	Self-diffusivity in 10^{-8} ($\frac{m^2}{s}$)			
	10 ns	30 ns	50 ns	100 ns
1	0.2616 ± 0.0616	0.2504 ± 0.0606	0.2239 ± 0.0205	0.2311 ± 0.0240
2	0.2658 ± 0.0455	0.1844 ± 0.0103	0.2155 ± 0.0063	0.2149 ± 0.0133
10	0.1084 ± 0.0317	0.1040 ± 0.0240	0.0817 ± 0.0050	0.0829 ± 0.0091
20	0.0693 ± 0.0150	0.0646 ± 0.0038	0.0850 ± 0.0113	0.0862 ± 0.0165
36	0.0750 ± 0.0075	0.0638 ± 0.0161	0.0788 ± 0.0163	0.0722 ± 0.0017

Table 4.8: Adsorption energies for H_2O in Mg-MOF-74 at 300 K.

Force field	Cutoff radius (nm)	Adsorption energy ($\frac{kJ}{mol}$)		
		Monte Carlo	Molecular Dynamics	DFT
Canepa et al.[127]	—	—	—	73.3
Rudenko et al.[227]	2.00	70.9 ± 0.1	—	—
This work (rigid, DFT)	1.28	68.3 ± 0.2	71.2 ± 1.1	—
	1.50	68.5 ± 0.4	—	—
UFF[227]	1.28	51.3 ± 3.2	46.3 ± 0.6	—
This work (flexible, DFT)	1.28	—	68.7 ± 1.1	—

Part III

Olefin/paraffin-separation

5

Olefin/paraffin-separation using ZIF-8, ZIF-9, and ZIF-71: A combined experimental and theoretical investigation

Three nanoporous materials, ZIF-8, ZIF-9 and ZIF-71, are evaluated by experiments and molecular simulations regarding their potential towards olefin/paraffin separation. Pure component adsorption isotherms are measured and compared to grand canonical Monte Carlo (GCMC) simulations. Experiments show that the paraffin is favorably adsorbed in all three structures. While the isotherms are predicted well by simulations for ZIF-8 and ZIF-71, in case of ZIF-9 only the saturation loading could be computed accurately because the crystal seems to undergo a so-called gate opening effect upon adsorption of guest molecules. All structures show promising results with respect to olefin/paraffin-separation.

5.1 Introduction

One of the most difficult separation problems to date is olefin/paraffin separation, for example steam cracker effluents, because the molecular shape and properties of the involved molecules are quite similar. Moreover, thermodynamic properties such as saturation pressure and boiling point are comparable. Currently, this separation is carried out by cryogenic distillation because of the low boiling temperatures of the involved compounds. Despite the relatively high selectivity and yield of the low temperature distillation process, its energy consumption is very high. Thus, alternative processes are desired that reduce the costs without losing the effectiveness of the separation. One possible solution is the adaptation of adsorption or membrane processes. Providing that a suitable adsorbent or membrane material is developed, this technique does not require costly solvent recovery, low temperatures or high pressures.[275–277]

Compared with other MOFs, zeolitic imidazolate frameworks (ZIFs) exhibit high thermal and chemical stability, which is a prerequisite for an adsorbent to be used in industry.[131] ZIFs are also considered to be flexible, allowing molecules with larger critical diameter than the pore window to diffuse into their pores.[137,138] For example, it was found that methane molecules (kinetic diameter: 0.38 $\mathring{A}$) are able to diffuse through the pore windows (size: 0.34 $\mathring{A}$) of ZIF-8.[278,279] Even bigger molecules such as ethane and ethene have been found to be adsorbed within the structure.[280] Similar observations have been made for various other ZIF structures.[278,281–285]

Several studies were conducted to investigate the framework flexibility of the fourfold coordinated ZIF structures, and different mechanisms were reported: One effect is referred to as "gate-opening effect", which describes opening up of the previously closed pockets to guest molecules. In principle, this does not change the total volume of the unit cell but it increases the accessible pore volume because initially closed pores are then open towards the guest molecules. The trigger can be either temperature or pressure.[135,266,279] The second effect is called "breathing effect", which describes an enlargement of the crystal structure because of its recoordination, resulting in higher total and (accessible) pore volume. This phenomenon has been reported first for MIL-53[286] and is also found in ZIFs. For example, Wharmby et al.[287] used density functional theory (DFT) to investigate the triggers and implications of this transition in ZIF-4. Deformation of the crystal structure was reported by Gücüyener et al.[288] for ZIF-7.

MOFs in general show good promise for separating olefin - paraffin mixtures. MOFs containing unsaturated metal sites, for example HKUST-1 and

Mg-MOF-74, have a high adsorption selectivity towards olefins.[45,53,72,207,289–294] One of the first experimental studies involving the use of ZIFs for separating olefins and paraffins was conducted by Li et al.[295] in 2009. In their work, the effect of the organic linker with respect to the kinetic separation of propane and propene was described showing that ZIF-8 is a promising structure. Böhme et al.[45,296] reported breakthrough curves for C_2 and C_3 mixtures and the respective pure component adsorption isotherms for ZIF-8, highlighting the fact that the olefin breaks through first followed by the paraffin. In another study, Chmelik et al.[81] reported that the diffusivity is significantly higher for ethene compared with ethane in ZIF-8, which could be exploited for separation as well. Several groups studied ZIF-8 membranes and their effectiveness for propane/propane separation. They reported intriguing results such as high selectivity and permeability towards the olefin.[296–299] Isotherms for ethane and ethene were determined by Chen et al.[300] and van den Bergh et al.[288,301] for ZIF-7. Recently, Hartmann et al.[302] reported isotherms and breakthrough curves for C_2 and C_3 olefin/paraffin mixtures in ZIF-4. Japip et al.[303] investigated mixed-matrix membranes based on ZIF-71 with respect to their ethene/ethane and propene/propane separation capabilities, reporting favorable selectivities towards the olefins.

With respect to olefin/paraffin separation, various studies investigating different classes of MOFs by theoretical approaches have been reported. Altintas and Keskin[304] screened more than 250 different MOFs for their potential to separate C_2H_6/C_2H_4 and C_2H_6/CH_4 mixtures based on the DREIDING[240] force field. This recently published study highlights the capabilities of these materials in addition to identifying multiple very promising crystal structures that can be used to address the respective separation problems. Kim et al.[305] screened more than 30,000 theoretical and experimentally known zeolite topologies including ZIFs regarding C_2H_6/C_2H_4 separation using the universal force field (UFF).[239] They were able to identify the most promising structures and binding sites to achieve the separation effectively.

The majority of studies, however, focus on single crystals of open metal site containing MOFs, such as Mg-MOF-74 and HKUST-1. For example, Bao et al.[207] and Krishna et al.[306] calculated pure component adsorption isotherms for C_2 and C_3 olefins and paraffins in Mg-MOF-74. Theoretical investigations for HKUST-1 were carried out by Jorge et al.,[307,308] Lamia et al.,[291] and Krishna et al.[306] It was shown by all groups that for both structures the agreement with experiments for the paraffins is quite good, whereas the olefin isotherms were not described accurately. By means of DFT calculations it was shown by Jorge et al.[307,308] that the π-bond interaction with the open metal site was not described accurately by the classical force

fields, effectively causing the observed discrepancy between experiments and simulations.

For ZIFs this particular separation has not been investigated extensively by simulation. In a study combining IR microscopy detection and molecular dynamic simulations Bux et al.[73] explained the performance of a ZIF-8 membrane. It was found that the ethane selectivity of the membrane is reduced because of the preferential diffusion selectivity towards ethane. Wang et al.[309] studied ternary mixtures of methane, ethane, and propane in ZIF-8 and ZIF-10 by grand canonical Monte–Carlo (GCMC) simulations. It was shown that propane was favorably adsorbed over the investigated pressure range. Adsorption isotherms for ethane and ethene in ZIF-3, ZIF-6, ZIF-8, and ZIF-10 were determined by Wu et al.[310] using GCMC as well. Furthermore, residence probability plots were calculated showing the preferential adsorption sites within the respective crystal. Chen et al.[300] investigated ethane/ethene breakthrough curves in ZIF-7 both experimentally and by simulation. In addition to breakthrough experiments, van den Bergh et al.[301] carried out DFT calculations to shed some light on the separation mechanism occurring in ZIF-7. They concluded that the anomalous alkane selectivity is due to the energetic differences of the respective formed adsorption complexes at the external surface of the pore window.[301]

Clearly, the accuracy of predictions made by molecular simulations is based on how good a force field is able to describe the interaction between the guest molecules and the framework atoms.[159] The most used and widely accepted force fields for various systems are AMBER,[311] CHARMM,[312] DREIDING,[240] and UFF[239] despite the limitations they might have for the adsorption of guest molecules in MOFs.[313] Various studies show that the main problem of classical force fields is the inaccurate description of unsaturated or open metal sites.[125,126,227,307,314–317] DFT or higher levels of quantum theories are used to fit a force field to the potential energy surface, which leads to high accuracy but low transferability. The review by Fang et al.[318] summarizes the recent developments in first-principles force fields for molecules in nanoporous materials. Addicoat et al.[313] extended UFF for transition metals, which had not yet been included in the original force field. For ZIFs, two approaches are used by the scientific community: the adjustment of parameters provided by DREIDING,[240] UFF,[239] and so forth to fit experimental data, or the derivation of a force field from ab initio calculations. Based on DFT calculations, for example, McDaniel et al.[317] designed force fields to specifically reproduce CO_2 isotherms in ZIF-8 and ZIF-71, and Zheng et al.[266] proposed a force field for ethane and propane adsorption in ZIF-8. The development of force fields that incorporate the flexibility of the frameworks

can be very difficult. Furthermore, molecular simulations become more computationally expensive, because all inter- and intramolecular interactions of the framework atoms have to be calculated, which clearly is not the case for a rigid structure, thus effectively extending the calculation time. However, some groups have proposed the use of flexible force fields. For example, Hertag et al.[319] combined and adjusted the AMBER[311] and DREIDING[240] force fields to investigate the influence of structure flexibility on CH_4 diffusion in ZIF-8. Similarly, Perez Pellitero et al.[320] and Fairen-Jimenez et al.[321] adjusted UFF parameters to improve the accuracy of adsorption isotherms for small guest molecules such as CH_4 and CO_2, in ZIF-8. Zhang et al.[135] proposed a new force field and a hybrid MC/MD method for N_2 adsorption in ZIF-8, which successfully described the gate-opening effect present at 77 K.

To date, adsorption isotherms with respect to ethane, ethene, propane, and propane, were hardly, if ever, investigated for ZIF-9 (see Figure 5.1 (b)) and ZIF-71 (see Figure 5.1 (a)) either experimentally or by molecular simulations. In this work, we report pure component adsorption isotherms and breakthrough curves for the aforementioned hydrocarbons in ZIF-9 and ZIF-71. Grand canonical Monte-Carlo simulations were employed for ZIF-8, ZIF-9, and ZIF-71 for the same compounds. The resulting isotherms are compared to the experimental data. Monte-Carlo simulations in the NVT-ensemble were carried out to compute residence probabilities for the species within the structures.

5.2 Experimental and simulation methods

5.2.1 Synthesis and characterization

As a disclaimer, the experimental part of this chapter was executed by the group of Prof. M. Hartmann's group of the Erlangen Catalysis Resource Center (Germany).

ZIF-71

For the synthesis of ZIF-71, the procedure reported by Lively et al.[322] was used. Zinc acetate dihydrate (0.439 g, $2.0{\cdot}10^{-3}$ mol) and 4,5-dichloroimidazole (1.096 g, $8.0{\cdot}10^{-3}$ mol) were each dissolved in methanol (75 mL) and then mixed in a 250 mL round-bottom flask at room temperature. After 24 h reaction, the solid material was first filtered off and washed with ethanol (3x35 mL). Subsequently, the solid material was dried at 80°C under vacuum.

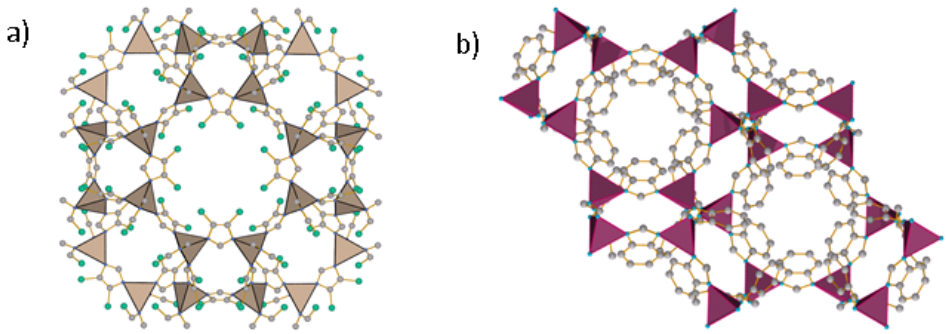

Figure 5.1: Schematic view of the crystal structure of ZIF-71 (a) and ZIF-9 (b). For clarity, hydrogen atoms and guest molecules are not displayed. The tetrahedra represent the connected metal centers with the nitrogen atoms of the linker molecules.

ZIF-9

The material ZIF-9 was synthesized by following the procedure described by Park et al.[131] with a few modifications developed in our laboratory. Cobalt nitrate hexahydrate (2.1 g, $7.22 \cdot 10^{-3}$ mol) and benzimidazole (0.6 g, $5.08 \cdot 10^{-3}$ mol) were first filled into a 250 mL round-bottom flask and then dissolved in dimethylformamide (DMF) (180 mL). The solution was mixed with a rate of 100 rpm and heated to a constant temperature of 130°C by using a reflux condenser for 48 h. After cooling to room temperature, the solid material was filtered, centrifuged, and dried as described for ZIF-71.

Characterization

The structure and porosity of the adsorbents were determined by powder X-ray diffraction with a PANalytical X'Pert diffractometer [Cu-K_α (λ = 1.54 $\AA$)] and nitrogen adsorption measurements at 77 K, respectively (Micromeritics ASAP 2010).

5.2.2 Adsorption measurements

The pure component adsorption isotherms of ethane, ethene, propane, and propene on ZIF-71 and ZIF-9 were measured at 20°C with a modified Micromeritics ASAP 2010 instrument. Prior to the volumetric adsorption measurements, ZIF-71 and ZIF-9 were outgassed under vacuum (10^{-3} hPa) at 110°C for 24 h and at 180°C for 1 h, respectively.

5.2.3 Simulation details

Adsorption isotherms of the C_2 and C_3 olefins and paraffins at 293 K and pressures ranging from 0.01 to 1 bar were calculated by using grand canonical Monte-Carlo (GCMC) simulations employing an inhouse code. The chemical potential was connected to the pressure by the Peng-Robinson equation of state. The probability distribution for the allowed MC steps "swap", "translation", "rotation", and "regrow" was 50%, 12.5%, 12.5%, and 25%, respectively. The simulations consist of 1 x 10^5 initialization and 5 x 10^5 production steps, in which the system was first equilibrated and then sampled. The obtained absolute loading nabs needed to be converted into the excess loading n_{exc} as described by Myers and Monson[78,323] so that the simulation results could be compared to experimental data. Each pressure point was sampled twice; the results reported represent the average.

Residence probability plots and isosteric heats of adsorption at zero loading (q^0_{st}) were calculated from results generated by Monte-Carlo simulations in the NVT-ensemble at 293 K. The following moves were allowed: "translation", "rotation", and "regrow" with a probability of 20, 10, and 70%, respectively. As shown by Smit and Siepmann,[255] q^0_{st} is calculated based on the ensemble average of the total energy of the system $\langle U_{tot} \rangle$.

The atoms of the crystal structures were fixed at their respective crystallographic positions for the simulations. Vlugt and Schenk[251] showed for zeolites that rigidity introduces only a small error compared with flexible structures. The cutoff radius was set to 15 $\mathring{A}$.[320,324] Periodic boundary conditions were applied in every direction and Lorentz–Berthelot mixing rules were employed. The number of unit cells was chosen in a way that the simulation box was at least twice the length of the cutoff radius in each dimension to avoid system sized induced errors. Since the solutes were modelled chargeless, electrostatic interactions were neglected. To reduce the calculation time on the cluster, energy grids with a spacing of 0.1 $\mathring{A}$ were created before the calculation of isotherms.[159]

The Lennard–Jones parameters for the ZIF structures were taken from Rappe et al.[239] and the work of Perez-Pellitero et al.,[320] who modified the universal force field (UFF). Their force field successfully reproduced experimental data for CO_2 and CH_4 in ZIF-8 at ambient temperatures.[320,324] The solutes were modelled flexible based on the TraPPE description.[175,325] The bond vibration and bond-angle parameters were taken from Dubbeldam et al.[326] and Liu et al.;[327] cross-terms for the solute interaction were taken from Dubbeldam et al.[326] and Jakobtorweihen et al.[187] A summary of the parameters is given in Chapter 5.5.

5.3 Results

5.3.1 Material characterization

ZIF-71

The X-ray powder patterns of ZIF-71 and ZIF-9 are shown in Figure 5.11. For both materials, the "as synthesized" as well as the activated form is compared to the simulated data.[322] According to the XRD data, ZIF-71 appears to be a pure crystalline phase without impurities. Additionally, there is no change of the XRD pattern after activation of the material. The nitrogen adsorption on ZIF-71 shows a Langmuir-type behavior with a saturation plateau at 270 $\frac{cm^3}{g}$ as shown in Figure 5.12. The BET surface area was calculated to be 1015 $\frac{m^2}{g}$ and specific pore volume is 0.42 $\frac{cm^3}{g}$ for a relative pressure $\frac{p}{p_0} = 0.99$.

ZIF-9

The powder X-ray pattern of ZIF-9 (Figure 5.11) agrees very well with the simulated data.[131] However, the peak intensity of the diffraction pattern decreases upon activation of the solid material. Moreover, characteristic reflexes disappear during the activation step, which reappear after adsorption of the solvent N,N- dimethylformamide (DMF). The amount of nitrogen adsorbed is low compared with ZIF-71 and ZIF-8, and has a plateau at 6 $\frac{cm^3}{g}$, see Figure 5.12.

5.3.2 Experimental adsorption isotherms for pure olefins and paraffins

ZIF-71

The adsorption isotherms of ethane, ethene, propane, and propene on ZIF-71 and ZIF-9 are shown in Figure **??**. The desorption data are omitted for clarity, but the isotherms for ZIF-71 are fully reversible. For both adsorbents, the capacity for the C_3 gases is higher than for the C_2 gases. Whereas the C_2 isotherms for ZIF-71 show a Langmuir-type behavior, the shapes of the C_3 isotherms are somewhat unusual. The uptake at 1 bar is 1.4 $\frac{mmol}{g}$ for ethane, 1.1 $\frac{mmol}{g}$ for ethene, 3.28 $\frac{mmol}{g}$ for propane, and 3.52 $\frac{mmol}{g}$ for propene. ZIF-71 shows favorable adsorption of ethane over ethene but finally a higher uptake of propene compared with propane. The experimental data

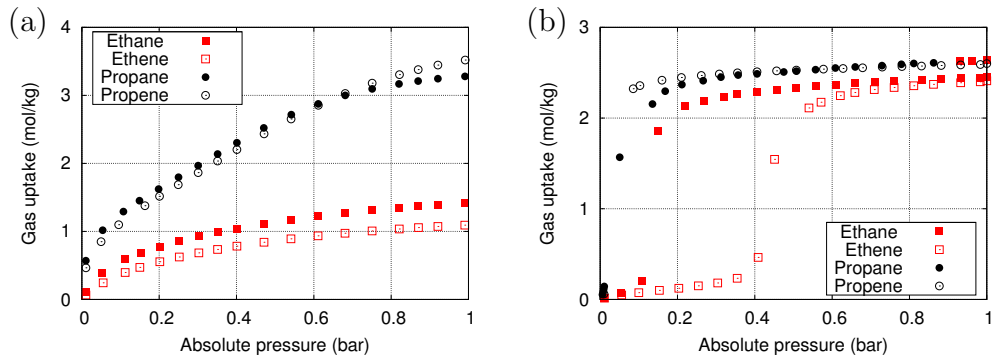

Figure 5.2: Pure component adsorption isotherms of ethane, ethene, propane, and propene on ZIF-71 (a) and ZIF-9 (b) at 293 K.

Table 5.1: Separation factors for ZIF-71 and ZIF-9 compared with ZIF-8 at zero loading.

	ZIF-71	ZIF-9	ZIF-8
$\alpha_{Ethane/Ethene}$ /-	1.91	1.39	2.14
$\alpha_{Ethane/Ethene}$ /-	1.26	1.84	1.37

reported by Japip et al.[303] agree well with the isotherms determined in this work. However, the deviations observed above 0.5 bar are likely the result of different measurement techniques (volumetric vs. gravimetric adsorption). The separation factors (Table 5.1) at zero loading exhibit favorable adsorption of the paraffin over the olefin in all cases, which is advantageous for the intended purification of C_2 and C_3 olefins.

ZIF-9

The shapes of the adsorption isotherms of the hydrocarbon gases on ZIF-9 are similar to the Type V isotherm of the IUPAC classification.[328] For each gas measured, a hysteresis loop is found that occurs at different partial pressure of the adsorptive, which is depicted in Figure 5.3 for the gases ethane and ethene. The sigmoidal shape of the isotherms on ZIF-9 results in saturation plateaus at 2.44 $\frac{mmol}{g}$ for ethane and 2.39 $\frac{mmol}{g}$ for ethene. For pressures below 0.4 bar, ethane almost reaches its saturation plateau, whereas the uptake of ethene remains below 0.5 $\frac{mmol}{g}$. This large difference in uptake might be beneficial for a separation process. For C_3 hydrocarbon gases the

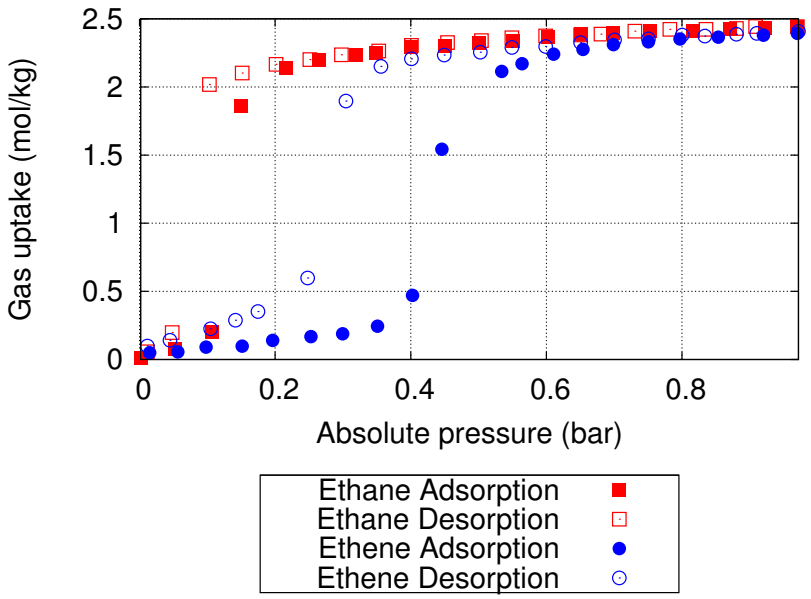

Figure 5.3: Adsorption and desorption isotherms of ethane and ethene on ZIF-9 at 293 K.

saturation loading is 2.63 $\frac{mmol}{g}$ for propane and 2.58 $\frac{mmol}{g}$ for propene. The occurrence of the hysteresis loop for ZIF-9 displayed in Figure 5.3 indicates a structural change of the adsorbent. This effect, often called "gate opening" effect, has been observed for different structures of the group of metal-organic frameworks such as MIL-53[288] and ZIF-7, which is similar to ZIF-9, but is connected by zinc instead of cobalt metal centers. ZIF-7 also exhibits a change in the structure, which is triggered by a certain pressure of an adsorptive. The pressure controls the rotation of the organic linker molecules and therefore the accessibility of the pore structure.[288,301]

The adsorption branch of the hysteresis loop of ethane has a steep increase at a partial pressure of 0.1 bar and the adsorption branch of ethene increases sharply at 0.4 bar. Both desorption branches reach the adsorption branch at a very low partial pressure. Moreover, the adsorption/desorption loop of ethane is much smaller than the loop of ethene, therefore the width decreases with increasing kinetic diameter of the adsorbed molecule.

Whereas the gases ethane, ethene, and propene reach their equilibrium value within minutes, propane adsorption requires a lot of time to reach equilibrium. This effect of mass transfer limitation of propane by the narrow pore structure of ZIF-9 is reduced for adsorption isotherm measurements at higher temperatures.

5.3.3 Simulated adsorption isotherms for pure olefins and paraffins

The force fields applied in this work were the UFF[239] and a modified version obtained by Perez-Pellitero et al.[320] (from here on called "modified-UFF"), which was adjusted in a way that it reproduced the experimental CH_4 and CO_2 isotherms in ZIF-8 accurately.[324] The reproduction of the adsorption isotherm for CH_4, C_2H_6, C_2H_4, C_3H_8, and C_3H_6 in ZIF-8 can be found in the following. After that, ZIF-9 and ZIF-71 are investigated by simulations and compared to the experimental data.

ZIF-8

ZIF-8 is arguably one of the most investigated ZIF crystals by the scientific community. Thus, a variety of experimental data and simulations regarding adsorption of small molecules can be found, including methane, ethane, ethene, propane and propene, making it one of the best choices to test the force fields.

As a first step, the methane isotherms based on the UFF and the modified-UFF were calculated and compared to the results from Perez-Pellitero et al.,[320] who did experiments and also calculated isotherms with grand-canonical Monte Carlo (GCMC) using the UFF and the modified-UFF. The results are shown in Figure 5.4. The agreement between the literature simulation data and from this work is excellent for both force fields. Clearly, the classical UFF overestimates the experimental data while the modified UFF predicts the experimental adsorption isotherm accurately. This is similar to the findings of Perez-Pellitero et al.[320] recently.

The adsorption isotherms regarding ethane and ethene in ZIF-8 at 293 K can be found in Figure 5.5. The results obtained from experiments (Böhme et al.[45] and Bux et al.[73]) are compared with the simulations based on the modified-UFF and the UFF (a,b). The comparisons of the simulations with literature simulation data obtained by Bux et al.,[73] Wu et al.,[310] and Krishna et al.[306] can be found in Figure 5.5(c) and (d). Please note that the temperatures of the literature data differs between 293 K (Böhme et al.[45]), 298 K (Wu et al.[310]), 300 K (Bux et al.[73]) and 301 K (Reyes et al.[285]). In Figure 5.5(a) and (b), one can see that the simulation results for ethane and ethylene based on the modified-UFF agree well with experimental data. The shapes of the isotherms are reproduced accurately over the investigated pressure range. The calculated loading at 1 bar is 2.81 $\frac{mol}{kg}$ for ethane and 1.57 $\frac{mol}{kg}$ for ethylene, respectively, which is slightly lower than the results from

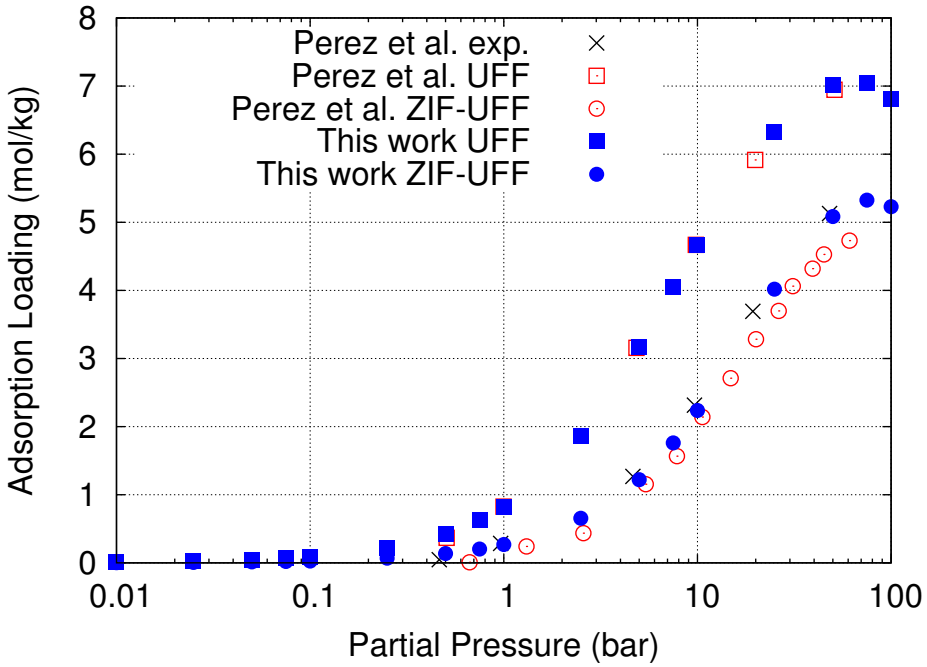

Figure 5.4: GCMC simulation results in mol/kg as a function of pressure for methane from Perez-Pellitero et al.[320] and based on the modified-UFF and the UFF at 293 K.

Bux et al.[73] but higher than the ones from Böhme et al.[45] and Reyes et al.[285] The results based on the UFF are not able to reproduce the shapes of the isotherms correctly. The loading is greatly overestimated resulting in loadings of 5.32 $\frac{mol}{kg}$ and 4.72 $\frac{mol}{kg}$ at 1 bar for ethane and ethylene, respectively, which are more than twofold the corresponding experimental values.

As for the simulations our results coincide well with the results by Bux et al.[73] and Wu et al.[310] for ethane (Figure 5.5 (c)) and ethylene (Figure 5.5 (d)), respectively. The deviations are barely recognizable and can be attributed to the small differences in the applied force fields and the slightly different temperatures. In case of the UFF the same applies as for the experiments, since the predicted loading is way higher than the literature data and the results from the modified-UFF.

The results for propane and propene compared to experimental data are shown in Figure 5.6(a) and (b). The propane isotherms obtained by simulations reproduce both data sets of Böhme et al.[45,296] accurately. In case of propylene the simulations lie on top of Böhme et al.[45,296] second experimental data set. The loadings predicted by GCMC at 1 bar are almost at the

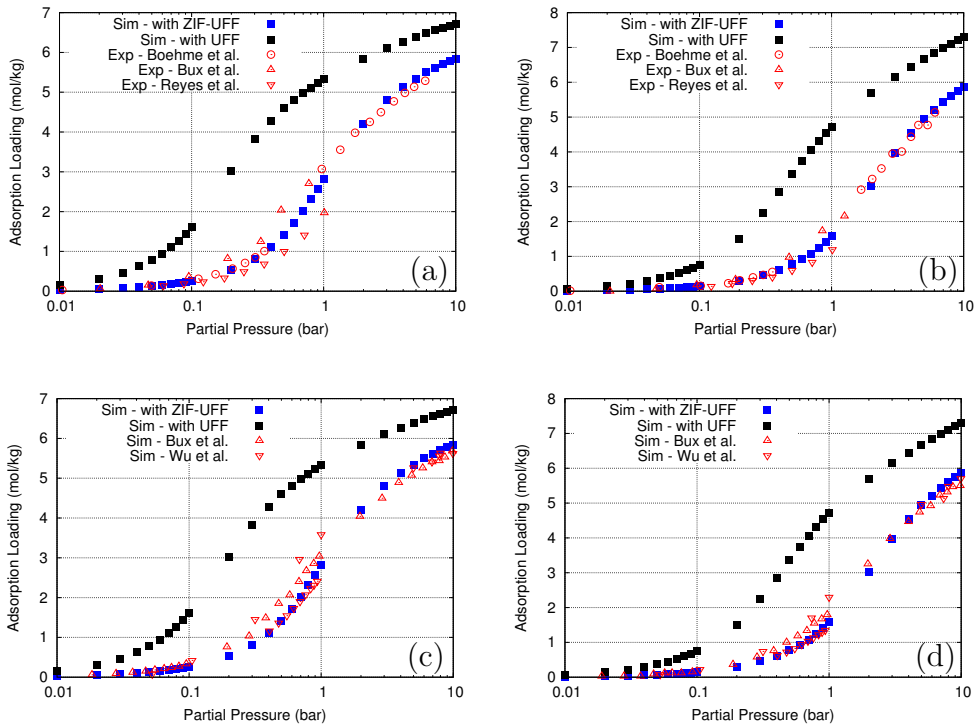

Figure 5.5: Adsorption isotherms for ethane (a,c) and ethene (b,d) at 293 K in ZIF-8 obtained by experiments and simulations based on the modified UFF and the UFF. The results for the C_2 molecules from both force fields are compared to experimental data from Böhme et al.,[45] Bux et al.[73] and Reyes et al.[285] (top row: a and b) and to simulation data from Bux et al.[73] and Wu et al.[310] (bottom row: c and d).

same value of 4.78 $\frac{mol}{kg}$ and 4.80 $\frac{mol}{kg}$ for propane and propylene, respectively, and close to the experiments. The results obtained from UFF are again too high resulting in an incorrect description of the isotherm. The loading at 1 bar is 5.32 $\frac{mol}{kg}$ and 5.57 $\frac{mol}{kg}$ for propane and propylene, respectively, is twice the experimental data.

The comparison between the simulated isotherms to the ones calculated by Krishna et al.[306] shows good agreement between both while the UFF is too high, see Figure 5.6(c) and (d). Thus, a similar trend is here observed as for the C_2 molecules. Again, the deviations are caused by different force fields, but they are pronounced more strongly in this case than for ethane and ethylene. It is likely that the deviation between the experiments and the results predicted by the UFF is caused by an incorrect description of the

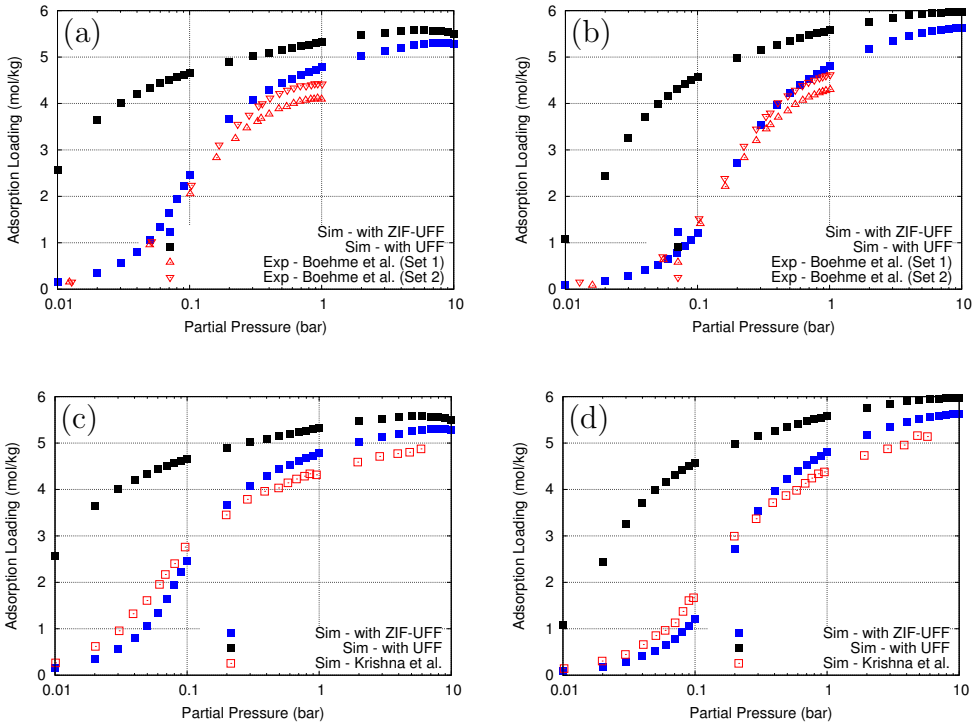

Figure 5.6: Adsorption isotherms for propane (a,c) and propene (b,d) at 293 K in ZIF-8 obtained by experiments and simulations based on the modified UFF and the UFF. The results for the C_3 molecules from both force fields are compared to the experimental data from Böhme et al.[45,296] (a,b) and the simulation results from Krishna et al.[306] (c,d).

framework adsorbate interaction, which seems to be weaker in reality.

ZIF-9

The calculated isotherms for the C_2 and C_3 olefins and paraffins based on two different force fields (UFF and modified-UFF) and two differently accessible crystal structures (one with blocked pores and one fully accessible) in ZIF-9 at 293 K are shown in Figure 5.7 in comparison to the experimental data. Based on the positions of the framework atoms, several pores cannot be accessed by the guest molecules because their kinetic diameters are larger than the respective entrances to the cages. Hence, they are blocked during the simulation, effectively reducing the helium void fraction (accessible pore volume for helium divided by total volume) of the crystal from 0.3167 to 0.1187 for the UFF and from 0.2664 to 0.1056 for the modified-UFF, respec-

tively. Firstly, we computed isotherms based on the blocked structure: The behaviors of the isotherms of ethane (Figure 5.7(a)), ethene (b), propane (c), and propane (d) are quite similar. The simulations overestimate the experimental results in the lower pressure region ($\leq$ 0.1 bar) by almost one order of magnitude. The isotherm calculated applying the UFF is already close to its predicted saturation loading at 0.01 bar for all four gases and does not vary much with pressure, whereas the values calculated using the modified-UFF do not reach saturation until a pressure of 0.5 bar. The experimental isotherms show for each adsorbent a steep increase at 0.1 bar, 0.35 bar, ca. 0.05 bar, and ca. 0.08 bar for ethane, ethene, propane, and propane, respectively. This effect is not observed at all in the simulation results. Due to the step in the experimental isotherms, the results obtained by experiments and simulations differ significantly at higher pressures. In fact, the experimental value at 1 bar is between 2.3 and 2.5 times higher than the simulated value (see Table 5.2). In general, (small) deviations between simulation and experiment, as seen for all compounds in Figure 5.7, can be explained by differences between the assumed perfect crystal structure in the simulations and the real sample. It may be that not all pores are accessible for adsorbent molecules, which results in higher loadings in the simulations. With this constraint in mind, the results indicate that something happened with the framework during adsorption. For example, certain pores of the pore system might not be accessible for the gas molecules, because the kinetic diameter of the molecule is larger than the diameter of the pore window in the rigid structure. Thus, these pores are blocked so that molecules cannot be inserted in them during the simulations. After the results for the partially accessible crystal structure, we made the complete crystal pore volume accessible. The resulting isotherms do not exhibit the step observed in the experiment and saturation is reached at low pressures. However, for the investigated pressure range, the loading is approximately tripled compared with the partially accessible structure. As a result, the saturation loading is predicted successfully by both force fields and only overestimated by roughly 10–20% (Table 5.2), which can be explained by the assumed perfect crystal structure in the simulations. The isotherms below 0.8 bar, on the other hand, are dramatically overpredicted.

The reasons for the force fields failing to reproduce the isotherms correctly at low pressures can have two origins: An inaccurate description of the framework–guest interactions by the force field and/or entropic effects (e.g. flexibility). To rule out the former we performed DFT calculations to determine adsorption energies at infinite dilution (zero loading) exemplarily for ethane and compared them to the results obtained by GCMC (see Ta-

ble 5.7). Two important findings have to be mentioned: Firstly, considering the GCMC data, there is no difference between the blocked and unblocked structure. Thus, the main/first adsorption site is the same (see Figure 5.18). Secondly, the difference between the result obtained by DFT compared with the UFF is marginal ($|2\frac{kJ}{mol}|$) and to the mod.-UFF slightly larger ($|9\frac{kJ}{mol}|$). Consequently, the interactions are described accurately (UFF) and decently (mod. UFF), thus, the deviation in the predictions of the isotherms are tentatively ascribed to an entropic effect, which is indicated by the steps observed in the experimental isotherms. These steps are caused by a "gate-opening" effect, a "breathing" effect or a combination of the two. It is well established that ZIFs are flexible[137,138] and, presumably, this causes the observed discrepancy between experiment and simulation. Due to the structural similarity between ZIF-7 and ZIF-9, conclusions drawn for ZIF-7 likely apply to ZIF-9 as well. Gücüyener et al.[288] reported similar behavior for the C_2 and C_3 adsorption isotherms in ZIF-7 to ours in ZIF-9. They concluded that a change in the conformation and/or a re-coordination of the organic linkers was taking place due to adsorbate–framework interaction, resulting in the so- called "gate opening" effect.[286,301] If structures are not flexible, then the simulations should predict higher loadings due to the perfect framework structure used in the simulations. In other words, one can say that the simulations represent the upper limit of what a structure can adsorb of a certain guest species when flexibility is not taken into account. This is the case for ZIF-9, when the crystal is fully accessible and the experimental data are slightly lower than the results from simulations. This means that the accessible pore volume is correctly described by the force fields. That all leads to the assumption that ZIF-9 exhibits "gate opening" at a certain pressure instead of a breathing effect. Clearly, effects caused by the flexibility of the structure cannot be observed in simulations with rigid structures, which lead to the failure of the force field in this particular scenario. The solution to this problem is to include the flexibility of the framework into the simulation. This can be modelled by using standard force fields or deriving one using quantum mechanical calculations. The GCMC is then expanded by MD steps to relax the structure.[135,266]

The residence probability plots allow the main adsorption sites of the framework in the limit of zero loading to be located. Due to the similar outcome for the four gases, the result for ethane in both the blocked and fully accessible crystal structure is shown as an example in Figure 5.8. The plot shows a cut in the transverse plane of the channel in the x–y–direction (front view), whereas the volume is oriented longitudinally into the z direction. Red indicates the highest, whereas blue indicates the lowest and white indicates

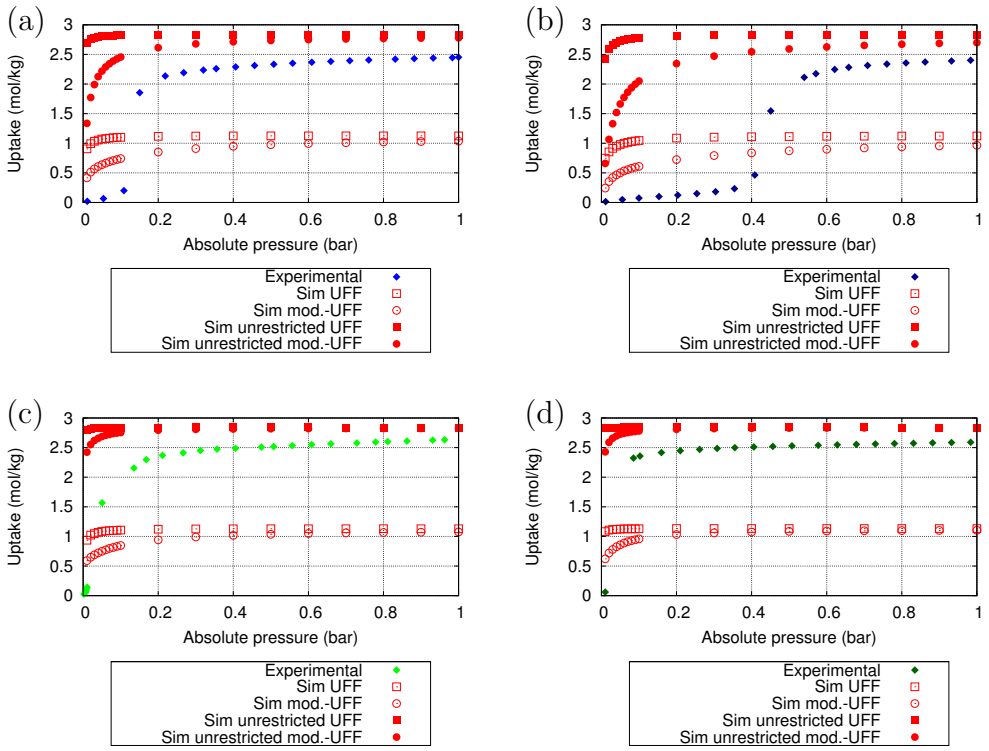

Figure 5.7: Adsorption isotherms for ethane (a), ethene (b), propane (c), and propene (d) at 293 K in ZIF-9 obtained by experiments and simulations based on the modified UFF and the UFF. Closed symbols represent crystal structure with blocked pores, whereas open symbols represent fully accessible crystal structure. The error bars for the results obtained from simulation are smaller than the symbols and are thus omitted.

Table 5.2: Uptake in $\frac{mol}{kg}$ at 1 bar for ethane, ethene, propane, and propene obtained from experiments and simulations based on the modified-UFF and UFF at 293 K in ZIF-9 and ZIF-71, respectively.

	ZIF-9			ZIF-71		
	Experiment	Simulation mod.-UFF	Simulation UFF	Experiment	Simulation mod.-UFF	Simulation UFF
Ethane	2.453	1.036 2.780	1.124 2.831	1.417	0.880	1.739
Ethene	2.411	0.965 2.698	1.122 2.832	1.092	0.621	1.428
Propane	2.642	1.076 2.823	1.130 2.838	3.279	2.060	3.595
Propene	2.601	1.104 2.834	1.132 2.837	3.520	1.605	3.374

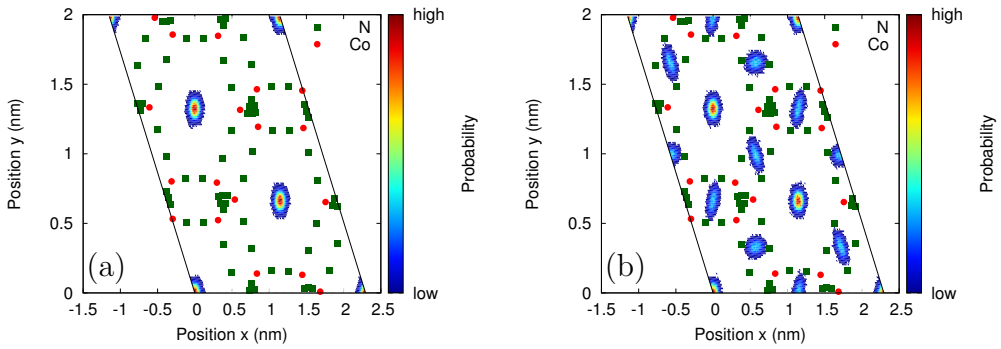

Figure 5.8: Residence probability for the center of mass of an ethane molecule in ZIF-9 with blocked (a) and fully accessible pores (b) at 293 K and infinite dilution. The highest probability is indicated in red, the lowest in blue and (exactly) zero in white.

(exactly) zero probability of finding the center of mass of an ethane molecule within the framework. In Figure 5.8 (a) the topology of the structure is depicted, which consists of one-dimensional small channels intersected by cages.[106] The residence plots for ZIF-9 reveal that the molecules are mainly found inside the cages and are rarely located in the small channels between them.

Ethane is most likely found in the center of the cages. This is expected to be the case below the gate-opening pressure. Above this threshold, it appears that the full crystal structure is accessible. In Figure 6.5 (b) the residence probability for this case is shown. In addition to the main channel structure, intersections with small cages inhabit molecules as well. In conclusion, the force fields are not able to predict the isotherms correctly due to effects induced by the framework flexibility of the structure which is modelled rigid in the simulations. By using the fully accessible crystal structure, the saturation loading can be predicted accurately by both force fields. Despite the inaccuracy of the force fields at low pressure, the position of the residence probability plots are believed to be correct. Mainly, the guest molecules are expected to be in the cages of the one-dimensional channels or the intersecting cages once the framework opens up.

ZIF-71

The experimental and simulation results for ZIF-71 reported by Japip et al.[303] and in this work show a different picture. In Figure 5.9 the results

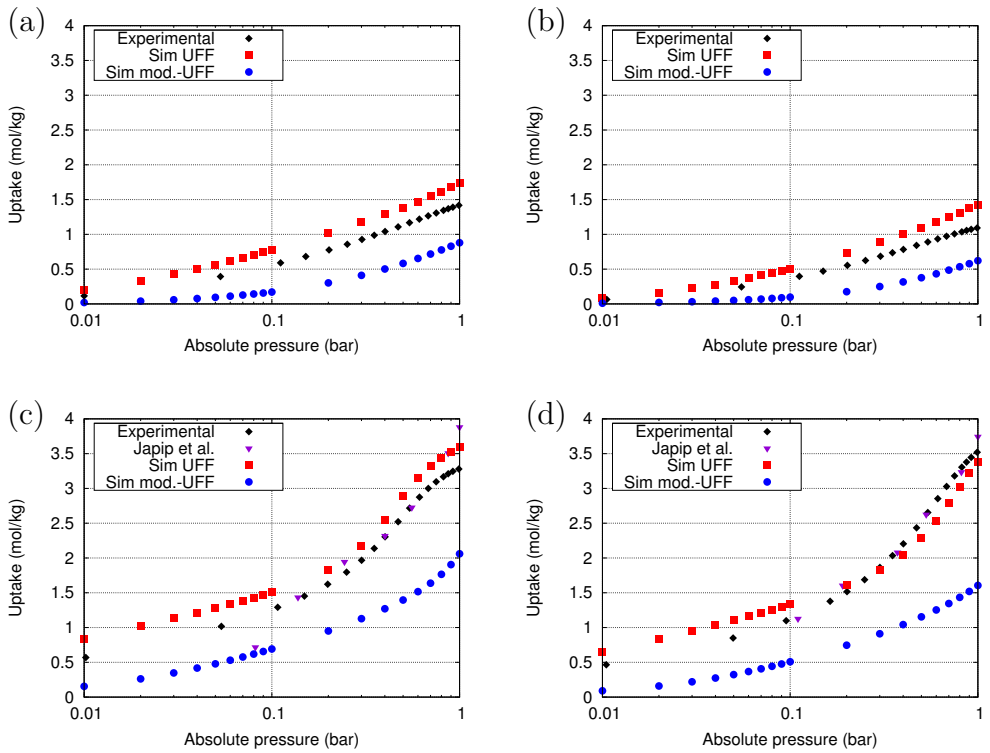

Figure 5.9: Adsorption isotherms for ethane (a), ethene (b), propane (c), and propene (d) at 293 K in ZIF-71 obtained by experiments by Japip et al. and in this work. Simulations are based on the modified UFF and the UFF. For the simulations, the error bars are smaller than the symbol and thus are omitted.

for ethane (a), ethane (b), propane (c), and propene (d) at 293 K obtained from experiments and simulations based on the modified-UFF and UFF are presented. For the investigated pressure range and all four guest molecules, the shapes of the adsorption isotherms obtained from simulations match the experimental data, and the experimental data agree well with one another. They increase monotonically with pressure and do not reach saturation at 1 bar in all cases.

However, saturation for propane seems to be imminent. Although the shapes of the isotherms are reproduced accurately for the four compounds, the calculated uptake based on the modified-UFF are only half the values obtained in the experiments. For example, at 1 bar, the loadings obtained by simulation are only 62, 57, 63, and 46% of the experimental values for ethane, ethene, propane, and propane, respectively (Table 5.2). The reason

for this poor agreement could be that the interaction between the framework and the guest molecules is stronger in reality than it is modelled with the modified-UFF. This contradicts the results obtained for ZIF-8 for which the loading was predicted accurately. It seems that the topology, which is more complex in the case of ZIF-71 compared with ZIF-8, results in this large deviation. In comparison, the UFF predicts slightly higher loading than the experiments in case of ethane and ethane (see Table 5.2). The deviation between experiments and the UFF is higher for the C_2 gases than for C_3. In case of propane and propene, the experimental values are higher than the simulation results at pressures above 0.3 bar. The slightly higher loading from the simulations is generally ascribed to the assumed perfect crystal structure in the simulation, which cannot be obtained experimentally.

The reason for the smaller differences between experiments and the UFF for propane and propene (Figure 5.9, (c) and (d)) may indicate that the larger C_3 molecules trigger a crystal expansion when adsorbed, resulting in slightly higher loading. This would explain the crossing of the experimental isotherm and UFF results for propene at approximately 0.3 bar. The simulation results do not follow the steadily increasing trend of the experimental data at higher pressures.

In contrast to the simple topology of ZIF-9, i.e. 1-d channels, the open structure of ZIF-71 has various intersecting channels and pores,[106] which makes the interpretation of the residence probability not straightforward (see Figure 5.10). The large pores of the material are positioned as in a body centered cubic cell. Small channels are found along the edges of the unit cell and larger ones along the (111), (–111), (1–11), and (11–1) directions of the crystal. Thus, the structure is very open with plenty of space for the molecules.[106] There is no clear adsorption site identified, however, ethane is most likely to be found in the larger channels or at the walls of the large pores. One can assume that those channels are the likely diffusion path of the molecules.

In conclusion, in contrast to ZIF-8, for which the modified-UFF is the better choice, for ZIF-71 the UFF is in better agreement with the experimental results. The reason for this could be the more accurate description of the framework interactions with the guest molecules. No clear adsorption site is identified in this structure because of its open nature. The molecules most likely reside in the pores and larger channels of the framework.

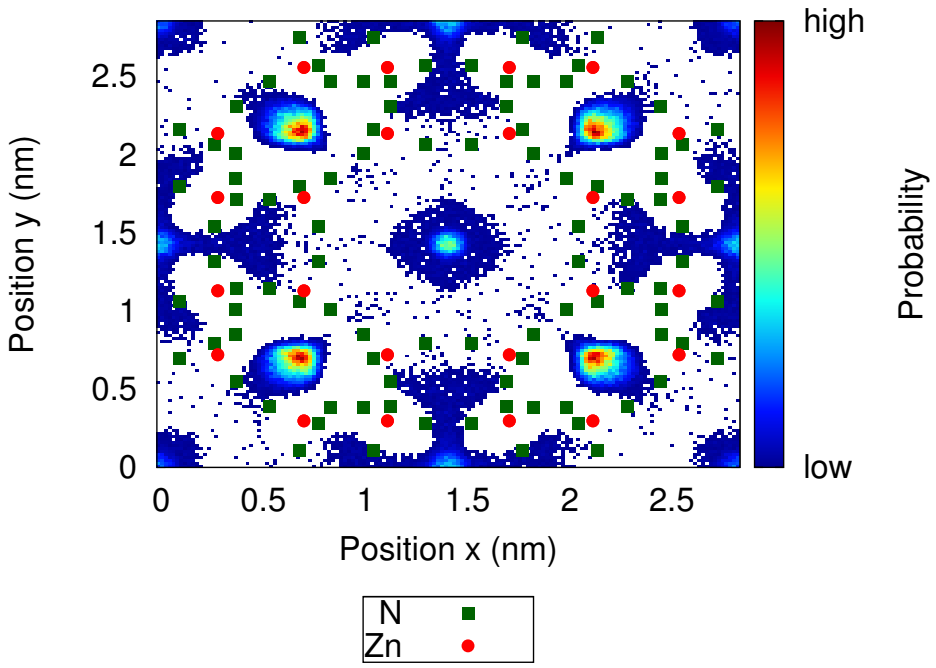

Figure 5.10: Residence probability for the center of mass of an ethane molecule in ZIF-71 at 293 K and infinite dilution. The highest probability is indicated in red, the lowest in blue and (exactly) zero in white.

5.4 Conclusions

Three nanoporous materials from the ZIF family, namely ZIF-8, ZIF-9, and ZIF-71 were synthesized and evaluated with respect to their olefin/paraffin separation capabilities both experimentally and by molecular simulations. Adsorption isotherms for ethane, ethene, propane, and propene in the latter two structures were measured experimentally by Prof. M. Hartmann's group whereas ZIF-8 serves as a mean to validate the adjusted force fields for grand canonical Monte-Carlo simulations which agree well with experimental data. In all three structures, the paraffin is favorably adsorbed compared to the olefin. Based on the results from experiments and simulations, we suspect that ZIF-9 exhibits a "gate opening" effect that is reflected by the shape of the adsorption isotherms. Hence, the force fields failed to describe the experimental adsorption isotherms in the low pressure region except the saturation loading. In case of ZIF-71, the experimentally determined isotherms for the hydrocarbons under study match well with the available reported data. Adsorption isotherms obtained from GCMC predict accurately the experi-

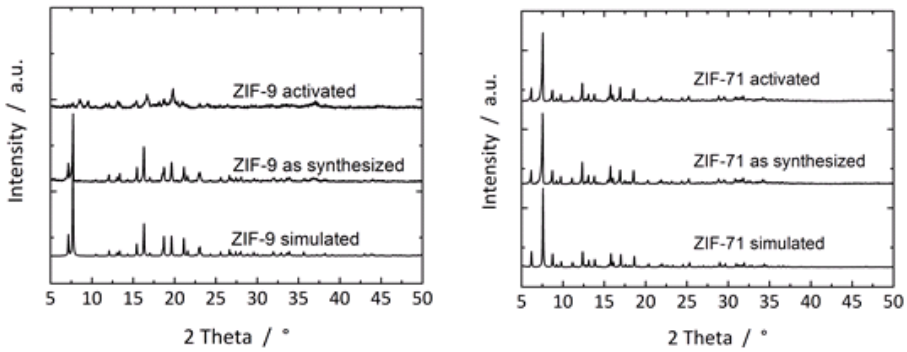

Figure 5.11: X-ray-diffraction pattern of simulated, as synthesized and activated ZIF-9 (left) and ZIF-71 (right).

mentally determined results in case of the UFF, whereas the modified-UFF underestimates the loadings by a factor of approx. 2. Overall, all three structures were found to be promising candidates for separating olefin/paraffin mixtures.

5.5 Supporting information

5.5.1 Synthesized material

Here, the results from the XRD for ZIF-9 and ZIF-71 based on simulations and experiments are presented, see Figure 5.11. Furthermore, the XRD pattern of ZIF-9 after the adsorption of DMF on the activated sample is also displayed. The structural change of ZIF-9 is induced by guest molecules and is reversible. The adsorption isotherms of N_2 in ZIF-8,[45] ZIF-9, and ZIF-71 obtained from experiments are given in Figure 5.12.

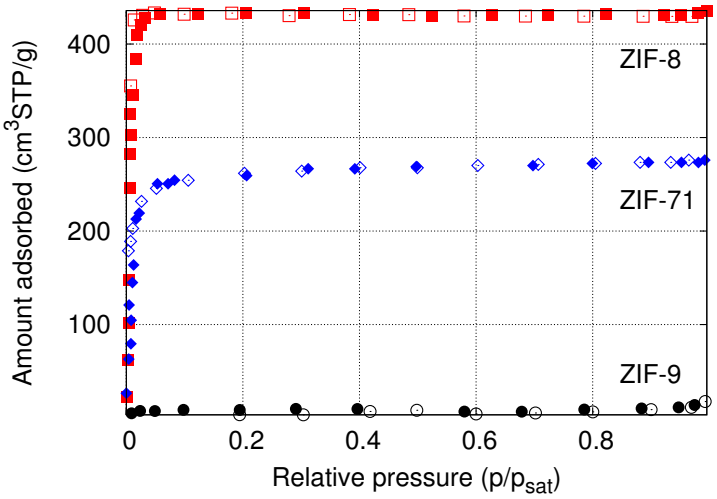

Figure 5.12: The N_2-adsorption isotherms of ZIF-9, ZIF-71, and ZIF-8 are given in $\frac{cm^3_{STP}}{g}$ as a function of the relative pressure. Open symbols represent desorption data and closed symbols adsorption data. The results for ZIF-8 are taken from reference Böhme et al.[45] for comparisons.

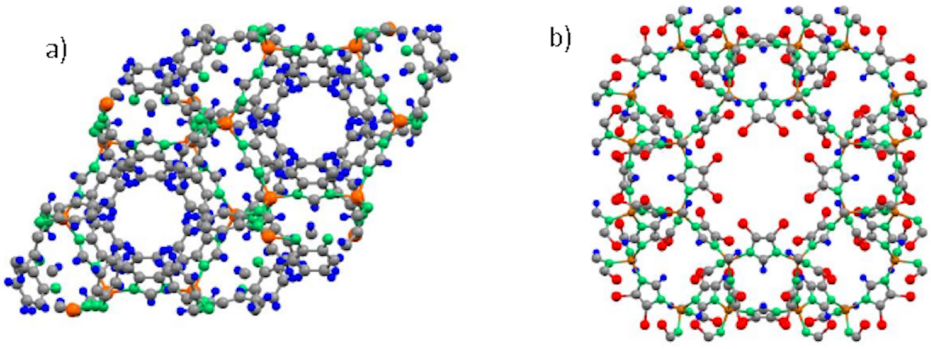

Figure 5.13: Structures of ZIF-9 (a) and ZIF-71 (b): Hydrogen atoms are depicted by blue, nitrogen by green, carbon by grey, chlorine by red and zinc by brown spheres.

5.5.2 Force field parameters

Here, the applied force field parameters as well as the atomtype definition for the investigated ZIFs are given. The Lennard-Jones parameters for the framework atoms are taken from Rappe et al.[239] (UFF) and Perez-Pellitero et al.[320] (modified- UFF) and presented in Table 5.3 and Table 5.4, respectively. The TraPPE forcefield by Siepmann et al.[175,325] is used to model the guest molecules of methane, ethane, ethene, propane and propene. The crossterms are taken from the works of Dubbeldam et al.,[326] Liu et al.[327] and Jakobtorweihen et al.[187]

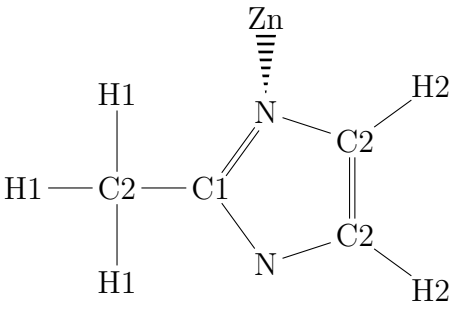

Figure 5.14: Description (schematically) of the atomtypes found in the organic linker of ZIF-8.

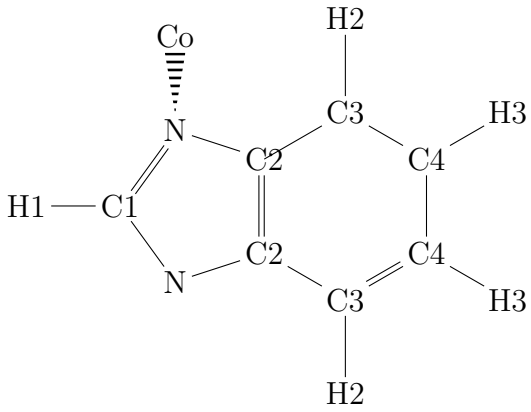

Figure 5.15: Description (schematically) of the atomtypes found in the organic linker of ZIF-9.

Residence probability in ZIF-8

Residence probability plots based on the modified-UFF for ethane, ethylene, propane and propylene in ZIF-8 were calculated at 293 K in order to identify

Table 5.3: Lennard-Jones Parameters for ZIF atom types (UFF).[239]

Atom	$\frac{\epsilon}{k_B}$ (K)	σ ($\mathring{A}$)
Zn	62.399	2.462
In	301.429	3.976
Co	7.045	2.559
H	22.142	2.571
N	34.722	3.261
C	52.838	3.431

Table 5.4: Lennard-Jones Parameters for ZIF atom types (modified UFF).[320,324]

Atom	$\frac{\epsilon}{k_B}$ (K)	σ ($\mathring{A}$)
Zn	43.056	2.338
In	207.980	3.777
Co	4.861	2.431
H	15.278	2.443
N	23.958	3.098
C	36.458	3.259

Table 5.5: Lennard-Jones parameters for the guest molecules based on TraPPE model. The crossterms are taken from Ref 326, 327, and 187. The first row of each cell is ϵ in (K) and the second row is σ in ($\AA$).

ϵ **in (K)** σ **in** ($\AA$)	$\mathbf{CH_4(sp^3)}$	$\mathbf{CH_3(sp^3)}$	$\mathbf{CH_2(sp^3)}$	$\mathbf{CH_2(sp^2)}$	$\mathbf{CH(sp^2)}$
$\mathbf{CH_4(sp^3)}$	148.0 3.73	not included	not included	not included	not included
$\mathbf{CH_3(sp^3)}$	not included	108.0 3.76	77.77 3.86	77.77 3.86	54.48 3.85
$\mathbf{CH_2(sp^3)}$	not included	77.77 3.86	56.0 3.96	77.77 3.86	54.48 3.85
$\mathbf{CH_2(sp^2)}$	not included	77.77 3.86	77.77 3.86	93.0 3.685	70.21 3.71
$\mathbf{CH(sp^2)}$	not included	54.48 3.85	54.48 3.85	70.21 3.71	53.0 3.74

Table 5.6: Isosteric heat of adsorption at zero loading in (kJ/mol) obtained from simulations based on the UFF[239] and the modified-UFF[320] at 293 K.

$\mathbf{Q_{st}}$**@ zero loading**	**ZIF-9**		**ZIF-71**	
$(\frac{kJ}{mol})$	ZIF-UFF	UFF	ZIF-UFF	UFF
Ethane	35.1	46.7	19.2	27.5
Ethene	31.1	41.9	16.6	24.1
Propane	43.6	56.5	25.7	36.4
Propene	40.5	53.3	23.2	33.4

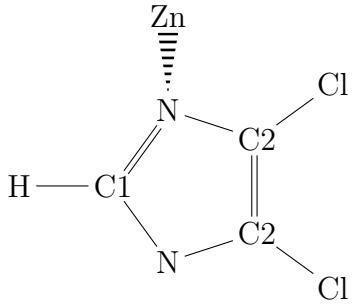

Figure 5.16: Description (schematically) of the atomtypes found in the organic linker of ZIF-71.

the main adsorption sites. Due to the similar outcome for all four species and the two different force fields the result for ethane is shown exemplary in Figure 5.17.

The plots show a cut in the transverse plane of the channel in the x-y direction (front view), while the volume is oriented longitudinally into the z-direction. Red indicates the highest, blue indicates the lowest and white exact zero probability of finding the center of mass of the respective molecules within the framework. The framework consists of almost spherical pores with a diameter of approx. 11 $\mathring{A}$.[106,306] One can see that the molecules preferably sit on the edges of the pockets. This finding is in agreement with Wu et al.[310]

5.5.3 DFT calculations of adsorption energies for ethane in ZIF-9

For the DFT calculations the PBE functional in combination with the van-der-Waals: Grimme method was used.[329] A projected-augmented-wave (PAW) scheme[241] has been used in order to describe the interactions between the valence electrons and the nuclei (ions) as implemented in the VASP package.[242,243] The electronic wave functions have been expanded into plane waves up to an energy cutoff of 400 eV. Convergence was considered to be achieved when the forces were smaller than 0.01 $\frac{eV}{\mathring{A}}$. In order to compute the adsorption energies, the total energies for the vacuum molecules (ethane) had to be computed. This has been done by considering each of these molecules isolated in a large 25 x 25 x 25 $\mathring{A}^3$ unit cell. As a consequence of the supercell size, only one single K-point, the Gamma point, was necessary to span the Brillouin zone. Minima on the PBE potential energy surface were located using the conjugate gradient algorithm with fully relaxed atomic positions. The results for the adsorption energy of ethane in ZIF-9 at infinite dilution

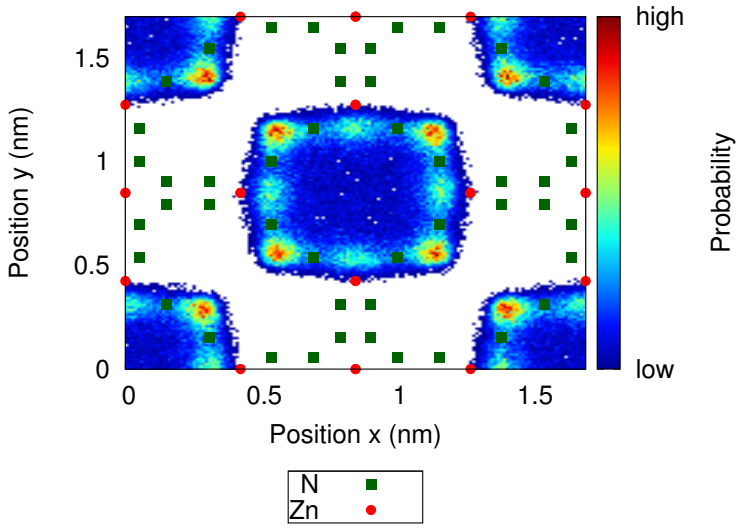

Figure 5.17: Residence probability for the center of mass of an ethane molecule in ZIF-8 at 293 K. The highest probability is indicated in red, the lowest in blue and zero in white.

Table 5.7: Adsorption energy for ethane in ZIF-9 at 298 K at infinite dilution (zero loading).

Adsorption energy ($\frac{kJ}{mol}$)	**blocked**	**unblocked**
UFF (GCMC)	46.3 ± 0.4	46.7 ± 0.4
ZIF-UFF (GCMC)	34.9 ± 0.3	35.1 ± 0.3
DFT	—	44.4 ± 0.7

(zero loading) are shown in Table 5.7. The first/main adsorption sites for which the energies were determined are depicted in Figure 5.18.

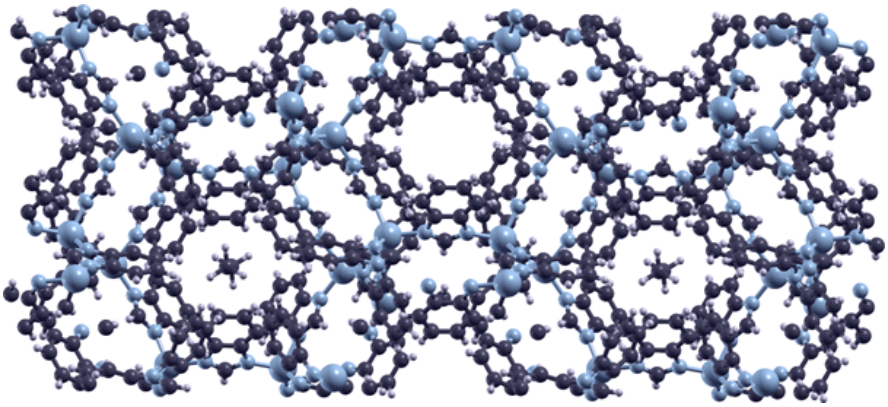

Figure 5.18: View of the x-y-plane of ZIF-9 with two ethane molecules in the main adsorption sites (cages).

6

Experimental and theoretical analysis of the influence of different linker molecules in Imidazolate Frameworks Potsdam (IFP-n) on the separation of olefin/paraffin mixtures

Four metal-organic frameworks with similar topology but different chemical environment inside their pore structure, namely, IFP-1, IFP-3, IFP-5, and IFP-7, have been investigated with respect to the separation potential for olefin/paraffin mixtures as well as the influence of the different linkers on adsorption properties using experiments and Monte Carlo simulations. All IFP structures show a higher adsorption saturation of ethane compared to ethene with the exception of IFP-7 which shows no selectivity in breakthrough experiments. For propane/propane separation, all adsorbents show a higher adsorption for the olefin. The experimental results agree quite well with the simulated values except for the IFP-7, which is presumably due to the flexibility of the structure. Moreover, the experimental and simulated isotherms were confirmed with breakthrough experiments that render IFP-1, IFP-3, and IFP-5 as suitable for the purification of ethene from ethane.

6.1 Introduction

Industrial separation of gases with close evaporation temperatures like olefins and paraffins is still realized with expensive low-temperature distillation processes. Promising alternatives include the continuous purification by pressure swing adsorption plants, for example, for the production of oxygen from air,[330] and the simulated moving bed (SMB) technology.[290] A laboratory version of the former process, a rapid pressure swing adsorption rig, was already used to separate olefin-paraffin mixtures employing binderless zeolite 13X beads.[331] Due to the fact that zeolite 13X shows higher adsorption affinity for the olefin compared to the paraffin, it is only possible to recover the olefin from the desorption branch of a breakthrough experiment. This, however, complicates the recovery of pure olefins out of a mixed gas stream. This problem is not so prominent, when using the SMB technology as indicated in the study of Martins et al.,[290] who successfully demonstrated the separation of ethane/ethene mixtures employing the SMB approach.

In recent years, suitable adsorbents have been found showing isotherms with higher adsorption affinity for paraffins and good separation performances in dynamic separation processes. Most of these materials belong to the group of metal-organic frameworks such as FIR-51,[332] IRMOF-8,[333] as well as ZIF-8,[45] ZIF-4,[302] and ZIF-71[334] from the subgroup of zeolitic imidazolate frameworks (ZIFs). For ZIF-4 and ZIF-8, the dynamic separation potential was also confirmed with breakthrough experiments at ambient pressure and room temperature.[45,302] A more extensive discussion covering the literature of olefin/paraffin separation on porous materials is given in our previous work on ZIFs.[334]

Another group of MOFs that meet the requirements is the so-called Imidazolate Frameworks Potsdam (IFP) family; when changing just the substituent of the linker, the topology of the material remains the same (see Figure 6.1). Therefore, only the chemical environment as well as the diameter of the apertures to the pores, are varied.[140,142,143] The IFP structures are quite similar to the group of zeolitic imidazolate frameworks[133] as explained in Chapter 2.3.3.

In order to improve the separation performance of these porous materials, it is necessary to understand the influence of their different linkers and metal atoms. But when the topology is altered by changing the linker molecule it is complicated to verify the direct influence of the chemical interactions between adsorbents and adsorptives. To circumvent this issue, it would be useful to synthesize MOFs with different linker molecules whereas the topology stays the same. One quick way to investigate the influence of changing linkers is

to calculate pore volumes and surface areas of the nanoporous materials.[335] However, using Monte Carlo simulations in combination with experiments a deeper understanding of not only the steric effect but also the energetic one on the guest molecules is obtained.[336] Hence the investigations with the IFP family of crystals.

In this chapter, adsorption isotherms for ethane, ethene, propane, and propene in IFP-1, IFP-3, IFP-5, and IFP-7 are determined by experiment and simulation. The influence of the organic linker on the adsorption properties on a molecular level is investigated using Monte Carlo simulations. GCMC simulations for binary mixtures were conducted and compared to the IAS theory.[71] Furthermore, experimental breakthrough curves were measured in order to evaluate the performance of these materials for the continuous separation of olefins and paraffins.

6.2 Materials and methods

As a disclaimer, the synthesis part of this chapter was executed by the group of Prof. H.-J. Holdt's group of the Institute of Inorganic Chemistry of Potsdam University (Germany), while the experimental part was carried out by Prof. M. Hartmann's group of the Erlangen Catalysis Resource Center (Germany).

6.2.1 Adsorbents

The materials IFP-1, IFP-3, IFP-5, and IFP-7 were synthesized as described in previous publications.[140,142,143] Nitrogen sorption isotherms were measured at 77 K (Figure 6.10), and the textural properties are collected in Table 6.1 in Chapter 6.5.

6.2.2 Pure component isotherms

The pure component isotherms of ethane, ethene, propane, and propene have been measured with a modified ASAP 2010 from Micromeritics. The measurement temperature of 30°C was kept constant by using a stand-alone thermostat. All adsorbents have been activated at 200°C under vacuum for 20 h.

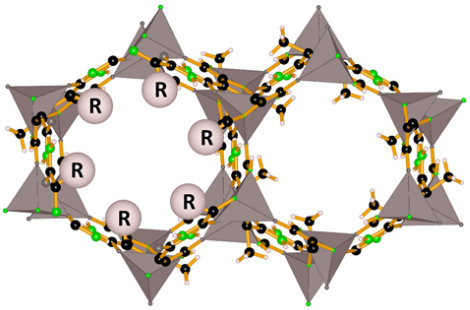

	M	R
IFP-1	Zn	Me
IFP-3	Zn	Br
IFP-5	Co	Me
IFP-7	Zn	OMe

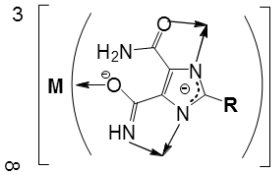

Figure 6.1: Crystal structure and lattice atoms of the different employed IFP materials.

6.2.3 Breakthrough experiments

The mixed breakthrough experiments were carried out using one column of a commercial lab-scale pressure swing adsorption instrument (L&C Science and Technology). A constant temperature of 30°C was realized by a bed thermostat equipped with Peltier elements. All samples (0.7 g) have been activated in situ under constant nitrogen flow at 200°C for 5h after heating them ex situ in a vacuum oven at 200°C for 20h. For the breakthrough experiments, a constant feed flow of 2 $\frac{mL_N}{min}$ of an equimolar mixture of ethane and ethene was used. The fixed bed was regenerated by flushing with a helium stream ($\dot{V} = 15\ \frac{mL_N}{min}$).

6.2.4 Simulation details

Adsorption isotherms of four different guest molecules (ethane, ethene, propane, and propene) in IFP-1, -3, -5, and -7 were calculated for 30°C with pressures ranging up to 1 bar (5 pressure points per magnitude), whereby each point was calculated at least twice. The results are given as averages with error bars.

Monte Carlo simulations in the grand canonical ensemble (GCMC) were conducted to compute adsorption isotherms. The chemical potential was linked to pressure via the Peng-Robinson equation of state. Three different force fields were used to model the interactions of the crystal structures with guest molecules: The first one was the universal force field ("UFF"),[239] which is widely accepted regardless of its minor shortcomings for MOFs.[313] The second one was a modified UFF, which was fitted to reproduce adsorption isotherms of methane and CO_2 in ZIF-8 by Perez-Pellitero et al.[320] (here

called "ZIF-UFF"). The potential parameters of the UFF were multiplied by a factor of 0.69 (epsilon) and 0.95 (sigma), respectively. Based on experiences from earlier studies,[321,334] a third force field was used for which the epsilon and sigma values of the UFF were changed by the factors of 0.85 and 0.975, respectively. This force field is referred to as "mod-UFF". The parameters were chosen to be in between the UFF and the ZIF-UFF values. As a result, the interactions are not as strong as for the UFF but not as weak as the ZIF-UFF. All guest molecules are modelled using the TraPPE force field.[175,325] The bond vibration and bond-angle parameters were taken from refs 326 and 327, and crossterms for the solute interaction from refs 326 and 187. For the parameters, the reader is referred to Tables 6.3 and 6.4 in Chapter 6.5.

The crystallographic data were taken from 142 and 337. Each simulation box consists of 2x2x2 unit cells of the respective crystal structure, and cutoff distances of 15 $\mathring{A}$ are applied.[320,324] Framework atoms are kept rigid at their respective crystal positions. Using zeolites as an example, it was shown by Vlugt and Schenk[251] that the difference between adsorption isotherms based on simulations with rigid frameworks or flexible structures is marginal. Periodic boundary conditions were applied in all directions. Lorentz-Berthelot mixing rules were employed.

Potential grid calculations are carried out with a grid spacing of 0.1 $\mathring{A}$ before the GCMC simulations in order to save computational time. The helium void fractions of the three structures are calculated for each of the three force fields with 10^6 cycles using Widom insertion. The simulation of the isotherms at the previously mentioned conditions was performed with 10^5 initialization steps and 10^6 production steps per calculation. The following probabilities are chosen for the different Monte Carlo steps: insertion/deletion 50%, translation 12.5%, rotation 12.5% and regrow 25%. Residence probability plots and isosteric heats of adsorption (q_{st}^0) at zero loading were calculated from results generated by Monte Carlo simulations in the NVT-ensemble at 303 K allowing only the "regrow" move. The value q_{st}^0 can be calculated based on the ensemble average of the total energy of the system $\langle U_{tot} \rangle$. Free energy profiles at zero loading are obtained with the Widom insertion and mapping the values onto the (one-dimensional) reaction coordinate, here the c-axis.[159]

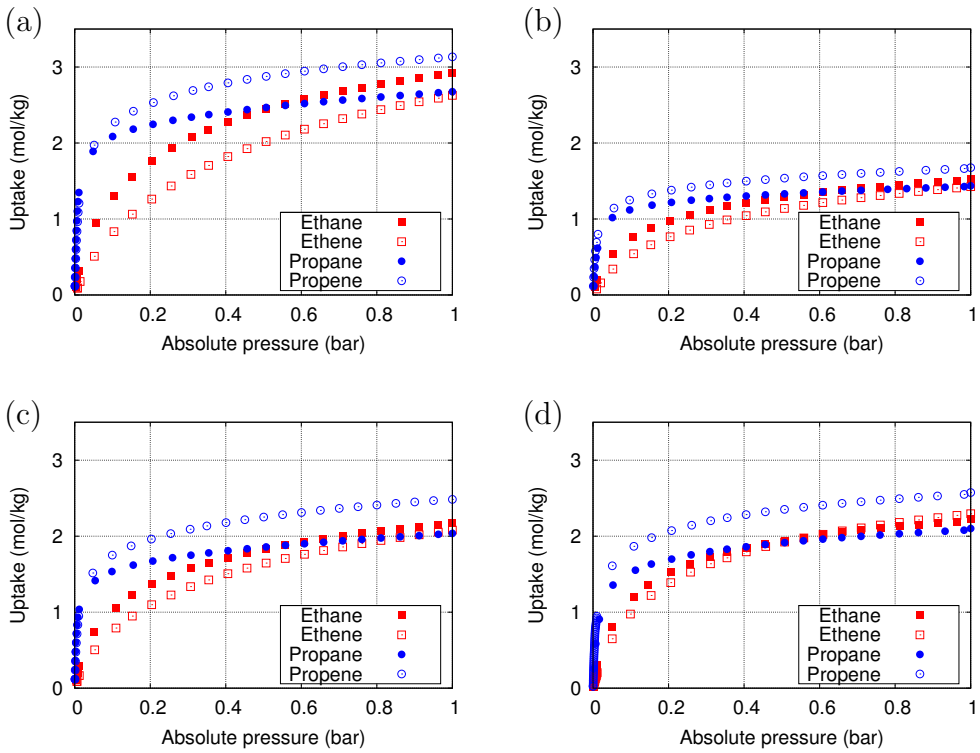

Figure 6.2: Pure component isotherms of ethane, ethene, propane, and propene on the different adsorbents under study at 30°C.

6.3 Results

6.3.1 Experimental adsorption isotherms

In Figure 6.2, the pure component isotherms of ethane, ethene, propane, and propene at 30°C for the materials IFP-1, IFP-3, IFP-5, and IFP-7 are displayed within an absolute pressure range from zero to one bar. In Figure 6.11, the same data are plotted in such a way that the isotherms of one gas for the different materials are shown in comparison.

Figure 6.2(a) shows stronger adsorption of the ethane over ethene at 30°C for IFP-1 which is beneficial for ethene purification. The selectivity factor at zero loading $\alpha_{ethane/ethene} = 2.60$ is slightly higher than that of ZIF-4 ($\alpha_{ethane/ethene} = 1.71$).[302] For C_3 separation, the uptake of the paraffin is only stronger at very low pressure. At a pressure of 0.05 bar, the isotherms intersect and a higher uptake of the olefin is observed.

The IFP-3 structure (Figure 6.2(b) shows a behavior similar to IFP-1,

but a much smaller uptake and selectivity for ethane and ethene are found as a consequence of the bromide substituent.

The capacity of IFP-5 is just between the other materials IFP-1 and IFP-3, which is in line with the pore diameter of 3.8 $\AA$,[337] a value between the pore diameter of the other two materials (Table 6.1). Because of the same substituent as IFP-1, the change in pore size for IFP-5 is due to the different center metal cobalt.

IFP-7 (Figure 6.2(d) surprisingly shows a similar uptake for the paraffins compared to IFP-5, which was unexpected because of the low nitrogen isotherm at 77 K (Figure 6.10). This could be due to a temperature-dependent phase transition of the crystal structure between 77 K and 303 K. A similar effect was reported by Hartmann et al. for ZIF-4.[302] Up to high $\frac{p}{p_0}$ ratios the uptake of nitrogen at 77 K was zero. Wharmby et al.[287] investigated this behavior using DFT and traced it back to the fact that the rotational flexibility of the linker is a function of temperature: At low temperatures and due to the lack of flexibility, the methoxy groups do not allow the nitrogen molecules to diffuse into the structure, acting as a blockade. At room temperature, the linkers are flexible enough to allow diffusion of the nitrogen molecules.

Although the selectivity factor at zero loading $\alpha_{ethane/ethene}$ is 1.87 (see Table 6.2), the selectivity for ethene and the adsorption capacity are higher compared to the paraffin above a pressure of 0.6 bar.

The results presented above suggest that these materials are suitable for the separation of ethane and ethene at 1 bar except for IFP-7, for which an almost simultaneous breakthrough of both gaseous components is expected. For propane and propene, selectivity for the olefin is significantly higher, which allows purification at the desorption branch of a breakthrough experiment. These hypotheses were further tested by measuring breakthrough curves of the respective gas mixtures (Section 6.3.3).

6.3.2 Simulation results

Adsorption isotherms

IFP-1

The adsorption isotherms for ethane, ethene, propane and propene determined by experiments and simulations at 30°C with pressures ranging up to 1 bar using three different force fields (UFF, ZIF-UFF, and mod-UFF) are compared in Figure 6.3. The simulated results show good agreement with the experimental data for the C_2 molecules: The shapes of the iso-

therms as well as the loadings are predicted quite well; the mod-UFF and the UFF overestimate while the ZIF-UFF slightly underestimates the experimental results. As for the C_3 components, the agreement is satisfactory but the accuracy decreases with increasing pressure, most notably for propene. However, the behavior is still predicted well. Thus, the trend observed in our experiments that paraffins are favorably adsorbed, is reproduced by the simulations. The best agreement between experimental and simulation data is found for the mod-UFF, because it predicts a loading only marginally higher than the experiments, whereas the UFF overestimates the loading and the ZIF-UFF leads to even lower adsorption values than found for the experimental loadings. Please note that, in contrast to the experiments, the crystallite structure in simulations is perfect due to defect free unit cells and periodic boundary conditions, namely, no defects or blocked passages are reducing the pore volume. Thus, assuming the force field describes the interactions very accurately and flexibility can be neglected, adsorption isotherms obtained from simulations will always have higher loadings compared to experimental results at equal pressure. That is the reason for choosing the mod-UFF over the other two force fields. The same argument is valid for all four materials under study when comparing the three force fields.

IFP-3

The results for the adsorption isotherms of ethane, ethene, propane, and propene in IFP-3 at 30°C for pressures up to 1 bar are presented in Figure 6.4. The qualitative agreement for the C_2 molecules in IFP-3 is reasonable for all three force fields: The trends of the isotherms, as well as the loadings, are reproduced quite accurately for the investigated pressure range. Similar to the experiments, the results of the simulations show that ethane is favorably adsorbed over ethene In the case of propane, the experimental data are well below the results obtained from the simulations. At 1 bar, the experimental uptake is at 1.43 $\frac{mmol}{g}$ whereas the ZIF- UFF, the force field obtaining the lowest loading, predicts over 1.65 $\frac{mmol}{g}$. This deviation stands out compared to the propene results, for which the experiments are more or less following the trend of the ZIF-UFF based adsorption isotherm. One reason for the inaccurate reproduction of the experimental data for the C_3 molecules may be found in the flexibility of the IFP-3 structure, which was not taken into account. While the presence of flexibility effects cannot be ruled out completely, the simulation results suggest that their effect is not very strong in this pressure region, with IFP-7 being the exception. The second one is potentially the bromine atom reaching into the channel, for which the interaction parameters might not be optimal. Therefore, simulations were conducted, for which the σ parameter of the bromine was altered based on

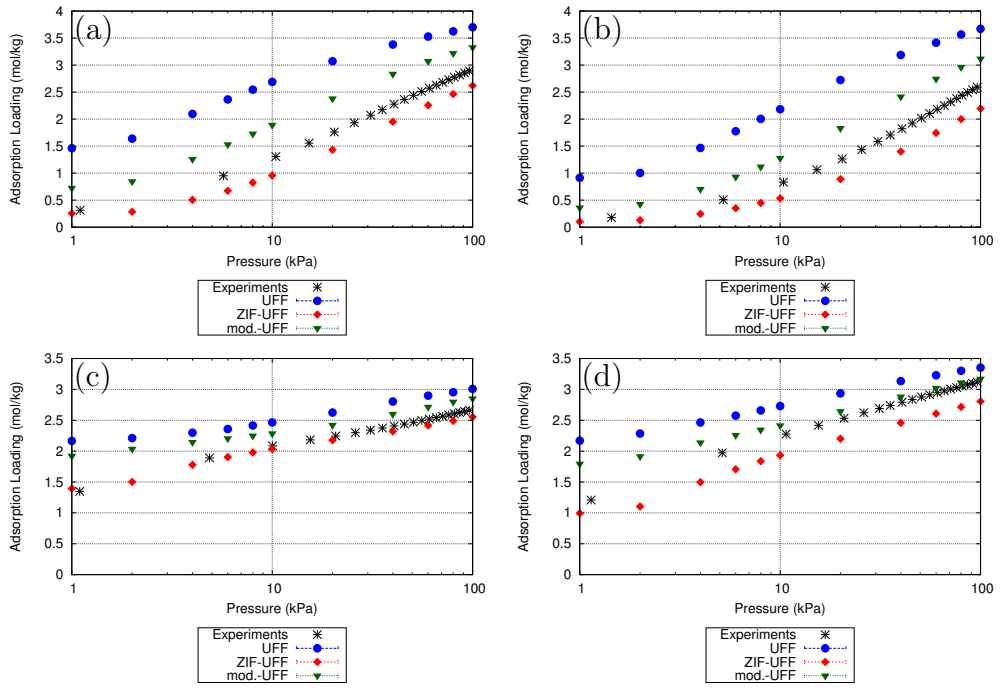

Figure 6.3: Adsorption isotherms in IFP-1 for ethane (a), ethene (b), propane (c), and propene (d) at 30°C in the pressure range up to 1 bar. The experimental data are depicted as stars, the results from simulations based on the UFF as blue dots, mod-UFF as red diamonds, and ZIF-UFF as green triangles; error bars too small to be visible.

the mod-UFF. Essentially, it makes the atom bigger while keeping the interaction strength unchanged. The resulting adsorption isotherms for ethane and propane are given in Figure 6.12. Clearly, the influence of this parameter is not negligible but it does not really lead to an improved description of the experimental isotherms. While it can be argued that the reproduction of the experimental isotherm for ethane is better at higher pressures, it is paid for by the worse description of the overall trend. Thus, adjusting the only parameter for the bromine is not a way to reduce the inaccuracy of the force fields. Improving parameters of all present atom types, however, should improve the accuracy of the simulations. A third possibility is that the material used to determine the adsorption isotherm experimentally was not activated completely, thus resulting in the reduction of accessible pore volume and surface or some diffusion limitation is present. Yet out of the three force fields tested, the mod-UFF performs best.

IFP-5

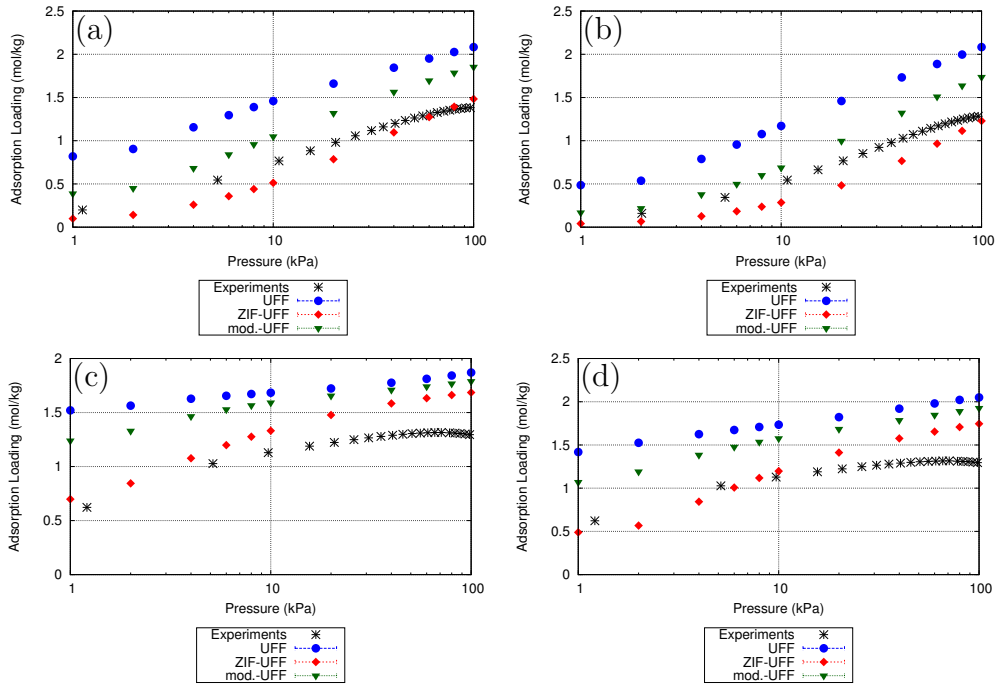

Figure 6.4: Adsorption isotherms in IFP-3 for ethane (a), ethene (b), propane (c), and propene (d) at 30°C in the pressure range up to 1 bar. The experimental data are depicted as stars, the results from simulations based on the UFF as blue dots, mod-UFF as red diamonds, and ZIF-UFF as green triangles; error bars too small to be visible.

The simulation results for ethane, ethene, propane, and propene in IFP-5 at 30°C with pressures ranging up to 1 bar are shown in Figure 6.5. The agreement of the simulation results with the experimental data for the C_2 molecules is very good since the trends, as well as the absolute values, are reproduced accurately (see Figure 6.5(a) and (b)). The force fields UFF and mod-UFF overestimate the loading, whereas the ZIF-UFF predicts lower loadings than obtained by experiments. The quality of the agreement is as good as for IFP-1. For propene, the experimental isotherm is reproduced successfully by the simulations. In the case of propane, however, all three force fields overestimate the experimental isotherm over the investigated pressure range. The reason why the force fields deviate so much from the experiments for propane compared to propene, ethane, and ethene is not clear though. A similar effect has been observed for IFP-3 and the same possible explanations as mentioned above apply here as well. While all force fields perform quite well, the most accurate results are again obtained using the mod-UFF.

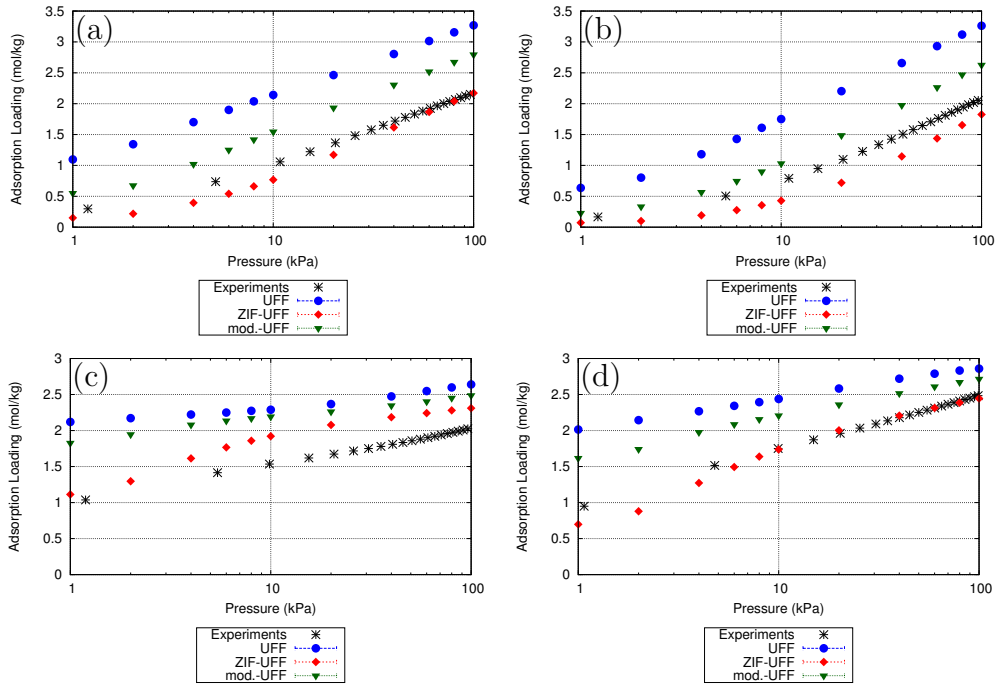

Figure 6.5: Adsorption isotherms in IFP-5 for ethane (a), ethene (b), propane (c), and propene (d) at 30°C in the pressure range up to 1 bar. The experimental data are depicted as stars, the results from simulations based on the UFF as blue dots, mod-UFF as red diamonds, and ZIF-UFF as green triangles; error bars too small to be visible.

IFP-7

Adsorption isotherms for ethane, ethene, propane, and propene at 30°C calculated employing three force fields (UFF, mod-UFF, and ZIF-UFF) are compared to the experimental isotherms. The results are shown in Figure 6.6. While the agreement between the experimentally determined isotherms and the ones based on the mod-UFF force field is good for IFP-1 and reasonable for IFP-3 and IFP-5, the situation is slightly different for IFP-7. While the experimental isotherms for ethane and ethene are predicted reasonably well by the simulations, the simulation results for the C_3 molecules propane and propene deviate from the experimental ones at higher pressure. The accuracy decreases with increasing pressure up to a point where the isotherms predicted by simulations are lower than the one determined experimentally. One reason for the discrepancy could be that the force field parameters are not very good at describing the interactions between the guest molecules and the host structure. However, this is improbable, since those parameters

are describing the interactions in the other three investigated IFPs quite well. It is more likely that the flexibility of the IFP-7 causes the inaccurate predictions. Whereas simulations predict that saturation is almost reached at one bar, see Figure 6.6(c) and (d), the experimental isotherms do not indicate this state yet. Given the fact that this effect occurs for the larger molecules, it is a strong indicator that the pore volume of the crystal is higher than the one used in the (rigid) simulation which is based on the low temperature crystal structure. Clearly, allowing the crystal to be flexible should improve the quality of the prediction by the simulations as the pore volume is expected to increase with flexibility.

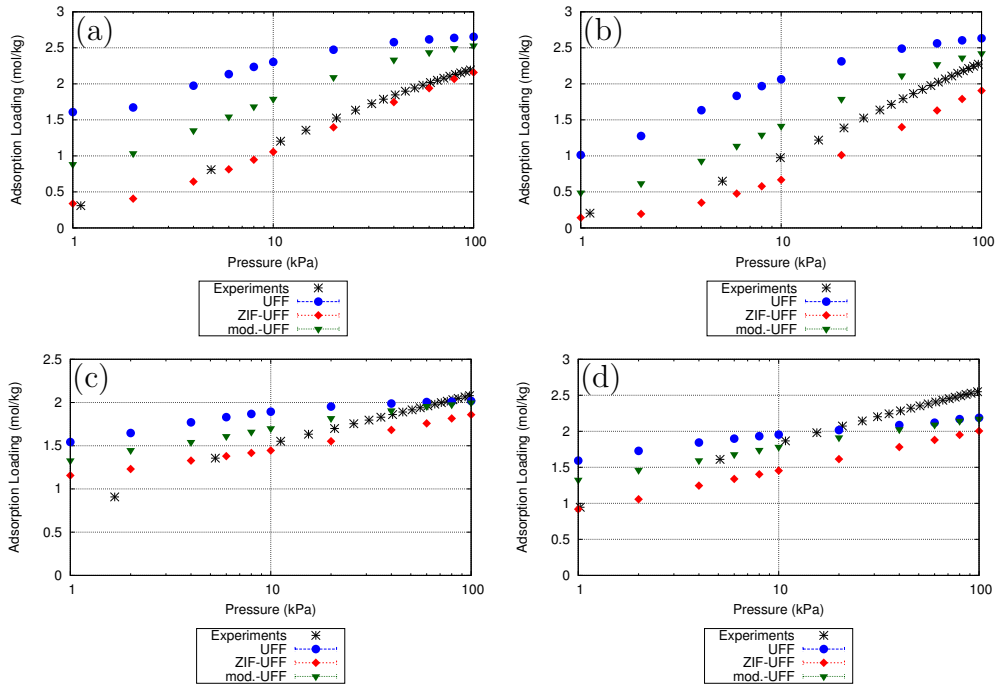

Figure 6.6: Adsorption isotherms in IFP-7 for ethane (a), ethene (b), propane (c), and propene (d) at 30°C in the pressure range up to 1 bar. The experimental data are depicted as stars, the results from simulations based on the UFF as blue dots, mod-UFF as red diamonds, and ZIF-UFF as green triangles; error bars too small to be visible.

Influence of linker and ion

In order to understand the influence of the different linkers, we will treat IFP-1 as the reference structure. Thus, IFP-3, IFP-5, and IFP-7 can be viewed as

derivatives of it, since only small changes are made: substituting the methyl group with bromine in IFP-3, cobalt with zinc in IFP-5, and the methyl group with a methoxy group in IFP-7, respectively. Obviously, the influence of the part of the linker protruding into the channel or substituting the metal-ion on the topology is depicted in the adsorption isotherms, see Figure 6.7. However, calculating the isosteric heat of adsorption and free energy profiles at zero loading helps to gain insight into the interaction between the crystal atoms and the guest molecules without the presence of other guest molecules. As established before, the most accurate force field based on the comparison with experimental data is the mod-UFF, which is used for all of the following calculations.

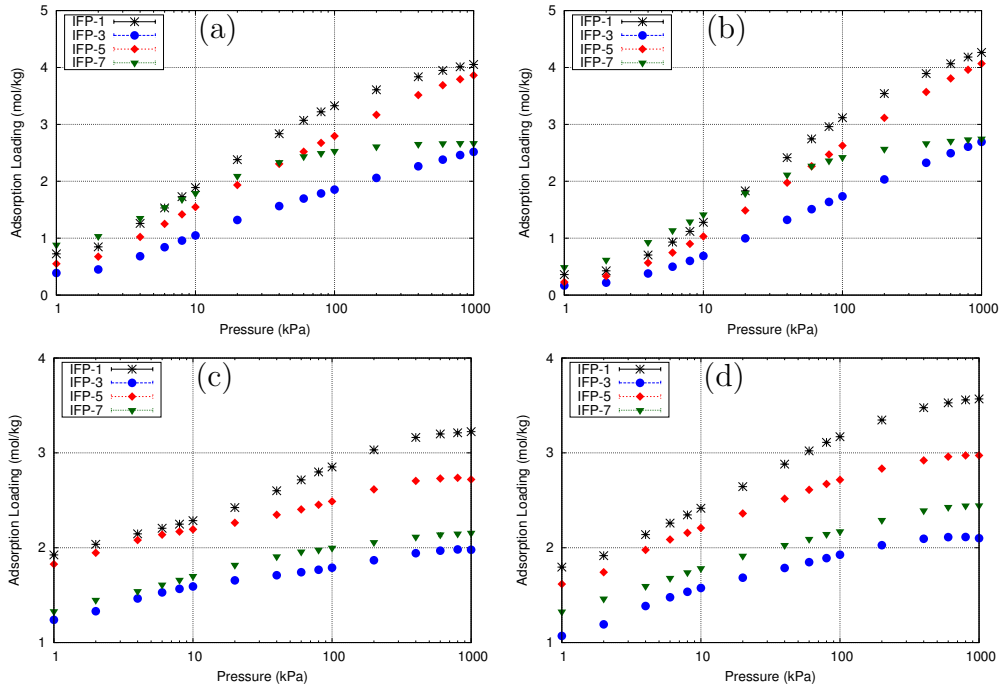

Figure 6.7: Adsorption isotherms based on the mod-UFF for ethane (a), ethene (b), propane (c), and propene (d) at 30°C in the pressure range from 0.01 to 10 bar. The results for IFP-1 are depicted as stars, for IFP-3 as blue dots, for IFP-5 as red diamonds, and for IFP-7 as green triangles; error bars too small to be visible.

From a steric point of view, obviously, the channel size is heavily influenced by the linker choice, see Table 6.1, as well as the helium void fraction. The methoxy group is the largest of employed substituents, whereas bromine and the methyl groups are equal in size. The isosteric heats of adsorption at

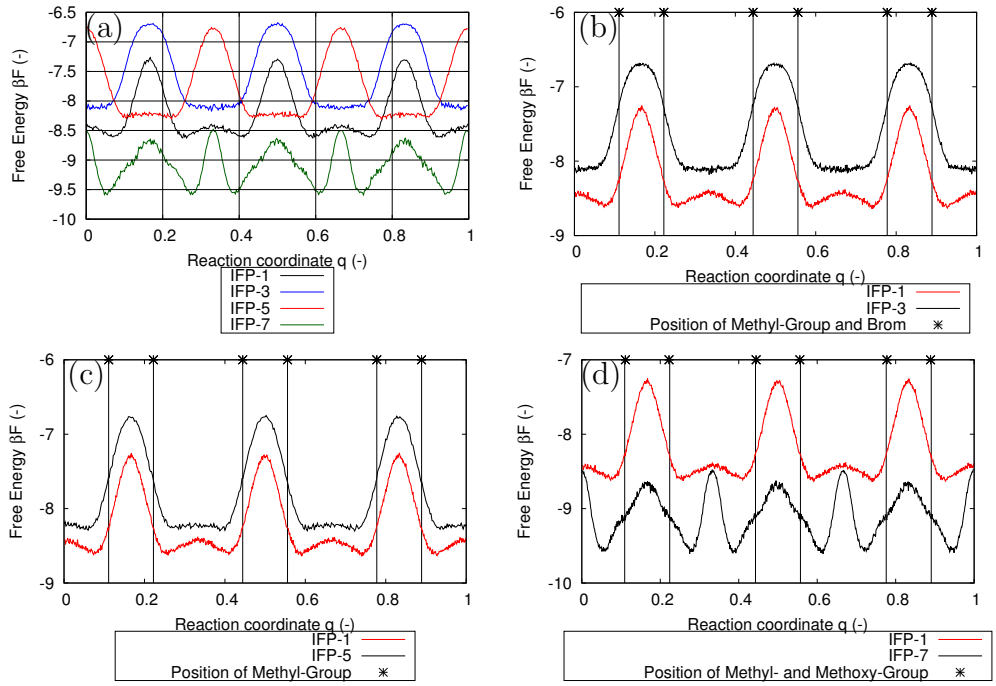

Figure 6.8: Free energy profiles at zero loading for ethane: Comparison of the four crystals (a), IFP-1 to IFP 3 (b), IFP-1 to IFP-5 (c), and IFP-1 to IFP-7 (d); the asterisks on the x2-axis denote the positions of the fraction of the linker protruding into the channel.

zero loading for all investigated materials and guest molecules are collected in Table 6.5. These values are basically a metric for the interaction strength between the host structure and one guest molecule. For all five guest species, it can be seen that IFP-7 has the highest heat of adsorption followed by IFP-1 and IFP-5 and IFP-3. The reason that the results for the last three crystals are quite similar can be found in the force field parameters: The van der Waals interaction parameters in the Lennard-Jones potential (Table 6.3) for the methyl group and bromine are comparable, which leads to similar interaction energies (IFP-3). The parameters for cobalt and zinc differ noticeably more, however, the influence in the regime of zero loading has only little impact since the adsorption does not take place next to those atoms (IFP-5). As for the IFP-7 case, the additional oxygen in the methoxy group does not increase the interaction strength of the framework with guest molecules but it also serves as a secondary interaction atom which is favorable for adsorption.

Exemplary, the results of the free energy profiles at zero loading for ethane

are shown in Figure 6.8. The curves for the other species (ethene, propane, and propene) are given in the Figures 6.13 and 6.14. In Figure 6.8(a), the free energy profiles for ethane in all investigated materials are given for comparison. Note that the lower the free energy is, the stronger becomes the interaction between the host crystal and guest molecule is. As expected, the results coincide with the calculated isosteric heats of adsorption: The lowest baseline is found for IFP-7 followed by IFP-1, IFP-5, and IFP-3. The energy minima also correspond to the highest probability finding a guest molecule in a certain space, for example, the adsorption sites of the crystal. The energy maxima are found at the positions of the bromine, the methyl or methoxy group, respectively. As a result, one can see that the molecules most likely reside in the confinement caused by these chemical groups of the organic linker. In Figure 6.8(b), the profiles for IFP-1 and IFP-3 are shown. The substitution of bromine (one atom) for the methyl group (four atoms) increases the free energy, in general, making the materials less attractive. The difference between maximum and minimum is almost identical in both materials. The small influence of the size of the organic rest is indicated by the small hill between the restriction as well as an extension of the energy maxima. As shown in Figure 6.8(c), switching from zinc to cobalt (IFP-1 to IFP-5) increases the free energy, making IFP-5 a weaker adsorbent as is evident from the values of the isosteric heat of adsorption. The energy maxima are basically the same, since the linker is the same though showing different energy levels. Having a methoxy group narrowing the channels in ZIF-7, instead of a methyl group, lowers the free energy more strongly than the results shown for the other two derivatives, see Figure 6.8(d). Additionally, the energy landscape changes as another energy maximum is found beside the one caused by the linker, however, this maximum does not change the main adsorption site. It just emphasizes the effect of the methoxy group has on the guest molecules since they are only found close to it.

In conclusion, without taking the flexibility of the structure into account, the methoxy group in the IFP-7 creates a stronger interaction with the guest molecules due to its size and interacting atoms at the cost of a reduction in pore volume. As for IFP-3 and IFP-5, the influence of the cobalt and bromine atom on energy related properties, such as isosteric heat of adsorption and free energy profiles, is small, which is not true for geometric properties as helium void fraction, pore diameters, and channel sizes.

Mixed-GCMG and IAST

For all four materials, mixed-GCMC simulations were carried out based on the most accurate force field in this study, the mod-UFF. Different mixtures (olefin-rich (9:1, 3:1, 2:1), equimolar, and paraffin- rich (9:1)) for each of the two olefin/paraffin combinations, for example, ethane/ethene and propane/propene, were defined and isotherms for those bulk gas compositions were calculated. The results are presented in Figure 6.16 and 6.17. Although the loading capacity and the behavior of the isotherms for the olefin and paraffin are quite similar, one can see that a higher quantity of paraffin is adsorbed for the paraffin-rich and equimolar compositions compared to the olefin-rich composition. The separation is very good in those cases. When the bulk gas phase consists mainly of the olefin, a larger fraction of the olefin is adsorbed compared to the paraffin. These results are consistent with the observations from our experiments and simulations. It shows the ability of those IFPs to separate olefin-paraffin mixtures. However, it can be seen that the selectivity is dependent on the bulk phase composition which is important since a change in selectivity removes the advantage of those materials for this specific separation problem. In Figures 6.18 and 6.19, the ratio of paraffin to olefin uptake, θ, in the crystal is presented as a function of (total) pressure and gas phase composition. For clarity, only the mixtures with equal or higher amount of olefin compared to the paraffin present in the gas are depicted. Values above unity mean that more paraffin is adsorbed, while more olefin is adsorbed when the values are lower than one, resulting in a change in selectivity once that threshold is crossed. As expected, θ is decreasing with increasing pressure, since the larger paraffins are replaced by the smaller olefins because of packing effects for all crystals and types of mixtures. In the case of C_2 mixtures (Figure 6.18), the results for all materials are basically the same: Increasing the olefin fraction leads to the reduction of the ratio θ. Compositions of 3:1 in favor of the olefin result in ratios θ below 1 for the investigated pressure range meaning that more olefin is adsorbed. The limit for this phenomenon is an olefin-paraffin mixture of 2:1 where θ reaches approximately 1 at 10 bar. As for C_3 mixtures (Figure 6.19), the situation is slightly different since the general selectivity for the separation of propene from propane is not as pronounced as for the C_2 molecules. Consequently, across all four materials, the ratio θ is below one at relevant pressures above 0.1 bar except for equimolar composition. At a total pressure of 10 bar, the ratio is also approximately one. In conclusion, the investigated adsorbents are capable of separating ethane/ethene mixtures with high ethene concentration (2:1). For the larger propane and propene molecules, only equimolar or paraffin-rich mixtures are suitable.

Measuring adsorption isotherms for gas mixtures is a difficult procedure. The Ideal Adsorbed Solution Theory (IAST),[71] which uses (classical) isotherm functions as input, is a tool to predict multicomponent adsorption isotherms based on adsorption isotherms of the pure components. In order to check whether IAST is applicable for the investigated systems, the isotherms generated using IAST were compared to the aforementioned GCMC results of binary mixtures of ethane/ ethene and propane/propene with equimolar, olefin-rich and paraffin-rich gas phase. The results for the C_2 molecules from simulation and IAST (Figure 6.16) agree very well for all gas compositions and materials. The slightly less accurate results in the case of IFP-7 can be attributed to the fact that the isotherm fits are not as good as for the other three materials. Unfortunately, the agreement for the C_3 mixtures (Figure 6.17) is not very good, because the fit of the simulation data to Langmuir, Freundlich or SIPS isotherms were not accurate. As a result, the trend of the GCMC data are reproduced and the absolute values are overpredicted for the olefin and underestimated for the paraffin. The worst agreement is found for IFP-7. Taking all into consideration, IAST is valid only for the smaller C_2 molecules whereas for the C_3 molecules the accuracy is not satisfactory. However, the trends are reproduced.

6.3.3 Experimental breakthrough experiments

The breakthrough experiments of binary gas mixtures for IFP-1, IFP-3, and IFP-5 show, as predicted from the pure component and mixed-GCMC isotherms, a higher retention of ethane compared to ethene. The breakthrough of ethene is generally followed by an overshoot that decays to the inlet concentration. The highest overshoot is observed for IFP-1 followed by IFP-3 and IFP-5. There is no overshoot measured for IFP-7. As a result, the separation of ethane/ethene is feasible with IFP-1, IFP-3, and IFP-5 (Figure 6.9(a)-(c). IFP-7, on the other hand, does not separate an equimolar gas mixture, but the paraffin shows a slightly faster breakthrough compared to the olefin (Figure 6.9(d). This was also implied by the pure component isotherms. For all breakthrough experiments the adjusted retention time is displayed which was calculated by the total, measured retention time minus the dead time of the experimental setup.

The results in Figure 6.9 show the largest delay between olefin and paraffin breakthrough for IFP-1 (Figure 6.9(a). The delay for IFP-3 (Figure 6.9(b) seems to be somewhat smaller compared to the measurement of IFP-5 (Figure 6.9(c). This matches with insight gained from the pure component isotherms showing a related selectivity at 1 bar. Moreover, the different retention times

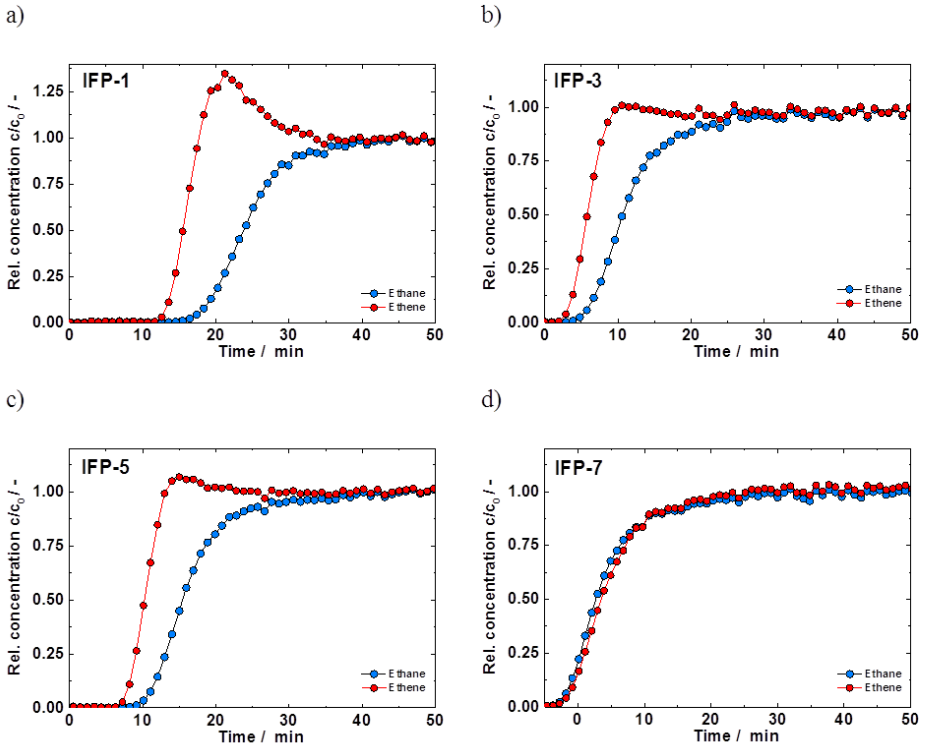

Figure 6.9: Binary breakthrough experiments for an equimolar ethane/ethene mixture at 30°C.

are in line with the difference in uptake of the different isotherms; therefore IFP-1 has the largest retention time followed by IFP-5, IFP-3, and IFP-7. The short retention time of IFP-7 is in contrast to the similar uptake capacity of the isotherms of IFP-5. This can be tentatively explained by a slower diffusion into the pore structure which was also observed for the adsorption isotherms, where equilibrium times were significantly larger. Because of this low retention and axial dispersion effects, parts of the breakthrough curves are related to negative time values using the adjusted retention time in figures. Compared to other porous materials the IFP-1 exhibits better separation performance than ZIF-8[45] but a similar separation behavior like ZIF-4 as reported by Hartmann et al.[302]

6.4 Conclusions

Four materials of the IFP family, namely, IFP-1, IFP-3, IFP-5, and IFP-7, were studied with respect to their olefin paraffin separation potential. All materials possess the same topology and vary only by the substituent of the linking molecules protruding into the channel allowing systematic investigation of their influence on adsorption properties of light hydrocarbons. The shapes of the adsorption isotherms for ethane, ethene, propane and propene as well as saturation capacities are quite similar for the four porous materials. It was found that ethane is more favorable adsorbed compared to ethene. This is also true for the C_3 molecules as is evident from the isosteric heats of adsorption. However, since the saturation capacities for propane and propene are reached at low pressures, no separation effect is observed. On the contrary, the selectivity is shifted toward the olefin, as the smaller olefin has a slightly higher saturation loading than the paraffin. The results obtained by grand-canonical Monte Carlo simulations reproduce well the experimental adsorption isotherms. However, the agreement between experiments and calculations for the C_3 molecules in IFP-7 is not as good as for the other materials. It is likely that the reason for the observed discrepancy is the flexibility of the framework, which is neglected in the calculations. Calculating isosteric heats of adsorption and free energy profiles at zero loading show that guest molecules adsorb close to the part of the linker protruding into the channel. The effect of changing the metal-ion from zinc to cobalt is not as strong as a change of the organic linker as evident from the calculated adsorption enthalpies and pore volumes. GCMC simulations for the binary system and experimental breakthrough curves confirm the fact that the potential of those structures for the separation of olefin/paraffin mixtures, IFP-1 in particular, is high.

6.5 Supporting information

6.5.1 Geometric properties of IFP-1, IFP-3, IFP-5, and IFP-7

Table 6.1: Geometric properties of IFP-1, IFP-3, IFP-5, and IFP-7 based on zeo++.[338,339]

Structure	Helium void fraction (-)	Channel size (Å)	Largest sphere along channel (Å)
IFP-1	0.457	4.21	7.72
IFP-3	0.411	3.22	7.78
IFP-5	0.437	3.97	7.60
IFP-7	0.344	2.23	6.65

6.5.2 Nitrogen adsorption

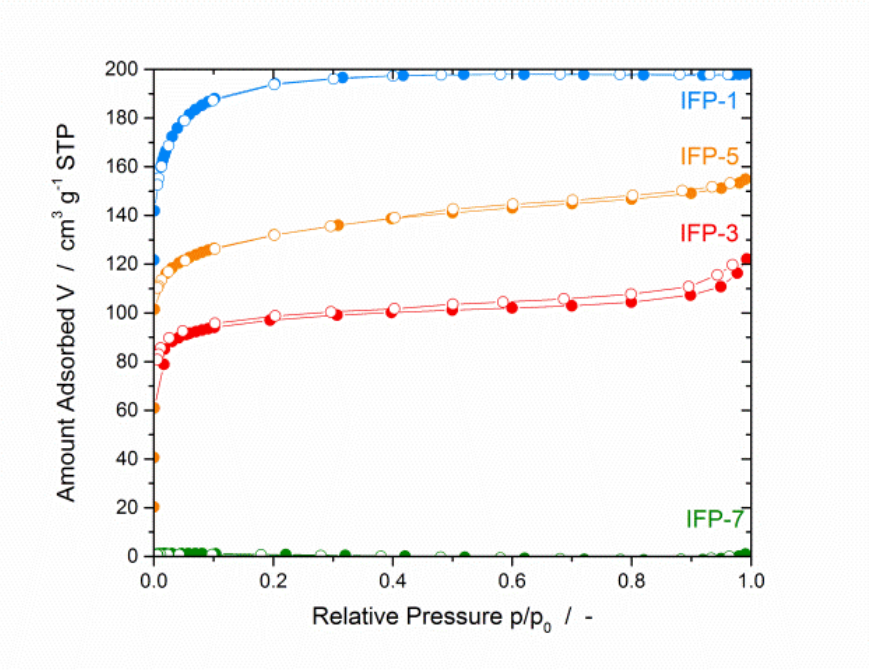

Figure 6.10: Nitrogen adsorption and desorption isotherms at 77 K for IFP-1, IFP-3, IFP-5 and IFP-7.

6.5.3 Selectivity and pore diameters

Table 6.2: Separation factors at zero loading and channel diameter for IFP-1, IFP-3, IFP-5, and IFP-7.

	IFP-1	**IFP-3**	**IFP-5**	**IFP-7**
$\alpha_{Ethane/Ethene}$ / (-)	2.60	2.45	2.17	1.87
$\alpha_{Propane/Propene}$ / (-)	1.52	0.57	2.02	0.41
Pore diameter / ($\AA$)	4.21	3.22	3.97	2.23

6.5.4 Experimental isotherms for C_2 and C_3 molecules

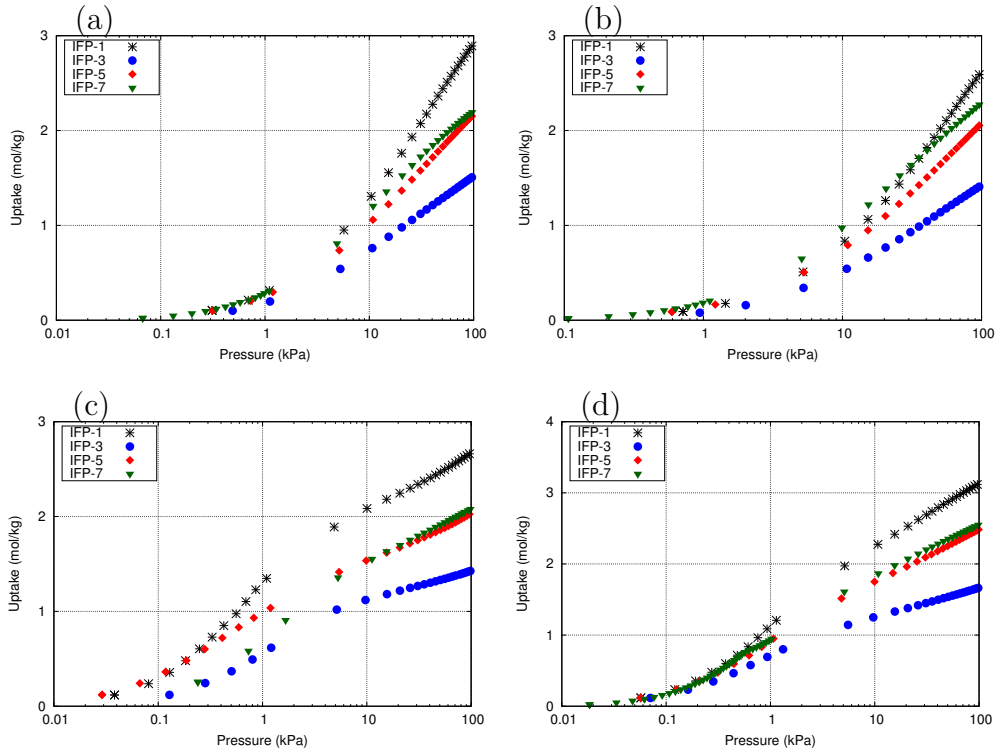

Figure 6.11: Experimental isotherms at 303 K and pressures up to 100 kPa for ethane (a), ethene (b), propane (c), and propene (d) with IFP-1 depicted as black star, IFP-3 as blue dot, IFP-5 as red diamond, and IFP-7 as green triangle, respectively.

6.5.5 Force field parameters

The force field parameters are given in Table 6.3 and 6.4. They are taken from Rappe et al.[239] and from Perez-Pellitero et al.,[320] respectively. Guest molecules, namely methane, ethane, ethene, propane, and propene, are modelled by the TraPPE united atom model of Siepmann et al.[175,325] The parameters describing interactions between different atom species are taken from Dubbeldam et al.,[326] Liu et al,[327] and Jakobtorweihen et al.[187]

Table 6.3: Lennard-Jones parameters of the framework atoms for the three force fields applied in this work are taken from Rappe et al.[239] and Perez-Pellitero et al.[320]

Framework atom	UFF		ZIF-UFF		Mod.-UFF	
	σ ($\AA$)	ϵ (K)	σ ($\AA$)	ϵ (K)	σ ($\AA$)	ϵ (K)
Br	3.732	126.308	3.545	87.153	3.639	107.362
C	3.431	52.838	3.259	36.458	3.345	44.912
Co	2.559	7.045	2.431	4.861	2.495	5.988
H	2.571	22.142	2.443	15.278	2.507	18.820
N	3.261	34.722	3.098	23.958	3.179	29.514
O	3.118	30.193	2.962	20.833	3.040	25.664
Zn	2.462	62.399	2.338	43.055	2.400	53.039

Table 6.4: Lennard-Jones parameters for the guest molecules based on TraPPE model. Cross terms are derived by Dubbeldam et al.,[326] Liu et al,[327] and Jakobtorweihen et al.[187] The first row of each cell is ϵ in (K) and the second row is σ in ($\mathring{A}$).

ϵ **in (K)** σ **in** ($\mathring{A}$)	$\mathbf{CH_4(sp^3)}$	$\mathbf{CH_3(sp^3)}$	$\mathbf{CH_2(sp^3)}$	$\mathbf{CH_2(sp^2)}$	$\mathbf{CH(sp^2)}$
$\mathbf{CH_4(sp^3)}$	148.0 3.73	not included	not included	not included	not included
$\mathbf{CH_3(sp^3)}$	not included	108.0 3.76	77.77 3.86	77.77 3.86	54.48 3.85
$\mathbf{CH_2(sp^3)}$	not included	77.77 3.86	56.0 3.96	77.77 3.86	54.48 3.85
$\mathbf{CH_2(sp^2)}$	not included	77.77 3.86	77.77 3.86	93.0 3.685	70.21 3.71
$\mathbf{CH(sp^2)}$	not included	54.48 3.85	54.48 3.85	70.21 3.71	53.0 3.74

6.5.6 Influence of the van-der-Waals parameter for bromine

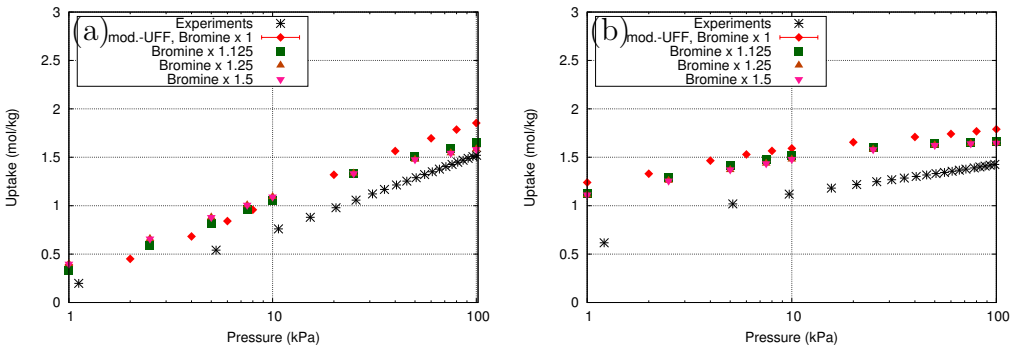

Figure 6.12: The influence of the σ parameter of the Lennard-Jones potential for bromine on the adsorption isotherm of ethane (a) and propane (b) in IFP-3 as a function of pressure at 303 K.

6.5.7 Isosteric heats of adsorption at zero loading based on simulations

Table 6.5: Isosteric heats of adsorption at zero loading based on the mod.-UFF given in $\frac{kJ}{mol}$ for IFP-1, IFP-3, IFP-5, and IPF-7.

Structure	Methane	Ethane	Ethene	Propane	Propene
IFP-1	16.9 ± 0.1	29.3 ± 0.1	25.5 ± 0.2	39.2 ± 0.1	35.4 ± 0.3
IFP-3	16.3 ± 0.1	28.3 ± 0.1	24.8 ± 0.2	37.7 ± 0.1	34.2 ± 0.1
IFP-5	16.5 ± 0.1	28.6 ± 0.1	25.0 ± 0.1	38.2 ± 0.1	34.5 ± 0.1
IFP-7	19.5 ± 0.1	33.1 ± 0.1	29.3 ± 0.1	43.5 ± 0.1	40.0 ± 0.3

6.5.8 Free energy profiles at zero loading

Ethene

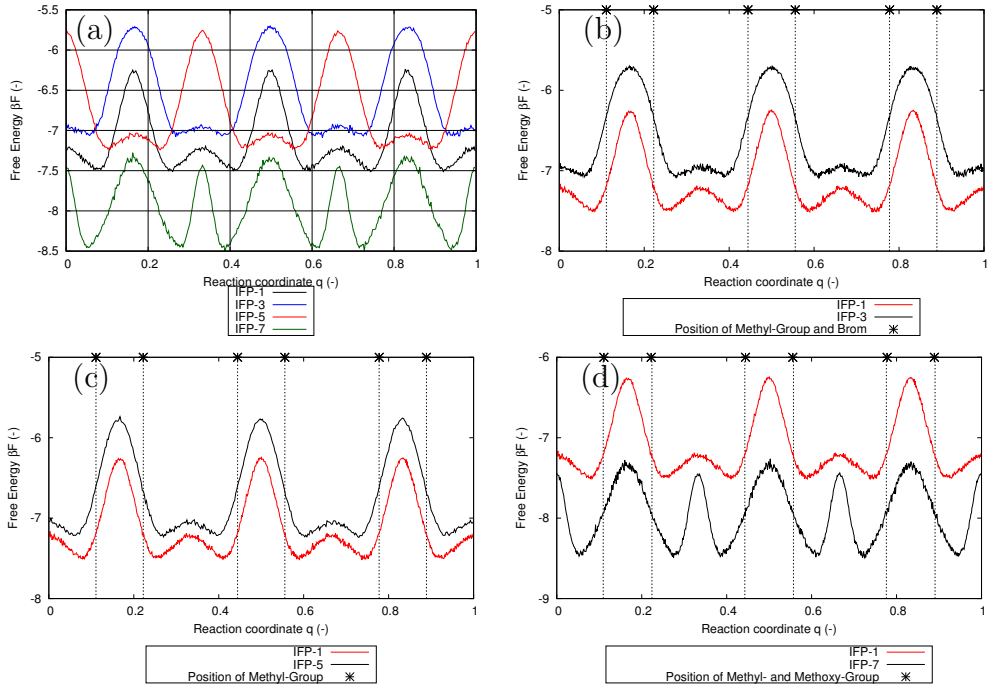

Figure 6.13: Free energy profiles at zero loading for ethene: Comparison of the four materials (a), comparison of IFP-1 to IFP-3 (b), comparison of IFP-1 to IFP-5 (c), and comparison of IFP-1 to IFP-7 (d); the (stars) on the x2-axis denote the positions of the fraction of the linker protruding into the channel.

Propane

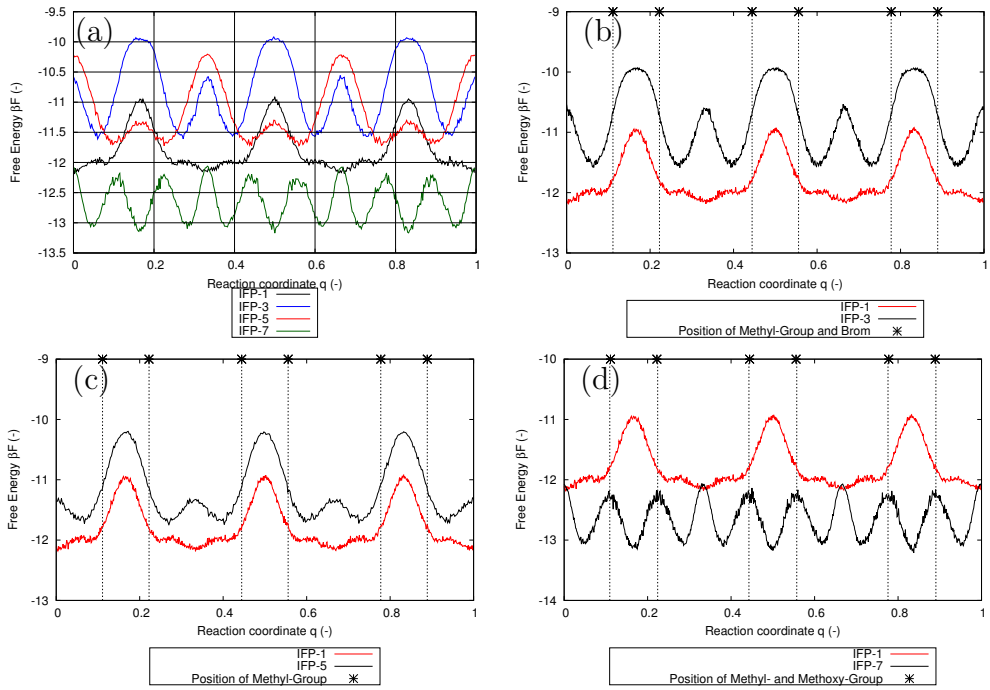

Figure 6.14: Free energy profiles at zero loading for propane: Comparison of the four materials (a), comparison of IFP-1 to IFP-3 (b), comparison of IFP-1 to IFP-5 (c), and comparison of IFP-1 to IFP-7 (d); the (stars) on the x2-axis denote the positions of the fraction of the linker protruding into the channel.

Propene

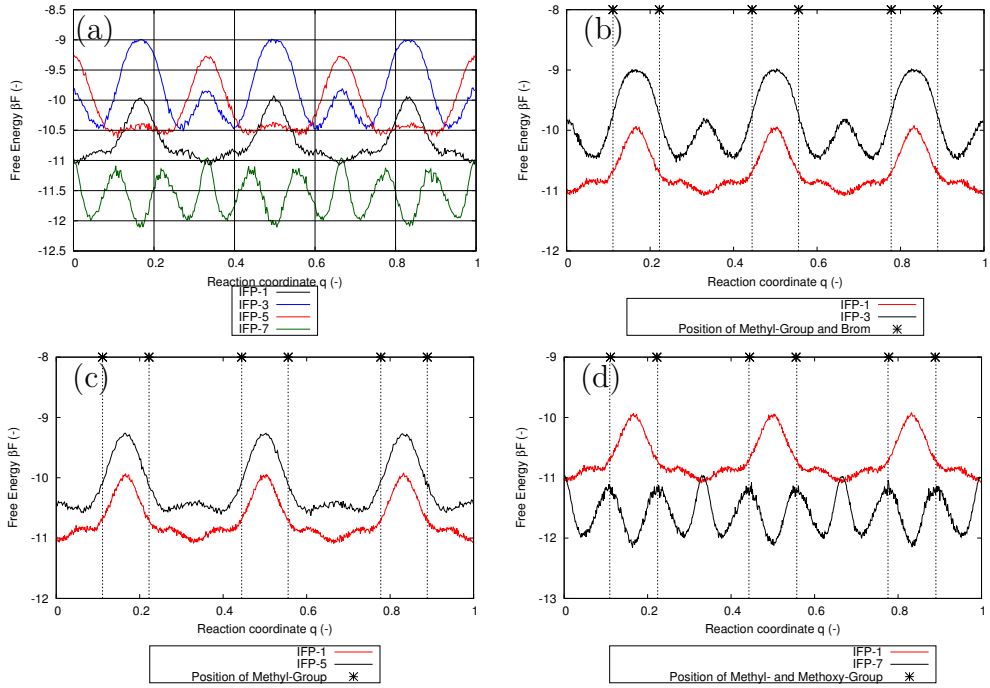

Figure 6.15: Free energy profiles at zero loading for propene: Comparison of the four materials (a), comparison of IFP-1 to IFP-3 (b), comparison of IFP-1 to IFP-5 (c), and comparison of IFP-1 to IFP-7 (d); the (stars) on the x2-axis denote the positions of the fraction of the linker protruding into the channel.

6.5.9 Comparison of mixed-GCMC with IAST

C_2 mixtures

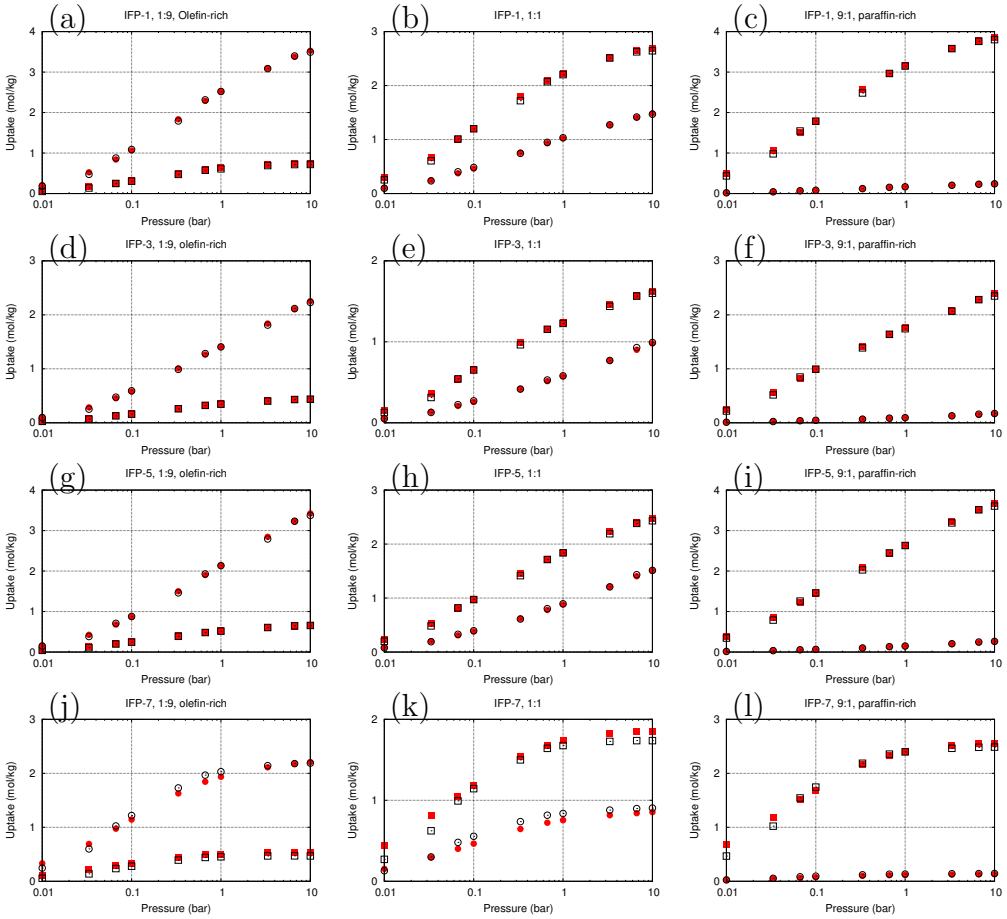

Figure 6.16: Binary adsorption isotherms in mol/kg for three compositions (paraffin/olefin ratio of 9:1, 1:1, and 1:9) at 303 K and pressures up to 10 bar based on the mod-UFF for IFP-1 (a)-(c), IFP-3 (d)-(f), IFP-5 (g)-(i), and IFP-7 (j)-(l); circles represent data for ethane and squares for ethene; open symbols are data based on IAST and closed ones based on GCMC.

C_3 mixtures

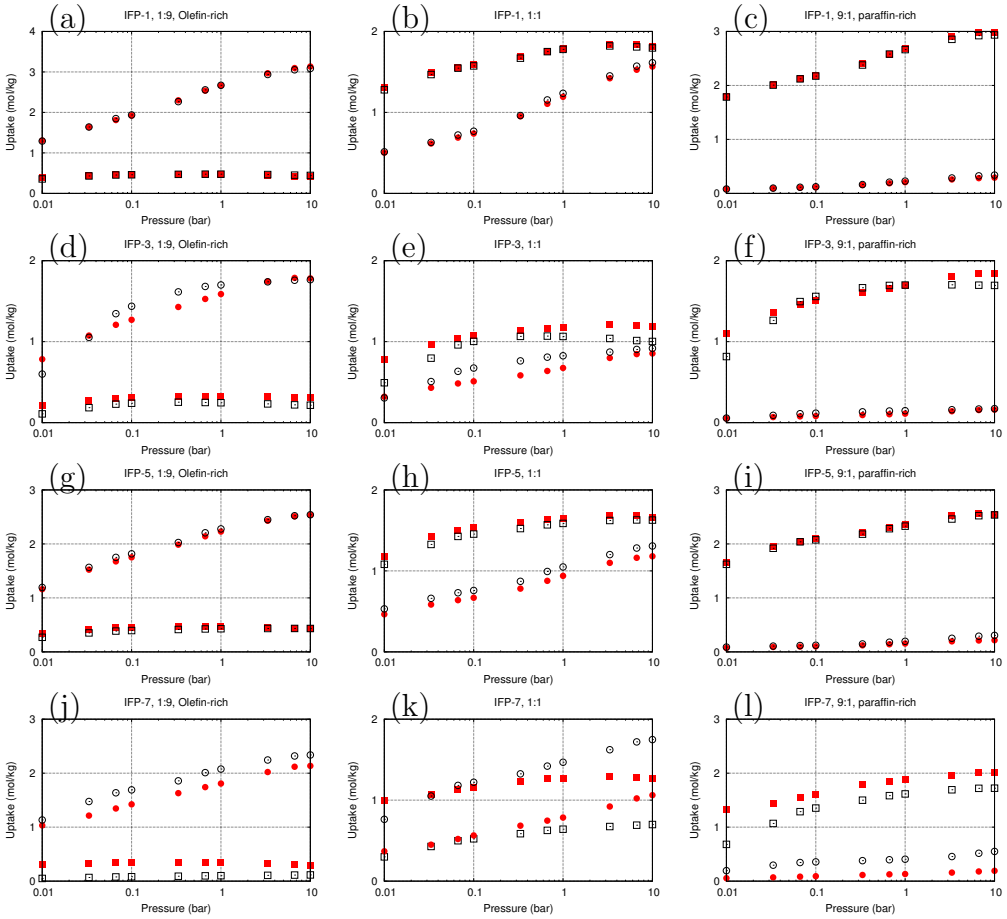

Figure 6.17: Binary adsorption isotherms in mol/kg for three compositions (paraffin/olefin ratio of 9:1, 1:1, and 1:9) at 303 K and pressures up to 10 bar based on the mod-UFF for IFP-1 (a)-(c), IFP-3 (d)-(f), IFP-5 (g)-(i), and IFP-7 (j)-(l); circles represent data for propane and squares for propene; open symbols are data based on IAST and closed ones based on GCMC.

6.5.10 Ratio of paraffin-olefin uptake for binary mixtures as a function of composition and pressure

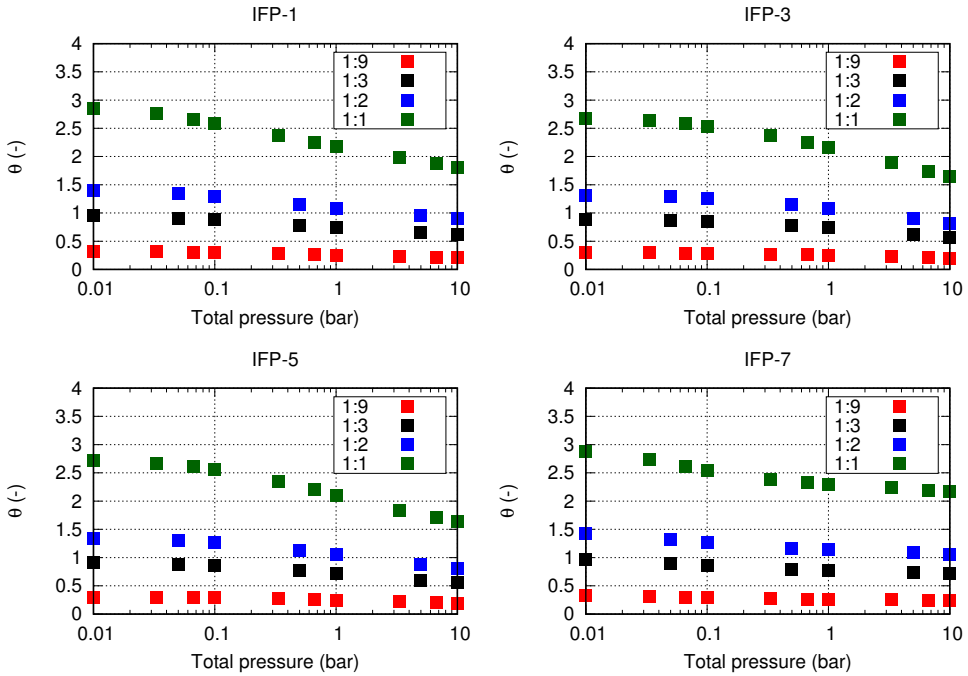

Figure 6.18: Ratio of paraffin to olefin uptake θ for binary mixtures of ethane/ethene as a function of pressure and composition at 303 K.

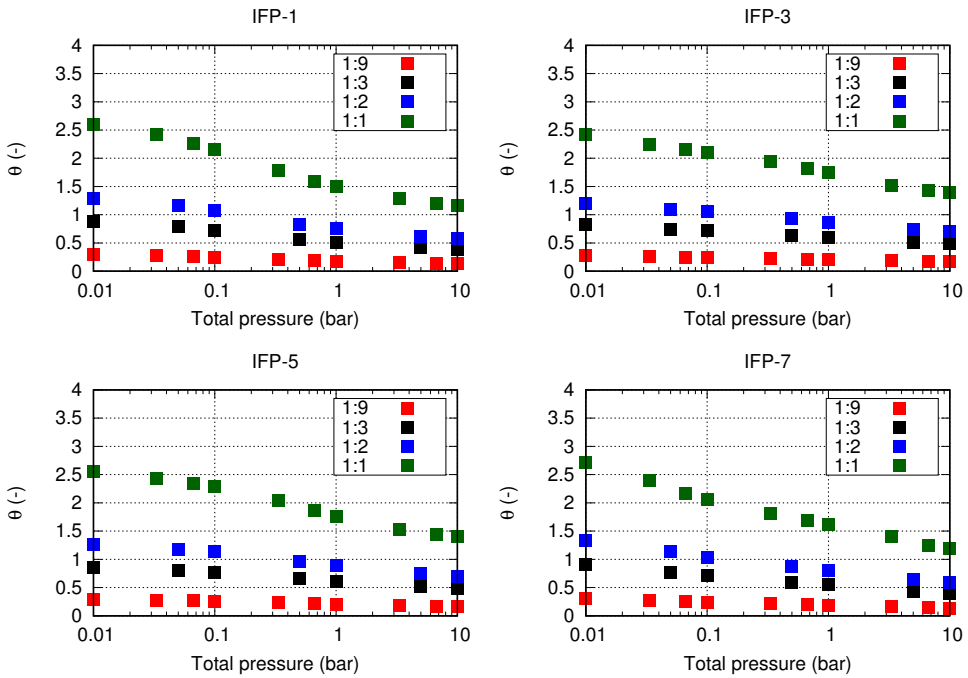

Figure 6.19: Ratio of paraffin to olefin uptake θ for binary mixtures of propane/propene as a function of pressure and composition at 303 K.

7

Diffusion of small hydrocarbons in ZIF-8, ZIF-9, and ZIF-71

Self-diffusivity for small hydrocarbons (methane, ethane, and ethene) in three nanoporous materials, ZIF-8, ZIF-9, and ZIF-71, is calculated using molecular dynamics simulations. The crystal frameworks are modelled as rigid and flexible to investigate the influence of flexibility on the transport resistance in each individual material. Modelling the frameworks in a rigid manner is not an option, since even methane is not able to move through the crystal because of the small windows connecting the pores with the exception of ZIF-71, which has larger pores in comparison. Enabling flexibility in ZIF-8 results in self-diffusivity in good agreement with experimental and simulation data from the literature whereas methane diffuses faster than ethene and ethane. In ZIF-71 the results obtained in the simulation have reproduced reference data accurately as well. Preliminary results for ZIF-9 show that when flexibility is introduced the molecules move three-dimensionally through the porous network which has not been expected from the residence plots, suggesting movement along channels.

7.1 Introduction

Olefins like propene and ethene are the two most important organic feedstocks. They are widely used precursors in the chemical industry especially for the production of plastics.[46] Thus, the separation of olefins and paraffins is one of the most important and at the same time most challenging processes in the chemical and petrochemical industry.[44,46,54] The emerging class of metal-organic frameworks (MOFs) are widely considered to fulfill requirements for this separation. They offer high porosities and surface areas, making them attractive for various applications such as catalysis, gas storage, and chemical separation.[73,88,279] Their topology consists of metal centres, which are connected to organic linkers through coordination bonds.[79] This theoretically allows to create millions of MOFs because of the ability to change the metal nodes and/or the linkers. One MOF sub-class, zeolitic imidazolate frameworks (ZIFs), exhibits a remarkable chemical and thermal stability up to 550°C in addition to the good separation potential, making them a reliable and multifunctional material.[131] Their name reveals resemblance to zeolites because their angle between the metal-linker-metal is the same as between Si-O-Si in zeolites.[133]

The adsorption behavior of gases in multiple ZIFs, e.g. N_2, CO_2, paraffins, and olefins, has been investigated for applicable separation processes in many studies.[84,133,284,288,295,299,302,303,320,324,334,340–346] As for the paraffin/olefin separation, ZIFs were found to adsorb paraffins preferentially.[73,288,295,299,302,334] Based on that, Hartmann et al.[302] proposed the possibility to obtain the desired olefins with a high pressure stream in pressure swing adsorption (PSA) processes. The separation performance, however, is influenced by diffusion as well, since adsorption and diffusion are connected to each other: In general, if a molecule is strongly adsorbed, it diffuses slower and vice versa. Hence, diffusion studies focusing on ZIFs have been published also with respect to paraffin/olefin separation.[77,81,85,86,88,266,347,348] These observations were also found in Chapter 5. One of the most investigated ZIF to date is the ZIF-8. It has outstanding chemical, thermal, and long-term stability, and could potentially be synthesized economically. In addition, it allows a good separation performance so that it is a serious candidate for adsorption based processes.[299] Most research related to ZIF-8 focused on the purification of natural gas meaning the separation of methane and carbon dioxide.[82,84,319,320,324,342,344,349–352]Therefore, Jobic et al.[353] deployed quasi-elastic neutron scattering (QUENS) to trace the way of diffusing CH_4 molecules in ZIF-8. Other experimental studies report that molecules, like methane or even bigger ones with a kinetic diameter up to 6.7 $\AA$, were able

to surpass the smaller pore apertures.[73,82,84,136,342,347,353]

ZIFs are known to be flexible compared to the rather stiff zeolites enabling molecules to surpass pore windows, which are even bigger than the window itself.[354] This phenomenon was observed in experiments for example in ZIF-8 whose pore window diameter is estimated to be 3.4 $\AA$. Larger molecules like methane (critical diameter 3.6 $\AA$) and n-alkanes are adsorbed despite being too big for the gates or windows, respectively. This is called gate-opening effect.[73,82,84,342,347,353] The biggest observed molecule diffused in ZIF-8 so far was a xylene isomer with a kinetic diameter of 6.7 $\AA$.[136] This implies an immense influence of flexibility on the crystal. In the literature, this phenomenon is known as the gate-opening or saloon-door effect as is described in several studies.[88,136,279] Peralta et al.[136] even observed a structural change in topology at high loadings of N_2 at 77 K, leading to a higher diffusivity. Obviously, diffusion simulation studies have to model the framework as flexible to deliver reliable data. In adsorption simulations, however, the influence of flexibility showed to be negligible as Zhang and coworkers[344] pointed out. They did not find a significant deviation between a flexible and rigid framework in their CO_2/CH_4 separation study, which also correlated in good agreement to experimental results. Thus, assuming rigidity of the host atoms in molecular dynamics simulations would lead to the problem that molecules known to diffuse in ZIF-8 like methane would not fit through the windows.[137,266,324,344,347,349,350,355] But even if the window size is not the hindrance of diffusion, Amirjalayer et al.[267] reported a significant difference in the diffusion of benzene in MOF-5. Because of the flexibility of the framework, pockets were formed in the MOF in which the benzene adsorbed leading to a lower diffusivity than anticipated. Therefore, it is crucial to apply flexibility to the host framework to gather reliable information about diffusion. The simulation work of Verploegh et al.[88] investigated the diffusion of paraffins and olefins in ZIF-8 respective to their temperature- and loading-dependency. Thereby, they stated that the activation energy for diffusion is almost linearly ascending with a rising kinetic diameter offering an explanation for the paraffin selectivity. They also showed via dcTST simulations a decrease of the free energy at the aperture with rising temperature but also a corresponding increase of the transmission coefficient κ.

Other potential candidates for paraffin/olefin separation are ZIF-9 and ZIF-71 as shown in Chapter 5. We reported adsorption isotherms for ethane/ethene and propane/propene showing an adsorption selectivity towards the paraffins. The crystal has been investigated for different fluids in the past.[284,303,334,340,341,345,356] Calero and Gomez-Alvarez[340] studied the adsorption of water in ZIF-71 and ZIF-90. Via MC simulations they conlculded that

ZIF-71 is hydrophilic. The research group of Houndonougbo[284] performed a combined experimental-computational investigation of methane and carbon dioxide adsorption in ZIF-25, -71, -93, -96, and -97. As a result, the adsorption of CH_4 is roughly linear to the BET surface area, independent of functionalization, whereas the symmetry of the ZIF-71 caused a lower CO_2 adsorption. Japip et al.[303] reported for ZIF-71 a significantly higher diffusivity towards olefins in ethene/ethane and propene/propane separation in mixed-matrix membranes based on ZIF-71. The work of Ray et al.[356] is the only one, which applied Molecular Dynamics to determine CO_2/CH_4 diffusion selectivities in rigid ZIF-71 to the best of our knowledge.

The development of suitable parameters for simulations has been crucial since the beginning. In MC simulations the flexibility usually does not make any significant difference. Most of the time only Lennard-Jones parameters are needed because the lattice is kept rigid. The most commonly used force fields are DREIDING[240] and the Universal Force Field (UFF),[239] for MD simulations the AMBER[357] and DREIDING force field. Each one offers more or less results correlated to experimental data. Therefore, the generic force fields reach their boundaries in specific situations as the flexibility of crystals is introduced. While these force fields have been tested, new parameters or even completely new force fields have been developed recently to include flexibility of the crystals. Hu et al.[358] parametrized effectively three force constants for ZIF-8 involving Zn atoms by fitting them to experimental lattice constants, whereas all other parameters were taken from the AMBER force field. The same approach was used by Krokidas et al.:[77] they employed DFT and ab initio calculations to fill up the list of missing parameters and geometries in the AMBER force field, respectively.

In this chapter the diffusion coefficients of methane, ethane, and ethene in ZIF-8, ZIF-9, and ZIF-71 are calculated using molecular dynamics simulations and compared to experimental data if present. The aim of the study consists of validating the used force fields, describing the phenomenon of loading dependency, and performing the first molecular dynamic simulations in a fully flexible ZIF-9 and ZIF-71, respectively.

7.2 Simulation details

Since adsorption studies using simulations related to nanoporous materials commonly show a very good agreement with experimental data by modelling the host lattice as being rigid, there is no need to use the more complicated model of a flexible crystal, so that only Lennard-Jones parameters and

atomic charges are required.[251,344] In general, rigid means that the framework is frozen at the crystallographic positions, whereas in a flexible model there are no such constraints. In MD simulations, however, one can receive different results compared to experiments when omitting structural flexibility. One example is the diffusion of methane through pore apertures of ZIF-8, even though the average aperture diameter is smaller than the molecule. Therefore, the display of structural flexibility in this work was established by using the Universal Force Field (UFF) by Rappe et al.[239]

The crystal structure of ZIF-8, ZIF-9, and ZIF-71 were taken from Park et al.[131] and Banerjee et al.,[33] respectively. As a reminder, in Table 2.4 the unit cell dimensions for the crystals are given. In Figure 2.7, one can see the unit cells of all three ZIFs. Note, that there is no observable bond between zinc and nitrogen, since it is an ionic bond. In the Figures 5.14, 5.15, and 5.16, the atom types for each linker according to the force fields is defined and illustrated.

The hydrocarbons methane, ethane, and ethene were described by the force field found in references 326 and 327, which is an evolution of the TraPPE force field.[175] The corresponding force fields are given in Table 7.5. The UFF[239] is a common used force field in adsorption and diffusion studies, which predicts relatively good results, which are in line with experimental data.[334] Better agreement was found by scaling the UFF down by multiplying ϵ with 0.69 and σ with 0.95.[334] LJ parameter sets are found in Chapters 7.5.1, 7.5.3, and 7.5.4 for ZIF-8, ZIF-9 and ZIF-71, respectively. To predict flexible behavior of the crystal the bond and angle force constants, $k_{ij}^{stretch}$ and k_{ijk}^{θ}, the bond length in equilibrium, b_{ij}, and the angle in equilibrium, θ^0, were calculated from the UFF as described by Rappe et al.[239] The UFF and the modified-UFF share the same intramolecular forces and constants. Dihedrals and point charges are not sufficiently described so that one has to rely on other sources. For the dihedrals we took the values given by Krokidas et al.,[77] which again are based on the AMBER[357] force field. Some of the required dihedral parameters were not given, so that different values of the missing force constants were estimated and tested. The point charges for all ZIF-8 simulations were adopted from Krokidas et al.[77] as well. For the ZIF-71 the atomic charges of Ding et al.[341] were implemented, whereas for ZIF-9 they were obtained via the REPEAT method.[181]

The self diffusion coefficients D^S were obtained from MD simulations in the NVT-ensemble. The MD simulations were carried out by the simulation package GROMACS. Before starting a MD run, a MC simulation program was used for 10^5 cycles to get an equilibrated starting configuration of the respective system. All settings, which are described in the following, for

GROMACS apply for the in-house MC code as well, if the options were required.

For integrating the equations of motion the velocity-Verlet algorithm was employed with a time step of 1.0 fs. The standard simulation time was 10 ns long which proved to be sufficient in these cases. If the MSD plot did not show the desired linear trend over a sufficient period of time, the simulations were extended. Periodic boundary conditions were applied in all directions. The cut-off radius for the intermolecular interactions was set to 1.3 nm whereas the potentials were shifted and truncated. The calculation of the electrostatics was realized by Particle-mesh Ewald technique,[189] and for the LJ parameters the Lorentz-Berthelot mixing rules were used. Only 1-4 interactions were considered. The temperature was set to 298 K and controlled by a Nose-Hoover chain thermostat for every 0.1 ps. To extract the self-diffusivity out of the simulated trajectories the mean-squared displacement (MSD) was calculated. In contrast to Mg-MOF-74, see Chapter 4, the movement of guest molecules in ZIFs is not restricted to a specific direction, e.g. the z-axis. Thus unless specifically mentioned, the self-diffusion coefficient takes all directions into account. That means D_{xyz}^{self}=D^{self}. By employing a order-n algorithm in the main phase in which the slope in log-log-scale is one the self-diffusion coefficient is finally obtained using the Einstein equation:[159]

$$D_{xyz}^{self} = \frac{1}{2 \cdot 3} \cdot \lim_{t \to \infty} \frac{\partial \langle \Delta \mathbf{r}_i^2(t) \rangle}{\partial t} \tag{7.1}$$

The minimum size for a simulation box in the present case is 2x2x2 unit cells. This is because of the cut-off radius, which has to be smaller than half of the simulation box. Otherwise finite size effects can occur.[159] As a minimum, the loading of such a simulation box was chosen to be 64 molecules to get good statistics. The box size and the amount of molecules were adjusted in the respective way to gather loadings from 0.5 up to $20 \frac{mole}{UC}$ for the ZIF-8 and from 0.65 up to $75 \frac{mole}{UC}$.

7.3 Results

7.3.1 ZIF-8

Methane

In order to use a force field, it has to be verified as reliable against literature data. This was done by comparing the obtained results of the most studied hydrocarbon methane in ZIF-8. The force field developed by Krokidas

et al.[77] was used as a guidance since they are the only research group using GROMACS for MD simulations as far as we know. In Figure 7.1, the obtained self-diffusivities over a loading range from 0.5 to 15 molecules per unit cell $\left(\frac{mole}{UC}\right)$ are compared to simulation and experimental data. Since adsorption studies found a saturation loading of about 14 $\frac{mole}{UC}$, most of the investigations set their loading limit in this region. Verploegh et al.[88] chose to carry out simulations up to a loading of almost three-times above the saturation loading, which is referred to as a liquid phase.

In Figure 7.1 an increasing diffusivity can be observed with higher loadings as an overall trend. Because of the exceptional high loading chosen by Verploegh et al.[88] the diffusivity decreases finally. At this point the cages are filled up with molecules to a maximum, which leads to a decrease of the self-diffusion because of sterical hindrance.

The UFF shows great agreement compared to most of the studies. It can be seen as an average of all collected literature data. At low loadings the values are almost the same as the experimental data from Jobic et al.[353] ($\sim$ 1 x $10^{-10}\frac{m^2}{s}$). At a loading of 10 $\frac{mole}{UC}$ the experimental data increases sharply, whereas the UFF has a more or less constant slope. The simulations based on mod-UFF, however, are about one magnitude higher than the average region of 1 x $10^{-10}\frac{m^2}{s}$ and at the same time higher than the ones from UFF. It is important to note that synthesized crystals like the ZIF-8 exhibit defects in their topology, which leads to a decrease of the self-diffusion in comparison to perfect crystals assumed in simulations. Hence, a higher diffusivity as found for the mod-UFF is not a criterion for exclusion, especially when adsorption studies are taken into consideration, which exhibit good adsorption agreement for the mod-UFF to experimental results.[320,334]

The same studies also report that methane adsorption in ZIF-8 based on the mod-UFF is weaker than simulations based on the UFF, which consequently means that the diffusion in the mod-UFF must be faster than in the UFF. By comparing both force fields only the intermolecular van-der-Waals LJ parameters are lower in the mod-UFF while the intramolecular ones are the same. This indicates a strong and sensitive influence of the van-der-Waals interactions on the diffusion behavior.

The results gathered by using the force field of Krokidas et al.[77] do not show a clear trend for the investigated loading range. Methane exhibits a slight loading dependency as the diffusivity increases with higher loadings, see Figure 7.2. This is true for both UFF force fields. The loading dependency has been observed in ZIF-8 for all three hydrocarbons as found in the computed results as well as in literature. Different explanations have been formulated in various studies to explain this behavior. Pusch et al.,[82] who

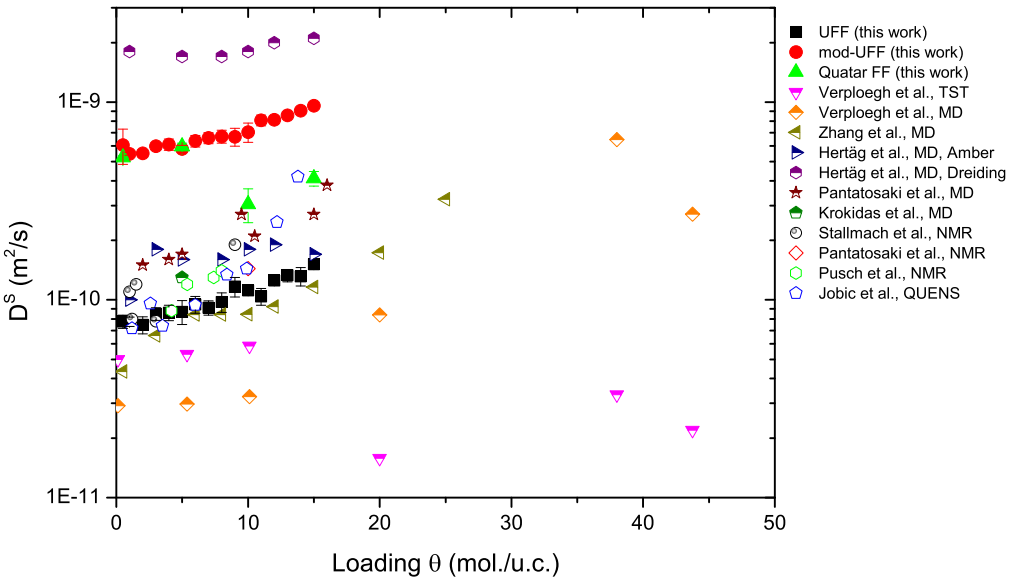

Figure 7.1: Comparison of the self-diffusion coefficients D^S for methane as a function of loading in ZIF-8 at around $T = 300K$. Full symbols represent values obtained in this work. Simulation data (top half full) were taken from Verploegh et al.,[88] Zhang et al.,[344] Hertäg et al.,[319] Pantatosaki et al.,[351] and Krokidas et al.[77] Experimental data (open symbols) were taken from Stallmach et al.,[352] Pantatosaki et al.,[351] Pusch et al.,[82] and Jobic et al.[353]

studied the diffusion of methane and carbon dioxide in ZIF-8, suggested that at higher loadings the probability of one molecule pushing another through a window becomes higher leading to a larger diffusivity. Thereby, the pushing molecule remains in the original cage. A more sophisticated answer was given by Zhang et al.,[344] who examined adsorption and diffusion of the same molecules. By computing free energy profiles at different loadings of methane they were able to show a decrease of the free energy barrier for diffusion near the aperture with increasing loading. This coincides with the observation of preferentially adsorbing methane molecules near the pore apertures as Bux et al.[84] presented. The same phenomenon of a decreasing free energy barrier of diffusion with increasing loading was detected for the bigger hydrocarbon propane by Verploegh et al.[88] In addition, they noted an opposing decrease of the transmission coefficient κ at the same time because of enhancing adsorbate-adsorbate interactions. However, the decrease of the free energy barrier was found to be larger than the one of the transmission coefficient κ because of which an increasing diffusivity can be recognized with

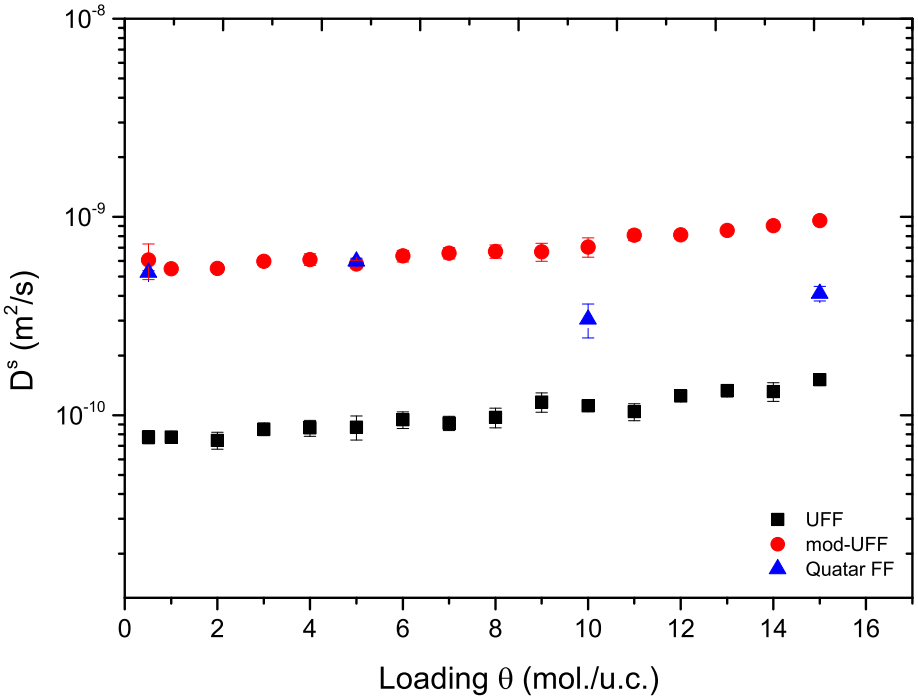

Figure 7.2: Methane self-diffusion coefficients D^S as a function of loading for the investigated force fields UFF, mod-UFF, and Quatar FF[77] at $T = 298\ K$.

increasing loading. In other words: By reducing the resistance to overcome the pore window because of more molecules it is easier for a single molecule to hop from one cage to another. At the same time there are more molecules in the adjacent cage, which can either push a surpassing molecule back into its origin cage or they block the aperture themselves. In the present case the diffusivity increases because more molecules successfully hop from one cage to another than being pushed back.

Methane is the smallest molecule among the examined hydrocarbons. As aforementioned in Chapter 7.1, even methane is too big to overcome a pore in a rigid ZIF-8 framework. A set of test points were computed for demonstration. Figure 7.3 (a) shows exemplarily the MSD plot for methane in rigid ZIF-8 at a loading of $5\frac{mole}{UC}$. There is a sharp increase of the MSD in the very first picoseconds before it stagnates for the rest of the simulation.

The methane molecules are only able to move inside of the cage. As soon as the molecules hit the walls including the insuperable pore apertures in case of a rigid ZIF-8 they are trapped in the cages. Therefore, they reach in

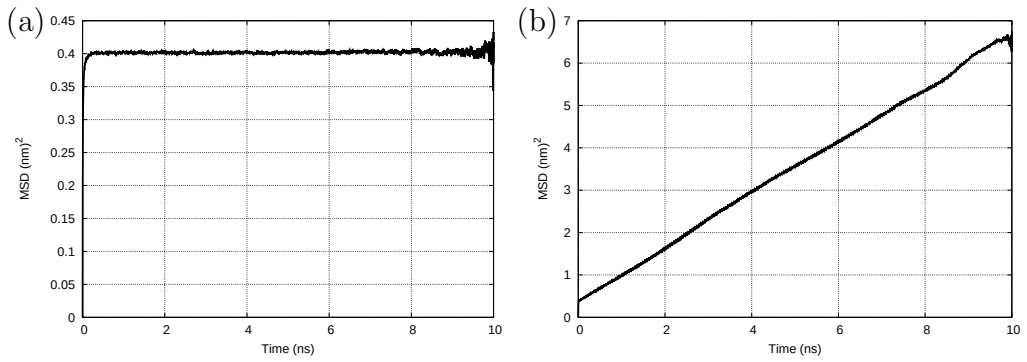

Figure 7.3: MSD plots for methane in ZIF-8 with a loading of $5\frac{mole}{UC}$; (a) shows a rigid framework and (b) a flexible one.

the very first picoseconds their maximum displacement, which is the distance from one end of the cavity to the opposite one. As a result, computing the self-diffusion coefficient D^S is meaningless, so that there have not been MD simulations conducted in a rigid ZIF-8 for the even bigger molecules ethane and ethene. Figure 7.3 (b) illustrates the MSD plot with the same conditions as before except that the crystal is flexible. The MSD has an almost linear course over the examined time.

In conclusion, the newly implemented force field parameters for the flexibility of the ZIF-8 derived from the UFF illustrate in good agreement compared to other simulations as well as to experiments regarding methane.

Ethane and Ethene

Similarily to methane, the self-diffusion coefficients of ethane and ethene were computed in a flexibly modelled ZIF-8. The maximum loading was again the saturation loading of ethane and ethene of about $20\frac{mole}{UC}$. In Figure 7.4, one can see the self-diffusion coefficients D^S of ethane and ethene as a function of loading. Results obtained from both force fields and both species show the same trend: Before the D^S is increasing at $10\frac{mole}{UC}$ it remains nearly constant to about $10\frac{mole}{UC}$; with increasing loading D^S increases. Thereby, it is observable that the UFF simulations have a somewhat steeper slope than the mod-UFF, which can be explained by the loading dependency. Since the LJ parameters are higher for the UFF than for the mod-UFF and both molecules exhibit higher values for the parameters than methane as well, the free energy barrier at the pore window is higher because of the stronger guest-host interactions in the case of the UFF. Therefore, a higher loading decreases

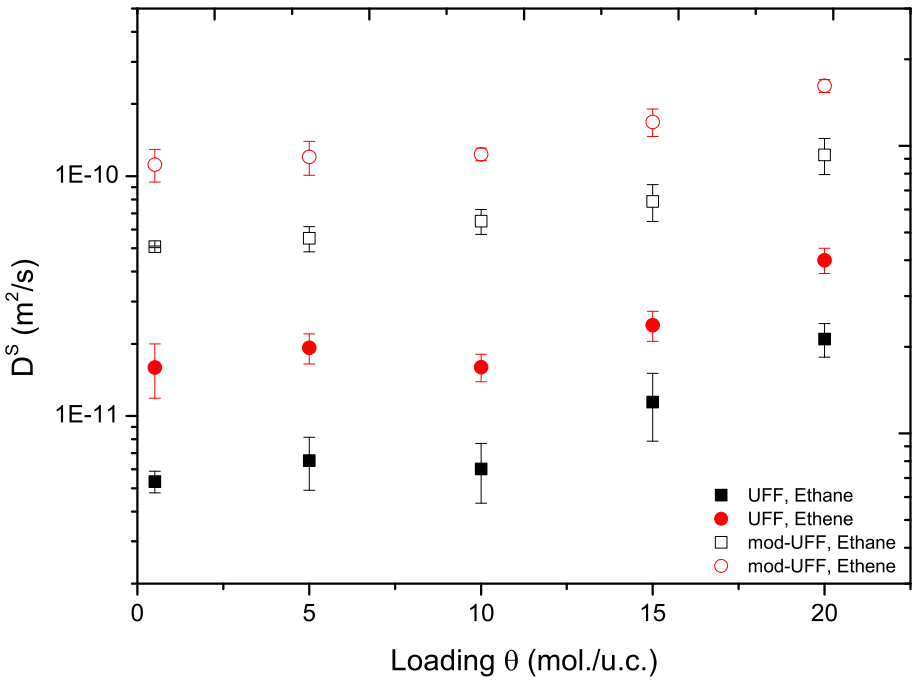

Figure 7.4: Ethane and ethene self-diffusion coeffients D^S in the investigated force fields UFF and mod-UFF as a function of loading at $T = 298\,K$.

more significantly the energy resistance for molecules to diffuse through the window. As a consequence, the mod-UFF is almost one magnitude higher than the UFF.

Comparing the ethane and ethene diffusion behaviour, ethene exhibits approximately twice the value for the self-diffusion coefficient D^S of ethane: for instance at the lowest loading of 0.5 $\frac{mole}{UC}$ the UFF predicts for ethene a diffusivity of 1.6 x $^{-11}\frac{m^2}{s}$ and ethane to 5.3 x $^{-12}\frac{m^2}{s}$. This is in line with adsorption works, which state a paraffin selective adsorption in ZIFs, which consequently implies a lower diffusivity.[73,85,135,288,299,302] These adsorption studies and those studies examining the diffusion explain the kinetic selectivity by the size difference between paraffins and olefins.[77,85,88,266,295,348] Furthermore, Chmelik et al.[81] reported a higher activation energy for diffusion for ethane in comparison to ethene in ZIF-8 offering a thermodynamic interpretation. The same was found for propane and propene, respectively, by Li et al.[295] and Krokidas et al.[77] Also, Verploegh et al.[88] support the observations by stating that the activation energy of diffusion is linear ascending with rising kinetic diameter.

Figures 7.5 and 7.6 show the data obtained in comparison to the literature

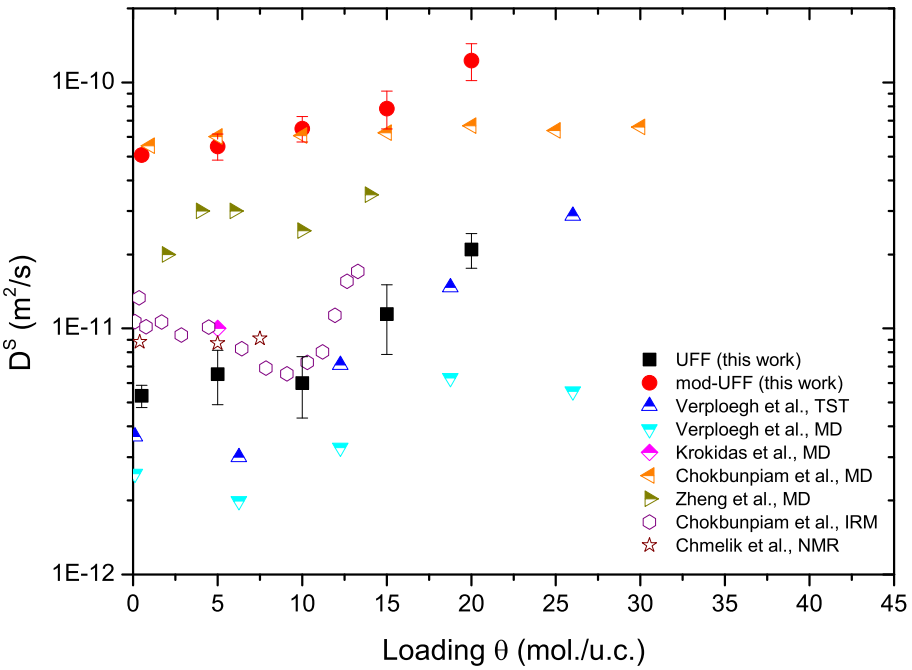

Figure 7.5: Comparison of the self-diffusion coefficients D^S for ethane as a function of loading in ZIF-8 at around $T = 300\ K$. Full symbols represent values obtained in this work. Simulation data (top half full) were taken from Verploegh et al.,[88] Krokidas et al.,[77] Chokbunpiam et al.,[347] and Zheng et al.[266] Experimental data (empty) were taken from Chokbunpiam et al.,[347] and Chmelik et al.[359]

for ethane and ethene, respectively. The UFF describes the self-diffusivity slightly slower than the experimental reports whereas the simulation data are scattered around 1 x $10^{-11} \frac{m^2}{s}$. The mod-UFF predicts the highest values. A trend of increasing diffusivity with higher loadings is also observed for the data provided by Verploegh et al.[88] and Chokbunpiam et al.[347] The course published by Zheng et al.[266] exhibits a local maximum as found for the UFF. For the self-diffusion of ethane the UFF is within the range of the documented values whereas the mod-UFF seems to be too high compared to the available data.

Self-diffusion coefficients for ethene in ZIF-8 reported in literature are quite rare in comparison to ethane and methane as can be seen in Figure 7.6. Note, in that case there is no experimental data. Again, the simulation data based on the UFF agree well with the literature data and the ones based on the modified UFF are the highest ones. The courses of Verploegh et al.[88]

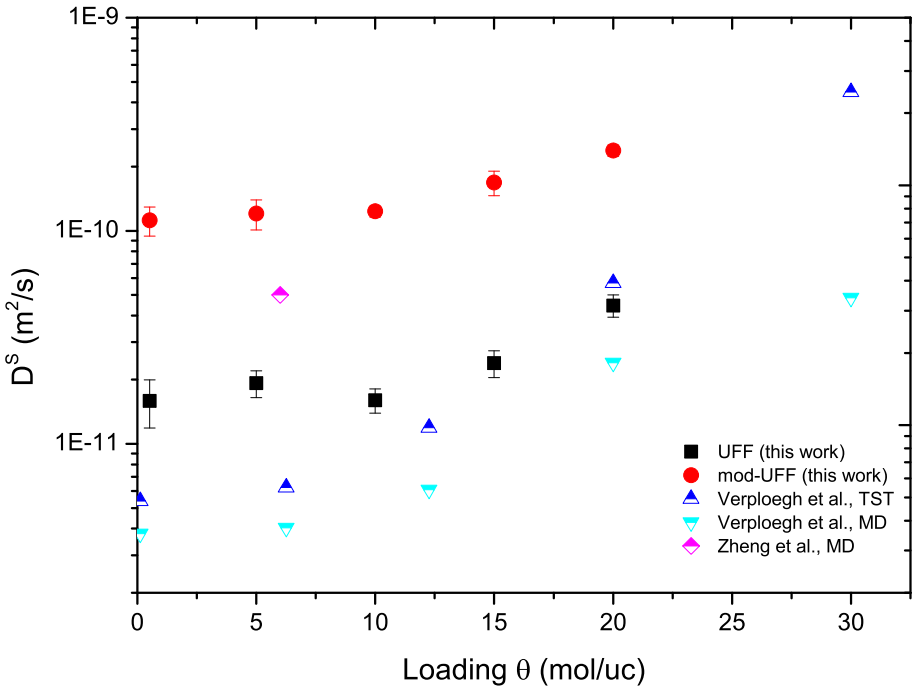

Figure 7.6: Comparison of the self-diffusion coefficients D^S for ethene as a function of loading in ZIF-8 at around $T = 300\ K$. Full symbols represent values obtained in this work. Simulation data (top half full) were taken from Verploegh et al.,[88] and Zheng et al.[266]

show an ascending self-diffusivity with higher loadings as well.

Figure 7.7 recaps all results gathered for the ZIF-8. The self-diffusion coefficients for the three small hydrocarbons methane, ethane, and ethene in flexible ZIF-8 were computed. Independent of the used force field methane is the fastest diffusing molecule since it is the smallest. About half a magnitude slower is the olefin, ethene, and the paraffin, ethane, is the slowest one because of the bigger size and the corresponding higher heat of adsorption and higher activation energy for diffusion in comparison.[77,81,88,295] Both UFF versions show excellent agreement with all literature data whereas the mod-UFF data are too high.

In conclusion, ethane diffuses slower for both force fields in comparison to ethene. For both molecules, the mod-UFF is around an order of magnitude higher than the unmodified and forms in analogy to literature the highest values. The UFF however, is for ethane and ethene in very good agreement with experimental and simulation data, respectively.

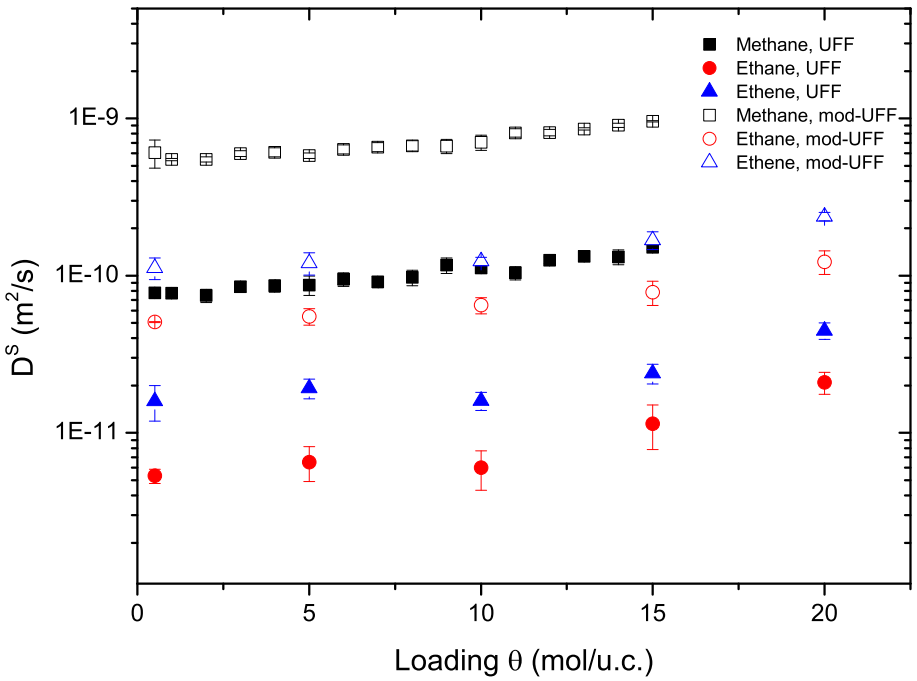

Figure 7.7: Recap of the obtained self-diffusion coefficients D^S for methane, ethane and ethene as a function of loading in ZIF-8 based on the UFF (full symbols) and the mod-UFF (empty symbols) at $T = 298\ K$.

7.3.2 ZIF-71

Methane

ZIF-71 is a new candidate for the paraffin/olefin separation. So far and to the best of our knowledge, only two adsorption studies have investigated its separation potential in this field, which has revealed a very good performance regarding that matter.[303,334] In the following sections the self-diffusion coefficients of methane, ethane, and ethene in a fully flexible ZIF-71 framework are presented, which to the best of our knowledge no one has done yet for any molecule. Therefore, comparisons to data reported in literature are not possible.

Figure 7.8 displays the self-diffusion coefficients of methane in a rigid as well as in a flexible ZIF-71 over a loading of 0.65 to 20 $\frac{mole}{UC}$, which corresponds to the saturation loading.[334] In contrast to ZIF-8, the pore aperture of ZIF-71 has a pore limiting diameter of 5.4 $\mathring{A}$ instead of 3.4 $\mathring{A}$.[131] This allows the the molecules to move quite freely through the windows whether the crystal is modelled as rigid or flexible.

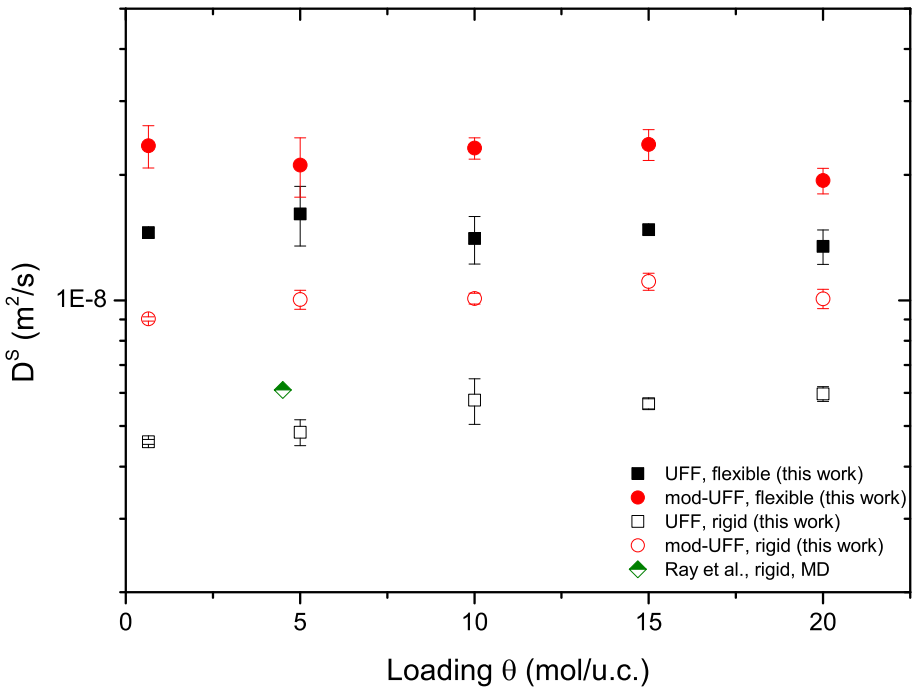

Figure 7.8: Comparison of the self-diffusion coefficients D^S for methene as a function of loading in flexible and rigid ZIF-71 at $T = 298\,K$. Full symbols represent values obtained in this work based on the UFF and empty symbols based on the mod-UFF. Simulation data (top half full) for a rigid framework were taken from Ray et al.[356]

In general, the self-diffusion coefficient D^S for the flexible framework is almost constant up to $15\frac{mole}{UC}$ before it marginally decreases independent of the applied force field. For the rigid framework based on the UFF, there is a slight increase over loading observable. Overall, there is a constant trend in the diffusion behavior for methane for the observed loading range to report. A plausible cause for the non-existence of loading dependency for methane for the examined loading range could be its small size compared to the free accessible volume in ZIF-71. Thus, a decrease of the diffusivity due to sterical hindrance is not present.

As expected, the values for the mod-UFF are higher than the ones for the UFF due to the lower LJ parameters. Interestingly, however, the difference is not as pronounced as for the ZIF-8, namely, only twice the value instead of an order of magnitude. A reason for that could be the lower influence of the guest-host interactions since the pore volume and window size is bigger than for the ZIF-8, and consequently, the molecules have more pore volume

available to diffuse into.

Using a rigid framework reduces the diffusivity by more than a half for both force fields. One possible answer to this phenomenon could be the opening of the pore apertures or, more likely, the movement of the cavity itself. This means that a flexible framework is narrowing and stretching, reducing the transport resistance and possibly forcing the molecules into the cavities, which leads to a faster movement. Among others, Jakobtorweihen[191] studied in his dissertation the influence of host lattice flexibility in similar zeolites. He computed free energy profiles for a rigid and flexible AFI zeolite in order to prove that by modelling the structure as being flexible the energy barriers are reduced in comparison to a rigid framework. Hence, the diffusivity is larger in a flexible crystal.

Because of the lack of diffusion studies related to ZIF-71 and its structural flexibility, there are no other approaches for explanation as far as we know. The only comparable data was the work of Ray et al.,[356] who computed only one data point for methane in a rigid ZIF-71 (see Figure 7.8). Measured to that the obtained results for a rigid framework lay in the same order of magnitude.

Ethane and Ethene

In Figure 7.9, the results for the paraffin ethane in ZIF-71 are shown over a loading from 0.65 to 75$\frac{mole}{UC}$ The latter is equivalent to the saturation loading for ethane as well as for ethene in ZIF-71.[334]

The diffusion coefficient D^S of ethane exhibits for both force fields and lattice models a maximum at 25$\frac{mole}{UC}$. Except for the simulations in the flexible crystal based on the mod-UFF, the other three cases have a more or less strong increase from the low to the medium loading. Perhaps, the explanation of Verploegh et al.[88] can also be applied for the ZIF-71, which states that the increase may arise from the possible decreasing free energy barrier during loading, whereas the opposing influence of the simultaneous decrease of the transmission coefficient κ is smaller. This accelerates the movement. At a loading of 25$\frac{mole}{UC}$, a turning point seems to be reached where the decrease of κ gains influence over the lowering free energy barrier resulting in a loss of diffusivity.

Another observation is that for the flexible framework the UFF and mod-UFF are approaching each other at high loadings whereas the rigid framework simulations keep almost the same distance to each other. A plausible answer to this phenomenon could be the following: the effect of different LJ parameters found in the two force fields could fade into the background, because the

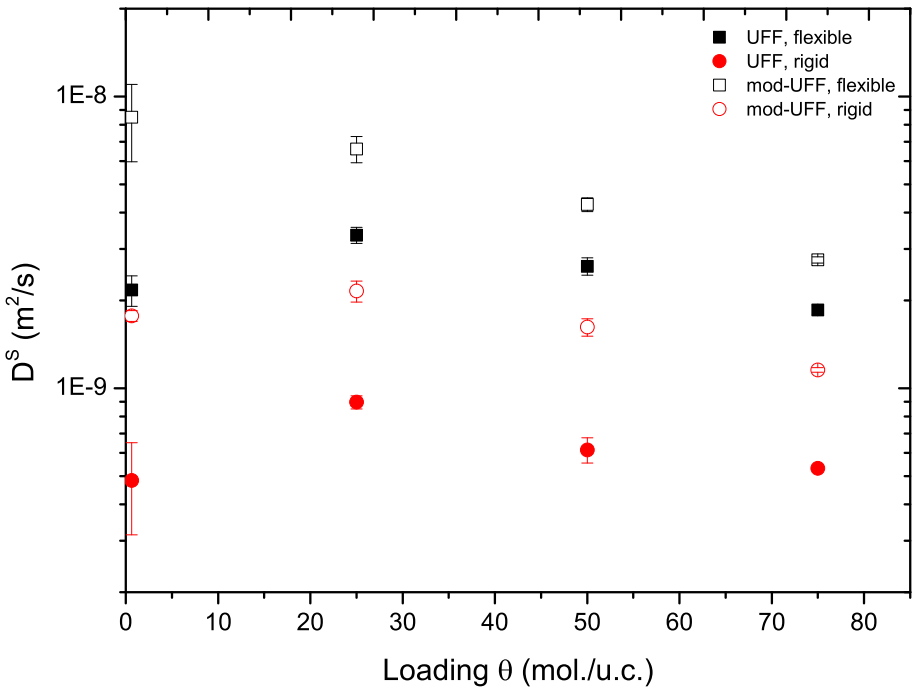

Figure 7.9: Ethane self-diffusion coeffients D^S in the investigated force fields UFF (full) and mod-UFF (empty) as a function of loading in flexible and rigid ZIF-71 at $T = 298\ K$.

high loading of the cavities confines the free movement of single molecules. On the whole, however, the mod-UFF is on average about twice the value of the UFF. The rigid framework predicts a more than one half lower diffusivity than the flexible one, which was observed for methane as well. Thus, the same possible explanation by Jakobtorweihen[191] is applicable: the free energy barrier is lower in a flexible framework compared to a rigid one.

Except for the first point, the self-diffusion of ethene shows an anomaly for the rigid framework. The MSD plot resembles a third order function, which does not correspond to the trajectories (see Figure 7.14). So far, we are not able to explain why the MSD shows this behavior. As a result, D^S cannot be calculated because it is meaningless. Thus, only a loading of 0.65 $\frac{mole}{UC}$ is presented for the rigid framework using both force fields. One can assume that the loading dependency follows the same pattern as seen for ethane in the rigid ZIF-71 because the simulations using a flexible framework for the ethene system show the same diffusion behavior like ethane. Again, the possible change of the major influence at $25\frac{mole}{UC}$ from the decreasing free energy barrier towards the decreasing κ might explain the course.

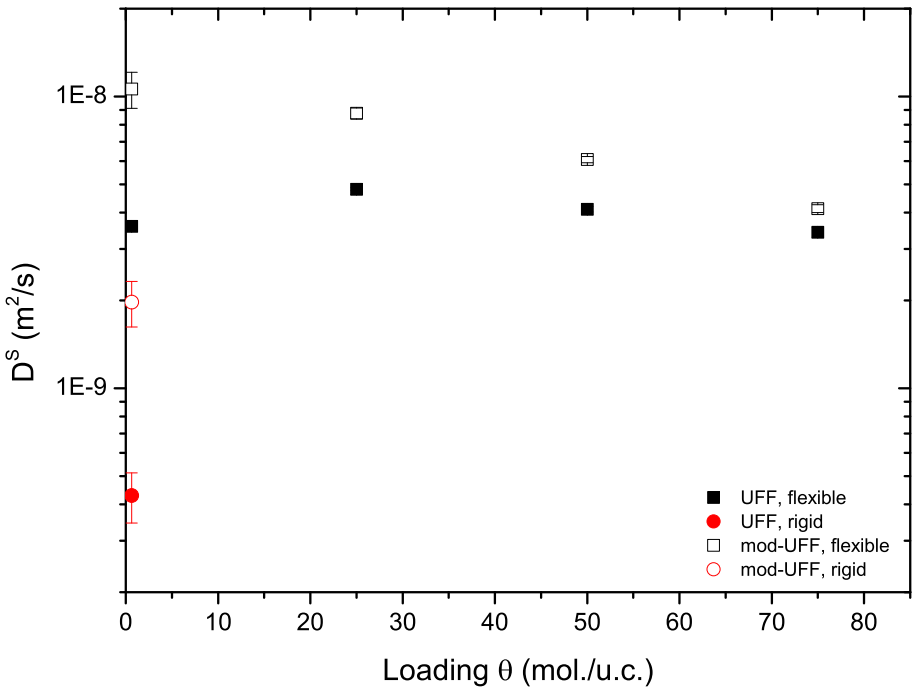

Figure 7.10: Ethene self-diffusion coeffients D^S in the investigated force fields UFF (full) and mod-UFF (empty) as a function of loading in flexible and rigid ZIF-71 at $T = 298\ K$.

Moreover, with increasing loading the deviation between both force fields gets smaller as can be seen for ethane in Figure 7.9. A plausible cause could be the fading influence of the different LJ parameters while the cage is getting loaded due to sterical hindrance.

For a better understanding of the separation properties, all diffusivities for the investigated hydrocarbons in a flexible ZIF-71 are brought together in Figure 7.11. The rigid framework is omitted for clarity. The differences between the species in the respective force field are smaller to the ones found in ZIF-8. However, a faster diffusion of ethene in comparison to ethane can be seen again. Overall, the diffusivity in the ZIF-71 is about one magnitude higher than in the ZIF-8, which can be attributed to the larger pore volume and window size of ZIF-71.

To summarize, the self-diffusion coefficients were computed for methane, ethane, and ethene in a rigid as well as in a flexible ZIF-71. All simulations using a flexible framework exhibit more than twice the values found for a

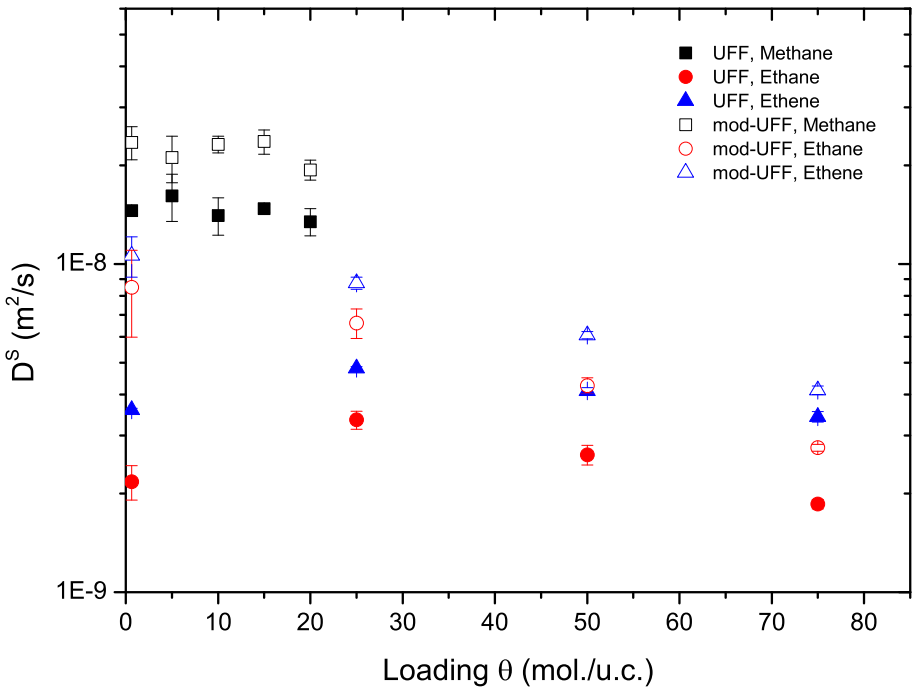

Figure 7.11: Recap of the obtained self-diffusion coefficients D^S for methane, ethane and ethene as a function of loading in flexible ZIF-71 based on the UFF (full) and the mod-UFF (empty) at $T = 298\ K$.

rigid framework. The mod-UFF predicts once again the highest values, even if the difference to the UFF is not very pronounced (from one magnitude at low loading to half or less at high loading). With increasing loading the differences between those force fields also decrease. The influence of the loading is different than in ZIF-8 because of different topologies.

Figure 7.12 displays the self-diffusivity for methane, ethane, and ethene in flexible ZIF-8 and ZIF-71 based on the UFF. The mod-UFF data was excluded since they are following the same trend as the UFF. The higher loadings for ethane and ethene in ZIF-71 compared to ZIF-8 are caused by the higher accessible pore volume. Methane, however, has a quite low saturation loading in ZIF-71 because of its small kinetic diameter and the bigger pore of the crystal there is a low contact surface. One can see the higher values of about two magnitudes in the ZIF-71.

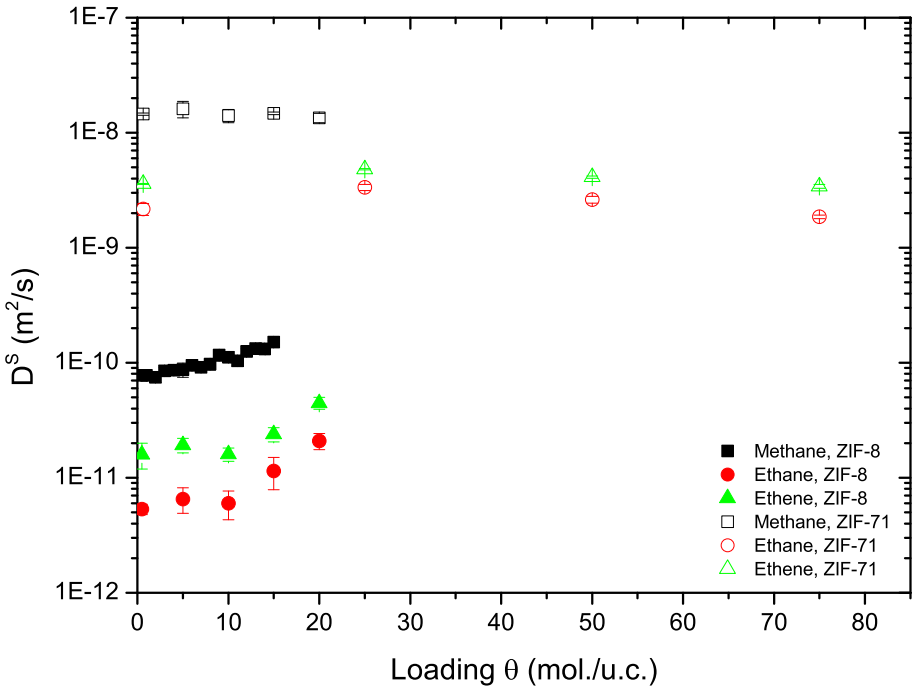

Figure 7.12: Recap of the obtained self-diffusion coefficients D^S for methane, ethane and ethene as a function of loading in flexible ZIF-8 (full) and flexible ZIF-71 (empty) based on the UFF at $T = 298\,K$.

7.3.3 ZIF-9

It has been already established in Chapter 5.3.3 that the saturation for ZIF-9 can only be predicted accurately by MC simulations, when in the rigid case inaccessible pore volumes are made available. This proves that the flexibility of the structure has to be taken into account, especially for diffusion. As a disclaimer, two things are important to mention up front: Firstly, there are no experimental or simulated (self-)diffusion coefficients available in the literature. Secondly, because of time constraints there was not enough time to investigate the diffusion behavior in detail. Moreover, simulations for each situation was only carried out once, hence the error can only be guessed and is otherwise not available. Consequently, the results presented here are not complete and show only indications of trends. Thus, conclusions cannot be drawn. For example, for only one species at one given loading, methane at 8 $\frac{mole}{UC}$, has been simulated. The investigation regarding this framework is not complete, yet the data of the results is merely put into this work for completeness.

Since the pore diameters and window diameters of ZIF-9 are similar to the ones in ZIF-8, it was expected that even the smallest hydrocarbon species, methane, would not be able to diffuse through the system despite the experimental evidence, see Chapter 5.3.2. Furthermore, if modelled rigid, some of the pores are inaccessible for the guest molecules, hence the definition of a "blocked" (inaccessible pore volume) and "unblocked" (accessible volume) system. Since MC generated starting frames are needed to run MD simulations, this results in slightly different starting positions at equilibrium, see the difference in the residence probability in Figure 5.8. The results for the MSDs of CH_4 in ZIF-9 in the rigid framework based on the two force fields UFF and mod.-UFF are shown in Figure 7.13. In case of free random walk like movement, the MSD is supposed to be a straight line with a slope of one in a log-log-MSD plot. Here, the traveled distance by any molecule is capped at a certain level, meaning that there exists a barrier or hindrance whether it is static or energetic which cannot be overcome. This means that the CH_4 molecules are trapped inside the pore space they currently are in, translating to a diffusion coefficient of zero. Clearly, the results are similar to the ones found for ZIF-8 as shown in Figure 7.3.

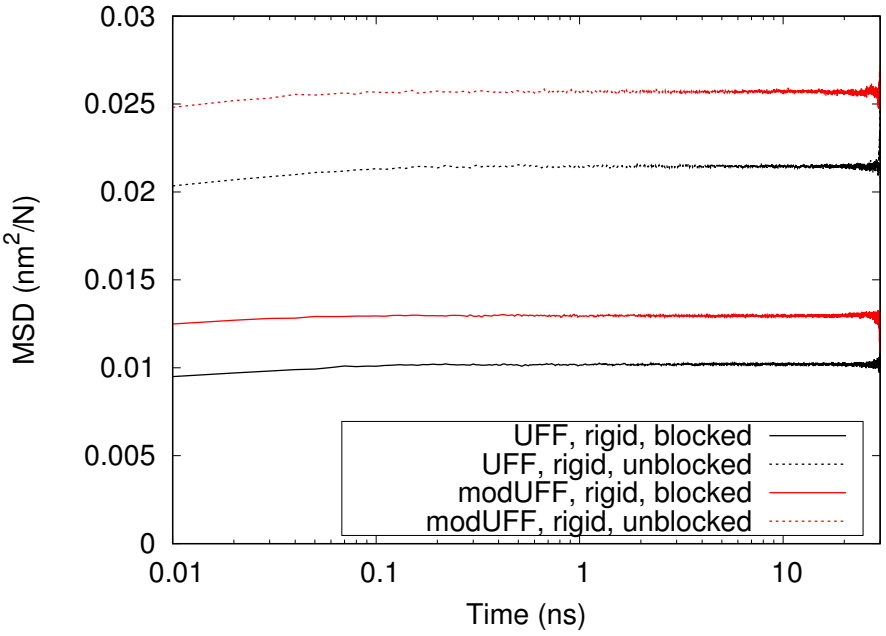

Figure 7.13: MSD as a function of simulation time for CH_4 in a rigid modelled ZIF-9 using UFF (red lines) and mod-UFF (black lines) at 298 K, respectively.

The lack of experimental data makes it difficult to investigate the impact of flexibility in ZIF-9. Therefore, for each force field (UFF and mod-UFF) four kinds of simulations were carried out in which the energy parameter of the bond, angle, torsion or no parameter at all was varied, e.g. reduced by $\frac{2}{3}$. Additionally, the parameter of the bonds, bonds+angles, and bonds+angles+torsions were modified as well. In other words, the force parameters describing the bonds, angles, and torsions were altered in a way that the framework becomes more and more loosely bound and thus more flexible. The idea behind these modifications is to identify, which type (bonds, angles or torsion) is most impactful on the diffusivity and whether or not the movement of the molecules is one, two or three dimensional through the network.

Table 7.1: Self-diffusion coefficients for methane in a flexible and unblocked ZIF-9 at 298 K and a loading of 8 $\frac{mole}{UC}$ varying the force field; simulation length was 100 ns.

Force field	Diffusion coefficent in $10^{-10}\frac{m^2}{s}$			
	D^s_x	D^s_y	D^s_z	D^s_{xyz}
UFF	0.002	0.005	0.001	0.005
mod-UFF	0.086	0.161	0.093	0.113

Firstly, we take a look at the directions of the diffusion through the crystal. Considering the way ZIF-9 is build and the residence probability plots suggested (Figure 5.8), it is expected that the main diffusion direction was along the z-axis. As it turns out, the molecules diffuse mainly along the y-axis and x-axis as evident by the diffusion coefficients Table 7.1). On average the mobility in y-dircetion is higher than in x and z- direction: $D^s_y < D^s_x < D^s_z$. Apparently despite the slightly larger window diameter in z-direction, the transport resistance is higher than in the other directions. The diffusivity is in the range of 10^{-11} to $10^{-12}\frac{m^2}{s}$, which is slightly lower than the ones determined for ZIF-8. This has been somewhat expected considering the pore dimensions of the two crystals. Obviously, the comparison to experimental data would be welcomed to verify this magnitude and general behavior. Regardless, methane molecules move three dimensionally through the framework.

Secondly, based on the small sample size from this study it seems that the main influence on the flexibility is caused by varying the torsion force parameters, whereas reducing the parameters for the bond and angle interactions does not have great impact on the diffusivity. This effect is more pronounced

when the mod-UFF is used since it is a reduced version of the UFF (Table 7.2). Reducing the force field parameter for bond and angle interactions increases the diffusivity, but only in combination with the reduction of the torsion interactions the mobility is increased significantly. The same observation was reported by Fairen-Jimenez et al.[279] for ZIF-8, who found that the gate opening is attributed to the torsion of the framework atoms building the windows. These preliminary results emphasise the fact that the correct modelling of the diffusion mechansim inside ZIF-9 is tied to an accurate description of the torsion interactions of the framework.

Table 7.2: Self-diffusion coefficients for the xyz-direction (D^s_{xyz}) for methane in a flexible modelled ZIF-9 at 298 K and a loading of 8 $\frac{mole}{UC}$ using the UFF and mod-UFF; simulation length was 100 ns.

methane	UFF		mod-UFF	
reduced parameters	blocked[a]	unblocked[a]	blocked[a]	unblocked[a]
(at $\frac{1}{3}$)	D^s_{xyz} in $10^{-10}\frac{m^2}{s}$	D^s_{xyz} in $10^{-10}\frac{m^2}{s}$	D^s_{xyz} in $10^{-10}\frac{m^2}{s}$	D^s_{xyz} in $10^{-10}\frac{m^2}{s}$
none	0.006	0.005	0.110	0.113
bond	0.004	0.004	0.128	0.138
angle	0.006	0.006	0.135	0.130
torsion	0.008	0.007	0.467	0.478
bond+angle	0.005	0.005	0.225	0.196
bond+angle+torsion	0.011	0.011	0.590	0.616

[a]status of the inaccessible pores in the framework

7.4 Conclusions

In this chapter, the diffusion of the small hydrocarbons methane, ethane, and ethene in ZIF-8, ZIF-9, and ZIF-71 was investigated. Molecular dynamics simulations in the NVT-ensemble were carried out to obtain the self-diffusivities for the pure components. Parameters were taken from the UFF, and the results for methane in ZIF-8 were validated by comparison against literature data. The agreement is excellent in the case of the UFF, whereas the mod-UFF is arguably too high.

As for the ZIF-8, for all three species the self-diffusivity increases with higher loadings. Verploegh et al.[88] argued that if more molecules of a species are put in a cavity, the free energy barrier near the aperture decreases significantly. Thereby, this effect is stronger than the simultaneous opposing decrease of the transmission coefficient κ resulting in a higher diffusivity.[88]

Methane is diffusing the fastest followed by ethene and by ethane, which is true for both force fields applied. Molecules diffuse only for a flexible model since in a rigid one they are not able to surpass the apertures. In contrast, the self-diffusion coefficient D^S for all examined hydrocarbons in ZIF-71, which has a larger pore volume and pore aperture size than ZIF-8, has a different behavior: in case of methane, the diffusivity as a function of loading remains constant while for ethane and ethene it has a maximum at $25\frac{mole}{UC}$. It is assumed that the effect of the decreasing transmission coefficient κ is stronger than the decrease of the free energy barrier for which reason the diffusivity is reduced. This trend of loading dependency at higher loadings is more natural than the one in the ZIF-8 since with higher loading the guest-molecules are restricting each other in their movement in such a way that the self-diffusivity declines with higher loadings. In ZIF-71, molecules diffuse whether the crystal is modelled as rigid or flexible. In the flexible one they are move more quickly. A possible explanation could be the following: Based on the idea of Jakobtorweihen,[191] free energy profiles rigid and flexible zeolites were computed, which show a decrease of the free energy by modelling the host lattice as flexible compared to rigid. In this work, first simulations of methane diffusion were carried out in which ZIF-9 was modelled rigid or flexible. The preliminary results indicate that the diffusion through the crystal is three dimensional and that a correct description of the torsion interactions between the framework atoms is essential for accurate predictions. Ultimately, all hydrocarbons diffuse about one magnitude faster in ZIF-71 than in the ZIF-8. The potential for kinetic separation for paraffins and olefins can be confirmed for the two crystals.

7.5 Supporting information

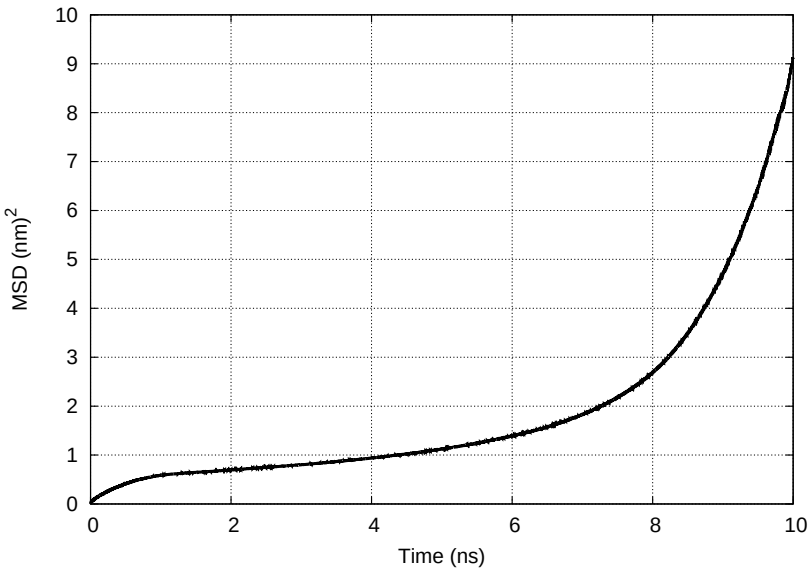

Figure 7.14: MSD plot of ethene in rigid ZIF-71 at a loading of 25 $\frac{mole}{UC}$ based on UFF at $T = 298\,K$.

7.5.1 UFF & mod-UFF parameters for ZIF-8

Table 7.3: UFF LJ parameters[239] and atomic charges taken from Quatar FF[77] for ZIF-8.

Atom	σ (nm)	ϵ (kJ/mol)	Charge (e)
Zn	0.2462	0.5191	1.3429
N	0.3261	0.2889	-0.6822
C1	0.3431	0.4396	-0.0622
C2	0.3431	0.4396	0.7551
C3	0.3431	0.4396	-0.2697
H1	0.2571	0.1842	0.0912
H2	0.2571	0.1842	0.0499

Table 7.4: Mod-UFF LJ parameters[239] and atomic charges taken from Quatar FF[77] for ZIF-8.

Atom	σ (nm)	ϵ (kJ/mol)	Charge (e)
Zn	0.2338	0.3582	1.3429
N	0.3098	0.1993	-0.6822
C1	0.3259	0.3033	-0.0622
C2	0.3259	0.3033	0.7551
C3	0.3259	0.3033	-0.2697
H1	0.2443	0.1271	0.0912
H2	0.2433	0.1271	0.0499

Table 7.5: UFF & mod-UFF guest-molecules.[326,327]

Atom	σ (nm)	ϵ (kJ/mol)
CH_4	0.3730	1.2297
CH_3 (sp3)	0.3750	0.8142
CH_2 (sp2)	0.3675	0.7072

Table 7.6: UFF & mod-UFF bonds for ZIF-8.[239]

i	j	b_{ij} (nm)	$k_{ij}^{stretch}$ (kJ/mol/nm^2)
Zn	N	0.1892	136,612.43
N	C2	0.1357	541,245.41
N	C1	0.1357	541,245.41
C1	C1	0.1379	387,624.98
C1	H1	0.1081	299,653.65
C2	C3	0.1486	398,776.25
C3	H2	0.1109	277,524.94

Table 7.7: UFF & mod-UFF angles for ZIF-8.[239]

i	j	k	θ_{ijk}^0 (deg)	k_{ijk}^θ (kJ/mol)
N	Zn	N	109.47	813.58
Zn	N	C2	120.00	376.70
Zn	N	C1	120.00	376.70
C1	N	C2	120.00	978.57
C1	C1	N	120.00	1270.77
C1	C1	H1	120.00	480.10
C2	C3	H2	109.47	523.20
H2	C3	H2	109.47	316.44
N	C2	N	120.00	1732.41
N	C2	C3	120.00	1117.40
N	C1	H1	120.00	657.82

Table 7.8: UFF & mod-UFF dihedrals for ZIF-8 taken from Quatar FF.[77]

i	j	k	l	ϕ^0 (deg)	k_{ijkl}^{phi} (kJ/mol)	n (-)
N	C1	C1	N	180	90.0	2
N	C1	C1	H1	0	90.0	2
C1	C1	N	Zn	180	25.1	2
C1	C1	N	C2	0	25.1	2
C3	C2	N	Zn	180	41.8	2
C3	C2	N	C1	180	41.8	2
C2	N	Zn	N	180	0	2
H2	C3	C2	N	180	0	2

7.5.2 Quatar FF parameters

Table 7.9: Quatar FF, LJ parameters and atomic charges for ZIF-8.[77]

Atom	σ (nm)	ϵ (kJ/mol)	Charge (e)
Zn	0.1960	0.0523	1.3429
N	0.3250	0.7113	-0.6822
C1	0.3400	0.3598	-0.0622
C2	0.3400	0.3598	0.7551
C3	0.3400	0.4577	-0.2697
H1	0.2511	0.0628	0.0912
H2	0.2650	0.0657	0.0499

Table 7.10: Quatar FF guest-molecules.[77]

Atom	σ (nm)	ϵ (kJ/mol)
CH_4	0.3730	1.2297

Table 7.11: Quatar FF bonds for ZIF-8.[77]

i	j	b_{ij} (nm)	$k_{ij}^{stretch}$ (kJ/mol/nm^2)
Zn	N	0.2048	52,802.1
N	C2	0.1360	257,818.1
N	C1	0.1376	253,048.3
C1	C1	0.1375	339,991.8
C1	H1	0.1077	327,690.9
C2	C3	0.1498	203,760.8
C3	H2	0.1091	286,855.0

Table 7.12: Quatar FF angles for ZIF-8.[77]

i	j	k	θ^0_{ijk} (deg)	k^{θ}_{ijk} (kJ/mol/rad^2)
N	Zn	N	109.5	296.23
Zn	N	C2	130.3	462.74
Zn	N	C1	125.1	475.30
C1	N	C2	104.5	1077.80
C1	C1	N	107.9	909.61
C1	C1	H1	130.6	552.29
C2	C3	H2	110.8	565.68
H2	C3	H2	108.1	317.98
N	C2	N	113.8	955.63
N	C2	C3	123.1	958.97
N	C1	H1	121.5	549.78

Table 7.13: Quatar FF dihedrals for ZIF-8.[77]

i	j	k	l	ϕ^0 (deg)	k^{phi}_{ijkl} (kJ/mol)	n (-)
N	C1	C1	N	180	90.0	2
N	C1	C1	H1	180	90.0	2
C1	C1	N	Zn	180	25.1	2
C1	C1	N	C2	180	25.1	2
C3	C2	N	Zn	180	41.8	2
C3	C2	N	C1	180	41.8	2
C2	N	Zn	N	180	0.0	2
H2	C3	C2	N	180	0.0	2

7.5.3 UFF & mod-UFF parameters for ZIF-9

Table 7.14: UFF LJ parameters[239] and atomic charges calculated using REPEAT[181] for ZIF-9.

Atom	σ (nm)	ϵ (kJ/mol)	Charge (e)
Co	0.2559	0.0586	0.7237
N	0.3261	0.2889	-0.4131
C1	0.3431	0.4396	0.1857
C2	0.3431	0.4396	0.2048
C3	0.3431	0.4396	-0.2385
C4	0.3431	0.4396	-0.1350
H1	0.2571	0.1842	0.0690
H2	0.2571	0.1842	0.1482
H3	0.2571	0.1842	0.1251

Table 7.15: Mod-UFF LJ parameters[239] and atomic charges using REPEAT[181] for ZIF-9.

Atom	σ (nm)	ϵ (kJ/mol)	Charge (e)
Co	0.2431	0.0404	0.7237
N	0.3098	0.1992	-0.4131
C1	0.3259	0.3031	0.1857
C2	0.3259	0.3031	0.2048
C3	0.3259	0.3031	-0.2385
C4	0.3259	0.3031	-0.1350
H1	0.2443	0.1270	0.0690
H2	0.2443	0.1270	0.1482
H3	0.2443	0.1270	0.1251

Table 7.16: UFF & mod-UFF bonds for ZIF-9.[239]

i	j	b_{ij} (nm)	$k_{ij}^{stretch}$ (kJ/mol/nm^2)
Co	N	0.2007	214642.5
C1	N	0.1357	541434.4
C	H	0.1081	299306.3
C	C	0.1379	387408.8
C2	N	0.1357	555771.7

Table 7.17: UFF & mod-UFF angles for ZIF-9.[239]

i	j	k	θ_{ijk}^0 (deg)	k_{ijk}^θ (kJ/mol)
N	Co	N	90.0	2379.56
N	C1	N	120.0	2368.03
N	C1	H1	120.0	889.36
C2	C2	C3	120.0	1240.60
C2	C2	N	120.0	1713.24
C2	C3	C4	120.0	1240.60
C2	C3	H2	120.0	638.58
Co	N	C1	120.0	840.68
C1	N	C2	120.0	2368.03

Table 7.18: UFF & mod-UFF dihedrals for ZIF-9.[239]

i	j	k	l	ϕ^0 (deg)	k_{ijkl}^{phi} (kJ/mol)	m (-)
N	Co	N	C	0	0.0	2
N	C	N	Co	180	10.45	2
N	C	N	C	180	10.45	2
H	C	N	Co	180	10.45	2
H	C	N	C	180	10.45	2
C3	C2	C2	C3	180	52.25	2
C3	C2	C2	N	180	52.25	2
N	C	C	N	180	52.25	2
C2	C2	C3	C4	180	10.45	2
C	C	C	H	180	10.45	2
N	C	C	C	180	10.45	2
N	C	C	H	180	10.45	2
C2	C2	N	Co	180	10.45	2
C2	C2	N	C1	180	10.45	2
C3	C2	N	Co	180	10.45	2
C3	C2	N	C1	180	10.45	2
C2	C3	C4	C4	180	52.25	2
C2	C3	C4	H3	180	52.25	2
H2	C3	C4	C4	180	52.25	2
H2	C3	C4	H3	180	52.25	2
C	C	C	C	180	10.45	2
C3	C4	C4	H3	180	10.45	2
H3	C4	C4	H3	180	10.45	2

7.5.4 UFF & mod-UFF parameters for ZIF-71

Table 7.19: UFF LJ parameters[239] and atomic charges taken from Reference 341 for ZIF-71.

Atom	σ (nm)	ϵ (kJ/mol)	Charge (e)
Zn	0.2462	0.5191	-1.560
N	0.3261	0.2889	0.898
C1	0.3431	0.4396	-0.920
C2	0.3431	0.4396	-0.314
H1	0.2571	0.1842	0.346
Cl	0.3516	0.9504	0.093

Table 7.20: Mod-UFF LJ parameters[239] and atomic charges taken from Reference 341 for ZIF-71.

Atom	σ (nm)	ϵ (kJ/mol)	Charge (e)
Zn	0.2338	0.3582	-1.560
N	0.3098	0.1993	0.898
C1	0.3259	0.3033	-0.920
C2	0.3259	0.3033	-0.314
H1	0.2443	0.1271	0.346
Cl	0.3341	0.6558	0.093

Table 7.21: UFF & mod-UFF bonds for ZIF-71.[239]

i	j	b_{ij} (nm)	$k_{ij}^{stretch}$ (kJ/mol/nm^2)
Zn	N	0.1892	136,612.43
N	C2	0.1357	541,245.41
N	C1	0.1357	541,245.41
C1	C1	0.1379	387,624.98
C2	H1	0.1081	299,653,65
C1	Cl	0.1751	232,517.86

Table 7.22: UFF & mod-UFF angles for ZIF-71.[239]

i	j	k	θ_{ijk}^0 (deg)	k_{ijk}^{θ} (kJ/mol)
N	Zn	N	109.47	813.58
Zn	N	C2	120.00	376.70
Zn	N	C1	120.00	376.70
C1	N	C2	120.00	978.57
C1	C1	N	120.00	1270.77
N	C2	N	120.00	1732.41
N	C2	H1	120.00	657.82
C1	C1	Cl	120.00	769.179
N	C1	Cl	120.00	494.402

Table 7.23: UFF & mod-UFF dihedrals for ZIF-71 taken from Quatar FF.[77]

i	j	k	l	ϕ^0 (deg)	k_{ijkl}^{phi} (kJ/mol)	n (-)
N	C1	C1	N	180	90.0	2
N	C1	C1	Cl	180	90.0	2
C1	C1	N	Zn	180	25.1	2
C1	C1	N	C2	180	25.1	2
N	C2	N	Zn	180	41.8	2
C2	N	Zn	N	180	0.0	2

Part IV

Adsorber simulation

8 Adsorber Simulation

Simulations of adsorption processes using fixed-beds are tested for three different systems, namely CH_4/C_2H_6 separation using carbon nanotubes, N_2/CO_2 separation using Mg-MOF-74, and C_2H_4/C_2H_6 separation using ZIF-8. The code is based on a rudimentary version written by A. Heyden.[360] The code has been modified and more features have been added, using more accurate equations for species properties, like viscosity for example, implementing the ideal adsorbed solution theory (IAST) for more accurate calculation of mixture adsorption, and a general clean-up of the code itself to improve accuracy and speed. The first of the three systems allows to compare the old and the new version of the program showing that the overall trends agree well. It also shows the correct behaviour regarding the break through of both compounds. The second and third systems are considered to be prove of principle simulations, proving the feasibility of adsorption to solve the separation problem, especially Mg-MOF-74 proves its capability in this regard by showing a very high selectivity towards CO_2.

8.1 Introduction

When it comes to designing real processes, engineers are usually confronted not with a binary but a multi-component mixture from which the product compounds need to be separated from the unwanted side products or waste. There are several ways to separate the high value target species from the rest of the mixture. For example, liquid compounds can be separated via liquid-liquid extraction or distillation whereas for solid-liquid mixtures cyclones or membrane processes are valid options.[361,362] For fluid phases successful operations besides membrane processes include the rectification, which utilises the vapor-liquid equilibrium to separate mixtures.[361] An alternative to this method is adsorption in which the gas molecules are separated using porous solids. This technique is frequently used in solvent drying, cleaning of flue gases or catalytic reactions.[361,363,364] According to Ruthven,[184] the main advantages for this separation technique is the lack of solvent recovery and low energy consumption since the process is usually carried out at ambient conditions. Moreover, it is relatively easy to design the process reliably and its capital and maintenance costs are moderate compared to other separation processes.[184]

The adsorption process itself is divided into two parts: The first is the adsorption part, which is carried out at the higher pressure or lower temperature levels, respectively. During this step the adsorbent gets loaded with the (feed) gas molecules. The desorption is carried out at lower pressure or higher temperature levels, respectively. Here, the adsorbent will be cleaned of the adsorbed species for the next adsorption cycle. In general, this offers the following technical implementations of this principle:

- Temperature swing adsorption (TSA) - variation of temperature
- Pressure swing adsorption (PSA) or vacuum swing adsorption (VSA) - variation of pressure
- Composition swing adsorption (CSA) - variation of composition of the fluid phase
- Combination of the aforementioned variants

Having the option to vary multiple process parameters independently as well as using different adsorption materials makes the adsorption process way more flexible than the rectification for example.[184,361]

In light of the separation problems investigated in this work, i.e. CO_2 separation from flue gas and olefin/paraffin-separation, the reasoning for substituting state-of-the-art technologies for the respective problem is quite different: As already mentioned, CO_2 is currently separated from flue gas via

amine scrubbing, which has the disadvantage of high energy consumption because of the required solvent recovery present in the process. The idea is that CO_2 can be separated more effectively with adsorption based on optimal adsorption materials and process conditions. The optimization of the energy consumption was investigated by Haghpanah et al.[365] with respect to CO_2 separation. They used a vacuum swing adsorption (VSA) module with molecular sieves to determine the energy consumption and maximize productivity. Flue gas is usually saturated with water vapor. This leads to a higher energy consumption compared to dry flue gas. The study emphasizes the role of impurities on the effectiveness of adsorbers.[365] Chou and Chen[366] studied the influence of cycle scheduling on the performance of adsorbers using a VSA module as well. They varied adsorber configurations and scheduling to maximize the purity of CO_2. It was reported that results based on simulations were generally lower than the experimental findings because of the sensitivity of the simulations toward the adsorption isotherm parameters used as input. They concluded that the quality of the predictions is very much dependent on the quality of the input parameters and starting conditions.[366]

Regarding olefin/paraffin-separation in the petrochemical industry the state-of-the-art technology is the cryogenic distillation. This process has a high energy consumption because of the fact that the process is carried out at temperatures below -100°C.[44,367] The low temperature is necessary since the boiling temperatures of the small hydrocarbons, like ethane, ethene, propane, and propene for example, are in the range of -170°C to -200°C. Since adsorption can be carried out at ambient temperatures, there is no energy required to cool down the system. Furthermore, provided proper adsorption materials the product (usually the olefin) is gathered at higher pressures during the adsorption step which is very advantageous. Grande and Rodrigues[367] performed a sensitivity analysis for a PSA module using zeolite 4A to separate a propane/propene mixture. They solved the system of partial differential equations (PDEs) using gPROMS by Process Systems Enterprise Ltd. and concluded that a longer blowdown step leads to higher product purity at the cost of productivity of the module. Furthermore, in this type of system, i.e. olefin/paraffin mixtures, the window of optimization is relatively small to remove the propane from the system without desorption of the propene.[366]

In order to design and estimate the costs of an adsorption plant properly, it is mandatory to understand the fundamental processes taking place and responsible for the separation. In addition to adsorption and desorption, several other phenomena are present, such as diffusion, dispersion, and

heat transport.[368] Obtaining the necessary data required for the design of the process solely from experiments is generally considered time consuming and expensive. Consequently, the prediction of data and simulations of the process can reduce time and other resources significantly due to its flexibility regarding components and conditions.[369] Clearly, the process can only be designed optimally when experiments and simulations both are taken into account. One without the other is not a viable design strategy nowadays.[370] The goal is to improve the purity, yield, and productivity via new materials, like MOFs,[92] or optimizing critical process parameters or the cycle scheduling.[371]

Obviously, the "quickest and easiest" way to simulate adsorption modules is the use of commercial programs, such as "Aspen Adsorption" von AspenTech or "Comsol Multiphysics". The advantage is that the system of PDEs are already implemented and the search for solvers handling the problem efficiently and accurately has been taken care of by the code. Besides the cost for the programs, which can be substantial, this black box system is a strength and a weakness at the same time. Since the code is merely a black box to the user, little is known on how the system is solved when problems occur. One is not able to check the code itself, and thus, relies heavily on the support of the company. To date, it is still common to verify the simulation results by short-cut methods.[89] Developing an adsorption module by oneself can be beneficial because of the fact that it can be specifically adjusted to the problem at hand. Furthermore, the inner workings of the solver and the code are available, which helps identifying errors and bugs, hence the problem is more open to the user. Once the module functions properly there is no real difference between the commercially available and in-house codes quality-wise.

The usage of new (porous) materials as well as implementation of simulations for the design of adsorber plants and optimization of cycle scheduling are possible ways to maximize the effectiveness of the adsorption processes, making them viable to replace state-of-the-art separation technologies for various separation problems. From an academic point of view, simulations allow to investigate materials and critical process parameters very thoroughly in creative ways to find new ideas and technologies. For industry, simulation based design processes effectively reduce the costs, experiments, and time needed to design adsorption plants.

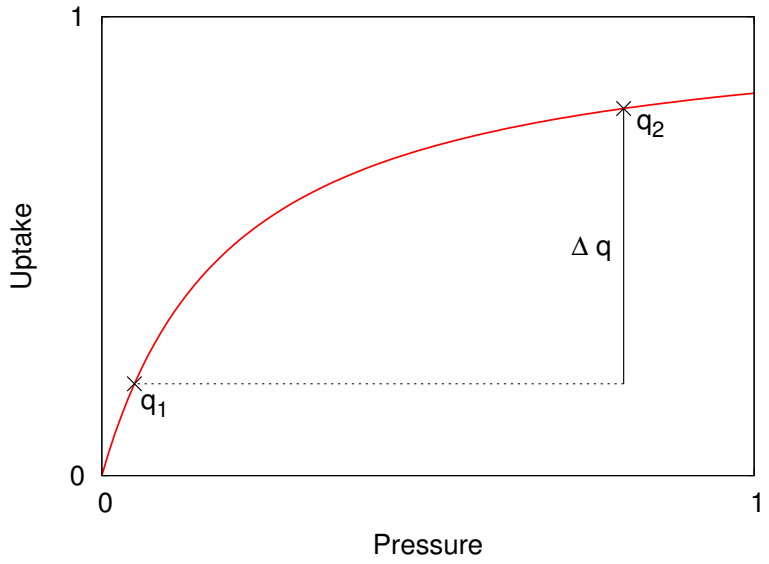

Figure 8.1: Definition of working capacity for a given isotherm.

8.2 Fundamentals of pressure swing adsorption

When it comes to the selection of potential materials for adsorption processes, there are a couple of criteria that have to be met: In addition to good selectivity one is interested in a high working capacity for the desired species. Let us assume that the adoption isotherm of our product A on a given material can be described by a Langmuir isotherm, see Eq. 2.29. During a pressure swing adsorption process generally two pressures are defined: one for adsorption p_{ads} and one for desorption p_{des} which defines the (maximum) uptake accordingly, i.e. q_{ads}=f(p_{ads}) and q_{des}=f(p_{des}), respectively, whereas $p_{ads} > p_{des}$ and $q_{ads} > q_{des}$. Clearly, a high working capacity is desired since the material needed is reduced and it is used more efficiently. For any given adsorption material it is defined as:

$$\Delta q = q_{ads} - q_{des}. \tag{8.1}$$

In order to evaluate the adsorption process itself as well as the influence of critical process parameters and geometric properties of the fixed-bed, break through curves are generated and break through times determined. At the outlet of the adsorber (bed) the concentration of each species present in the system is measured as a function of time. The break through curve is ideally

a step function. However, bevcause of diffusion and dispersion effects this shape is only approximated and smeared.[372] In practice, one refers to the break through of a species once the mole fraction reaches 5% of the outlet composition.[373] Based on those break through times and dead times of a system, the selectivity can be calculated both of which play an important role for the design of the adsorber.

Each species of a multi-component mixture adsorbs to different degrees on the adsorbent. In order to quantify this difference selectivity is introduced whereas the higher the selectivity toward one species is the more favourable it is adsorbed. For a binary mixture 1 and 2 the selectivity is defined as:[361]

$$S_{1,2} = \frac{x_1 \cdot y_2}{x_2 \cdot y_1}, \tag{8.2}$$

where x_i is the mole fraction of the adsorbed and y_j of the gas phase, respectively. Is $S_{1,2} > 1$, then component 1 is more favourably adsorbed. In chromatography processes the selectivity can be determined by the retention time (break through time) t_R and dead time t_0 of a system:

$$S_{1,2} = \frac{t_{R,1} - t_0}{t_{R,2} - t_0} = \frac{\kappa_1}{\kappa_2}, \tag{8.3}$$

with κ_i being the retention factor. $t_{R,i}$ is the time until the component breaks through whereas t_0 is the time a non-adsorbing species needs to break through. To calculate t_0 the saturation loading q_i^{max} is set to zero, thus, it does not adsorb at all. Optimizing the interactions between the working capacity of the adsorption material and the selectivity enhances the effectiveness of the separation process.[374]

Let us assume that we have a binary mixture consisting of component 1 and 2, whereas component 1 is also the unwanted species and also adsorbs more strongly than component 2, similar to the paraffin in an olefin/paraffin mixture. It is obvious that for the pressure swing adsorption to function properly the process needs to be stopped right before the undesired component breaks through, e.g. the process needs to be shut down before $t = t_{R,1}$. This is done by closing the inlet, thus, stopping the feed flow. Afterwards, the pressure inside the adsorber is reduced, which causes the adsorbed species to desorb partially, which yields a regeneration of the adsorption material. In general, there are several steps involved, which ultimately form a cycle for this particular column. Although the process itself is unsteady the periodic repetition of these cycles can lead to a steady state, the so-called cyclic steady state (CSS).[371] It is noteworthy that because of heat generation

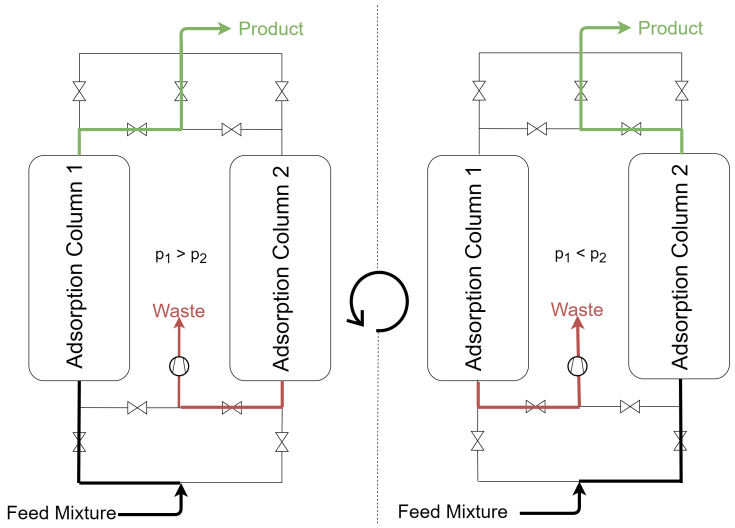

Figure 8.2: Schematic representation of the setup and workflow of the Skarstrom cylce.[376]

during the process, multiple CCSs may exist for a given system and set of process parameters.[375]

The first patent for this technique was written by Charles Skarstrom in 1960 for the oxygen enrichment without the exchange of heat.[376] The process is completed with the help of a second column, which runs through the same steps anti-cyclically, see Figure 8.2. In general, the four steps employed are: feed, blowdown (or evacuation), purge and repressurization of the column. First, the feed is fed into column 1 at higher pressures. During this step, the aforementioned component 1 adsorbs favourably and the exit stream only consists of component 2 (in the ideal case). Once the adsorber bed in column 1 is saturated the feed is inserted into coulumn 2. Meanwhile, the flow in column 1 is reversed and the pressure is reduced. During this blowdown step the uptake of the adsorption bed, which consists purely of component 1, is reduced according to the adsorption isotherms. Usually, the bed is purged and the column is pressurized by the feed to start the adsorption step. First modifications proposed by Guerin de Montgareuil and Domine[377] included the usage of the enriched gas for pressurization purposes as well as to regenerate the bed under vacuum, effectively inventing the vacuum pressure swing adsorption (VSA). The next step was to include more than two columns to the adsorption process, which allowed multiple pressure equalization steps, which leads to higher recovery factors of the process,[214,378–380] resulting in the state-of-the-art methodology of multiple adsorption columns being present in PSAs.

8.3 Results

8.3.1 Methane/ethane in carbon nanotubes

Comparison to the original code

The code for the adsorption module is based on the diploma thesis from A. Heyden.[360] In that work the separation of a methane/ethane mixture by carbon nanotubes was used to test the program. This system will serve as a reference for the implementation and the improvements made. The species properties, isotherm parameters, and diffusion coefficients are given in Tables 8.3, 8.4 and 8.5, respectively. The starting conditions for the adsorption process are given in Table 8.6, the data for the fixed-bed in Table 8.7. Initially, the adsorber bed is empty and the gas present in the system is inert and does not adsorb (helium). It should be noted that in the original work only two species were present, i.e. methane and ethane, whereas only the mass balance for ethane was solved and the methane concentration was determined from the total mass balance. The concentration for methane in the gas phase is shown in Figure 8.14. In our case with the introduction of an inert gas it allows to solve both mass balances separately since our system contains three species: methane, ethane, and helium. As a consequence, we can only really compare the results for the ethane concentration and ethane loading to the version of A. Heyden, see Figure 8.3 and 8.4, respectively.

Overall the agreement is reasonable for time and position as the concentration front moves similarly forward in time (Figure 8.3). Eventually the break through times vary by approximately 10 seconds. In the original code ethane breaks through at about 140 seconds. At that time, the concentration of ethane at the outlet is circa 20 $\frac{mol}{m^3}$ in our version. The difference in the behaviour of the concentration profiles is because of the way the mass balances are closed, e.g. without or with helium present. The influences of other small adjustments, like adsorption parameters or methods to calculate gas properties, are only marginal.

Comparing the loading as a function of time and position for ethane (Figure 8.4) one can see that the agreement is slightly better than for the ethane concentration in the gas phase. With increasing time the uptake increases. In both simulations the saturation (approx. 1.7 $\frac{mol}{kg}$) at the beginning of the bed is reached at around 140 seconds. At the end of the bed, however, the ethane loading is already at around 0.1 $\frac{mol}{kg}$ in the new version, which is consistent with the results for the gas phase concentration, i.e. the break through of ethane. The original simulation does not predict the break through yet.

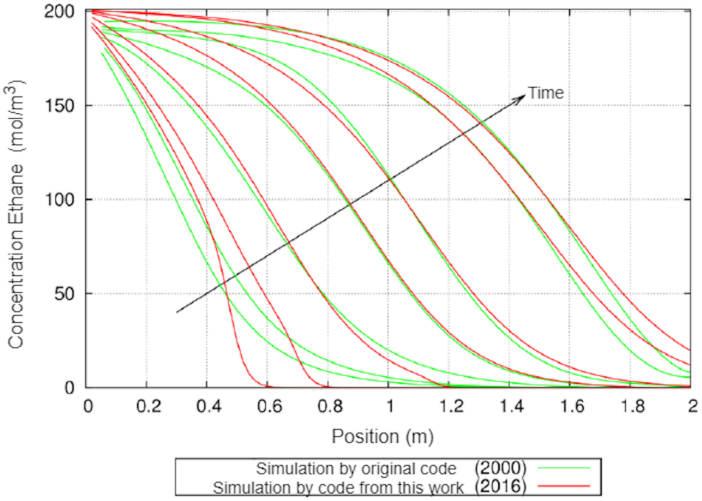

Figure 8.3: Comparison of the simulated concentration for ethane in the gas phase as a function of bed position and at the time 10, 20, 40, 70, 90, 130, and 140 seconds.

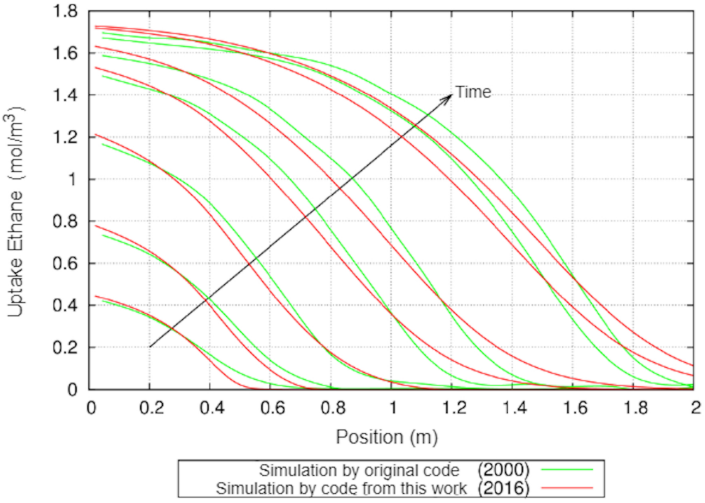

Figure 8.4: Comparison of the simulated loading for ethane as a function of bed position and at the time 10, 20, 40, 70, 90, 130, and 140 seconds.

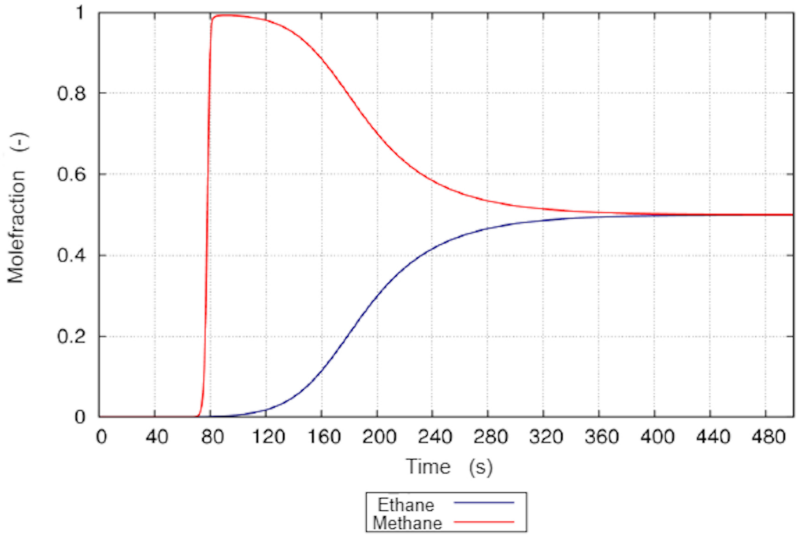

Figure 8.5: Concentration of the gas phase species at the outlet as a function of time.

Again, these deviations can be attributed to the difference in how the mass balances are closed.

Break through curves

The break through curve and the corresponding break through time are important properties when it comes to the characterization of the adsorber material, like selectivity for example. They are the foundation on which the process is designed ultimately as it has significant influence on the cycle scheduling and so on.[183] The concentration of methane and ethane in the gas phase as a function of time at the end of the fixed bed is shown in Figure 8.5. After approximately 70 seconds the concentration front of methane arrives at the end of the bed. In comparison to the inlet for which the ratio of methane to ethane is one, the concentration at the out let at around 80s is pure methane. This is known as a roll-up effect since the weaker bound species displaces the stronger adsorbing one in the gas phase.[183] In other words, because of the lower adsorption enthalpy and higher diffusivity compared to ethane in carbon nanotubes the first species leaving the fixed-bed in the gas phase is methane. This results in a selectivity of 1.8 in favour of ethane. After around 400 seconds the composition at the inlet and outlet are the same (methane to ethane ratio being 1:1).

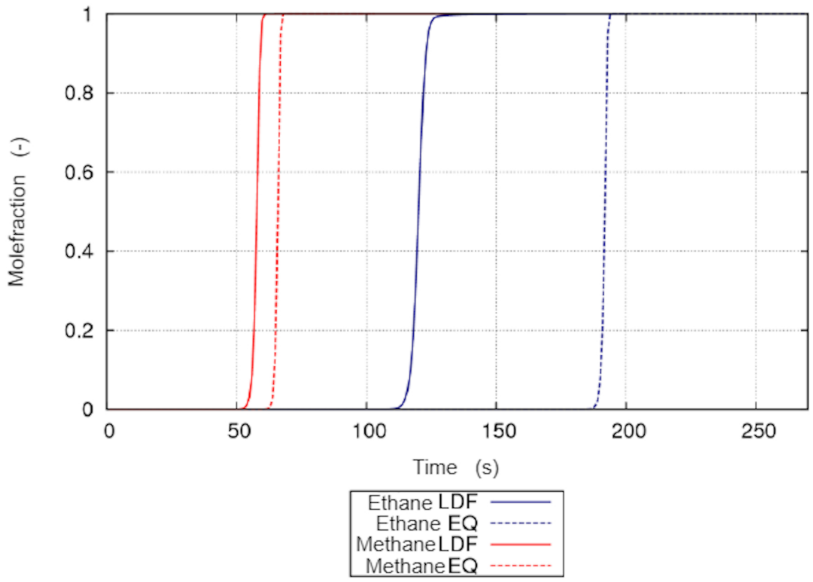

Figure 8.6: Break through curves for pure methane and ethane, respectively, using the equilibrium or LDF ansatz.

Influence of kinetic modelling of adsorption

Since a good description of the mass transport into the adsorber material is vital to the accuracy of the simulation results, the choice of kinetic model becomes very important. Despite the shortcomings and the lack of validation the LDF approach is still the most commonly used ansatz.[183] In Figure 8.6, the composition of the outlet as a function of time and ansatz (equilibrium or LDF) is shown. The influence of the kinetics is obvious for both species: When the equilibrium model is used, the break through is later than in case of the LDF model. The reason for that is the lack of transport resistance from the gas phase to the pores. As a result, more molecules are adsorbed since the gradient between gas phase and adsorbent is higher, hence the capacity to adsorb. This leads to slowing down the progression of the concentration front, and thus, in later break through times. The influence becomes more noticeable the higher the affinity and saturation for a given gas species is. While the difference between the two models for methane is merely 10 to 15 seconds, for ethane it becomes more than a minute.

Conclusion

In general, the results from the new version agree reasonably well with the original code, considering the changes made with the implementation of IAST, different solver, and so on. The code allows to extract a lot of information, such as time dependent output of concentration and loading profiles along the bed as well as tracking the composition of the outlet.

8.3.2 CO_2/N_2 in Mg-MOF-74

The limitation of water in the gas phase

It has already been mentioned that flue gas from coal-based power plants consists of various species of which N_2 represents the majority followed by CO_2, H_2O, and O_2 along with impurities, such as SO_2 , NO_x , and CO.[7,212–214] The likely destruction of the MOF by water because of the OH^- ions in the proximity of the Mg^{2+}[117] makes it very important that water is removed prior to the adsorption step because of that. Even if water did not have the property to weaken the structure, it would still be very disruptive to the adsorption process since it adsorbs far more strongly than CO_2, see Chapter 3. In that case one needs to know, what the maximum fraction of H_2O in the gas phase could be without affecting the efficiency of the adsorber bed. By predicting mixture adsorption isotherms using IAST,[71] see Chapter 2.1.2, one can get a fast and reliable way to roughly estimate the impact of water on the CO_2 adsorption capacity of Mg-MOF-74. The interesting property to look for is the mole fraction of CO_2 and water in the adsorbed phase. The amount of nitrogen adsorbed is in presence of the other two species negligible (up to 5% at maximum). For two different pressures, 1 and 100 kPa, at 300 K, 6 compositions are used in the IAST calculations, in which the fraction of CO_2 is kept constant at 10% while the fraction of water varies from 5% to 0.0001% (Table 8.1). The pressures are chosen, because they represent the pressure during the adsorption and the desorption step 100 kPa and 1 kPa, respectively. The pure component isotherms are fitted using a simple Langmuir function using the parameters given in Table 8.2. The results for the IAST calculations are given in Figure 8.7.

The general trend for both pressures is that with an increase of water in the gas phase more water is adsorbed. At as low as 1% water present in the bulk phase, basically only water is present in the adsorbed phase and no CO_2. Reducing the water content opens up capacity for CO_2 to be adsorbed. The molar fraction of CO_2 increases from 0 over 30% and 80% to 94% with decreasing the water in the gas phase from 1% to 0.001%. Below this content

Table 8.1: Compositions for the gas phases for the IAST calculations.

Index	$\mathbf{x}_{CO2}$ (%)	$\mathbf{x}_{N2}$ (%)	$\mathbf{x}_{H2O}$ (%)
1	10	85	5
2		89	1
3		89.9	0.1
4		89.99	0.01
5		89.999	0.001
6		89.9999	0.0001

Table 8.2: Langmuir coefficients for CO_2, N_2, and H_2O for the IAST calculations.

Index	θ $(\frac{mol}{kg})$	$\mathbf{b}_i$ (kPa^{-1})
$\mathbf{CO_2}$	10.989	0.1500
$\mathbf{N_2}$	23.718	0.0004
$\mathbf{H_2O}$	27.301	6.6001

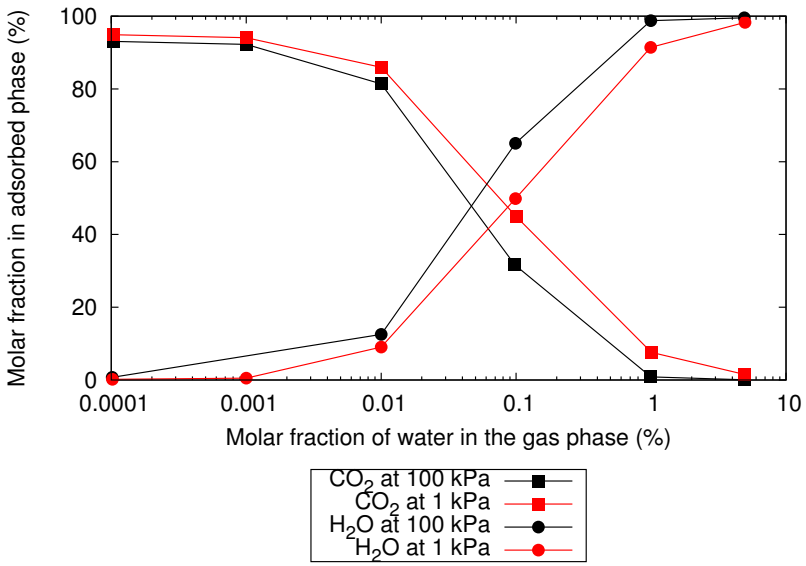

Figure 8.7: Molar fractions of the adsorbed phase as a function of the molar fraction of water in the gas phase for 1 and 100 kPa at 300K calculated using IAST.

water does not have any effect on the adsorption of CO_2. These findings are in agreement with the ones reported by Lin et al.[226] That means that in order to fully utilize Mg-MOF-74 for CO_2 sequestration, the water in the flue gas needs to be removed almost completely.

Proof of principle

Since water needs to be completely removed for Mg-MOF-74 from the flue gas to work effectively, it is assumed that a mixture of N_2/CO_2 with a 85:15 mole fraction ratio enters the adsorber bed. In the following the influence of different geometry parameters of the adsorber bed as well as the inlet concentration on the break through curves are investigated. The species properties, isotherm parameters, and diffusion coefficients are summarized in Tables 8.3, 8.4 and 8.5, respectively. The starting conditions for the adsorption process are given in Table 8.6, the data for the fixed-bed in Table 8.7. Initially, the adsorber bed is empty and the gas present in the system is inert and does not adsorb (helium). The adsorption isotherms reported by Sun et al.[215] are fitted to Langmuir isotherm functions for convenience, see Table 8.2. the effective diffusion coefficient for CO_2 was calculated from the self diffusivity in the rigid framework using the UFF, see Chapter 4. The reasoning to take these coefficients was the agreement with literature data despite its shortcomings. Since N_2 is less strongly adsorbed than CO_2, the diffusivity is estimated by multiplying that diffusivity by 10 (Table 8.5).

The length and the diameter of the adsorber when modelled as a cylinder play an important role with respect to investment (size, material) and maintenance (break through times, cycle scheduling) costs. The bed length is varied between 1m and 3m, see Figure 8.8, and the bed diameter between 0.25m and 0.55m, see Figure 8.9. Clearly, with an increase of both parameters the mass of adsorbent as well as volume increases. For instance increasing the bed length from 1.5m to 3m increases the break through time for CO_2 from 1200 s to 2530 s and for N_2 from 15 s to 30 s (Figure 8.8). This is to be expected: If the length is doubled the amount of adsorbent material is doubled, which results in a doubled break through time. The reason that the break through time is not exactly doubled in case of CO_2 is the dispersion of the flow inside the bed.

With the length kept constant a doubling of the diameter results in a quadrupling of the volume and the mass of the adsorber bed, which in turn leads to a quadrupling of the break through time. For CO_2, the break through time increases from 565s to 2650 s, a factor of roughly 4.6, with the doubling of the radius from 0.25m to 0.5m. The deviation is again likely caused by

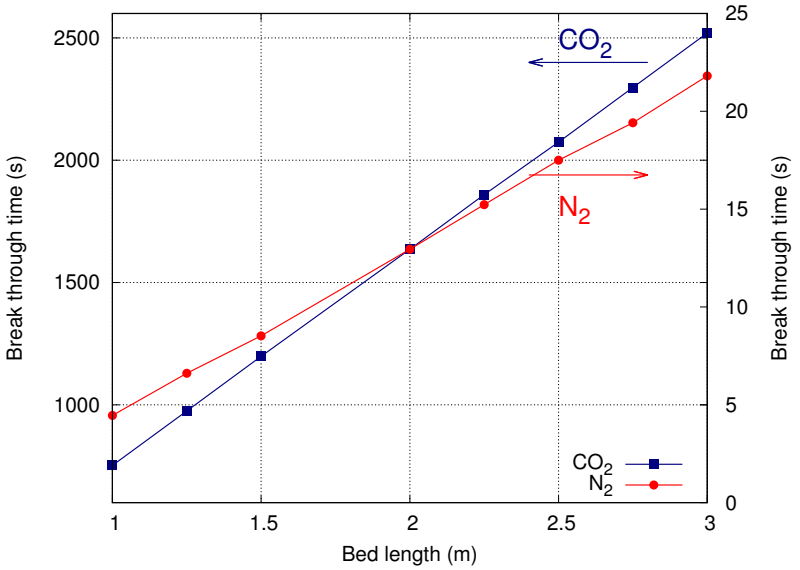

Figure 8.8: Break through times as a function of bed length.

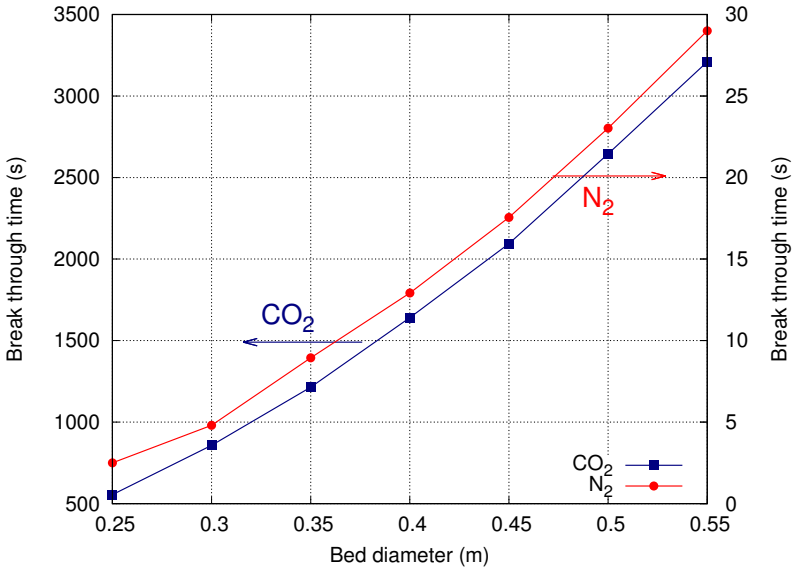

Figure 8.9: Break through times as a function of bed diameter.

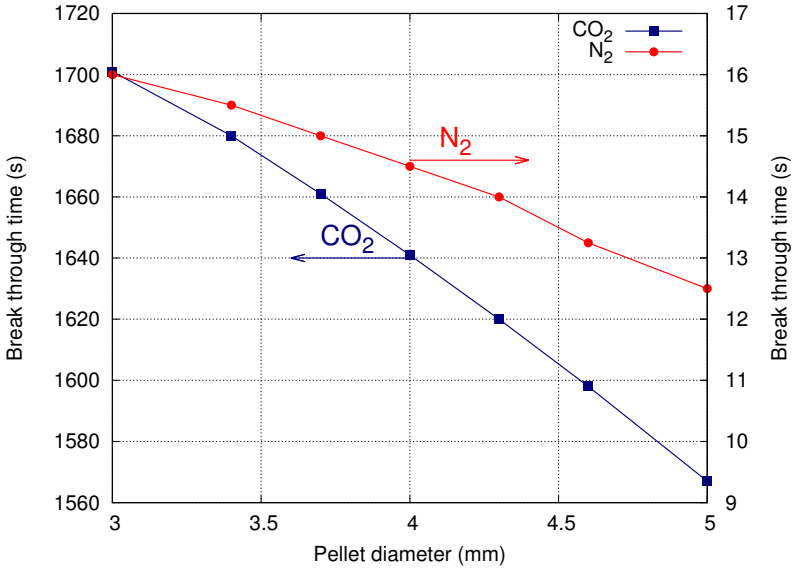

Figure 8.10: Break through times as a function of pellet diameter.

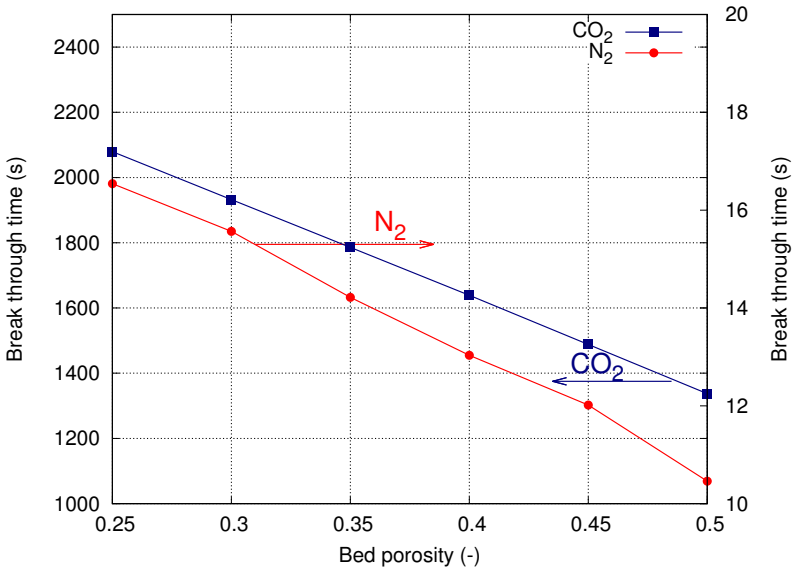

Figure 8.11: Break through times as a function of bed porosity.

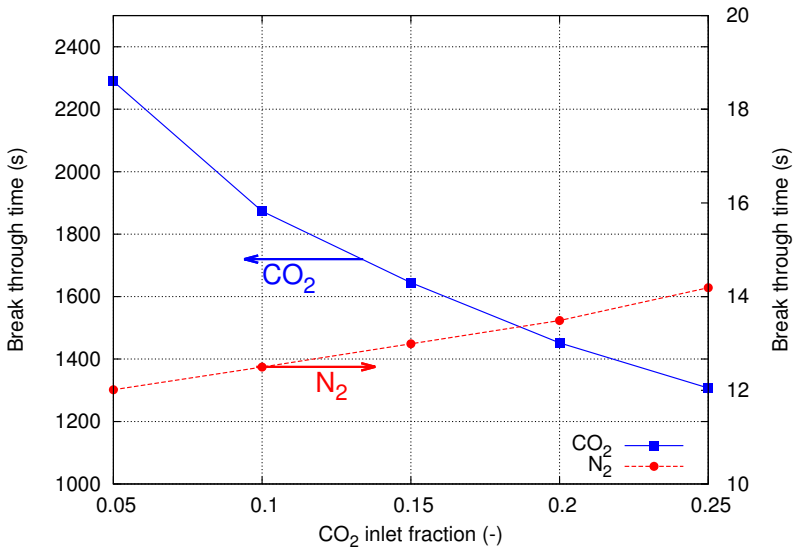

Figure 8.12: Break through times as a function of CO_2 inlet molar fraction.

dispersion effects in the bed, which seem to have more impact on the break through times when the diameter is varied, see Figure 8.9.

Other interesting properties to look at are the average pellet diameter in the bed as well as its porosity ϵ. The former is varied between 3mm and 5mm while the latter is varied from 0.25 to 0.5. The break through times as a function of pellet diameter and the porosity are shown in Figure 8.10 and Figure 8.11, respectively. Increasing the pellet diameter results in a shorter break through time because of a decrease of surface area leading to worse mass transport, see Eq. 2.189, for example, the break through time for CO_2 decreases from 1700s to 1565s when the pellet diameter is increased from 3mm to 5 mm while for N_2 that time is reduced from 15s to 10s (Figure 8.10). Changing the pellet diameter however, is not as impactful as changing the porosity of the bed. Reducing the bed porosity ϵ from 0.5 to 0.25 leads to an increase of the break through time for CO_2 from 1350s to 2100s and for N_2 from 10s to 16s, see Figure 8.11. This is because of the fact that with decreasing porosity $\epsilon = \frac{V^{gas}}{V^{gas}+V^{solid}} = \frac{V^{gas}}{V^{total}}$ the volume fraction occupied by the gas phase is decreased, which results in an increase of adsorbent material. Of course, the bed pressure drop increases by lowering its porosity.

When it comes to the design of any process there are constraints attached to the problem. For example, the educts have a certain pressure, temperature, and viscosity, thus a given volume flow and composition. In case of flue gas the fraction of CO_2 can vary between 5 to 25 mol-%,[370,381] which is

quite significant. While changing all other parameters mentioned impact the dimension of the adsorber bed, in the following part the effect of the CO_2 fluctuation on the break through time is investigated. The break through times for CO_2 and N_2 as a function of the molar fraction of CO_2 at the inlet is presented in Figure 8.12. At a constant pressure the increase of the molar fraction of CO_2 leads to an increase of its partial pressure, while the molar fraction and the partial pressure of N_2 as a result decrease. Unsurprisingly, as the inlet partial pressure of CO_2 increases the break through time decreases, for instance from 1900s at 10 mol-% to 1450s at 20 mol-% for CO_2. At the same time the break through time for N_2 increases marginally from 12.5s to 13.5s. Moreover, the selectivity decreases from 170 (5 mol-% CO_2) to 100 (25 mol-% CO_2) because of the shorter break through time for CO_2. These results point out how important it is that the inlet conditions do not deviate greatly from the values used during the design. It could potentially disturb the cycle schedule or at the worst case damage the down stream processes. In this case fluctuations of $\pm$ 5% of the CO_2 fraction at the inlet already have significant implications on the break through times.

In conclusion, Mg-MOF-74 is a very potent (nano-)porous material when used to separate CO_2 from flue gas in an fixed adsorber bed. The selectivity based on the break through times is in the range from 100 to 200. This evaluation, however, does not take into account the potential structural and chemical problems this framework has or could have in a real process. The program itself is consistent in its evaluations of geometry parameters, such as bed length and diameter. Additionally, the adsorber program was able to calculate the impact of inlet fluctuations on the break through times, and to take then into account by increasing the bed length or diameter to balance out the implications on the cycle schedule.

8.3.3 Olefin/paraffin separation

Since the state-of-the-art technology currently employed to separate olefin/paraffin mixtures is the high energy consuming cryogenic distillation,[44,90,367] adsorption processes can be a potential replacement because of their potentially higher separation efficiency and lower energy consumption. As an example of this type of separation problem we chose an equimolar ethane/ethene mixture using ZIF-8, which showed high potential because of its excellent kinetic properties for this separation.[45,296,302,334] The species properties, isotherm parameters, and diffusion coefficients are summarized in Tables 8.3, 8.4 and 8.5, respectively. The starting conditions for the adsorption process are given in Table 8.6, the data for the fixed-bed in Table 8.7. The

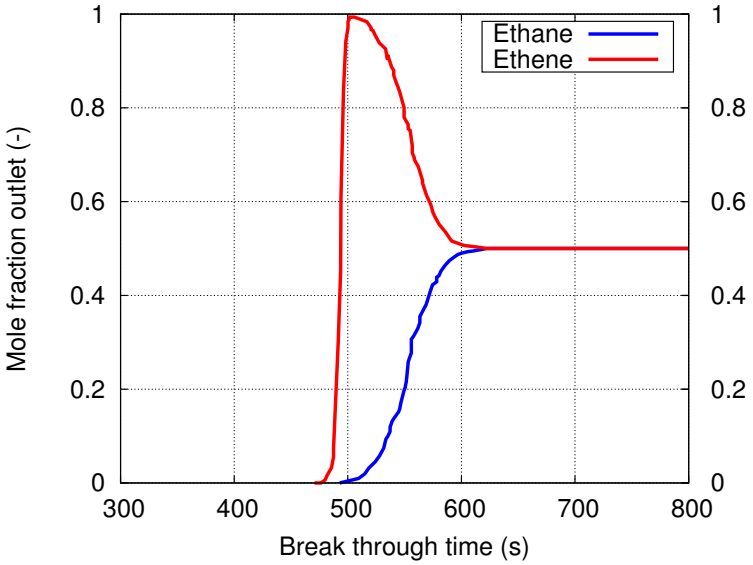

Figure 8.13: Molar fractions for ethane and ethene at the adsorber bed exit as a function of time (break through curves) using the equilibrium ansatz.

adsorber bed is empty and the gas present in the system is inert and does not adsorb (helium).

Since the adsorption isotherms for ethane and ethene are quite similar with respect to their behaviour and Langmuir parameters, the separation is based on the difference in the kinetic properties of the two species. Because of its slightly lower adsorption enthalpy ethene is more mobile than ethane with results in higher diffusivity. Unfortunately, the LDF model did not work in this particular system. The reason for the failure is most likely that the resulting gradients of the respective gas concentrations in combination with the IAST were very small, causing numerical issues. Changing the space step size as well as the time step size yielded no improvement of the problems. Therefore, this system was only simulated with the equilibrium model. Again, while it does not describe the kinetic nature of the system accurately, it is a first approximation of the potential to separate the olefin/paraffin mixture using ZIFs, here ZIF-8. Consequently, models for the solid phase need to include some sort of transport resistance to take this effect into account, resulting in the equilibrium model being only a first approximation of the system. Thus, the LDF ansatz as well as more sophisticated models describing the mass transport into the pores are necessary to simulate the system accurately.

The break through curve for ethane and ethene is shown in Figure 8.13.

The break through time at 1 bar pressure for the two species are quite close with 480s and 510s for ethene and ethane, respectively, resulting in a selectivity of 1.06. This order is expected since ethene adsorbed not as strong as ethane. The general effect was reported by Boehme et al.,[296] who determined break through times of 48 min for ethene and 43 min for ethane in their experiments, yielding a separation factor of 1.2 for the system. The experimental results show a roll-up effect of the weaker adsorbed species, here ethene, which is reproduced by the simulation. The only difference is the height of the amplitude, which is at a maximum of 1.3 in the experiments and 2.0 in the simulation. As explained earlier, because of the equilibration model the kinetic differences of the two compounds are not really taken into account, thus, the selectivity is underestimated by the simulation results. Despite our simulation and the experimental results not having the exact same process parameters, the comparison still shows that the code with the less accurate models is able to evaluate an adsorber bed successfully.

8.4 Conclusions

In this chapter a code was presented with the task to simulate a fixed-bed adsorption process. The general concept of the program was tested for three different separation problems: methane/ethane separation using carbon nanotubes, N_2/CO_2 separation using Mg-MOF-74, and ethane/ethene separation using ZIF-8. The latter two problems are separated by different mechanisms, i.e. different adsorption strength for N_2/CO_2 in Mg-MOF-74 and different diffusivity for ethane/ethene in ZIF-8, in order to check whether or not the simulation code is able to correctly reproduce expectations and experiments.

Because of the changes to the mass balances as well as the addition of an IAST calculation compared to the original code, in the first step the results based on the newer version were compared to the ones based on the old code. The system for that validation was an equimolar mixture of methane and ethane, which were separated using carbon nanotubes. While the concentration profile for methane could not be compared because of the changes made, there was an overall good agreement between both versions of the program with respect to the concentration and loading profiles as a function of time for ethane. Furthermore, the influence of the modelling of the solid material, the equilibrium and the LDF ansatz, were compared. It was shown that the selectivity was the highest, when the equilibrium model was used. This is because of the lack of transport resistance in the mass transfer equation, which results in higher concentration gradients established between

the two phases compared to the LDF approach, emphasizing the influence of different mass transport models in the process.

The second system was the CO_2 separation from flue gas by means of Mg-MOF-74. Initially, it was proven that even if water was harmless to the nanoporous framework it should be removed prior to the adsorber since it adsorbs more strongly than CO_2, rendering the process useless. The gas phase for the adsorber simulation consisted of 85% N_2 and 15% CO_2. The results showed that Mg-MOF-74 is very useful under these circumstances to extract the greenhouse gas CO_2 from the flue gas stream, reaching selectivities of 100 to 200 depending on the diameter and length of the adsorber bed. In addition to that, reducing the pellet diameter or the porosity of the bed resulted in an increase of the break through times for both species. Since the inlet fraction of CO_2 is considered to fluctuate significantly (5% to 25%), we investigated its influence on the break through times. It was shown that the increase of the CO_2 fraction in the gas phase lowered the break through time by a wide margin. This could be potentially harmful to the process and the cycle schedule and the overall efficiency, and therefore, would have to be addressed during detail engineering.

As for the third separation problem, the ethane/ethene separation using ZIF-8, simulations with the LDF model did not succeed, which is likely caused by large gradients in combination with the IAST calculations. Thus, only simulations with the equilibrium model were carried out, which did not take the differences in the diffusivities of the species accurately into account. Nevertheless, the correct trends were reproduced, however, the calculated selectivities were lower than the ones obtained from experiments.

Despite some problems regarding the models in the code, the simulations reproduce the expected trends correctly and experiments quite accurately. This program is in a bare-bone state, yet its possibilities to simulate the adsorption process and identify as well as optimize critical process parameters has been proven in principle. Obviously, there is room for improvement, such as implementing more sophisticated models for the solid phase, the implementation of energy balances, and fixing numerical issues for instance.

Table 8.3: Properties of species used in the adsorber program taken from Ref. 194.

Property	CH_4	C_2H_6	C_2H_4	CO_2	N_2
Molar weight $\left(\frac{g}{mol}\right)$	16.0	30.1	28.0	44.0	28.0
Critical temperature (K)	305.4	190.4	169.4	304.1	126.2
Critical Pressure (bar)	46.0	48.8	50.4	73.7	34.0
Critical molar volume $\left(\frac{mol}{m^3}\right)$	10101.0	6756.8	7736.2	10624.9	11210.3
acentric factor (-)	0.011	0.100	0.087	0.224	0.022
Diffusion volume (-)	24.42	44.8	40.9	26.9	17.9

8.5 Supporting information

8.5.1 Methane concentration in carbon nanotubes

In Figure 8.14, a comparison for the methane concentration in the gas phase is shown based on the original and our version of the code. Here, the difference between the two versions is obvious on how the system of partial differential equations and thus the closing of the mass balances varies. As a consequence, in the original work methane reaches the exit of the bed very quickly despite it being impossible because of the low flow rate. With the introduction of the inert gas one gets a physical representation of the displacement of the inert gas with methane. The break through of methane is in our version between 70 and 90 seconds compared to the 0 seconds in the original code. This allows to monitor the outlet gas composition and calculate selectivities

Table 8.4: Effective transport diffusivites for the investigated systems. Estimated values are taken from Refs 360 and 88 as well as Chapters 4 and 7.

Species	Material	Effective transport diffusivity $\frac{m^2}{s}$
CH_4	Carbon nanotubes	$0.804 \cdot 10^{-8}$
C_2H_6		$5.230 \cdot 10^{-8}$
CO_2	Mg-MOF-74	$0.8 \cdot 10^{-8}$
N_2		$8.0 \cdot 10^{-8}$
C_2H_6	ZIF-8	$1.0 \cdot 10^{-11}$
C_2H_4		$5.0 \cdot 10^{-11}$

Table 8.5: Pure component adosprtion isotherms fitted to the Langmuir isotherm function for the investigated systems. The parameter are taken from Refs 360 and 215 as well as Chapters 3 (converted to from SIPS to Langmuir isoterm) and 5.

Langmuir parameter	**Carbon nanotubes**		**ZIF-8**		**Mg-MOF-74**	
	CH_4	C_2H_6	C_2H_4	C_2H_6	N_2	CO_2
$\mathbf{q}^{max}$ $\left(\frac{mol}{kg}\right)$	4.098	3.301	8.348	6.978	16.818	10.646
K (bar^{-1})	0.0272	0.265	0.197	0.440	0.015	5.482

Table 8.6: Conditions for the adsorber processes for each investigated system.

Framework	Carbon nanotubes		Mg-MOF-74		ZIF-8	
Species	CH_4	C_2H_6	CO_2	N_2	C_2H_4	C_2H_6
Molar fraction (-)	0.5	0.5	0.15	0.85	0.5	0.5
Temperature (K)	300		300		300	
Pressure (bar)	10		1		1	
Total molar flow $\left(\frac{mol}{s}\right)$	4		4		4	

Table 8.7: Properties of the adsorber for each of the investigated systems.

Length of adsorber bed	2 m
Diameter of adsorber bed	0.4 m
Porosity of fixed-bed	0.4
Pellet diameter	4 mm
Density of the solid	1500 $\frac{kg}{m^3}$

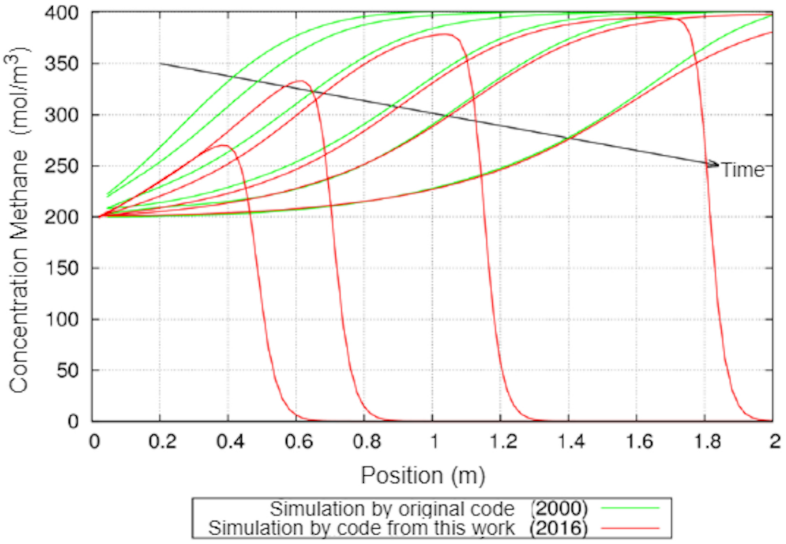

Figure 8.14: Comparison of the simulated concentration in the gas phase for methane as a function of bed position and at the time 10, 20, 40, 70, 90, 130, and 140 seconds.

based on break through times.

Part V

Summary and outlook

9 Conclusions

This thesis aimed towards the development of a methodology for a multi-scale design approach of adsorption processes in which simulations at the atomistic scale, Monte Carlo, and molecular dynamics simulations, are combined with simulations at continuum scale.

This methodology addressed two different separation problems with the first being CO_2 sequestration from flue gas and the second being the separation of olefin/paraffin-mixtures. The motivation regarding the former was based on the need to find an alternative for the state-of-the-art technology, which is amine scrubbing. While it is relatively effective removing the greenhouse gas CO_2 from the flue gas stream, its high energy cost because of the regeneration of water by evaporation reduces the overall performances of coal-based power plants. The new class of metal-organic frameworks (MOFs) offer the opportunity of substituting the current removal process by a less energy consuming one, while maintaining high productivity. MOFs exhibit large surface areas, are highly customisable, and can be tailor-made for the separation problems at hand. The adsorption processes are an alternative, since they can be designed with relative ease, the control is relatively simple, and no energy consuming regeneration step is necessary. The latter separation problem (olefin/paraffin-separation) also has a state-of-the-art process with a high energy consumption: Currently, cryogenic distillation is applied to separate olefins from their paraffin-counterparts by making use of the different boiling points, which are far below ambient temperatures. Similar to the first separation problem by using an optimised adsorption process, an energy intensive regeneration step can be circumvented, reducing the costs of separation. Furthermore, the desired product, the olefin, can be gathered at high(er) pressures, which leads to simpler downstream processing. This work has been divided into two main parts each of which is dedicated towards one of the aforementioned separation problems: CO_2 sequestration (chapters 3, 4, and 8) and olefin/paraffin separation (chapters 5, 6, 7, and 8).

Mg-MOF-74 (or CPO-27-Mg) had been identified in the literature as one of the promising materials for the separation of CO_2 from flue gas because of its open metal sites (OMS). This MOF shows high selectivity towards CO_2 in a flue gas representing CO_2/N_2-mixture. Additionally, the third main component, H_2O was reported to adsorb also very strongly on MOFs and potentially weaken the structural integrity of the crystal, while competing with CO_2 for the adsorption sites. Classical force fields are not able to correctly predict adsorption isotherms for N_2, CO_2, or H_2O because of the electrostatic potential induced by coordinatively unsaturated Mg^{2+} ions in the framework. To circumvent this inaccuracy, we employed DFT calculations including van-der-Waals-interactions to probe the entire potential energy surface of the crystal for various configurations for the different molecules inside the framework. Based on those results, force fields were fitted to reproduce the potential energy surface for CO_2 and H_2O. The adsorption isotherms generated with the newly developed force fields proved to be an appreciable improvement, especially in the low pressure regimes of the CO_2 and water isotherms. Based on those results, mixture adsorption isotherms were predicted using the ideal adsorbed solution theory in order to identify molar fraction of water at which the adsorption capacity of Mg-MOF-74 towards CO_2 was not influenced, resulting in 0.001 mol-% water in the bulk gas phase. Next, we investigated the diffusivity of CO_2 and H_2O using the DFT-based force fields as well as the influence of the framework flexibility. In the rigid crystal, CO_2 diffusivity decreases when the number of molecules is increased. Overall, the mobility is pretty low. Once flexibility is introduced to the system, the trends did not change, but the magnitude is overall increased as the mobility of the CO_2 molecules is enhanced. The diffusivity of water on the other hand has the contrary behaviour as it increases with increasing loading regardless of the flexibility. This effect can be attributed to the clustering effects whereas water experiences because of hydrogen bonding. Similar to CO_2, with the introduction of framework flexibility the overall mobility of the water molecules is enhanced, and hence, the diffusivity is higher than the rigid case at low loadings. The simulation of diffusion of CO_2/H_2O-mixtures in Mg-MOF-74 show a strong segregation effect, because at almost all times only water is found adsorbed at the OMS. The adsorption isotherms and (self-) diffusion coefficients obtained from the molecular simulations were used as inputs for an adsorber program which is written in FORTRAN code. This program solves the governing partial differential equations of the systems to obtain a dynamic solution. Ideal adsorbed solution theory was used to obtain mixture adsorption isotherm data on the fly. As prove of principal, it was shown that Mg-MOF-74 is indeed a highly promising material, when it comes to the separation of N_2/CO_2 mixtures in case no water is present, resulting in high

selectivities and high breakthrough times towards the unwanted compound CO_2.

Zeolitic imidazolate frameworks (ZIFs) and imidazolate frameworks Potsdam (IFPs) showed promise with respect to olefin/paraffin-separation. In those crystals the desired species, the olefin, is less strongly adsorbed, making it possible to obtain them during the high pressure step of the adsorption process. The adsorption isotherms of ZIF-8, ZIF-9, and ZIF-71 obtained from molecular simulations show that for C_2 molecules the paraffin is favourably adsorbed, although the selectivity is relatively low. In the case of C_3, the selectivity is reversed, barely favouring the olefins because of their smaller size. Of those three ZIFs, ZIF-8 proved itself to be the most promising candidate. As for the IFPs, we studied four different frameworks: IFP-1, IFP-3, IFP-5, and IFP-7. These series allows to investigate the influence of different linkers on geometries and adsorption properties, such as adsorption isotherms, adsorption energies and free energy profiles. The most influential parameter to quantify the difference because of the linkers was the free channel size of each framework. The smaller the linker is the larger the free channel diameter and the higher the adsorption capacity. The adsorption energies as well as the free energy profiles do not differ much between the four crystals. Similar to the ZIFs regarding C_2 molecules, the paraffin is favourably adsorbed, while for C_3 the olefin has a higher saturation at 1 bar. The most promising candidate for this separation is arguably IFP-1. We investigated the diffusion of the hydrocarbons as well as the influence of the flexibility of the crystallographic structures using molecular dynamics simulations for ZIF-8, ZIF-9, and ZIF-71. Studies showed gate-opening effects in ZIF-8, which could be confirmed by this thesis. Once this constraint was lifted, it was shown that the olefin has a higher diffusivity, which is in agreement with the previously obtained adsorption results. In ZIF-9, it could only be shown by simulations that the structure is highly flexible, opening up to create multiple intersections in the channels. This effect can not be modelled accurately because of its high complexity and the lack of experimental data for validation. Because of its larger windows and cavities, the movement of molecules in ZIF-71 was not hindered when modelled as rigid. However with flexibility introduced, the movement of the guest molecules was increased, resulting in a magnitude difference in diffusivity. The adsorber program was used as a prove of principal for the separation of olefin/paraffin-mixtures using a C_2 mixture and ZIF-8 as an example. We showed that the separation is possible in such a scenario. However, since the adsorption isotherms are very similar the adsorber program exhibited numerical issues, preventing a more detailed investigation.

In conclusion, we created and tested a methodology for multi-scale mod-

elling and design of adsorption processes in which adsorption isotherms and diffusion coefficients were determined by molecular simulations at the atomisitc scale. These results were then used as input for the adsorber process simulation at the continuum scale. Two goals were set in the beginning of this work. The first one was to obtain adsorption isotherms and diffusion properties for the investigated MOFs based on molecular simulations. This is achieved successfully for both separation problems investigated in this work, involving the generation of new force fields and taking the influence of flexibility of the frameworks into account. The second goal was to set up a simulation of a fixed-bed adsorber, using the adsorption isotherms and diffusion coefficients obtained from the molecular simualtions as inputs. This is achieved as well, since the continuum model ran successfully for both systems, proving that the state-of-the-art technologies could be replaced. However, the adsorber model ran into some numerical issues for the olefin/paraffin-separation because of the similar adsortpion isotherm behavior. Overall, the ansatz of designing adsorption processes based on computer simulations can be a useful tool to gain more insight in the adsorption process itself, while reducing the amount of experiments needed to scale up from the laboratory to larger scales at the same time.

10 Outlook

Based on the results presented and the conclusions drawn in this work, there are various starting points to continue on the research topics and to improve the methods of the methodology as well.

The CO_2 sequestration from flue gas is still an ongoing topic of research and discussion. We showed that Mg-MOF-74 has exceptional properties with respect to this separation problem if certain criteria are met, in particular the complete removal of water from the flue gas before the adsorption. Therefore, it is obvious that the screening process cannot be considered as finished in this regard. Evaluating hydrophobic MOFs or more chemically stable ones, which may or may not offer open metal sites can lead to a framework more suitable for real life and process conditions. Furthermore, one is also not restricted to MOFs. Other nanoporous materials, such as covalent organic frameworks or related materials, can be promising alternatives. Regarding olefin/paraffin-mixtures, this work presented several frameworks capable of separating of the olefin from its paraffin counterpart. However, the selectivity is not very high, hoovering around 1 to 1.5 mostly. Finding a more effective material may push the adsorption process towards being a real alternative to the cryogenic distillation. Whereas in both cases the search for an optimal adsorbent is important and essential in order to decide whether or not an adsorption process can replace the state-of-the-art technology (amine scrubbing or cryogenic distillation respectively), potential of the adsorption process can also be further improved by the way the process is run, controlled and scheduled, increasing the overall efficiency of the technology. Some of those aspects have been addressed in this work, giving a foundation from which to investigate the aforementioned facets. Using the simulation of the adsorption process to identify critical parameters or predict how the system reacts to disturbances are also crucial to deem a technology feasible for the industrial application.

Regarding the methodology, it should be noted that the molecular modelling as well as the adsorber program started with one specific or a small subset of nanoporous materials, which had been identified from the literature as very promising candidates for the respective separation problem. As it was mentioned throughout this work, that the number of MOFs is potentially almost infinite because of the immense number of combinations of (metal-)ions and organic linkers, making screening processes a valuable addition to this methodology. The methodology would look as follows: For any given separation problem one could identify a couple of promising structures. With this preselection it could be possible to run this methodology for a couple of frameworks for a more in-depth evaluation offering choices with respect to potential process constraints. As a consequence, the best materials could be used in laboratory experiments, reducing the number of experiments significantly. It was pointed out how important force fields are for the overall accuracy of the simulations, since based on those molecular simulations structures are identified in a screening process or their adsorption properties are evaluated. The generation of force fields working for a specific system, however, comes at the cost of hundreds of (costly) DFT calculations. Thus, an automatisation of the process of force field generation would be one way to negate that issue. A second ootion would be designing force fields, which work for all MOFs equally well. Framework flexibility should also be accounted for. The implementation of general force fields with those properties into the screening process via molecular simulation would improve the accuracy of the methodology. As mentioned in Chapter 8, the adsorber program is currently only able to simulate breakthrough curves. An important next step in the development would be the ability to simulate the blowdown, regeneration, and pressurisation steps as well. Moreover, bugs and numerical issues need to be addressed so that IAST and the program as a whole work better in conjunction in case when adsorption isotherm are similar in shape and uptake, like in the olefin/paraffin-case. Assuming these modifications would be implemented successfully, the optimisation of the adsorption process itself as well as the investigation of critical process parameters and their influence on the full cycle could be studied intensively and accurately.

Bibliography

[1] J. J. McCarthy, O. F. Canziani, N. A. Leary, D. J. Dokken, and K. S. White, *Climate Change 2001: Impacts, Adaptation, and Vulnerability - Contribution of Working Group II to the Third Assessment Report of the Intergovernmental Panel on Climate Change*. Cambridge: Cambridge University Press, first edition ed., 2001.

[2] N. Oreskes, "The scientific consensus on climate change," *Science*, vol. 306, pp. 1686–1686, Dec. 2004.

[3] S. van den Hove, "The oil industry and climate change: Strategies and ethical dilemmas," *Climate Policy*, vol. 2, pp. 3–18, May 2002.

[4] B. Metz, ed., *IPCC Special Report on Carbon Dioxide Capture and Storage*. Cambridge: Cambridge Univ. Press, 2005.

[5] "Treibhausgas-Emissionen in Deutschland." `https://www.umweltbundesamt.de/daten/klima/treibhausgas-emissionen-in-deutschland`, April 2019.

[6] R. H. Socolow and S. W. Pacala, "A plan to keep carbon in check," *Scientific American*, vol. 295, no. 3, pp. 50–57, 2006.

[7] D. M. D'Alessandro, B. Smit, and J. R. Long, "Carbon dioxide capture: Prospects for new materials," *Angewandte Chemie International Edition*, vol. 49, no. 35, pp. 6058–6082, 2010.

[8] Organization For Economic Cooperation Development, *CO_2 Emissions From Fuel Combustion: Overview 2017*. [S.l.]: OECD, 2017.

[9] M. Balser, "Zu viel Kohle, zu viel Gift." `https://www.sueddeutsche.de/wirtschaft/schmutzige-energie-zu-viel-kohle-zu-viel-gift-1.1959268`, May 2014.

[10] N. Klawitter, "Deutsche Kraftwerke sind die schmutzigsten in Europa." https://www.spiegel.de/wirtschaft/unternehmen/kohlekraftwerke-in-deutschland-stossen-mehr-co2-aus-als-im-eu-schnitt-a-962028.html, April 2014.

[11] B. Smit, J. A. Reimer, C. M. Oldenburg, and I. C. Bourg, *Introduction To Carbon Capture And Sequestration*. London: Imperial College Press, 1st edition ed., 2014.

[12] R. S. Haszeldine, "Carbon capture and storage: How green can black be?," *Science*, vol. 325, no. 5948, pp. 1647–1652, 2009.

[13] G. T. Rochelle, "Amine scrubbing for CO_2 capture," *Science*, vol. 325, no. 5948, pp. 1652–1654, 2009.

[14] R. Serna-Guerrero, E. Da'na, and A. Sayari, "New insights into the interactions of CO_2 with amine-functionalized silica," *Industrial & Engineering Chemistry Research*, vol. 47, no. 23, pp. 9406–9412, 2008.

[15] J. C. Hicks, J. H. Drese, D. J. Fauth, M. L. Gray, G. Qi, and C. W. Jones, "Designing adsorbents for CO_2 capture from flue gas - hyperbranched aminosilicas capable of capturing CO_2 reversibly," *Journal of the American Chemical Society*, vol. 130, no. 10, pp. 2902–2903, 2008.

[16] G. P. Knowles, S. W. Delaney, and A. L. Chaffee, "Diethylenetriamine[propyl(silyl)]-functionalized (dt) mesoporous silicas as CO_2 adsorbents," *Industrial & Engineering Chemistry Research*, vol. 45, no. 8, pp. 2626–2633, 2006.

[17] E. Berger, M. W. Hahn, T. Przybilla, B. Winter, E. Spiecker, A. Jentys, and J. A. Lercher, "Impact of solvents and surfactants on the self-assembly of nanostructured amine functionalized silica spheres for CO_2 capture," *Journal of Energy Chemistry*, vol. 25, no. 2, pp. 327–335, 2016.

[18] M. W. Hahn, J. Jelic, E. Berger, K. Reuter, A. Jentys, and J. A. Lercher, "Role of amine functionality for CO_2 chemisorption on silica," *The Journal of Physical Chemistry B*, vol. 120, no. 8, pp. 1988–1995, 2016.

[19] G. S. Foo, J. J. Lee, C.-H. Chen, S. E. Hayes, C. Sievers, and C. W. Jones, "Elucidation of surface species through in situ ftir spectroscopy of carbon dioxide adsorption on amine-grafted SBA-15," *ChemSusChem*, vol. 10, no. 1, pp. 266–276, 2017.

[20] C. Lu, H. Bai, B. Wu, F. Su, and J. F. Hwang, "Comparative study of CO_2 capture by carbon nanotubes, activated carbons, and zeolites," *Energy & Fuels*, vol. 22, no. 5, pp. 3050–3056, 2008.

[21] F. Su, C. Lu, W. Cnen, H. Bai, and J. F. Hwang, "Capture of CO_2 from flue gas via multiwalled carbon nanotubes," *The Science of the Total Environment*, vol. 407, no. 8, pp. 3017–3023, 2009.

[22] M. Rahimi, J. K. Singh, D. J. Babu, J. J. Schneider, and F. Müller-Plathe, "Understanding carbon dioxide adsorption in carbon nanotube arrays: Molecular simulation and adsorption measurements," *Journal of Physical Chemistry C*, vol. 117, no. 26, pp. 13492–13501, 2013.

[23] D. J. Babu, M. Bruns, R. Schneider, D. Gerthsen, and J. J. Schneider, "Understanding the influence of n-doping on the CO_2 adsorption characteristics in carbon nanomaterials," *Journal of Physical Chemistry C*, vol. 121, no. 1, pp. 616–626, 2016.

[24] D. J. Babu and J. J. Schneider, "Gas adsorption studies of CO_2 in carbon nanomaterials: A case study of vertically aligned carbon nano tubes," *Chemie Ingenieur Technik*, vol. 89, no. 10, pp. 1273–1287, 2017.

[25] A. Goj, D. S. Sholl, E. D. Akten, and D. Kohen, "Atomistic simulations of CO_2 and N_2 adsorption in silica zeolites: The impact of pore size and shape," *The Journal of Physical Chemistry B*, vol. 106, no. 33, pp. 8367–8375, 2002.

[26] R. V. Siriwardane, M.-S. Shen, and E. P. Fisher, "Adsorption of CO_2, N_2, and O_2 on natural zeolites," *Energy & Fuels*, vol. 17, no. 3, pp. 571–576, 2003.

[27] R. V. Siriwardane, M.-S. Shen, E. P. Fisher, and J. Losch, "Adsorption of CO_2 on zeolites at moderate temperatures," *Energy & Fuels*, vol. 19, no. 3, pp. 1153–1159, 2005.

[28] Z. Liang, M. Marshall, and A. L. Chaffee, "CO_2 adsorption-based separation by metal organic framework (Cu-BTC) versus zeolite (13X)," *Energy & Fuels*, vol. 23, no. 5, pp. 2785–2789, 2009.

[29] F. Su, C. Lu, S.-C. Kuo, and W. Zeng, "Adsorption of CO_2 on amine-functionalized Y-type zeolites," *Energy & Fuels*, vol. 24, no. 2, pp. 1441–1448, 2010.

[30] M. R. Hudson, W. L. Queen, J. A. Mason, D. W. Fickel, R. F. Lobo, and C. M. Brown, "Unconventional, highly selective CO_2 adsorption in zeolite SSZ-13," *Journal of the American Chemical Society*, vol. 134, no. 4, pp. 1970–1973, 2012.

[31] J. Kim, M. Abouelnasr, L.-C. Lin, and B. Smit, "Large-scale screening of zeolite structures for CO_2 membrane separations," *Journal of the American Chemical Society*, vol. 135, no. 20, pp. 7545–7552, 2013.

[32] Y. Li and R. T. Yang, "Gas adsorption and storage in metal-organic framework MOF-177," *Langmuir*, vol. 23, no. 26, pp. 12937–12944, 2007.

[33] R. Banerjee, A. Phan, B. Wang, C. Knobler, H. Furukawa, M. O\textquoterightKeeffe, and O. M. Yaghi, "High-throughput synthesis of zeolitic imidazolate frameworks and application to CO_2 capture," *Science*, vol. 319, no. 5865, pp. 939–943, 2008.

[34] F. Salles, A. Ghoufi, G. Maurin, R. G. Bell, C. Mellot-Draznieks, and G. Férey, "Molecular dynamics simulations of breathing mofs: Structural transformations of MIL-53(Cr) upon thermal activation and CO_2 adsorption," *Angewandte Chemie (Int. ed.)*, vol. 47, no. 44, pp. 8487–8491, 2008.

[35] D. Britt, H. Furukawa, B. Wang, T. G. Glover, and O. M. Yaghi, "Highly efficient separation of carbon dioxide by a metal-organic framework replete with open metal sites," *Proceedings of the National Academy of Sciences*, vol. 106, no. 49, pp. 20637–20640, 2009.

[36] S. Couck, J. F. M. Denayer, G. V. Baron, T. Rémy, J. Gascon, and F. Kapteijn, "An amine-functionalized MIL-53 metal-organic framework with large separation power for CO_2 and CH_4," *Journal of the American Chemical Society*, vol. 131, no. 18, pp. 6326–6327, 2009.

[37] Z. Zhao, Z. Li, and Y. S. Lin, "Adsorption and diffusion of carbon dioxide on metal−organic framework (MOF-5)," *Industrial & Engineering Chemistry Research*, vol. 48, no. 22, pp. 10015–10020, 2009.

[38] L. Hamon, E. Jolimaître, and G. D. Pirngruber, "CO_2 and CH_4 separation by adsorption using Cu-BTC metal-organic framework," *Industrial & Engineering Chemistry Research*, vol. 49, no. 16, pp. 7497–7503, 2010.

[39] D. Saha, Z. Bao, F. Jia, and S. Deng, "Adsorption of CO_2, CH_4, N_2O, and N_2 on MOF-5, MOF-177, and zeolite 5A," *Environmental Science & Technology*, vol. 44, no. 5, pp. 1820–1826, 2010.

[40] L. Valenzano, B. Civalleri, S. Chavan, G. T. Palomino, C. O. Areán, and S. Bordiga, "Computational and experimental studies on the adsorption of CO,N_2 , and CO_2 on Mg-MOF-74," *Journal of Physical Chemistry C*, vol. 114, no. 25, pp. 11185–11191, 2010.

[41] W. L. Queen, M. R. Hudson, E. D. Bloch, J. A. Mason, M. I. Gonzalez, J. S. Lee, D. Gygi, J. D. Howe, K. Lee, T. A. Darwish, M. James, V. K. Peterson, S. J. Teat, B. Smit, J. B. Neaton, J. R. Long, and C. M. Brown, "Comprehensive study of carbon dioxide adsorption in the metal-organic frameworks M_2(dobdc) (M = Mg, Mn, Fe, Co, Ni, Cu, Zn)," *Chemical Science*, vol. 5, no. 12, pp. 4569–4581, 2014.

[42] E. Braun, A. F. Zurhelle, W. Thijssen, S. K. Schnell, L.-C. Lin, J. Kim, J. A. Thompson, and B. Smit, "High-throughput computational screening of nanoporous adsorbents for CO_2 capture from natural gas," *Mol. Syst. Des. Eng.*, vol. 1, no. 2, pp. 175–188, 2016.

[43] R. Chanajaree, T. Chokbunpiam, J. Kärger, S. Hannongbua, and S. Fritzsche, "Investigating adsorption- and diffusion selectivity of CO_2 and CH_4 from air on zeolitic imidazolate framework-78 using molecular simulations," *Microporous and Mesoporous Materials*, vol. 274, pp. 266–276, 2019.

[44] R. B. Eldridge, "Olefin/paraffin separation technology: a review," *Industrial & Engineering Chemistry Research*, no. 32, pp. 2208–2212, 1993.

[45] U. Böhme, B. Barth, C. Paula, A. Kuhnt, W. Schwieger, A. Mundstock, J. Caro, and M. Hartmann, "Ethene/ethane and propene/propane separation via the olefin and paraffin selective metal–organic framework adsorbents CPO-27 and ZIF-8," *Langmuir*, vol. 29, no. 27, pp. 8592–8600, 2013.

[46] R. W. Baker, "Future directions of membrane gas separation technology," *Industrial & Engineering Chemistry Research*, vol. 41, no. 6, pp. 1393–1411, 2002.

[47] W. R. True, "Global ethylene capacity continues advance in 2011," *Oil & Gas Journal*, vol. 110, no. 7, p. n.a., 2012.

[48] *Kirk-Othmer Encyclopedia of Chemical Technology, Index to Volumes 1 - 26*. Wiley-Interscience, 2007.

[49] *CRC Handbook of Chemistry and Physics, 77th edition*. CRC Press, 1996.

[50] W. M. Haynes and D. R. Lide, eds., *CRC Handbook of Chemistry and Physics: A Ready-reference Book of Chemical and Physical Data*. Boca Raton, Fla.: CRC Press, 93. ed., 2012 - 2013 ed., 2012.

[51] K. Stork and K. Wagner, "Energy savings in ethylene separation," *Oil & Gas Journal*, vol. 60, no. 3, p. n.a., 1971.

[52] A. van Miltenburg, W. Zhu, F. Kapteijn, and J. A. Moulijn, "Adsorptive separation of light olefin/paraffin mixtures," *Chemical Engineering Research and Design*, vol. 84, no. 5, pp. 350–354, 2006.

[53] Y. He, R. Krishna, and B. Chen, "Metal-organic frameworks with potential for energy-efficient adsorptive separation of light hydrocarbons," *Energy & Environmental Science*, vol. 5, no. 10, p. 9107, 2012.

[54] P. Bernardo, E. Drioli, and G. Golemme, "Membrane gas separation: A review/state of the art," *Industrial & Engineering Chemistry Research*, vol. 48, no. 10, pp. 4638–4663, 2009.

[55] S. Kitagawa, "Porous materials and the age of gas," *Angewandte Chemie International Edition*, vol. 54, no. 37, pp. 10686–10687, 2015.

[56] J.-R. Li, R. J. Kuppler, and H.-C. Zhou, "Selective gas adsorption and separation in metal-organic frameworks," *Chemical Society Reviews*, vol. 38, no. 5, pp. 1477–1504, 2009.

[57] U. Mueller, M. Schubert, F. Teich, H. Puetter, K. Schierle-Arndt, and J. Pastré, "Metal-organic frameworks - prospective industrial applications," *Journal of Materials Chemistry*, vol. 16, no. 7, p. 626, 2006.

[58] A. U. Czaja, N. Trukhan, and U. Müller, "Industrial applications of metal-organic frameworks," *Chemical Society Reviews*, vol. 38, no. 5, pp. 1284–1293, 2009.

[59] N. Stock and S. Biswas, "Synthesis of metal-organic frameworks (MOFs): Routes to various MOF topologies, morphologies, and composites," *Chemical Reviews*, vol. 112, no. 2, pp. 933–969, 2012.

[60] D. D. Duong, *Adsorption Analysis: Equilibria and Kinetics*, vol. 2 of *Series on chemical engineering*. London and Singapore: Imperial College Press, 1998.

[61] F. Rouquerol, J. Rouquerol, and K. S. W. Sing, *Adsorption by Powders and Porous Solids: Principles, Methodology, and Applications*. San Diego: Academic Press, 1999.

[62] D. H. Everett, "Manual of symbols and terminology for physicochemical quantities and units, appendix ii: Definitions, terminology and symbols in colloid and surface chemistry," *Pure and Applied Chemistry*, vol. 31, no. 4, pp. 577–638, 1972.

[63] J. W. Gibbs, *The Collected Works of J. Willard Gibbs. Vol. 1, Vol. 1.* New York and London: Longmans, Green & Co, 1928.

[64] I. Langmuir, "The adsorption of gases on plane surfaces of glasss, mica, and platinum," *Journal of the American Chemical Society*, vol. 40, no. 9, pp. 1361–1403, 1918.

[65] H. Freundlich, "Of the adsorption of gases. section ii. kinetics and energetics of gas adsorption. introductory paper to section ii," *Trans. Faraday Soc.*, vol. 28, p. 195, 1932.

[66] R. Sips, "On the structure of a catalyst surface," *The Journal of Chemical Physics*, vol. 16, no. 5, pp. 490–495, 1948.

[67] E. C. Markham and A. F. Benton, "The adsorption of gas mixtures by silica," *Journal of the American Chemical Society*, vol. 53, no. 2, pp. 497–507, 1931.

[68] A. Dabrowski, "Adsorption - from theory to practice," *Advances in Colloid and Interface Science*, vol. 93, no. 1-3, pp. 135–224, 2001.

[69] M. Jaroniec and W. Rudzinski, "Adsorption of binary gas mixtures on heterogeneous surfaces," *Physics Letters A*, vol. 53, no. 1, pp. 59–60, 1975.

[70] R. P. Danner and E. C. F. Choi, "Mixture adsorption equilibria of ethane and ethylene on 13X molecular sieves," *Industrial & Engineering Chemistry Fundamentals*, vol. 17, no. 4, pp. 248–253, 1978.

[71] A. L. Myers and J. M. Prausnitz, "Thermodynamics of mixed-gas adsorption," *AIChE Journal*, vol. 11, no. 1, pp. 121–127, 1965.

[72] Y.-S. Bae, C. Y. Lee, K. C. Kim, O. K. Farha, P. Nickias, J. T. Hupp, S. T. Nguyen, and R. Q. Snurr, "High propene/propane selectivity in isostructural metal-organic frameworks with high densities of open metal sites," *Angewandte Chemie*, vol. 124, no. 8, pp. 1893–1896, 2012.

[73] H. Bux, C. Chmelik, R. Krishna, and J. Caro, "Ethene/ethane separation by the MOF membrane ZIF-8: Molecular correlation of permeation, adsorption, diffusion," *Journal of Membrane Science*, vol. 369, no. 1-2, pp. 284–289, 2011.

[74] A. Tarafder and M. Mazzotti, "A method for deriving explicit binary isotherms obeying the ideal adsorbed solution theory," *Chemical Engineering & Technology*, vol. 35, no. 1, pp. 102–108, 2012.

[75] J. A. Swisher, L.-C. Lin, J. Kim, and B. Smit, "Evaluating mixture adsorption models using molecular simulation," *AIChE Journal*, vol. 59, no. 8, pp. 3054–3064, 2013.

[76] J. Kärger and D. M. Ruthven, *Diffusion in Zeolites and Other Microporous Solids*. A Wiley Interscience publication, New York: Wiley, 1992.

[77] P. Krokidas, M. Castier, S. Moncho, E. Brothers, and I. G. Economou, "Molecular simulation studies of the diffusion of methane, ethane, propane, and propylene in ZIF-8," *The Journal of Physical Chemistry C*, vol. 119, no. 48, pp. 27028–27037, 2015.

[78] B. Smit and T. L. M. Maesen, "Molecular simulations of zeolites: Adsorption, diffusion, and shape selectivity," *Chemical Reviews*, vol. 108, no. 10, pp. 4125–4184, 2008.

[79] J. Kärger, *Diffusion in Nanoporous Materials*. Hoboken: John Wiley & Sons, 2012.

[80] D. Dubbeldam, E. Beerdsen, S. Calero, and B. Smit, "Dynamically corrected transition state theory calculations of self-diffusion in anisotropic nanoporous materials," *The Journal of Physical Chemistry B*, vol. 110, no. 7, pp. 3164–3172, 2006.

[81] C. Chmelik, D. Freude, H. Bux, and J. Haase, "Ethene/ethane mixture diffusion in the MOF sieve ZIF-8 studied by MAS PFG NMR diffusometry," *Microporous and Mesoporous Materials*, vol. 147, no. 1, pp. 135–141, 2012.

[82] A.-K. Pusch, T. Splith, L. Moschkowitz, S. Karmakar, R. Biniwale, M. Sant, G. B. Suffritti, P. Demontis, J. Cravillon, E. Pantatosaki, and F. Stallmach, "NMR studies of carbon dioxide and methane self-diffusion in ZIF-8 at elevated gas pressures," *Adsorption*, vol. 18, no. 5-6, pp. 359–366, 2012.

[83] F. J. Keil, *Chemische Reaktionstechnik: Teil II-B*. 2008.

[84] H. Bux, C. Chmelik, J. M. van Baten, R. Krishna, and J. Caro, "Novel MOF-membrane for molecular sieving predicted by IR-diffusion studies and molecular modeling," *Advanced Materials*, vol. 22, no. 42, pp. 4741–4743, 2010.

[85] C. Zhang, R. P. Lively, K. Zhang, J. R. Johnson, O. Karvan, and W. J. Koros, "Unexpected molecular sieving properties of zeolitic imidazolate framework-8," *The Journal of Physical Chemistry Letters*, vol. 3, no. 16, pp. 2130–2134, 2012.

[86] C. Chmelik and J. Kärger, "The predictive power of classical transition state theory revealed in diffusion studies with MOF ZIF-8," *Microporous and Mesoporous Materials*, vol. 225, pp. 128–132, 2016.

[87] N. E. R. Zimmermann, *Transport at Gas-Zeolite Interfaces Probed by Molecular Simulations*. Phd thesis, Hamburg University of Technology, Hamburg, 2013.

[88] R. J. Verploegh, S. Nair, and D. S. Sholl, "Temperature and loading-dependent diffusion of light hydrocarbons in ZIF-8 as predicted through fully flexible molecular simulations," *Journal of the American Chemical Society*, vol. 137, no. 50, pp. 15760–15771, 2015.

[89] D. Bathen and M. Breitbach, *Adsorptionstechnik*. VDI-Buch, Berlin: Springer, 2001.

[90] M. Baerns, *Technische Chemie*. Hoboken: Wiley, 2nd ed. ed., 2013.

[91] C. Y. Wen and L.-t. Fan, *Models for Flow Systems and Chemical Reactors*. New York: Dekker, 2. print ed., 1975.

[92] L. R. MacGillivray, ed., *Metal-Organic Frameworks: Design and Application*. Hoboken, N.J: Wiley, 2010.

[93] K. A. Hofmann and F. Küspert, "Verbindungen von Kohlenwasserstoffen mit Metallsalzen," *Z. Anorg. Chem.*, vol. 15, no. 1, pp. 204–207, 1897.

[94] J. H. Rayner and H. M. Powell, "Structure of molecular compounds. part x. crystal structure of the compound of benzene with an ammonia-nickel cyanide complex," *J. Chem. Soc.*, vol. 0, pp. 319–328, 1952.

[95] T. Iwamoto, T. Miyoshi, T. Miyamoto, Y. Sasaki, and S. Fujiwara, "The metal ammine cyanide aromatics clathrates. i. the preparation and stoichiometry of the diamminemetal(ii) tetracyano-niccolate(ii) dibenzene and dianiline," *Bulletin of the Chemical Society of Japan*, vol. 40, no. 5, pp. 1174–1178, 1967.

[96] T. Iwamoto, T. Nakano, M. Morita, T. Miyoshi, T. Miyamoto, and Y. Sasaki, "The hofman-type clathrate: $M(NH_3)_2M\prime(CN)_4$ 2G," *InOrganica Chimica Acta*, vol. 2, pp. 313–316, 1968.

[97] G. F. Walker and D. G. Hawthorne, "Complexes between n-alkylamines and nickel cyanide," *Trans. Faraday Soc.*, vol. 63, p. 166, 1967.

[98] B. F. Hoskins and R. Robson, "Infinite polymeric frameworks consisting of three dimensionally linked rod-like segments," *Journal of the American Chemical Society*, vol. 111, no. 15, pp. 5962–5964, 1989.

[99] M. Fujita, J. Yazaki, and K. Ogura, "Preparation of a macrocyclic polynuclear complex, $[(en)Pd(4,4'\text{-bpy})]_4(NO{-}3)_8$ (en = ethylenediamine, bpy = bipyridine), which recognizes an organic molecule in aqueous medium," *Journal of the American Chemical Society*, vol. 112, no. 14, pp. 5645–5647, 1990.

[100] M. Fujita, Y. J. Kwon, S. Washizu, and K. Ogura, "Preparation, clathration ability, and catalysis of a two-dimensional square network material composed of cadmium(ii) and 4,4'-bipyridine," *Journal of the American Chemical Society*, vol. 116, no. 3, pp. 1151–1152, 1994.

[101] S. Subramanian and M. J. Zaworotko, "Porous solids by design: $[Zn(4,4\prime\text{-bpy})_2(SiF_6)]_n\cdot$xDMF, a single framework octahedral coordination polymer with large square channels," *Angewandte Chemie International Edition in English*, vol. 34, no. 19, pp. 2127–2129, 1995.

[102] O. M. Yaghi and H. Li, "Hydrothermal synthesis of a metal-organic framework containing large rectangular channels," *Journal of the American Chemical Society*, vol. 117, no. 41, pp. 10401–10402, 1995.

[103] M. Kondo, T. Yoshitomi, H. Matsuzaka, S. Kitagawa, and K. Seki, "Three-dimensional framework with channeling cavities for small molecules:," *Angewandte Chemie International Edition in English*, vol. 36, no. 16, pp. 1725–1727, 1997.

[104] O. Ohmori, M. Kawano, and M. Fujita, "A two-in-one crystal: Uptake of two different guests into two distinct channels of a biporous coordination network," *Angewandte Chemie International Edition*, vol. 44, no. 13, pp. 1962–1964, 2005.

[105] H. Li, M. Eddaoudi, M. O'Keeffe, and O. M. Yaghi, "Design and synthesis of an exceptionally stable and highly porous metal-organic framework," *Nature*, vol. 402, no. 6759, pp. 276–279, 1999.

[106] E. L. First and C. A. Floudas, "MOFomics: Computational pore characterization of metal-organic frameworks," *Microporous and Mesoporous Materials*, vol. 165, pp. 32–39, 2013.

[107] S. S.-Y. Chui, S. M.-F. Lo, J. P. H. Charmant, A. G. Orpen, and I. D. Williams, "A chemically functionalizable nanoporous material $[Cu_3(TMA)_2(H_2O)_3]_n$," *Science*, vol. 283, no. 5405, pp. 1148–1150, 1999.

[108] J.-R. Li, J. Sculley, and H.-C. Zhou, "Metal-organic frameworks for separations," *Chemical Reviews*, vol. 112, no. 2, pp. 869–932, 2012.

[109] J. Klinowski, F. A. A. Paz, P. Silva, and J. Rocha, "Microwave-assisted synthesis of metal-organic frameworks," *Dalton transactions (Cambridge, England : 2003)*, vol. 40, no. 2, pp. 321–330, 2011.

[110] E. R. Parnham and R. E. Morris, "Ionothermal synthesis of zeolites, metal-organic frameworks, and inorganic-organic hybrids," *Accounts of Chemical Research*, vol. 40, no. 10, pp. 1005–1013, 2007.

[111] A. L. Garay, A. Pichon, and S. L. James, "Solvent-free synthesis of metal complexes," *Chemical Society Reviews*, vol. 36, no. 6, pp. 846–855, 2007.

[112] J. J. Perry, J. A. Perman, and M. J. Zaworotko, "Design and synthesis of metal-organic frameworks using metal-organic polyhedra as supermolecular building blocks," *Chemical Society Reviews*, vol. 38, no. 5, pp. 1400–1417, 2009.

[113] J.-R. Li, D. J. Timmons, and H.-C. Zhou, "Interconversion between molecular polyhedra and metal-organic frameworks," *Journal of the American Chemical Society*, vol. 131, no. 18, pp. 6368–6369, 2009.

[114] M. J. Zaworotko, "Metal-organic materials: A reversible step forward," *Nature Chemistry*, vol. 1, no. 4, pp. 267–268, 2009.

[115] L. Grajciar, O. Bludský, and P. Nachtigall, "Water adsorption on coordinatively unsaturated sites in CuBTC MOF," *The Journal of Physical Chemistry Letters*, vol. 1, no. 23, pp. 3354–3359, 2010.

[116] B. Liu and B. Smit, "Molecular simulation studies of separation of CO_2/N_2, CO_2/CH_4, and CH_4/N_2 by ZIFs," *Journal of Physical Chemistry C*, vol. 114, no. 18, pp. 8515–8522, 2010.

[117] S. Zuluaga, E. M. A. Fuentes-Fernandez, K. Tan, F. Xu, J. Li, Y. J. Chabal, and T. Thonhauser, "Understanding and controlling water stability of MOF-74," *Journal of Materials Chemistry A*, vol. 4, no. 14, pp. 5176–5183, 2016.

[118] P. D. C. Dietzel, Y. Morita, R. Blom, and H. Fjellvåg, "An in situ high-temperature single-crystal investigation of a dehydrated metal-organic framework compound and field-induced magnetization of one-dimensional metal-oxygen chains," *Angewandte Chemie International Edition*, vol. 44, no. 39, pp. 6354–6358, 2005.

[119] P. D. C. Dietzel, B. Panella, M. Hirscher, R. Blom, and H. Fjellvåg, "Hydrogen adsorption in a nickel based coordination polymer with open metal sites in the cylindrical cavities of the desolvated framework," *Chemical Communications*, no. 9, pp. 959–961, 2006.

[120] P. D. C. Dietzel, R. Blom, and H. Fjellvåg, "Base-induced formation of two magnesium metal-organic framework compounds with a bifunctional tetratopic ligand," *European Journal of InOrganic Chemistry*, vol. 2008, no. 23, pp. 3624–3632, 2008.

[121] P. D. C. Dietzel, V. Besikiotis, and R. Blom, "Application of metal-organic frameworks with coordinatively unsaturated metal sites in storage and separation of methane and carbon dioxide," *J. Mater. Chem.*, vol. 19, no. 39, pp. 7362–7370, 2009.

[122] L. Valenzano, B. Civalleri, K. Sillar, and J. Sauer, "Heats of adsorption of CO and CO_2 in metal–organic frameworks: Quantum mechanical study of CPO-27-M (M = Mg, Ni, Zn)," *Journal of Physical Chemistry C*, vol. 115, no. 44, pp. 21777–21784, 2011.

[123] N. Nijem, P. Canepa, L. Kong, H. Wu, J. Li, T. Thonhauser, and Y. J. Chabal, "Spectroscopic characterization of van der Waals interactions in a metal-organic framework with unsaturated metal centers: MOF-74-Mg," *Journal of Physics: Condensed Matter*, vol. 24, no. 42, p. 424203, 2012.

[124] Y. Yao, N. Nijem, J. Li, Y. J. Chabal, D. C. Langreth, and T. Thonhauser, "Analyzing the frequency shift of physiadsorbed CO_2 in metal-organic framework materials," *Physical Review B*, vol. 85, no. 6, 2012.

[125] L. Chen, C. A. Morrison, and T. Düren, "Improving predictions of gas adsorption in metal-organic frameworks with coordinatively unsaturated metal sites: Model potentials, ab initio parameterization, and GCMC simulations," *Journal of Physical Chemistry C*, vol. 116, no. 35, pp. 18899–18909, 2012.

[126] A. L. Dzubak, L.-C. Lin, J. Kim, J. A. Swisher, R. Poloni, S. N. Maximoff, B. Smit, and L. Gagliardi, "Ab initio carbon capture in open-site metal-organic frameworks," *Nature Chemistry*, vol. 4, no. 10, pp. 810–816, 2012.

[127] P. Canepa, N. Nijem, Y. J. Chabal, and T. Thonhauser, "Diffusion of small molecules in metal-organic framework materials," *Physical Review Letters*, vol. 110, no. 2, p. 026102, 2013.

[128] M. G. Lopez, P. Canepa, and T. Thonhauser, "NMR study of small molecule adsorption in MOF-74-Mg," *The Journal of Chemical Physics*, vol. 138, no. 15, p. 154704, 2013.

[129] L.-C. Lin, J. Kim, X. Kong, E. Scott, T. M. McDonald, J. R. Long, J. A. Reimer, and B. Smit, "Understanding CO_2 dynamics in metal-organic frameworks with open metal sites," *Angewandte Chemie International Edition*, vol. 52, no. 16, pp. 4410–4413, 2013.

[130] P. Canepa, C. A. Arter, E. M. Conwill, D. H. Johnson, B. A. Shoemaker, K. Z. Soliman, and T. Thonhauser, "High-throughput screening of small-molecule adsorption in MOF," *Journal of Materials Chemistry A*, vol. 1, no. 43, p. 13597, 2013.

[131] K. S. Park, Z. Ni, A. P. Cote, J. Y. Choi, R. Huang, F. J. Uribe-Romo, H. K. Chae, M. O'Keeffe, and O. M. Yaghi, "Exceptional chemical and thermal stability of zeolitic imidazolate frameworks," *Proceedings of the National Academy of Sciences*, vol. 103, no. 27, pp. 10186–10191, 2006.

[132] J. C. Tan, T. D. Bennett, and A. K. Cheetham, "Chemical structure, network topology, and porosity effects on the mechanical properties of zeolitic imidazolate frameworks," *Proceedings of the National Academy of Sciences*, vol. 107, no. 22, pp. 9938–9943, 2010.

[133] A. Phan, C. J. Doonan, F. J. Uribe-Romo, C. B. Knobler, M. O'Keeffe, and O. M. Yaghi, "Synthesis, structure, and carbon dioxide capture properties of zeolitic imidazolate frameworks," *Accounts of Chemical Research*, vol. 43, no. 1, pp. 58–67, 2010.

[134] M. O'Keeffe, M. A. Peskov, S. J. Ramsden, and O. M. Yaghi, "The Reticular Chemistry Structure Resource (RCSR) database of, and symbols for crystal nets," *Accounts of Chemical Research*, vol. 41, no. 12, pp. 1782–1789, 2008.

[135] K. Zhang, R. P. Lively, C. Zhang, R. R. Chance, W. J. Koros, D. S. Sholl, and S. Nair, "Exploring the framework hydrophobicity and flexibility of ZIF-8: From biofuel recovery to hydrocarbon separations," *The Journal of Physical Chemistry Letters*, vol. 4, no. 21, pp. 3618–3622, 2013.

[136] D. Peralta, G. Chaplais, J.-L. Paillaud, A. Simon-Masseron, K. Barthelet, and G. D. Pirngruber, "The separation of xylene isomers by ZIF-8: A demonstration of the extraordinary flexibility of the ZIF-8 framework," *Microporous and Mesoporous Materials*, vol. 173, pp. 1–5, 2013.

[137] A. Schneemann, V. Bon, I. Schwedler, I. Senkovska, S. Kaskel, and R. A. Fischer, "Flexible metal-organic frameworks," *Chem. Soc. Rev.*, vol. 43, no. 16, pp. 6062–6096, 2014.

[138] L. Sarkisov, R. L. Martin, M. Haranczyk, and B. Smit, "On the flexibility of metal-organic frameworks," *Journal of the American Chemical Society*, vol. 136, no. 6, pp. 2228–2231, 2014.

[139] F. Debatin, A. Thomas, A. Kelling, N. Hedin, Z. Bacsik, I. Senkovska, S. Kaskel, M. Junginger, H. Müller, U. Schilde, C. Jäger, A. Friedrich, and H.-J. Holdt, "In situ synthesis of an imidazolate-4-amide-5-imidate ligand and formation of a microporous zinc-organic framework with H_2-and CO_2-storage ability," *Angewandte Chemie*, vol. 122, no. 7, pp. 1280–1284, 2010.

[140] F. Debatin, K. Behrens, J. Weber, I. A. Baburin, A. Thomas, J. Schmidt, I. Senkovska, S. Kaskel, A. Kelling, N. Hedin, Z. Bacsik, S. Leoni, G. Seifert, C. Jäger, C. Günter, U. Schilde, A. Friedrich, and H.-J. Holdt, "An isoreticular family of microporous metal-organic frameworks based on zinc and 2-substituted imidazolate-4-amide-5-imidate: Syntheses, structures and properties," *Chemistry (Weinheim an der Bergstrasse, Germany)*, vol. 18, no. 37, pp. 11630–11640, 2012.

[141] S. S. Mondal, S. Dey, I. A. Baburin, A. Kelling, U. Schilde, G. Seifert, C. Janiak, and H.-J. Holdt, "Syntheses of two imidazolate-4-amide-5-imidate linker-based hexagonal metal-organic frameworks with flexible ethoxy substituent," *CrystEngComm*, vol. 15, no. 45, p. 9394, 2013.

[142] S. S. Mondal, A. Bhunia, I. A. Baburin, C. Jäger, A. Kelling, U. Schilde, G. Seifert, C. Janiak, and H.-J. Holdt, "Gate effects in a hexagonal zinc-imidazolate-4-amide-5-imidate framework with flexible methoxy substituents and CO_2 selectivity," *Chemical communications (Cambridge, England)*, vol. 49, no. 69, pp. 7599–7601, 2013.

[143] S. S. Mondal, A. Bhunia, S. Demeshko, A. Kelling, U. Schilde, C. Janiak, and H.-J. Holdt, "Synthesis of a Co(ii) imidazolate framework from an anionic linker precursor: Gas-sorption and magnetic properties," *CrystEngComm*, vol. 16, no. 1, pp. 39–42, 2014.

[144] M. Born and R. Oppenheimer, "Zur Quantentheorie der Molekeln," *Annalen der Physik*, vol. 389, no. 20, pp. 457–484, 1927.

[145] L. H. Thomas, "The calculation of atomic fields," *Mathematical Proceedings of the Cambridge Philosophical Society*, vol. 23, no. 05, p. 542, 1927.

[146] E. Fermi, "Un metodo statistico per la determinazione di alcune priorieta dell' atome," *Rend. Accad. Naz. Lincei*, vol. 6, p. 602, 1927.

[147] P. Hohenberg and W. Kohn, "Inhomogeneous electron gas," *Physical Review*, vol. 136, no. 3B, pp. B864–B871, 1964.

[148] A. R. Leach, *Molecular Modelling: Principles and Applications*. Harlow: Pearson/Prentice Hall, 2. ed., 12. [dr.] ed., 2009.

[149] W. Kohn and L. J. Sham, "Self-consistent equations including exchange and correlation effects," *Physical Review*, vol. 140, no. 4A, pp. A1133–A1138, 1965.

[150] D. M. Ceperley and B. J. Alder, "Ground state of the electron gas by a stochastic method," *Physical Review Letters*, vol. 45, no. 7, pp. 566–569, 1980.

[151] J. P. Perdew, K. Burke, and M. Ernzerhof, "Generalized gradient approximation made simple," *Physical Review Letters*, vol. 77, no. 18, pp. 3865–3868, 1996.

[152] J. P. Perdew, K. Burke, and M. Ernzerhof, "Generalized gradient approximation made simple," *Physical Review Letters*, vol. 78, no. 7, p. 1396, 1997.

[153] A. D. Becke, "Density-functional exchange-energy approximation with correct asymptotic behavior," *Phys. Rev. A*, vol. 38, no. 6, pp. 3098–3100, 1988.

[154] A. D. Becke, "Density–functional thermochemistry. i. the effect of the exchange-only gradient correction," *The Journal of Chemical Physics*, vol. 96, no. 3, pp. 2155–2160, 1992.

[155] P. J. Stephens, F. J. Devlin, C. F. Chabalowski, and M. J. Frisch, "Ab initio calculation of vibrational absorption and circular dichroism spectra using density functional force fields," *The Journal of Physical Chemistry*, vol. 98, no. 45, pp. 11623–11627, 1994.

[156] A. D. Becke, "A new mixing of hartree–fock and local density–functional theories," *The Journal of Chemical Physics*, vol. 98, no. 2, pp. 1372–1377, 1993.

[157] A. D. Becke, "Density–functional thermochemistry. iii. the role of exact exchange," *The Journal of Chemical Physics*, vol. 98, no. 7, pp. 5648–5652, 1993.

[158] C. Lee, W. Yang, and R. G. Parr, "Development of the colle-salvetti correlation-energy formula into a functional of the electron density," *Physical Review B*, vol. 37, no. 2, pp. 785–789, 1988.

[159] D. Frenkel and B. Smit, *Understanding Molecular Simulation: From Algorithms to Applications*, vol. 1 of *Computational science series*. San Diego, Calif.: Acad. Press, 2. ed. ed., 2009.

[160] N. Metropolis, A. W. Rosenbluth, M. N. Rosenbluth, A. H. Teller, and E. Teller, "Equation of state calculations by fast computing machines," *The Journal of Chemical Physics*, vol. 21, no. 6, pp. 1087–1092, 1953.

[161] N. G. van Kampen, *Stochastic Processes in Physics and Chemistry*. Amsterdam: North-Holland, 6. print ed., 1990.

[162] H. Meirovitch, "Statistical properties of the scanning simulation method for polymer chains," *The Journal of Chemical Physics*, vol. 89, no. 4, pp. 2514–2522, 1988.

[163] Z. Alexandrowicz, "Simulation of polymers with rebound selection," *The Journal of Chemical Physics*, vol. 109, no. 13, pp. 5622–5626, 1998.

[164] S. Consta, N. B. Wilding, D. Frenkel, and Z. Alexandrowicz, "Recoil growth: An efficient simulation method for multi-polymer systems," *The Journal of Chemical Physics*, vol. 110, no. 6, pp. 3220–3228, 1999.

[165] S. Consta, T. J. H. Vlugt, J. W. Hoeth, B. Smit, and D. Frenkel, "Recoil growth algorithm for chain molecules with continuous interactions," *Molecular Physics*, vol. 97, no. 12, pp. 1243–1254, 1999.

[166] B. Widom, "Some topics in the theory of fluids," *The Journal of Chemical Physics*, vol. 39, no. 11, pp. 2808–2812, 1963.

[167] H. C. Andersen, "Molecular dynamics simulations at constant pressure and/or temperature," *The Journal of Chemical Physics*, vol. 72, no. 4, pp. 2384–2393, 1980.

[168] W. Feller, *An Introduction to Probability Theory and Its Applications*. Wiley series in probability and mathematical statistics Probability and mathematical statistics, New York, NY: Wiley, 3. ed., rev. printing ed., 1968.

[169] E. A. Koopman and C. P. Lowe, "Advantages of a Lowe-Andersen thermostat in molecular dynamics simulations," *The Journal of Chemical Physics*, vol. 124, no. 20, p. 204103, 2006.

[170] S. Nosé, "A molecular dynamics method for simulations in the canonical ensemble," *Molecular Physics*, vol. 52, no. 2, pp. 255–268, 1984.

[171] S. Nosé, "A unified formulation of the constant temperature molecular dynamics methods," *The Journal of Chemical Physics*, vol. 81, no. 1, pp. 511–519, 1984.

[172] W. G. Hoover, "Canonical dynamics: Equilibrium phase-space distributions," *Phys. Rev. A*, vol. 31, no. 3, pp. 1695–1697, 1985.

[173] W. G. Hoover, "Constant-pressure equations of motion," *Phys. Rev. A*, vol. 34, no. 3, pp. 2499–2500, 1986.

[174] M. J. Abraham, T. Murtola, R. Schulz, S. Páll, J. C. Smith, B. Hess, and E. Lindahl, "GROMACS: High performance molecular simulations through multi-level parallelism from laptops to supercomputers," *SoftwareX*, vol. 1-2, pp. 19–25, 2015.

[175] M. G. Martin and J. I. Siepmann, "Transferable potentials for phase equilibria. 1. united-atom description of n-alkanes," *The Journal of Physical Chemistry B*, vol. 102, no. 14, pp. 2569–2577, 1998.

[176] R. A. Buckingham, "The classical equation of state of gaseous helium, neon and argon," *Proceedings of the Royal Society A: Mathematical, Physical and Engineering Sciences*, vol. 168, no. 933, pp. 264–283, 1938.

[177] H. Sun, "Compass: An ab initio force-field optimized for condensed-phase applications - overview with details on alkane and benzene compounds," *The Journal of Physical Chemistry B*, vol. 102, no. 38, pp. 7338–7364, 1998.

[178] T. A. Halgren, "Merck molecular force field. i. basis, form, scope, parameterization, and performance of MMFF94," *Journal of Computational Chemistry*, vol. 17, no. 5-6, pp. 490–519, 1996.

[179] W. L. Jorgensen, D. S. Maxwell, and J. Tirado-Rives, "Development and testing of the OPLS all-atom force field on conformational energetics and properties of organic liquids," *Journal of the American Chemical Society*, vol. 118, no. 45, pp. 11225–11236, 1996.

[180] P. P. Ewald, "Die Berechnung optischer und elektrostatischer Gitterpotentiale," *Annalen der Physik*, vol. 369, no. 3, pp. 253–287, 1921.

[181] C. Campañá, B. Mussard, and T. K. Woo, "Electrostatic potential derived atomic charges for periodic systems using a modified error functional," *Journal of Chemical Theory and Computation*, vol. 5, no. 10, pp. 2866–2878, 2009.

[182] E. Glueckauf, "Theory of chromatography. part 10.—formulae for diffusion into spheres and their application to chromatography," *Trans. Faraday Soc.*, vol. 51, no. 0, pp. 1540–1551, 1955.

[183] R. T. Yang, *Gas Separation by Adsorption Processes*. Burlington: Elsevier Science, 1987.

[184] D. M. Ruthven, S. Farooq, and K. S. Knaebel, *Pressure Swing Adsorption*. New York, N.Y: VCH Publishers, 1994.

[185] H. Brenner, *Adsorption Calculations and Modelling*. Burlington: Elsevier Science, 1994.

[186] A. I. Papadopoulos and P. Seferlis, *Process Systems and Materials for CO_2 Capture*. Chichester, UK: John Wiley & Sons, Ltd, 2017.

[187] S. Jakobtorweihen, N. Hansen, and F. J. Keil, "Molecular simulation of alkene adsorption in zeolites," *Molecular Physics*, vol. 103, no. 4, pp. 471–489, 2005.

[188] A. L. Myers and P. A. Monson, "Adsorption in porous materials at high pressure: Theory and experiment," *Langmuir*, vol. 18, no. 26, pp. 10261–10273, 2002.

[189] T. Darden, D. York, and L. Pedersen, "Particle mesh Ewald: A N·log(N) method for Ewald sums in large systems," *The Journal of Chemical Physics*, vol. 98, no. 12, pp. 10089–10092, 1993.

[190] U. Essmann, L. Perera, M. L. Berkowitz, T. Darden, H. Lee, and L. G. Pedersen, "A smooth particle mesh Ewald method," *The Journal of Chemical Physics*, vol. 103, no. 19, pp. 8577–8593, 1995.

[191] S. Jakobtorweihen, *Molcecular Simulation of Technically Relevant Molecules in Nanoporous Materials - Carbon Nanotubes and Zeolites*. PhD thesis, Hamburg University of Technology, Hamburg, 2007.

[192] S. Keskin, J. Liu, R. B. Rankin, J. K. Johnson, and D. S. Sholl, "Progress, opportunities, and challenges for applying atomically detailed modeling to molecular adsorption and transport in metal-organic framework materials," *Industrial & Engineering Chemistry Research*, vol. 48, no. 5, pp. 2355–2371, 2009.

[193] A. Heyden, T. Düren, M. Kolkowski, and F. J. Keil, "Design of a pressure swing adsorption module based on carbon nanotubes as adsorbent - a molecular modeling approach," *Hungarian Journal of Industrial Chemistry*, vol. 29, no. 2, pp. 95–104, 2001.

[194] *VDI-Wärmeatlas*. Berlin, Heidelberg: Springer Berlin Heidelberg, 2002.

[195] E. N. Fuller, P. D. Schettler, and J. C. Giddings, "New method for prediction of binary gas phase diffusion coefficients," *Industrial & Engineering Chemistry*, vol. 58, no. 5, pp. 18–27, 1966.

[196] R. Dawson, F. Khoury, and R. Kobayashi, "Self-diffusion measurements in methane by pulsed nuclear magnetic resonance," *AIChE Journal*, vol. 16, no. 5, pp. 725–729, 1970.

[197] P. Deuflhard and F. Bornemann, *Scientific Computing with Ordinary Differential Equations*, vol. 42 of *Texts in Applied Mathematics*. New York, NY: Springer, 2002.

[198] C. E. Wilmer, M. Leaf, C. Y. Lee, O. K. Farha, B. G. Hauser, J. T. Hupp, and R. Q. Snurr, "Large-scale screening of hypothetical metal-organic frameworks," *Nature Chemistry*, vol. 4, pp. 83–89, 2012.

[199] K. Sumida, D. L. Rogow, J. A. Mason, T. M. McDonald, E. D. Bloch, Z. R. Herm, T.-H. Bae, and J. R. Long, "Carbon dioxide capture in metal-organic frameworks," *Chemical Reviews*, vol. 112, no. 2, pp. 724–781, 2012.

[200] M. P. Suh, H. J. Park, T. K. Prasad, and D.-W. Lim, "Hydrogen storage in metal-organic frameworks," *Chemical Reviews*, vol. 112, no. 2, pp. 782–835, 2012.

[201] J. Liu, P. K. Thallapally, B. P. McGrail, D. R. Brown, and J. Liu, "Progress in adsorption-based CO_2 capture by metal-organic frameworks," *Chemical Society Reviews*, vol. 41, no. 6, pp. 2308–2322, 2012.

[202] R. Babarao and J. Jiang, "Diffusion and separation of CO_2 and CH_4 in silicalite, C168 schwarzite, and IRMOF-1: A comparative study from molecular dynamics simulation," *Langmuir*, vol. 24, no. 10, pp. 5474–5484, 2008.

[203] A. Ö. Yazaydın, R. Q. Snurr, T.-H. Park, K. Koh, J. Liu, M. D. LeVan, A. I. Benin, P. Jakubczak, M. Lanuza, D. B. Galloway, J. J. Low, and R. R. Willis, "Screening of metal−organic frameworks for carbon dioxide capture from flue gas using a combined experimental and modeling approach," *Journal of the American Chemical Society*, vol. 131, no. 51, pp. 18198–18199, 2009.

[204] L.-C. Lin, A. H. Berger, R. L. Martin, J. Kim, J. A. Swisher, K. Jariwala, C. H. Rycroft, A. S. Bhown, M. W. Deem, M. Haranczyk, and B. Smit, "In silico screening of carbon-capture materials," *Nature Materials*, vol. 11, no. 7, pp. 633–641, 2012.

[205] S. Han, Y. Huang, T. Watanabe, Y. Dai, K. S. Walton, S. Nair, D. S. Sholl, and J. C. Meredith, "High-throughput screening of metal-organic frameworks for CO_2 separation," *ACS combinatorial science*, vol. 14, no. 4, pp. 263–267, 2012.

[206] J. M. Huck, L.-C. Lin, A. H. Berger, M. N. Shahrak, R. L. Martin, A. S. Bhown, M. Haranczyk, K. Reuter, and B. Smit, "Evaluating different classes of porous materials for carbon capture," *Energy & Environmental Science*, vol. 7, no. 12, pp. 4132–4146, 2014.

[207] Z. Bao, L. Yu, Q. Ren, X. Lu, and S. Deng, "Adsorption of CO_2 and CH_4 on a magnesium-based metal-organic framework," *Journal of Colloid and Interface Science*, vol. 353, no. 2, pp. 549–556, 2011.

[208] Z. R. Herm, J. A. Swisher, B. Smit, R. Krishna, and J. R. Long, "Metal-organic frameworks as adsorbents for hydrogen purification and precombustion carbon dioxide capture," *Journal of the American Chemical Society*, vol. 133, no. 15, pp. 5664–5667, 2011.

[209] J. A. Mason, K. Sumida, Z. R. Herm, R. Krishna, and J. R. Long, "Evaluating metal-organic frameworks for post-combustion carbon dioxide capture via temperature swing adsorption," *Energy & Environmental Science*, vol. 4, no. 8, p. 3030, 2011.

[210] D.-A. Yang, H.-Y. Cho, J. Kim, S.-T. Yang, and W.-S. Ahn, "CO_2 capture and conversion using Mg-MOF-74 prepared by a sonochemical method," *Energy & Environmental Science*, vol. 5, no. 4, pp. 6465–6473, 2012.

[211] A. Ö. Yazaydın, A. I. Benin, S. A. Faheem, P. Jakubczak, J. J. Low, R. R. Willis, and R. Q. Snurr, "Enhanced CO_2-adsorption in metal-organic frameworks via occupation of open-metal sites by coordinated water molecules," *Chemistry of Materials*, vol. 21, no. 8, pp. 1425–1430, 2009.

[212] A. M. Wolsky, E. J. Daniels, and B. J. Jody, "CO_2 capture from the flue gas of conventional fossil-fuel-fired power plants," *Environmental Progress*, vol. 13, no. 3, pp. 214–219, 1994.

[213] E. J. Granite and H. W. Pennline, "Photochemical removal of mercury from flue gas," *Industrial & Engineering Chemistry Research*, vol. 41, no. 22, pp. 5470–5476, 2002.

[214] X. Xu, C. Song, R. Wincek, J. M. Andresen, B. G. Miller, and A. W. Scaroni, "Separation of CO_2 from power plant fule gas using a novel CO_2 molecular-basket adsorbent," *Fuel Chemistry Division*, vol. 48, no. 1, pp. 162–163, 2003.

[215] W. Sun, L.-C. Lin, X. Peng, and B. Smit, "Computational screening of porous metal-organic frameworks and zeolites for the removal of SO_2 and NO_x from flue gases," *AIChE Journal*, vol. 60, no. 6, pp. 2314–2323, 2014.

[216] K. Tan, S. Zuluaga, Q. Gong, Y. Gao, N. Nijem, J. Li, T. Thonhauser, and Y. J. Chabal, "Competitive coadsorption of CO_2 with H_2O, NH_3, SO_2, no, NO_2, N_2, O_2, and CH_4 in m-mof-74 (m = mg, co, ni): The role of hydrogen bonding," *Chemistry of Materials*, vol. 27, no. 6, pp. 2203–2217, 2015.

[217] K. Tan, S. Zuluaga, H. Wang, P. Canepa, K. Soliman, J. Cure, J. Li, T. Thonhauser, and Y. J. Chabal, "Interaction of acid gases SO_2 and NO_2 with coordinatively unsaturated metal organic frameworks: M-MOF-74 (M = Zn, Mg, Ni, Co)," *Chemistry of Materials*, vol. 29, no. 10, pp. 4227–4235, 2017.

[218] A. Kundu, G. Piccini, K. Sillar, and J. Sauer, "Ab initio prediction of adsorption isotherms for small molecules in metal-organic frameworks," *Journal of the American Chemical Society*, vol. 138, no. 42, pp. 14047–14056, 2016.

[219] J. Park, D. Yuan, K. T. Pham, J.-R. Li, A. Yakovenko, and H.-C. Zhou, "Reversible alteration of CO_2 adsorption upon photochemical or thermal treatment in a metal-organic framework," *Journal of the American Chemical Society*, vol. 134, no. 1, pp. 99–102, 2012.

[220] J. Yu and P. B. Balbuena, "Water effects on postcombustion CO_2 capture in Mg-MOF-74," *Journal of Physical Chemistry C*, vol. 117, no. 7, pp. 3383–3388, 2013.

[221] K. Sillar and J. Sauer, "Ab initio prediction of adsorption isotherms for small molecules in metal-organic frameworks: The effect of lateral interactions for methane/CPO-27-Mg," *Journal of the American Chemical Society*, vol. 134, no. 44, pp. 18354–18365, 2012.

[222] R. Krishna and J. M. van Baten, "In silico screening of metal–organic frameworks in separation applications," *Physical Chemistry Chemical Physics*, vol. 13, no. 22, pp. 10593–10616, 2011.

[223] A. Kundu, K. Sillar, and J. Sauer, "Ab initio prediction of adsorption isotherms for gas mixtures by Grand Canonical Monte Carlo simulations on a lattice of sites," *The Journal of Physical Chemistry Letters*, vol. 8, no. 12, pp. 2713–2718, 2017.

[224] M. Tafipolsky, S. Amirjalayer, and R. Schmid, "Atomistic theoretical models for nanoporous hybrid materials," *Microporous and Mesoporous Materials*, vol. 129, no. 3, pp. 304–318, 2010.

[225] M. Fischer and R. G. Bell, "Influence of zeolite topology on CO_2/CO_2 separation behavior: Force-field simulations using a DFT-derived charge model," *Journal of Physical Chemistry C*, vol. 116, no. 50, pp. 26449–26463, 2012.

[226] L.-C. Lin, K. Lee, L. Gagliardi, J. B. Neaton, and B. Smit, "Force-field development from electronic structure calculations with periodic boundary conditions: Applications to gaseous adsorption and transport in metal-organic frameworks," *Journal of Chemical Theory and Computation*, vol. 10, no. 4, pp. 1477–1488, 2014.

[227] A. N. Rudenko, S. Bendt, and F. J. Keil, "Multiscale modeling of water in Mg-MOF-74: From electronic structure calculations to adsorption isotherms," *Journal of Physical Chemistry C*, vol. 118, no. 29, pp. 16218–16227, 2014.

[228] C. Campbell, C. A. Ferreiro-Rangel, M. Fischer, J. R. B. Gomes, and M. Jorge, "A transferable model for adsorption in MOFs with unsaturated metal sites," *Journal of Physical Chemistry C*, vol. 121, no. 1, pp. 441–458, 2016.

[229] J. Kim, L.-C. Lin, K. Lee, J. B. Neaton, and B. Smit, "Efficient determination of accurate force fields for porous materials using ab initio total energy calculations," *Journal of Physical Chemistry C*, vol. 118, no. 5, pp. 2693–2701, 2014.

[230] X. Peng, L.-C. Lin, W. Sun, and B. Smit, "Water adsorption in metal-organic frameworks with open metal sites," *AIChE Journal*, vol. 61, no. 2, pp. 677–687, 2015.

[231] T. M. Becker, J. Heinen, D. Dubbeldam, L.-C. Lin, and T. J. H. Vlugt, "Polarizable force fields for CO_2 and CH_4 adsorption in M-MOF-74," *Journal of Physical Chemistry C*, vol. 121, no. 8, pp. 4659–4673, 2017.

[232] T. Grant Glover, G. W. Peterson, B. J. Schindler, D. Britt, and O. Yaghi, "MOF-74 building unit has a direct impact on toxic gas adsorption," *Chemical Engineering Science*, vol. 66, no. 2, pp. 163–170, 2011.

[233] P. M. Schoenecker, C. G. Carson, H. Jasuja, C. J. J. Flemming, and K. S. Walton, "Effect of water adsorption on retention of structure and surface area of metal-organic frameworks," *Industrial & Engineering Chemistry Research*, vol. 51, no. 18, pp. 6513–6519, 2012.

[234] J. B. DeCoste, G. W. Peterson, B. J. Schindler, K. L. Killops, M. A. Browe, and J. J. Mahle, "The effect of water adsorption on the structure of the carboxylate containing metal-organic frameworks Cu-BTC, Mg-MOF-74, and UiO-66," *Journal of Materials Chemistry A*, vol. 1, no. 38, pp. 11922–11932, 2013.

[235] H. Daglar and S. Keskin, "Computational screening of metal-organic frameworks for membrane-based $CO_2/N_2/H_2O$ separations: Best materials for flue gas separation," *The Journal of Physical Chemistry C*, vol. 122, no. 30, pp. 17347–17357, 2018.

[236] W. L. Jorgensen, J. Chandrasekhar, J. D. Madura, R. W. Impey, and M. L. Klein, "Comparison of simple potential functions for simulating liquid water," *The Journal of Chemical Physics*, vol. 79, no. 2, pp. 926–935, 1983.

[237] M. W. Mahoney and W. L. Jorgensen, "A five-site model for liquid water and the reproduction of the density anomaly by rigid, nonpolarizable potential functions," *The Journal of Chemical Physics*, vol. 112, no. 20, p. 8910, 2000.

[238] J. J. Potoff and J. I. Siepmann, "Vapor-liquid equilibria of mixtures containing alkanes, carbon dioxide, and nitrogen," *AIChE Journal*, vol. 47, no. 7, pp. 1676–1682, 2001.

[239] A. K. Rappe, C. J. Casewit, K. S. Colwell, W. A. Goddard, and W. M. Skiff, "UFF, a full periodic table force field for molecular mechanics and molecular dynamics simulations," *Journal of the American Chemical Society*, vol. 114, no. 25, pp. 10024–10035, 1992.

[240] S. L. Mayo, B. D. Olafson, and W. A. Goddard, "Dreiding: A generic force field for molecular simulations," *The Journal of Physical Chemistry*, vol. 94, no. 26, pp. 8897–8909, 1990.

[241] P. E. Blöchl, "Projector augmented-wave method," *Physical Review B*, vol. 50, no. 24, pp. 17953–17979, 1994.

[242] G. Kresse and D. Joubert, "From ultrasoft pseudopotentials to the projector augmented-wave method," *Physical Review B*, vol. 59, no. 3, pp. 1758–1775, 1999.

[243] J. Hafner, "Ab-initio simulations of materials using VASP: Density-functional theory and beyond," *Journal of Computational Chemistry*, vol. 29, no. 13, pp. 2044–2078, 2008.

[244] Y. Zhang and W. Yang, "Comment on "generalized gradient approximation made simple"," *Physical Review Letters*, vol. 80, no. 4, p. 890, 1998.

[245] M. Dion, H. Rydberg, E. Schröder, D. C. Langreth, and B. I. Lundqvist, "Van der Waals density functional for general geometries," *Physical Review Letters*, vol. 92, no. 24, p. 246401, 2004.

[246] D. C. Langreth, B. I. Lundqvist, S. D. Chakarova-Käck, V. R. Cooper, M. Dion, P. Hyldgaard, A. Kelkkanen, J. Kleis, L. Kong, S. Li, P. G. Moses, E. Murray, A. Puzder, H. Rydberg, E. Schröder, and T. Thonhauser, "A density functional for sparse matter," *Journal of Physics: Condensed Matter*, vol. 21, no. 8, p. 084203, 2009.

[247] J. Klimeš, D. R. Bowler, and A. Michaelides, "Van der Waals density functionals applied to solids," *Physical Review B*, vol. 83, no. 19, 2011.

[248] G. Kresse and J. Hafner, "Ab initio molecular dynamics for liquid metals," *Physical Review B*, vol. 47, no. 1, pp. 558–561, 1993.

[249] G. Kresse and J. Hafner, "Ab initio molecular dynamics simulation of the liquid-metal-amorphous-semiconductor transition in Germanium," *Physical Review B*, vol. 49, no. 20, pp. 14251–14269, 1994.

[250] S. Plimpton, "Fast parallel algorithms for short-range molecular dynamics," *Journal of Computational Physics*, vol. 117, no. 1, pp. 1–19, 1995.

[251] T. J. H. Vlugt and M. Schenk, "Influence of framework flexibility on the adsorption properties of hydrocarbons in the zeolite silicalite," *The Journal of Physical Chemistry B*, vol. 106, no. 49, pp. 12757–12763, 2002.

[252] D. J. Price and C. L. Brooks, "A modified TIP3P water potential for simulation with ewald summation," *The Journal of Chemical Physics*, vol. 121, no. 20, pp. 10096–10103, 2004.

[253] H. W. Horn, W. C. Swope, J. W. Pitera, J. D. Madura, T. J. Dick, G. L. Hura, and T. Head-Gordon, "Development of an improved four-site water model for biomolecular simulations: TIP4P-Ew," *The Journal of Chemical Physics*, vol. 120, no. 20, p. 9665, 2004.

[254] S. W. Rick, "A reoptimization of the five-site water potential (TIP5P) for use with ewald sums," *The Journal of Chemical Physics*, vol. 120, no. 13, p. 6085, 2004.

[255] B. Smit and J. I. Siepmann, "Computer simulations of the energetics and siting of n-alkanes in zeolites," *The Journal of Physical Chemistry*, vol. 98, no. 34, pp. 8442–8452, 1994.

[256] S. Grimme, S. Ehrlich, and L. Goerigk, "Effect of the damping function in dispersion corrected density functional theory," *Journal of Computational Chemistry*, vol. 32, no. 7, pp. 1456–1465, 2011.

[257] A. N. Rudenko, F. J. Keil, M. I. Katsnelson, and A. I. Lichtenstein, "Adsorption of diatomic halogen molecules on graphene: A van der Waals density functional study," *Physical Review B*, vol. 82, no. 3, p. 4, 2010.

[258] C. Vega, J. L. F. Abascal, M. M. Conde, and J. L. Aragones, "What ice can teach us about water interactions: A critical comparison of the performance of different water models," *Faraday Discuss*, vol. 141, pp. 251–276, 2009.

[259] Q. Yang, C. Zhong, and J.-F. Chen, "Computational study of CO_2 storage in metal-organic frameworks," *Journal of Physical Chemistry C*, vol. 112, no. 5, pp. 1562–1569, 2008.

[260] K. S. W. Sing, "Reporting physisorption data for gas/solid systems with special reference to the determination of surface area and porosity," *Pure and Applied Chemistry*, vol. 57, no. 4, pp. 603–619, 1985.

[261] R. M. Marti, J. D. Howe, C. R. Morelock, M. S. Conradi, K. S. Walton, D. S. Sholl, and S. E. Hayes, "CO_2 dynamics in pure and mixed-metal MOFs with open metal sites," *Journal of Physical Chemistry C*, vol. 121, no. 46, pp. 25778–25787, 2017.

[262] J. Xu, R. Sinelnikov, and Y. Huang, "Capturing guest dynamics in metal-organic framework CPO-27-M (M = Mg, Zn) by ^{2}H solid-state NMR spectroscopy," *Langmuir*, vol. 32, no. 22, pp. 5468–5479, 2016.

[263] R. Krishna and J. R. Long, "Screening metal-organic frameworks by analysis of transient breakthrough of gas mixtures in a fixed bed adsorber," *Journal of Physical Chemistry C*, vol. 115, no. 26, pp. 12941–12950, 2011.

[264] T. Chokbunpiam, R. Chanajaree, T. Remsungnen, O. Saengsawang, S. Fritzsche, C. Chmelik, J. Caro, W. Janke, and S. Hannongbua, "N_2 in ZIF-8: Sorbate induced structural changes and self-diffusion," *Microporous and Mesoporous Materials*, vol. 187, pp. 1–6, 2014.

[265] T. Chokbunpiam, S. Fritzsche, C. Chmelik, J. Caro, W. Janke, and S. Hannongbua, "Gate opening effect for carbon dioxide in ZIF-8 by molecular dynamics - confirmed, but at high CO_2 pressure," *Chemical Physics Letters*, vol. 648, pp. 178–181, 2016.

[266] B. Zheng, Y. Pan, Z. Lai, and K.-W. Huang, "Molecular dynamics simulations on gate opening in ZIF-8: Identification of factors for ethane and propane separation," *Langmuir*, vol. 29, no. 28, pp. 8865–8872, 2013.

[267] S. Amirjalayer, M. Tafipolsky, and R. Schmid, "Molecular dynamics simulation of benzene diffusion in MOF-5: Importance of lattice dynamics," *Angewandte Chemie International Edition*, vol. 46, no. 3, pp. 463–466, 2007.

[268] E. Braun, S. M. Moosavi, and B. Smit, "Anomalous effects of velocity rescaling algorithms: The flying ice cube effect revisited," *Journal of Chemical Theory and Computation*, vol. 14, no. 10, pp. 5262–5272, 2018.

[269] N. E. R. Zimmermann, S. Jakobtorweihen, E. Beerdsen, B. Smit, and F. J. Keil, "In-depth study of the influence of host-framework flexibility on the diffusion of small gas molecules in one-dimensional zeolitic pore systems," *Journal of Physical Chemistry C*, vol. 111, no. 46, pp. 17370–17381, 2007.

[270] A. García-Sánchez, D. Dubbeldam, and S. Calero, "Modeling adsorption and self-diffusion of methane in LTA zeolites: The influence of framework flexibility," *Journal of Physical Chemistry C*, vol. 114, no. 35, pp. 15068–15074, 2010.

[271] J. Heinen and D. Dubbeldam, "On flexible force fields for metal-organic frameworks: Recent developments and future prospects," *WIREs: Computational Molecular Science*, vol. 8, no. 4, p. e1363, 2017.

[272] J. Kärger and H. Pfeifer, "N.m.r. self-diffusion studies in zeolite science and technology," *Zeolites*, vol. 7, no. 2, pp. 90–107, 1987.

[273] R. Babarao and J. Jiang, "Molecular screening of metal-organic frameworks for CO_2 storage," *Langmuir*, vol. 24, no. 12, pp. 6270–6278, 2008.

[274] R. Krishna and J. M. van Baten, "Highlighting pitfalls in the Maxwell-Stefan modeling of water-alcohol mixture permeation across pervaporation membranes," *Journal of Membrane Science*, vol. 360, no. 1-2, pp. 476–482, 2010.

[275] A. Celzard and V. Fierro, "Preparing a suitable material designed for methane storage: A comprehensive report," *Energy & Fuels*, vol. 19, no. 2, pp. 573–583, 2005.

[276] J. L. Mendoza-Cortes, W. A. Goddard, H. Furukawa, and O. M. Yaghi, "A covalent organic framework that exceeds the DOE 2015 volumetric target for H_2 uptake at 298 k," *The Journal of Physical Chemistry Letters*, vol. 3, no. 18, pp. 2671–2675, 2012.

[277] A. M. Ribeiro, J. C. Santos, A. E. Rodrigues, and S. Rifflart, "Pressure swing adsorption process in coal to Fischer-Tropsch fuels with CO_2 capture," *Energy & Fuels*, vol. 26, no. 2, pp. 1246–1253, 2012.

[278] H. Bux, F. Liang, Y. Li, J. Cravillon, M. Wiebcke, and J. Caro, "Zeolitic imidazolate framework membrane with molecular sieving properties by microwave-assisted solvothermal synthesis," *Journal of the American Chemical Society*, vol. 131, no. 44, pp. 16000–16001, 2009.

[279] D. Fairen-Jimenez, S. A. Moggach, M. T. Wharmby, P. A. Wright, S. Parsons, and T. Duren, "Opening the gate: Framework flexibility in ZIF-8 explored by experiments and simulations," *Journal of the American Chemical Society*, vol. 133, no. 23, pp. 8900–8902, 2011.

[280] D. Peralta, G. Chaplais, A. Simon-Masseron, K. Barthelet, C. Chizallet, A.-A. Quoineaud, and G. D. Pirngruber, "Comparison of the behavior of metal-organic frameworks and zeolites for hydrocarbon separations," *Journal of the American Chemical Society*, vol. 134, no. 19, pp. 8115–8126, 2012.

[281] Y.-S. Li, F.-Y. Liang, H. Bux, A. Feldhoff, W.-S. Yang, and J. Caro, "Molecular sieve membrane: Supported metal-organic framework with high hydrogen selectivity," *Angewandte Chemie (International ed. in English)*, vol. 49, no. 3, pp. 548–551, 2010.

[282] A. Huang, H. Bux, F. Steinbach, and J. Caro, "Molecular-sieve membrane with hydrogen permselectivity: ZIF-22 in LTA topology prepared with 3-aminopropyltriethoxysilane as covalent linker," *Angewandte Chemie (International ed. in English)*, vol. 49, no. 29, pp. 4958–4961, 2010.

[283] A. Huang, W. Dou, and J. Caro, "Steam-stable zeolitic imidazolate framework ZIF-90 membrane with hydrogen selectivity through covalent functionalization," *Journal of the American Chemical Society*, vol. 132, no. 44, pp. 15562–15564, 2010.

[284] Y. Houndonougbo, C. Signer, N. He, W. Morris, H. Furukawa, K. G. Ray, D. L. Olmsted, M. Asta, B. B. Laird, and O. M. Yaghi, "A combined experimental-computational investigation of methane adsorption and selectivity in a series of isoreticular zeolitic imidazolate frameworks," *The Journal of Physical Chemistry C*, vol. 117, no. 20, pp. 10326–10335, 2013.

[285] S. C. Reyes, Z. Ni, C. S. Paur, P. Kortunov, J. Zengel, H. W. Deckman. U. S. Patent US Patent 8192709 B2.

[286] S. Bourrelly, B. Moulin, A. Rivera, G. Maurin, S. Devautour-Vinot, C. Serre, T. Devic, P. Horcajada, A. Vimont, G. Clet, M. Daturi, J.-C. Lavalley, S. Loera-Serna, R. Denoyel, P. L. Llewellyn, and G. Férey, "Explanation of the adsorption of polar vapors in the highly flexible metal organic framework MIL-53(Cr)," *Journal of the American Chemical Society*, vol. 132, no. 27, pp. 9488–9498, 2010.

[287] M. T. Wharmby, S. Henke, T. D. Bennett, S. R. Bajpe, I. Schwedler, S. P. Thompson, F. Gozzo, P. Simoncic, C. Mellot-Draznieks, H. Tao, Y. Yue, and A. K. Cheetham, "Extreme flexibility in a zeolitic imidazolate framework: Porous to dense phase transition in desolvated ZIF-4," *Angewandte Chemie (International ed. in English)*, vol. 54, no. 22, pp. 6447–6451, 2015.

[288] C. Gücüyener, J. van den Bergh, J. Gascon, and F. Kapteijn, "Ethane/ethene separation turned on its head: Selective ethane adsorption on the metal-organic framework ZIF-7 through a gate-opening mechanism," *Journal of the American Chemical Society*, vol. 132, no. 50, pp. 17704–17706, 2010.

[289] M. Hartmann, S. Kunz, D. Himsl, O. Tangermann, S. Ernst, and A. Wagener, "Adsorptive separation of isobutene and isobutane on $Cu_3(BTC)_2$," *Langmuir*, vol. 24, no. 16, pp. 8634–8642, 2008.

[290] V. F. Martins, A. M. Ribeiro, A. Ferreira, U.-H. Lee, Y. K. Hwang, J.-S. Chang, J. M. Loureiro, and A. E. Rodrigues, "Ethane/ethylene separation on a copper-benzene-1,3,5-tricarboxylate MOF," *Separation and Purification Technology*, vol. 149, pp. 445–456, 2015.

[291] N. Lamia, M. Jorge, M. A. Granato, F. A. Almeida Paz, H. Chevreau, and A. E. Rodrigues, "Adsorption of propane, propylene and isobutane on a metal–organic framework: Molecular simulation and experiment," *Chemical Engineering Science*, vol. 64, no. 14, pp. 3246–3259, 2009.

[292] A. Mundstock, U. Böhme, B. Barth, M. Hartmann, and J. Caro, "Propylen/Propan-Trennung im Festbettadsorber und durch Membranpermeation," *Chemie Ingenieur Technik*, vol. 85, no. 11, pp. 1694–1699, 2013.

[293] J.-W. Yoon, I.-T. Jang, K.-Y. Lee, Y.-K. Hwang, and J.-S. Chang, "Adsorptive separation of propylene and propane on a porous metal-organic framework, copper trimesate," *Bulletin of the Korean Chemical Society*, vol. 31, no. 1, pp. 220–223, 2010.

[294] A. F. Ferreira, J. C. Santos, M. G. Plaza, N. Lamia, J. M. Loureiro, and A. E. Rodrigues, "Suitability of Cu-BTC extrudates for propane-propylene separation by adsorption processes," *Chemical Engineering Journal*, vol. 167, no. 1, pp. 1–12, 2011.

[295] K. Li, D. H. Olson, J. Seidel, T. J. Emge, H. Gong, H. Zeng, and J. Li, "Zeolitic imidazolate frameworks for kinetic separation of propane and propene," *Journal of the American Chemical Society*, vol. 131, no. 30, pp. 10368–10369, 2009.

[296] U. Böhme, C. Paula, V. R. Reddy Marthala, J. Caro, and M. Hartmann, "Ungewöhnliche Adsorptions- und Trenneigenschaften des Molekularsiebs ZIF-8," *Chemie Ingenieur Technik*, vol. 85, no. 11, pp. 1707–1713, 2013.

[297] H. T. Kwon and H.-K. Jeong, "Highly propylene-selective supported zeolite imidazolate framework (ZIF-8) membranes synthesized by rapid microwave-assisted seeding and secondary growth," *Chemical communications (Cambridge, England)*, vol. 49, no. 37, pp. 3854–3856, 2013.

[298] M. Askari and T.-S. Chung, "Natural gas purification and olefin/paraffin separation using thermal cross-linkable Co-polyimide/ZIF-8-mixed matrix membranes," *Journal of Membrane Science*, vol. 444, pp. 173–183, 2013.

[299] Y. Pan, T. Li, G. Lestari, and Z. Lai, "Effective separation of propylene/propane binary mixtures by ZIF-8 membranes," *Journal of Membrane Science*, vol. 390-391, pp. 93–98, 2012.

[300] D.-L. Chen, N. Wang, C. Xu, G. Tu, W. Zhu, and R. Krishna, "A combined theoretical and experimental analysis on transient breakthroughs of C_2H_6/C_2H_4 in fixed beds packed with ZIF-7," *Microporous and Mesoporous Materials*, vol. 208, pp. 55–65, 2015.

[301] J. van den Bergh, C. Gücüyener, E. A. Pidko, E. J. M. Hensen, J. Gascon, and F. Kapteijn, "Understanding the anomalous alkane selectivity of ZIF-7 in the separation of light alkane/alkene mixtures," *Chemistry (Weinheim an der Bergstrasse, Germany)*, vol. 17, no. 32, pp. 8832–8840, 2011.

[302] M. Hartmann, U. Bohme, M. Hovestadt, and C. Paula, "Adsorptive separation of olefin/paraffin mixtures with ZIF-4," *Langmuir*, vol. 31, no. 45, pp. 12382–12389, 2015.

[303] S. Japip, H. Wang, Y. Xiao, and T. Shung Chung, "Highly permeable zeolitic imidazolate framework (ZIF)-71 nano-particles enhanced polyimide membranes for gas separation," *Journal of Membrane Science*, vol. 467, pp. 162–174, 2014.

[304] C. Altintas and S. Keskin, "Computational screening of MOFs for C_2H_6/C_2H_4 and C_2H_6/CH_4 separations," *Chemical Engineering Science*, vol. 139, pp. 49–60, 2016.

[305] J. Kim, L.-C. Lin, R. L. Martin, J. A. Swisher, M. Haranczyk, and B. Smit, "Large-scale computational screening of zeolites for ethane/ethene separation," *Langmuir*, vol. 28, no. 32, pp. 11914–11919, 2012.

[306] R. Krishna and J. M. van Baten, "Investigating the relative influences of molecular dimensions and binding energies on diffusivities of guest species inside nanoporous crystalline materials," *Journal of Physical Chemistry C*, vol. 116, no. 44, pp. 23556–23568, 2012.

[307] M. Jorge, N. Lamia, and A. E. Rodrigues, "Molecular simulation of propane/propylene separation on the metal-organic framework CuBTC," *Colloids and Surfaces A: Physicochemical and Engineering Aspects*, vol. 357, no. 1-3, pp. 27–34, 2010.

[308] M. Jorge, M. Fischer, J. R. B. Gomes, C. Siquet, J. C. Santos, and A. E. Rodrigues, "Accurate model for predicting adsorption of olefins and paraffins on MOFs with open metal sites," *Industrial & Engineering Chemistry Research*, vol. 53, no. 40, pp. 15475–15487, 2014.

[309] L. Zhang, Q. Li, Z. Lu, and X. Wang, "Understanding adsorption and separation behavior of shorter chain alkane mixtures in zeolitic imidazolate frameworks by molecular simulations," *Procedia Computer Science*, vol. 4, pp. 1193–1202, 2011.

[310] Y. Wu, H. Chen, D. Liu, Y. Qian, and H. Xi, "Adsorption and separation of ethane/ethylene on ZIFs with various topologies: Combining GCMC simulation with the ideal adsorbed solution theory (IAST)," *Chemical Engineering Science*, vol. 124, pp. 144–153, 2015.

[311] W. D. Cornell, P. Cieplak, C. I. Bayly, I. R. Gould, K. M. Merz, D. M. Ferguson, D. C. Spellmeyer, T. Fox, J. W. Caldwell, and P. A. Kollman, "A second generation force field for the simulation of proteins, nucleic acids, and organic molecules," *Journal of the American Chemical Society*, vol. 117, no. 19, pp. 5179–5197, 1995.

[312] B. R. Brooks, R. E. Bruccoleri, B. D. Olafson, D. J. States, S. Swaminathan, and M. Karplus, "CHARMM: A program for macromolecular energy, minimization, and dynamics calculations," *Journal of Computational Chemistry*, vol. 4, no. 2, pp. 187–217, 1983.

[313] M. A. Addicoat, N. Vankova, I. F. Akter, and T. Heine, "Extension of the universal force field to metal-organic frameworks," *Journal of Chemical Theory and Computation*, vol. 10, no. 2, pp. 880–891, 2014.

[314] L. Chen, L. Grajciar, P. Nachtigall, and T. Düren, "Accurate prediction of methane adsorption in a metal-organic framework with unsaturated metal sites by direct implementation of an ab initio derived potential energy surface in gcmc simulation," *Journal of Physical Chemistry C*, p. 111101104955009, 2011.

[315] J. A. Gee and D. S. Sholl, "Prediction of adsorption properties of cyclic hydrocarbons in MOFs using DFT-derived force fields," *Journal of Physical Chemistry C*, vol. 119, no. 29, pp. 16920–16926, 2015.

[316] J. G. McDaniel, S. Li, E. Tylianakis, R. Q. Snurr, and J. R. Schmidt, "Evaluation of force field performance for high-throughput screening of gas uptake in metal–organic frameworks," *Journal of Physical Chemistry C*, vol. 119, no. 6, pp. 3143–3152, 2015.

[317] J. G. McDaniel, K. Yu, and J. R. Schmidt, "Ab initio, physically motivated force fields for CO_2 adsorption in zeolitic imidazolate frameworks," *Journal of Physical Chemistry C*, vol. 116, no. 2, pp. 1892–1903, 2012.

[318] H. Fang, H. Demir, P. Kamakoti, and D. S. Sholl, "Recent developments in first-principles force fields for molecules in nanoporous materials," *Journal of Materials Chemistry A*, vol. 2, no. 2, pp. 274–291, 2014.

[319] L. Hertäg, H. Bux, J. Caro, C. Chmelik, T. Remsungnen, M. Knauth, and S. Fritzsche, "Diffusion of CH_4 and H_2 in zif-8," *Journal of Membrane Science*, vol. 377, no. 1-2, pp. 36–41, 2011.

[320] J. Pérez-Pellitero, H. Amrouche, F. R. Siperstein, G. Pirngruber, C. Nieto-Draghi, G. Chaplais, A. Simon-Masseron, D. Bazer-Bachi, D. Peralta, and N. Bats, "Adsorption of CO_2, CH_4, and N_2 on zeolitic imidazolate frameworks: Experiments and simulations," *Chemistry - A European Journal*, vol. 16, no. 5, pp. 1560–1571, 2010.

[321] D. Fairen-Jimenez, R. Galvelis, A. Torrisi, A. D. Gellan, M. T. Wharmby, P. A. Wright, C. Mellot-Draznieks, and T. Düren, "Flexibility and swing effect on the adsorption of energy-related gases on ZIF-8: Combined experimental and simulation study," *Dalton transactions (Cambridge, England : 2003)*, vol. 41, no. 35, pp. 10752–10762, 2012.

[322] R. P. Lively, M. E. Dose, J. A. Thompson, B. A. McCool, R. R. Chance, and W. J. Koros, "Ethanol and water adsorption in methanol-derived ZIF-71," *Chemical communications (Cambridge, England)*, vol. 47, no. 30, pp. 8667–8669, 2011.

[323] A. L. Myers, "Thermodynamics of adsorption in porous materials," *AIChE Journal*, vol. 48, no. 1, pp. 145–160, 2002.

[324] A. Battisti, S. Taioli, and G. Garberoglio, "Zeolitic imidazolate frameworks for separation of binary mixtures of CO_2, CH_4, N_2 and H_2: A computer simulation investigation," *Microporous and Mesoporous Materials*, vol. 143, no. 1, pp. 46–53, 2011.

[325] C. D. Wick, M. G. Martin, and J. I. Siepmann, "Transferable potentials for phase equilibria. 4. united-atom description of linear and branched alkenes and alkylbenzenes," *The Journal of Physical Chemistry B*, vol. 104, no. 33, pp. 8008–8016, 2000.

[326] D. Dubbeldam, S. Calero, T. J. H. Vlugt, R. Krishna, T. L. M. Maesen, and B. Smit, "United atom force field for alkanes in nanoporous materials," *The Journal of Physical Chemistry B*, vol. 108, no. 33, pp. 12301–12313, 2004.

[327] B. Liu, B. Smit, F. Rey, S. Valencia, and S. Calero, "A new united atom force field for adsorption of alkenes in zeolites," *The Journal of Physical Chemistry C*, vol. 112, no. 7, pp. 2492–2498, 2008.

[328] M. Thommes, K. Kaneko, A. V. Neimark, J. P. Olivier, F. Rodriguez-Reinoso, J. Rouquerol, and K. S. Sing, "Physisorption of gases, with special reference to the evaluation of surface area and pore size distribution (iupac technical report)," *Pure and Applied Chemistry*, vol. 87, no. 9-10, p. 160, 2015.

[329] S. Grimme, "Semiempirical GGA-type density functional constructed with a long-range dispersion correction," *Journal of Computational Chemistry*, vol. 27, no. 15, pp. 1787–1799, 2006.

[330] J.-G. Jee, M.-B. Kim, and C.-H. Lee, "Pressure swing adsorption processes to purify oxygen using a carbon molecular sieve," *Chemical Engineering Science*, vol. 60, no. 3, pp. 869–882, 2005.

[331] G. Narin, V. F. Martins, M. Campo, A. M. Ribeiro, A. Ferreira, J. C. Santos, K. Schumann, and A. E. Rodrigues, "Light olefins/paraffins separation with 13X zeolite binderless beads," *Separation and Purification Technology*, vol. 133, pp. 452–475, 2014.

[332] J. Fu, Y. Liu, Y. Tian, and J. Wu, "Density functional methods for fast screening of metal-organic frameworks for hydrogen storage," *The Journal of Physical Chemistry C*, vol. 119, no. 10, pp. 5374–5385, 2015.

[333] J. Pires, M. L. Pinto, and V. K. Saini, "Ethane selective IRMOF-8 and its significance in ethane-ethylene separation by adsorption," *ACS applied materials & interfaces*, vol. 6, no. 15, pp. 12093–12099, 2014.

[334] S. Bendt, M. Hovestadt, U. Böhme, C. Paula, M. Döpken, M. Hartmann, and F. J. Keil, "Olefin/paraffin separation potential of ZIF-9 and ZIF-71: A combined experimental and theoretical study," *European Journal of InOrganic Chemistry*, vol. 2016, no. 27, pp. 4440–4449, 2016.

[335] T. Düren, F. Millange, G. Férey, K. S. Walton, and R. Q. Snurr, "Calculating geometric surface areas as a characterization tool for metal-organic frameworks," *Journal of Physical Chemistry C*, vol. 111, no. 42, pp. 15350–15356, 2007.

[336] F.-X. Coudert and A. H. Fuchs, "Computational characterization and prediction of metal-organic framework properties," *Coordination Chemistry Reviews*, vol. 307, pp. 211–236, 2016.

[337] F. Debatin, J. Möllmer, S. S. Mondal, K. Behrens, A. Möller, R. Staudt, A. Thomas, and H.-J. Holdt, "Mixed gas adsorption of carbon dioxide and methane on a series of isoreticular microporous metal-organic frameworks based on 2-substituted imidazolate-4-amide-5-imidates," *Journal of Materials Chemistry*, vol. 22, no. 20, p. 10221, 2012.

[338] T. F. Willems, C. H. Rycroft, M. Kazi, J. C. Meza, and M. Haranczyk, "Algorithms and tools for high-throughput geometry-based analysis of crystalline porous materials," *Microporous and Mesoporous Materials*, vol. 149, no. 1, pp. 134–141, 2012.

[339] R. L. Martin, T. F. Willems, L.-C. Lin, J. Kim, J. A. Swisher, B. Smit, and M. Haranczyk, "Similarity-driven discovery of zeolite materials for adsorption-based separations," *ChemPhysChem*, vol. 13, no. 16, pp. 3595–3597, 2012.

[340] S. Calero and P. Gómez-Álvarez, "Underlying adsorption mechanisms of water in hydrophobic and hydrophilic zeolite imidazolate frameworks: ZIF-71 and ZIF-90," *Journal of Physical Chemistry C*, vol. 119, no. 41, pp. 23774–23780, 2015.

[341] L. Ding and A. O. Yazaydin, "The effect of SO_2 on CO_2 capture in zeolitic imidazolate frameworks," *Phys. Chem. Chem. Phys.*, vol. 15, no. 28, pp. 11856–11861, 2013.

[342] H. Huang, W. Zhang, D. Liu, B. Liu, G. Chen, and C. Zhong, "Effect of temperature on gas adsorption and separation in ZIF-8: A combined experimental and molecular simulation study," *Chemical Engineering Science*, vol. 66, no. 23, pp. 6297–6305, 2011.

[343] J. G. McDaniel and J. R. Schmidt, "Robust, transferable, and physically motivated force fields for gas adsorption in functionalized zeolitic imidazolate frameworks," *The Journal of Physical Chemistry C*, vol. 116, no. 26, pp. 14031–14039, 2012.

[344] L. Zhang, G. Wu, and J. Jiang, "Adsorption and diffusion of CO_2 and CH_4 in zeolitic imidazolate framework-8: Effect of structural flexibility," *The Journal of Physical Chemistry C*, vol. 118, no. 17, pp. 8788–8794, 2014.

[345] W. Morris, B. Leung, H. Furukawa, O. K. Yaghi, N. He, H. Hayashi, Y. Houndonougbo, M. Asta, B. B. Laird, and O. M. Yaghi, "A combined experimental-computational investigation of carbon dioxide capture in a series of isoreticular zeolitic imidazolate frameworks," *Journal*

of the American Chemical Society, vol. 132, no. 32, pp. 11006–11008, 2010.

[346] W. Mu, D. Liu, and C. Zhong, "A computational study of the effect of doping metals on CO_2/CH_4 separation in metal-organic frameworks," *Microporous and Mesoporous Materials*, vol. 143, no. 1, pp. 66–72, 2011.

[347] T. Chokbunpiam, R. Chanajaree, O. Saengsawang, S. Reimann, C. Chmelik, S. Fritzsche, J. Caro, T. Remsungnen, and S. Hannongbua, "The importance of lattice flexibility for the migration of ethane in ZIF-8: Molecular dynamics simulations," *Microporous and Mesoporous Materials*, vol. 174, pp. 126–134, 2013.

[348] P. Krokidas, M. Castier, S. Moncho, D. N. Sredojevic, E. N. Brothers, H. T. Kwon, H.-K. Jeong, J. S. Lee, and I. G. Economou, "ZIF-67 framework: A promising new candidate for propylene/propane separation. experimental data and molecular simulations," *The Journal of Physical Chemistry C*, vol. 120, no. 15, pp. 8116–8124, 2016.

[349] C. Chmelik, J. van Baten, and R. Krishna, "Hindering effects in diffusion of CO_2/CH_4 mixtures in ZIF-8 crystals," *Journal of Membrane Science*, vol. 397-398, pp. 87–91, 2012.

[350] E. Haldoupis, T. Watanabe, S. Nair, and D. S. Sholl, "Quantifying large effects of framework flexibility on diffusion in MOFs: CH_4 and CO_2 in ZIF-8," *ChemPhysChem*, vol. 13, no. 15, pp. 3449–3452, 2012.

[351] E. Pantatosaki, G. Megariotis, A.-K. Pusch, C. Chmelik, F. Stallmach, and G. K. Papadopoulos, "On the impact of sorbent mobility on the sorbed phase equilibria and dynamics: A study of methane and carbon dioxide within the zeolite imidazolate framework-8," *Journal of Physical Chemistry C*, vol. 116, no. 1, pp. 201–207, 2012.

[352] F. Stallmach, A.-K. Pusch, T. Splith, C. Horch, and S. Merker, "NMR relaxation and diffusion studies of methane and carbon dioxide in nanoporous ZIF-8 and ZSM-58," *Microporous and Mesoporous Materials*, vol. 205, pp. 36–39, 2015.

[353] H. Jobic, D. I. Kolokolov, A. G. Stepanov, M. M. Koza, and J. Ollivier, "Diffusion of CH_4 in ZIF-8 studied by quasi-elastic neutron scattering," *Journal of Physical Chemistry C*, vol. 119, no. 28, pp. 16115–16120, 2015.

[354] F.-X. Coudert, A. Boutin, M. Jeffroy, C. Mellot-Draznieks, and A. H. Fuchs, "Thermodynamic methods and models to study flexible fetal-organic frameworks," *ChemPhysChem*, vol. 12, no. 2, pp. 247–258, 2011.

[355] X. Wu, J. Huang, W. Cai, and M. Jaroniec, "Force field for ZIF-8 flexible frameworks: Atomistic simulation of adsorption, diffusion of pure gases as CH_4 , H_2, CO_2 and N_2," *RSC Advances*, vol. 4, no. 32, pp. 16503–16511, 2014.

[356] K. G. Ray, D. L. Olmsted, J. M. R. Burton, Y. Houndonougbo, B. B. Laird, and M. Asta, "Gas membrane selectivity enabled by zeolitic imidazolate framework electrostatics," *Chemistry of Materials*, vol. 26, no. 13, pp. 3976–3985, 2014.

[357] Y. Duan, C. Wu, S. Chowdhury, M. C. Lee, G. Xiong, W. Zhang, R. Yang, P. Cieplak, R. Luo, T. Lee, J. Caldwell, J. Wang, and P. Kollman, "A point-charge force field for molecular mechanics simulations of proteins based on condensed-phase quantum mechanical calculations," *Journal of Computational Chemistry*, vol. 24, no. 16, pp. 1999–2012, 2003.

[358] Z. Hu, L. Zhang, and J. Jiang, "Development of a force field for zeolitic imidazolate framework-8 with structural flexibility," *The Journal of Chemical Physics*, vol. 136, no. 24, p. 244703, 2012.

[359] C. Chmelik, H. Bux, J. Caro, L. Heinke, F. Hibbe, T. Titze, and J. Kärger, "Mass transfer in a nanoscale material enhanced by an opposing flux," *Phys. Rev. Lett.*, vol. 104, no. 8, p. 085902, 2010.

[360] A. Heyden, *Transition from Molecular Simulation of Adsorption and Diffusion to Process Simulation of a PSA Module*. Diploma thesis, TUHH, Hamburg, 2000.

[361] A. Mersmann, M. Kind, and J. Stichlmair, *Thermische Verfahrenstechnik: Grundlagen und Methoden*. Chemische Technik Verfahrenstechnik, Berlin: Springer, 2. edition ed., 2005.

[362] M. Bohnet, *Mechanische Verfahrenstechnik*. Hoboken: John Wiley & Sons, 2012.

[363] D. M. Ruthven, *Principles of Adsorption and Adsorption Processes*. A Wiley-Interscience publication, New York: Wiley, 1984.

[364] R. Haghpanah, A. Majumder, R. Nilam, A. Rajendran, S. Farooq, I. A. Karimi, and M. Amanullah, "Multiobjective optimization of a four-step adsorption process for postcombustion CO_2 capture via finite volume simulation," *Industrial & Engineering Chemistry Research*, vol. 52, no. 11, pp. 4249–4265, 2013.

[365] R. Haghpanah, A. Rajendran, S. Farooq, and I. A. Karimi, "Optimization of one- and two-staged kinetically controlled CO_2 capture processes from postcombustion flue gas on a carbon molecular sieve," *Industrial & Engineering Chemistry Research*, vol. 53, no. 22, pp. 9186–9198, 2014.

[366] C.-T. Chou and C.-Y. Chen, "Carbon dioxide recovery by vacuum swing adsorption," *Separation and Purification Technology*, vol. 39, no. 1-2, pp. 51–65, 2004.

[367] C. A. Grande and A. E. Rodrigues, "Propane/propylene separation by pressure swing adsorption using zeolite 4A," *Industrial & Engineering Chemistry Research*, vol. 44, no. 23, pp. 8815–8829, 2005.

[368] L. W. Bruch, M. W. Cole, and E. Zaremba, *Physical Adsorption: Forces and Phenomena*. Dover books on physics, Mineola NY: Dover, 2nd ed., 2007.

[369] H.-J. Bungartz, S. Zimmer, M. Buchholz, and D. Pflüger, *Modellbildung und Simulation: Eine anwendungsorientierte Einführung*. eXamen.press, Berlin and Heidelberg: Springer Spektrum, 2. edition ed., 2013.

[370] J. Schell, N. Casas, D. Marx, and M. Mazzotti, "Precombustion CO_2 capture by pressure swing adsorption (PSA): Comparison of laboratory PSA experiments and simulations," *Industrial & Engineering Chemistry Research*, vol. 52, no. 24, pp. 8311–8322, 2013.

[371] C. A. Grande, "Advances in pressure swing adsorption for gas separation," *ISRN Chemical Engineering*, vol. 2012, no. 9, pp. 1–13, 2012.

[372] B. Smit, J. A. Reimer, C. M. Oldenburg, and I. C. Bourg, *Introduction to Carbon Capture and Sequestration*, vol. 1st of *The Berkeley lectures on energy*. London and Singapore: Imperial College Press, 2014.

[373] J. D. Seader and E. J. Henley, *Separation Process Principles*. Hoboken, NJ: Wiley, 2. ed., 2006.

[374] E. J. García, J. Pérez-Pellitero, G. D. Pirngruber, C. Jallut, M. Palomino, F. Rey, and S. Valencia, "Tuning the adsorption properties of zeolites as adsorbents for CO_2 separation: Best compromise between the working capacity and selectivity," *Industrial & Engineering Chemistry Research*, vol. 53, no. 23, pp. 9860–9874, 2014.

[375] N. Sundaram and R. T. Yang, "On the pseudomultiplicity of pressure swing adsorption periodic states," *Industrial and Engineering Chemistry Research*, vol. 37, no. 1, pp. 154–158, 1998.

[376] Charles W. Skarstrom, "Method and apparatus for fractionating gaseous mixtures by adsorption." U. S. Patent US2944627A, 1960.

[377] P. Guerin de Montgareuil and D. Domine, "Process for separating a binary gaseous mixture by adsorption." U. S. Patent US3155468, 1964.

[378] J. L. Wagner, "Selective adsorption process." U. S. Patent US3430418, 1969.

[379] J. Xu and E. L. Weist Jr., "Six bed pressure swing adsorption process with four steps of pressure equalization." U. S. Patent US6454838, 2002.

[380] J. Xu, D. L. Rarig, T. A. Cook, K. K. Hsu, M. Schoonover, and R. Agrawal, "Pressure swing adsorption process with reduced pressure equalization time." U. S. Patent US6565628, 2003.

[381] S. P. Reynolds, A. D. Ebner, and J. A. Ritter, "Stripping PSA cycles for CO_2 recovery from flue gas at high temperature using a hydrotalcite-like adsorbent," *Industrial & Engineering Chemistry Research*, vol. 45, no. 12, pp. 4278–4294, 2006.